

Swirling pipe flow with axial strain : experiment and large eddy simulation

Citation for published version (APA):

Moene, A. F. (2003). *Swirling pipe flow with axial strain : experiment and large eddy simulation*. [Phd Thesis 1 (Research TU/e / Graduation TU/e), Applied Physics and Science Education]. Technische Universiteit Eindhoven. <https://doi.org/10.6100/IR565932>

DOI:

[10.6100/IR565932](https://doi.org/10.6100/IR565932)

Document status and date:

Published: 01/01/2003

Document Version:

Publisher's PDF, also known as Version of Record (includes final page, issue and volume numbers)

Please check the document version of this publication:

- A submitted manuscript is the version of the article upon submission and before peer-review. There can be important differences between the submitted version and the official published version of record. People interested in the research are advised to contact the author for the final version of the publication, or visit the DOI to the publisher's website.
- The final author version and the galley proof are versions of the publication after peer review.
- The final published version features the final layout of the paper including the volume, issue and page numbers.

[Link to publication](#)

General rights

Copyright and moral rights for the publications made accessible in the public portal are retained by the authors and/or other copyright owners and it is a condition of accessing publications that users recognise and abide by the legal requirements associated with these rights.

- Users may download and print one copy of any publication from the public portal for the purpose of private study or research.
- You may not further distribute the material or use it for any profit-making activity or commercial gain
- You may freely distribute the URL identifying the publication in the public portal.

If the publication is distributed under the terms of Article 25fa of the Dutch Copyright Act, indicated by the "Taverne" license above, please follow below link for the End User Agreement:

www.tue.nl/taverne

Take down policy

If you believe that this document breaches copyright please contact us at:

openaccess@tue.nl

providing details and we will investigate your claim.

Swirling pipe flow with axial strain
Experiment and Large Eddy Simulation

Arnold F. Moene

Copyright ©2003, Arnold F. Moene

CIP-DATA LIBRARY TECHNISCHE UNIVERSITEIT EINDHOVEN

Moene, Arnold Frank

Swirling pipe flow with axial strain : experiment and large eddy simulation / Arnold Frank Moene. – Eindhoven : Technische Universiteit Eindhoven, 2003. –

Proefschrift.

ISBN 90-386-1695-3

NUGI 926

Trefw.: stroming ; pijpleidingen / interne turbulente stroming / roterende stroming / axiale vervorming / laser-Doppler anemometrie / numerieke simulatie

Subject headings: pipe flow / swirling flow / axial strain / turbulence / laser-Doppler velocimetry / Large Eddy Simulation

Swirling pipe flow with axial strain

Experiment and Large Eddy Simulation

PROEFSCHRIFT

ter verkrijging van de graad van doctor aan de Technische Universiteit Eindhoven, op
gezag van de Rector Magnificus, prof.dr. R.A. van Santen, voor een commissie
aangewezen door het college voor promoties in het openbaar te verdedigen op
donderdag 19 juni 2003 om 16.00 uur

Arnold F. Moene

geboren te Amsterdam

Dit proefschrift is goedgekeurd door de promotoren:
prof.dr.ir. G.J.F. van Heijst
en
prof.dr.ir. F.T.M. Nieuwstadt

Contents

1	Introduction	1
1.1	Turbulent swirling flow with axial strain	1
1.2	Methodology of turbulence research	3
1.2.1	General	3
1.2.2	This study	3
1.3	Aims of this research	4
1.4	Outline of the thesis	6
2	Turbulence subject to swirl and axial strain	9
2.1	Turbulence and basic equations	9
2.1.1	Navier-Stokes equations	9
2.1.2	Phenomena in turbulent flows	10
2.1.3	Reynolds-averaged equations	12
2.1.4	Equations for the Reynolds-stresses	13
2.1.5	Equations for incompressible flow in a cylindrical geometry	14
2.2	Swirl	14
2.2.1	The link between phenomena in swirling flows	15
2.2.2	Streamline curvature and stability	17
2.2.3	Rotation	19
2.2.4	Three-dimensionality	21
2.2.5	Swirl decay	22
2.3	Axial strain	23
2.3.1	Effect of axial strain on mean flow	24
2.3.2	Effect of axial strain on turbulence	25
2.3.3	Relaxation of strained flow	27
2.4	Combined effect of swirl and axial strain	28
2.4.1	Inviscid analysis of simplified swirling flows subject to axial strain	28
2.4.2	Turbulent flows with swirl and axial strain	30
2.5	To conclude	32
3	Laser Doppler measurements	35
3.1	Principles of Laser Doppler Anemometry	35
3.1.1	Fundamentals	36
3.1.2	Implementation	39
3.1.3	Error sources	41
3.2	Experimental set-up	42

3.2.1	Pipe system	43
3.2.2	LDA system: optics, positioning and data processing	46
3.3	Measurement strategy	54
3.3.1	Flow types	54
3.3.2	Processed data	55
3.3.3	Raw data	56
4	Numerical simulation of turbulence	57
4.1	Principles of Large Eddy Simulation	58
4.1.1	Filtering the governing equations	58
4.1.2	The relationship between filtering and the SGS-model	60
4.1.3	Subgrid scale-stress modelling	61
4.1.4	Solution of the Navier-Stokes equations: some numerical issues	68
4.1.5	Comparison between LES results and laboratory experiments	71
4.1.6	Sources of error in LES	71
4.2	An LES model for pipe flow with swirl and axial strain	72
4.2.1	Coordinate system	73
4.2.2	Spatial discretisation	74
4.2.3	Temporal discretisation and pressure solution	75
4.2.4	Sub-grid scale model	77
4.2.5	Boundary conditions	78
4.3	Strategy of the simulations	82
5	Analysis of laboratory measurements	85
5.1	Mean flow and Reynolds stresses: data	85
5.1.1	A note on the presentation of data	85
5.1.2	Flow with axial strain and no swirl	86
5.1.3	Flow with axial strain and swirl	91
5.2	Mean flow and Reynolds stresses: analysis	99
5.2.1	Interpretation of the observations	99
5.2.2	Development of the swirl number	103
5.2.3	Three-dimensionality in swirling flow	106
5.2.4	Comparison of stress-anisotropy between non-swirling and swirling flow	106
5.2.5	Rapid distortion analysis of normal stresses at centreline	112
5.3	Analysis of time series data	116
5.3.1	Spectra	116
5.3.2	Integral scales	119
5.4	To conclude	120
5.4.1	Axial strain without swirl	120
5.4.2	Axial strain with swirl	121

6	Results of numerical simulations	123
6.1	Validation of the LES results	123
6.1.1	A note on the presentation of results	123
6.1.2	Flow with axial strain	124
6.1.3	Flow with swirl and axial strain	126
6.2	Further analysis of LES results	138
6.2.1	Velocity and stress fields	138
6.2.2	Budgets for turbulent stresses	141
6.2.3	Stress anisotropy at the pipe axis	156
6.2.4	Axial development of the swirl number	157
6.3	To conclude	158
6.3.1	Axial strain without swirl	158
6.3.2	Axial strain with swirl	159
7	Conclusion	161
7.1	Current knowledge	161
7.2	Experimental results	162
7.2.1	Axial strain without swirl	162
7.2.2	Axial strain with swirl	162
7.3	Development of LES model and validation	163
7.3.1	Development	163
7.3.2	Validation	164
7.4	LES results	165
7.4.1	Axial strain without swirl	165
7.4.2	Axial strain with swirl	165
7.5	Perspectives	166
A	Statistical analysis of turbulent data	169
A.1	Averages	169
A.1.1	Reynolds decomposition	169
A.1.2	Types of averages	169
A.2	Statistical errors	171
A.2.1	Statistics derived from series of independent samples	171
A.2.2	Statistics derived from a continuous series	172
A.2.3	Statistics derived from discretely sampled series	172
A.2.4	Extension of error estimates to averaging in more dimensions	173
A.3	Estimation of statistical errors in LDA data and LES results	173
A.3.1	LDA data	173
A.3.2	LES fields	174

B	Auxiliary equations	177
B.1	Equations in cylindrical coordinates	177
B.1.1	Navier-Stokes equations	177
B.1.2	Reynolds stress budget equations	177
B.2	Equations in spectral space	180
B.2.1	Navier-Stokes equations in spectral space	181
B.2.2	Reynolds stress budget equations	181
C	On the relationship between streamline curvature and rotation in swirling flows	183
C.1	Two reference frames	183
C.2	Application to swirling flows	184
C.2.1	Solid-body rotation without an axial velocity component	184
C.2.2	Solid-body rotation including an axial velocity component	185
C.2.3	General rotation including an axial velocity component	185
D	Errors in LDA measurements due to geometrical uncertainties	187
D.1	Error due to imperfection of theodolite calibration	187
D.2	Errors due to imperfections of the positioning of the LDA	187
D.2.1	Rotation around the x_1 -axis	188
D.2.2	Rotation around the x_2 -axis	188
D.2.3	Rotation around the x_3 -axis	188
D.3	Errors in 3D measurements	188
D.4	Application of error estimates	189
E	Details on the LES model	191
E.1	Example of equations in transformed coordinates	191
E.2	Example of spatial discretisation: divergence	191
E.3	Details on boundary conditions	193
E.3.1	Implementation of wall boundary condition for u_r	193
E.3.2	Implementation of wall boundary condition for \widehat{p}'	193
E.4	Details on the radial grid spacing	194
E.5	Test of methods to generate swirl	195
F	Dependence of simulations of developed pipe flow on size and shape of the grid	201
F.1	Grid size dependence	201
F.2	Grid shape dependence	203
G	Wiggles or oscillations in Large Eddy Simulation of swirling pipe flow	207
G.1	Introduction	207
G.2	Wiggles	207
G.2.1	Role of mesh-Reynolds number	207
G.2.2	Aliasing	208
G.3	Solutions	209

G.4 Conclusion	211
H Pressure strain terms in turbulent flow through an axially rotating pipe	213
H.1 Intro	213
H.2 Models for the pressure strain tensor	213
H.3 The flow and the simulation	216
H.4 Results	216
H.4.1 Simulation results	216
H.4.2 Results on the parameterisations	216
H.5 Conclusion	217
References	221
Samenvatting	231
Dankwoord	235
Curriculum Vitae	237

1

Introduction

1.1 Turbulent swirling flow with axial strain

The three ingredients in the title of this section are depicted in figure 1.1: turbulence, swirl and axial strain. *Turbulent* flows are irregular, both in space and time. On one hand the fluid is in chaotic motion and is mixed efficiently. On the other hand there is some structure in the motion: fluctuations appear both at short time scales and longer time scales. *Swirling* flows are characterised by the fact that the fluid rotates around an axis that is parallel to the main flow direction. This results in a cork-screw type of motion. *Strain* is the deformation of a substance: the relative positions of particles change. In the case of *axial strain* the deformation is composed only of extension and compression (no shear). As an example, figure 1.1 shows axially symmetric axial strain: extension in one direction, compression in the two perpendicular directions.

Swirling flows may either occur inadvertently and be considered as a disturbance (Steenbergen and Voskamp, 1998) or may be generated on purpose. Applications of swirling flows include cyclone separators, swirling spray dryers, swirling furnaces, vortex tubes used for thermal separation, agitators etc. (Kuroda and Ogawa, 1986). The combination of swirl and axial strain occurs in a number of industrial applications. In axial cyclone separators a contraction may be used to enhance the rotation in the inlet region. In cyclone separators, based on recirculation, a contraction is used to enhance the return flow and ensure that material that is gathered near the centre will flow upward, whereas the heavier material near the wall leaves the separator at the lower end (see e.g. figure 1.2). Other situations in which both swirl and axial strain occur are various parts of turbomachinery. In those cases the axial strain may either have the form of a contraction or a diffuser. The combination of swirling flow and a diffuser is also used for the stabilisation of flames in combustion chambers.

Understanding of flows in configurations like those mentioned before can be obtained by measurements: experimental determination of the velocity field, wall pressure, temperatures or

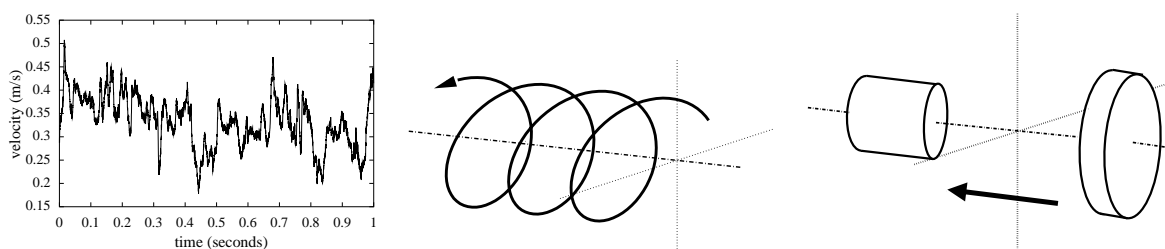


Figure 1.1: The three ingredients of this thesis: turbulence (left), swirl (centre) and axial strain (right).

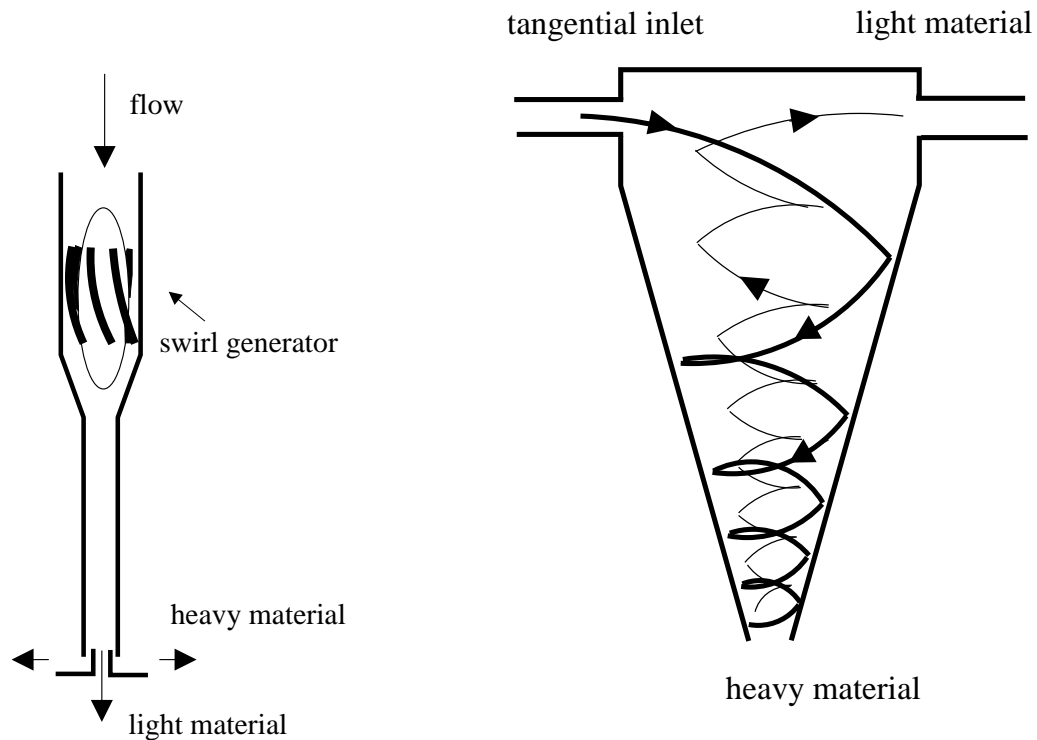


Figure 1.2: Sketches of cyclone separators: axial cyclone (left) and a tangential cyclone (right).

concentrations. However, there may be configurations in which measurements are difficult, if not impossible, or certain quantities may be hard to measure. Furthermore, it may happen that one needs to *predict* the flow in a not yet existing geometry. In those cases one needs to make a *model* of the flow. The main complication in such a model is how the turbulent character of the flow should be treated. Although it is becoming possible to fully calculate turbulent flows (in three dimensions and time-dependent), this is feasible only at low to moderate Reynolds numbers, and in simple geometries. Therefore, one usually reverts to a statistical description of the turbulence. This implies that the fluctuating quantities are characterised by their means, variances, covariances and possibly higher order moments, and models need to be devised that link those statistical quantities (see chapter 4). This is the research area of turbulence modelling.

In the context of turbulence modelling swirling flows with axial strain are considered 'complex flows' according to the definition of Bradshaw (1975):

... flows whose turbulence structure is affected by extra rates of strain (velocity gradients) in addition to the simple shear $\partial U/\partial y$, or by body forces: these effects are surprisingly large and can be spectacular.

The complexity of these flows is further discussed in chapter 2. It suffices here to state that, although increasingly successful, current turbulence models still have difficulty with some aspects of complex flows (e.g. Launder (1989) and Jakirlić *et al.* (2000)).

1.2 Methodology of turbulence research

1.2.1 General

Figure 1.3 gives a possible picture how different activities in turbulence research may be inter-related. Three different, but interrelated, ways of investigating turbulent flows be distinguished: theory, experiments and modelling. First, the left part of figure 1.3 is considered. Why are theories about turbulent flows developed in the first place? The answer is that theories may help to understand the processes that occur in a flow. This in turn may help to predict flows in –more or less– different configurations or conditions. Theoretical studies may rely on the governing equations, simplifications thereof, similarity reasoning or otherwise. But usually the development of theories will be inspired by experimental observations. Furthermore, once a theory has been developed, experimental results are needed to validate it. Finally, theoretical insights may lead to the development of models for a flow (in terms of parameterisations).

The next focus is on the role of experiments in turbulence research. In the first place, they may lead to more understanding of a flow, provided that the experiment has been designed such that the boundary conditions and initial conditions are well controlled. As mentioned before, experimental results may serve both as inspiration and validation for theories about the flow under consideration. Similarly, experimental results may also feed the development of turbulence models, often in terms of the determination of constants in a theoretical parametrisation (e.g. the Von Karman constant). Experimental validation should always be the final step in model *development*. Besides, experimental validation is useful when a model is *applied* to a flow that is slightly or grossly beyond the conditions for which it was developed.

Finally, the attention is focused on the role of models in turbulence research. Again, these are used to understand flows. One particular advantage of models over experiments is that the flow conditions in a model can be controlled extremely well. This opens the way to so-called parameter studies, in which important parameters in the flow are varied over a large range to see in which way the characteristics of the flow change. In that way models may also contribute to the development of theories. Especially, the results of Large Eddy Simulation (LES) and Direct Numerical Simulations (DNS) models are useful, since those give detailed spatial and temporal information on all variables in a flow. This information is (with a few exceptions) not accessible with experimental techniques. In some areas, LES and DNS results are already considered as pseudo-data (and thus would belong to the central panel in figure 1.3). Another important application of turbulence models is of course the prediction of practical flows. This is essential in the design of whatever structure or apparatus in which fluid flow is an issue.

1.2.2 This study

In the present study, only a subset of the activities sketched in figure 1.3 is present (see figure 1.4). The emphasis in this thesis is on experimentation and numerical simulation. The experiment is used to

- gain insight into the flow under consideration;
- validate theory;
- provide validation data for the numerical simulations.

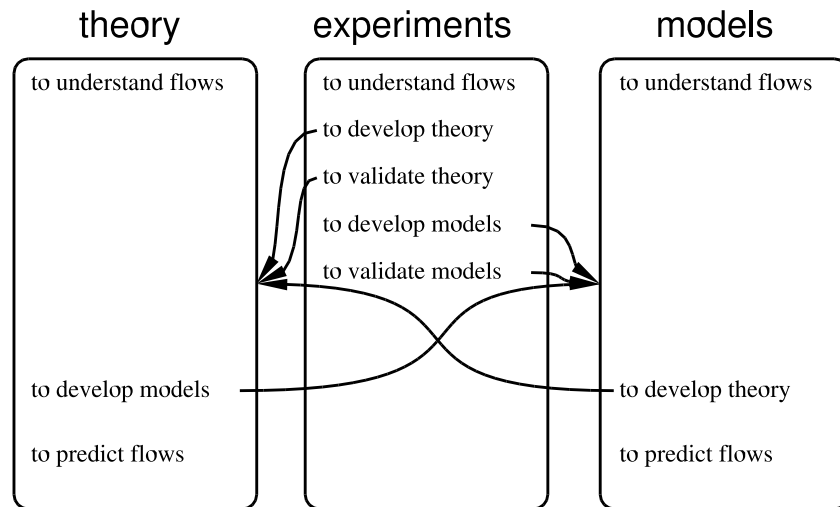


Figure 1.3: Sketch of relationships between different domains of turbulence research. In some cases the domains may not be as separate as sketched here: e.g. some theories about flows (e.g. K-diffusion theory) could as well be classified as models.

The numerical simulations in turn are used to

- better understand the flow, since they provide more and different data than the experiment;
- provide information on new flows, once the model is validated.

1.3 Aims of this research

The main objective of this thesis is to gain insight into the physics and modelling of turbulent swirling pipe flow with axial strain. More specifically, the configuration studied is the turbulent swirling pipe flow through a *contraction* (see figure 1.5).

The main objective can be translated into the following research questions:

- What is the current knowledge on the separate subjects of flows with swirl or axial strain, and on the combined effect of swirl and axial strain on turbulent flows?
- Which features and mechanisms can be derived from experimental data of swirling flow with axial strain, both in comparison to data *without* swirl but *with* strain, and in terms of Reynolds number effects? Apart from the conclusions drawn from the experimental data in this thesis, the data will be relevant as a benchmark for turbulence modellers as well.
- Which modifications need to be made to a Large Eddy Simulation model to apply it to a swirling flow with axial strain, and how well do the results match experimental data?
- Which features and mechanisms can be derived from LES results of turbulent (swirling) flow with axial strain?

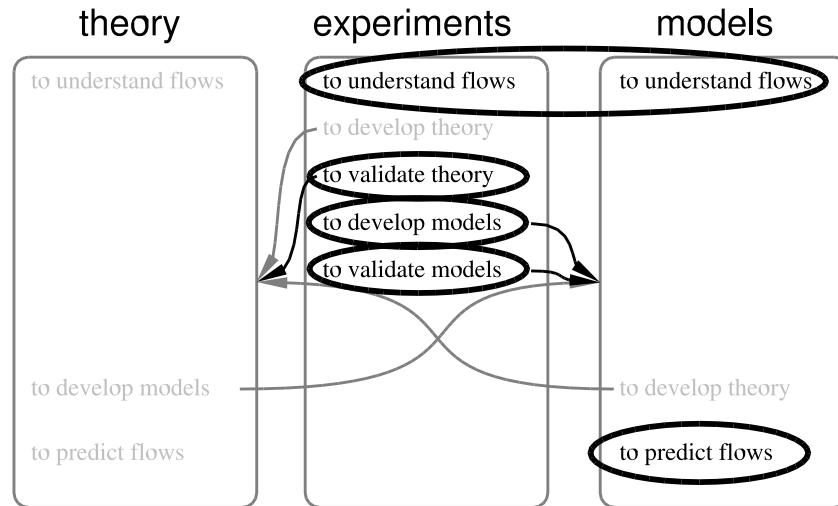


Figure 1.4: Sketch of the place of the present thesis in turbulence research.

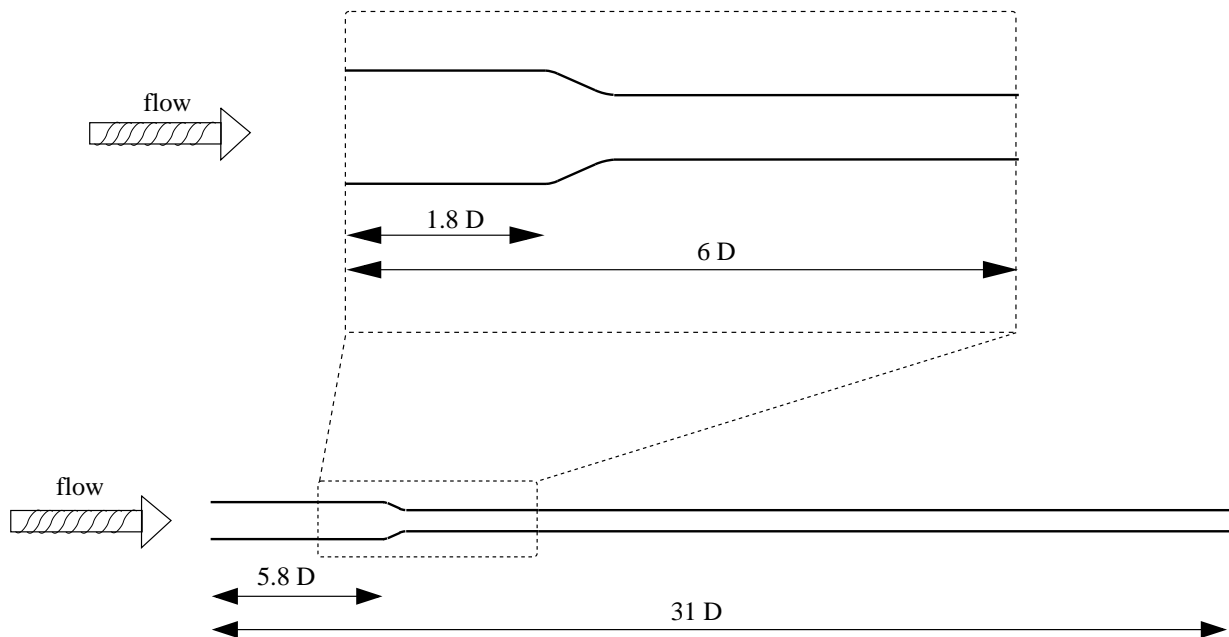


Figure 1.5: Configuration of the flow studied: swirling flow through a pipe contraction. Bottom: the domain of study for the laboratory experiment. Top: the domain used for the numerical simulations. Dimensions are expressed in the pipe diameter upstream of the contraction, D (70 mm); the pipe diameter downstream of the contraction is 40 mm.

2. Theory

turbulence
swirl
axial strain
swirl + axial strain

3. LDA

theory
experimental set-up

4. LES

theory
model development

5. Results LDA

data } axial strain
analysis } swirl + strain

6. Results LES

validation } axial strain
analysis } swirl + strain

Figure 1.6: Overview of the setup of this thesis. Not included are the introduction and the conclusion, as well as the appendices.

1.4 Outline of the thesis

The outline of this thesis is sketched in figure 1.6. Following this introduction, the thesis continues with a review of literature on various aspects of the flow under consideration, viz. turbulence, swirl, axial strain and the combined effect of swirl and axial strain (chapter 2). Then two chapters are devoted to the experimental and modelling techniques used:

- chapter 3 deals with the theory behind the experimental technique used: Laser Doppler Anemometry (LDA), and describes the experimental setup used in this study;
- chapter 4 highlights some relevant aspects of LES and describes the development of an LES model capable of simulating a swirling flow through a contraction.

The next two chapters present the results of the laboratory experiment and the numerical simulations:

- chapter 5 starts with a presentation and discussion of the laboratory results of the flows studied: swirling and non-swirling flow, both with axial strain. In the second part of the chapter the results are analysed in the light of the theoretical aspects presented in chapter 2.

- chapter 6 starts with a validation of the LES results, for swirling and non-swirling flow with axial strain. In the second part of the chapter those results of the LES are presented that have *not* been (and could not be) measured in the laboratory experiment.

Finally, chapter 7 concludes this thesis with a synthesis of the results of the previous chapters and a perspective of what could be the following steps.

This thesis contains a fair number of appendices that provide details for issues discussed in the respective chapters:

- Appendix A on statistical analysis of turbulent data supports chapters 2, 5 and 6.
- Appendix B presents some elaborate equations and supports chapters 2, 5 and 6
- Appendix C discusses the link between rotation and streamline curvature, two aspects of swirling flow that are dealt with in chapter 2.
- Appendix D summarises the results of Steenbergen (1995) regarding the errors in measured mean velocities and stresses, due to geometrical uncertainties in the experimental setup (relevant for chapters 3 and 5).
- Appendix E gives details on the LES model not covered in chapter 4.
- Appendices F and G discuss two numerical issues that surfaced during the development of the LES model (chapter 4).
- Appendix H presents the results of a separate study in which a Direct Numerical Simulation of a turbulent flow through a rotating pipe has been analysed. Although the configuration is different from the subject of this study, it is sufficiently related to warrant its inclusion.

2

Turbulence subject to swirl and axial strain

In the introductory chapter (section 1.1) the relevance was argued of turbulent flows in which both swirl and axial strain play a role. In order to better understand the dynamics of these types of flow, a first step is to highlight the various ingredients that contribute to this flow, i.e. turbulence (section 2.1), swirl (2.2) and axial strain (2.3). After understanding the contributing phenomena a complete picture of ‘swirling turbulent pipe flow subject to axial strain’ is expected to evolve: Section 2.4 discusses what is known at this moment of the combined effect of swirl and axial strain, and section 2.5 aims to summarise this chapter.

2.1 Turbulence and basic equations

For more than a century turbulent flows have been studied, and this has resulted in many, more or less commonly accepted, views on the nature of turbulence. However, none of the descriptions of turbulent flows has been successful in explaining all aspects of this flow (Tennekes and Lumley, 1972). In this section an introduction to the main aspects of turbulent flows will be given. This introduction is not meant to be exhaustive, but rather to provide the concepts and tools needed in forthcoming sections. For more information and details on turbulent flows the reader is referred to the numerous introductory and advanced textbooks that exist on the topic of turbulence. Examples are Tennekes and Lumley (1972), Hinze (1975) and Lesieur (1993).

The introduction starts with the presentation of the equations governing fluid flow. Subsequently phenomena and concepts regarding turbulent flows will be discussed. Finally, one technique to tackle the complexity of turbulent flows will be considered in more detail, i.e. the statistical description. The equations that describe the statistical properties of a turbulent flow are presented at the end of this section.

2.1.1 Navier-Stokes equations

In the case of an isothermal fluid, the fluid flow can be described with two conservation laws: the conservation of mass and the conservation of momentum. If it is furthermore assumed that the flow is incompressible, i.e. the density does not vary with pressure (Kundu, 1990), and that there are no other sources of density variations, the continuity equation reduces to:

$$\nabla \cdot \mathbf{u} = 0, \quad (2.1)$$

where \mathbf{u} is the velocity vector.

The conservation of momentum for a Newtonian fluid, assuming incompressibility, can be

expressed as:

$$\frac{\partial \mathbf{u}}{\partial t} + \nabla \cdot \mathbf{u}\mathbf{u} = -\frac{1}{\rho} \nabla p + \nabla \cdot \nu \mathbf{S} \quad (2.2)$$

where ρ is the density of the fluid, p is the pressure, ν is the kinematic viscosity and \mathbf{S} is the strain rate tensor¹: $\mathbf{S} = \frac{1}{2} (\nabla \mathbf{u} + (\nabla \mathbf{u})^T)$. Since in an isothermal fluid the viscosity is constant and $\nabla \cdot \mathbf{u} = 0$, the term $\nabla \cdot \nu \mathbf{S}$ can be replaced by $\nu \nabla^2 \mathbf{u}$. The resulting equation is known as the Navier-Stokes equation. Equations (2.1) and (2.2) form a system of four differential equations with four variables: the pressure and three components of the velocity vector. Given appropriate initial and boundary conditions and taking the pressure gradient as a parameter rather than a variable², these equations can be solved in principle, although the number of flows for which this is possible in practice is limited due to the non-linearity of the momentum equations.

The standard way to investigate the relative importance of the terms in (2.2), typical scales are assigned to all variables. Variables normalised by these typical scale are then expected to yield dimensionless variables that are of order 1. For the velocities a typical scale \mathcal{U} is used, and the lengths are scaled with \mathcal{L} . The pressure is scaled using the velocity scale as $\rho \mathcal{U}^2$ and the time scale is constructed as \mathcal{L}/\mathcal{U} . The dimensionless version of a variable (say x) is denoted by \check{x} . The scaled —dimensionless— version of (2.2) becomes (after division by $\mathcal{U}^2/\mathcal{L}$):

$$\frac{\partial \check{\mathbf{u}}}{\partial \check{t}} + \nabla \cdot \check{\mathbf{u}}\check{\mathbf{u}} = -\nabla \check{p} + \frac{\nu}{\mathcal{U}\mathcal{L}} \nabla \cdot \nu \check{\mathbf{S}}, \quad (2.3)$$

The inverse of the factor $\nu/(\mathcal{U}\mathcal{L})$ is known as the Reynolds number Re . When Re is large the viscous term does not play an important role, whereas the viscous term dominates over the non-linear term when Re is small. The Reynolds number will be large when either the length scale or the velocity scale (or both) of a flow are large (e.g. a planetary boundary layer with a length scale of 1000 m and a velocity scale of 5 m s⁻¹). Low Reynolds numbers will occur in the case of small length scales and velocity scales (e.g. flow of water through soil pores and the flow close to a wall).

2.1.2 Phenomena in turbulent flows

Starting with the pioneering work of Reynolds (1895), turbulent flows have been the subject of scientific research ever since (see e.g. Monin and Yaglom, 1971, for a review). Based on this research a more or less commonly accepted picture has evolved that describes turbulent flows both qualitatively and quantitatively. Based on this picture some general properties of turbulent flows can be summarised (after Tennekes and Lumley (1972); Lesieur (1993)):

¹The product $\nabla \mathbf{u}$ is a so-called dyad. A general example is the dyad $\mathbf{A} = \mathbf{a}\mathbf{b}$: a second order tensor with elements $A_{ij} = a_i b_j$. Although the notation used in Spencer (1988): $\mathbf{A} = \mathbf{a} \otimes \mathbf{b}$ is clearer in distinguishing between different types of products, the notation $\mathbf{A} = \mathbf{a}\mathbf{b}$ will be used for reasons of compactness. In general $\mathbf{a}\mathbf{b} \neq \mathbf{b}\mathbf{a} = (\mathbf{a}\mathbf{b})^T$. The gradient of a vector could be denoted either by $\nabla \mathbf{a}$ ($\frac{\partial}{\partial x_i} a_j$ in Cartesian coordinates) or $\mathbf{a}\nabla$ ($\frac{\partial}{\partial x_j} a_i$ in Cartesian coordinates), but the latter form would be confusing, so we will write $(\nabla \mathbf{a})^T$ instead. More information about dyads can be found in Phillips (1948) and Aris (1989).

²Where in a compressible flow the equations of state could be used as an independent equation for the pressure, there is no such equation in an incompressible flow. However, by taking the divergence of the momentum equations and using the continuity equation a Poisson equation for the pressure results. See section 4.2.3 for more information.

- a. Turbulence occurs in flows at high Reynolds numbers: i.e. the non-linear terms in the governing equations dominate over the linear viscous terms (see (2.2)).
- b. Turbulent flows are irregular or chaotic in space and time³: they are not reproducible in detail.
- c. Turbulent flows are diffusive : heat, momentum, as well as mass are mixed and transported efficiently by turbulent flows. In many practical applications this is a desirable feature of turbulence.
- d. Turbulence is essentially rotational and three-dimensional, which is a distinction to other chaotic flows. Rotating patches of fluid (loosely called *eddies*) have length scales ranging from the size of the flow domain down to the order of millimetres (see below for details).
- e. Turbulent flows are dissipative: the kinetic energy of the velocity fluctuations, produced at the largest scales, is dissipated at the smallest scales into heat through viscous diffusion (the Reynolds number is of order unity at this scale).

Whether a flow is turbulent or laminar depends on characteristics of both the fluid (i.e. the viscosity) and the flow (the velocity scale and length scale of the flow). Both factors are combined in the Reynolds number. When the Reynolds number exceeds a certain value the flow *in general* becomes unstable and turbulence develops ⁴.

As stated above, turbulent eddies can have sizes that span a large range of length scales. At the large-scale end of the spectrum eddies occur that have a length scale L ($\sim 0.1-1$ times the domain size), a velocity scale U (\sim square root of the turbulent kinetic energy) and a time scale T ($= L/U$). The smallest scales on the other hand are related to the length scale at which the turbulent kinetic energy is dissipated (η , see below). The large scales lose energy at a rate (ϵ) that is totally determined by large-scale properties:

$$\epsilon = \frac{U^3}{L} \quad (2.4)$$

The flow adjusts in such a way that the velocity fluctuations at the smallest scale are able to dissipate the amount of energy supplied by the large scales⁵. Thus the length scale of the smallest eddies, η , as well as the related velocity scale (v) and time scale (τ_m) only depend on ϵ and ν . In

³Chaotic is not equivalent to random or white noise: in turbulent flows correlations do exist over certain distances in time and space (see further in this section)

⁴For a pipe flow—for example—a logical choice for U would be the bulk velocity U_b and the pipe diameter D for L . Then the value of Re_D above which the flow is turbulent has been found experimentally to be about 2300, given that sufficient disturbances are present in the flow. But laminar pipe flows have been observed at Reynolds numbers of the order of 50000 (Schlichting, 1979; Draad, 1996). The process of transition from a laminar flow to turbulence is a complicated matter, which will not be discussed here. A lower bound for Re_D , below which no turbulent flow will exist is about 2000.

⁵Dissipation is more efficient at smaller scales, since velocity gradients are relatively large. Dissipation is also more efficient if viscosity is larger.

terms of dimensional analysis this leads to the following estimates for these scales:

$$\eta = (v^3/\epsilon)^{1/4} \quad (2.5a)$$

$$v = (v\epsilon)^{1/4} \quad (2.5b)$$

$$\tau_m = \eta/v = (v/\epsilon)^{1/2} \quad (2.5c)$$

When a Reynolds number is formed based on small-scale length and velocity scales ($Re_\epsilon = \eta v/\nu$) we see that this exactly equals 1, thus indicating that at the smallest scales viscous processes dominate.

In order to study the relationship between the characteristic scales of the large-scale and small-scale motion, (2.4) and (2.5) are combined to yield:

$$\frac{\eta}{L} = Re_L^{-3/4} \quad (2.6a)$$

$$\frac{v}{U} = Re_L^{-1/2} \quad (2.6b)$$

$$\frac{\tau_m}{T} = Re_L^{-1/4} \quad (2.6c)$$

It can be seen that with increasing Re_L the range of length scales increases, as well as the range of time scales and velocity scales. This is particularly relevant for the numerical simulation of turbulence: the spatial discretisation will be of the order of η whereas the total flow domain has a size L . Thus the total number of grid points in three dimensions will be of the order of $(Re_L^{3/4})^3$ and the number of time steps (as far as this is limited by turbulent time scales) will grow as $Re_L^{1/4}$.

2.1.3 Reynolds-averaged equations

Since turbulent flows are not reproducible in detail, and since one is usually not interested in these details, one needs to revert to a statistical description of the flow. This is done by a Reynolds decomposition of all variables (remind that the density is taken to be constant and thus is not a variable in the present case):

$$a = \bar{a} + a' , \quad (2.7)$$

where \bar{x} denotes the ensemble average of a and x' is the deviation from the ensemble average.⁶

First (2.7) is applied to the continuity equation (2.1) and the resulting equation is ensemble averaged again:

$$\overline{\nabla \cdot \bar{\mathbf{u}} + \nabla \cdot \mathbf{u}'} = \nabla \cdot \bar{\mathbf{u}} = 0 . \quad (2.8)$$

Thus the ensemble average field is divergence free.

⁶For more details on the subject of ensemble averaging and the relation with other types of averages, the reader is directed to Appendix A.

Subsequently the Reynolds decomposition is applied to (2.2) and the result is ensemble averaged with as result:

$$\frac{\partial \bar{\mathbf{u}}}{\partial t} + \nabla \cdot \overline{\mathbf{u}\mathbf{u}} + \nabla \cdot \overline{\mathbf{u}'\mathbf{u}'} = -\frac{1}{\rho} \nabla \bar{p} + \nabla \cdot \nu \bar{\mathbf{S}}. \quad (2.9)$$

The term $\nabla \cdot \overline{\mathbf{u}'\mathbf{u}'}$ is an extra term that is not present in the original NS-equations. It appears as a result of the averaging operation applied to the non-linear advection term. The tensor $\overline{\mathbf{u}'\mathbf{u}'}$ is the so-called Reynolds stress tensor and is a new unknown in the averaged equation of motion. The determination of the elements of this tensor is one of the main objectives of turbulence research.

2.1.4 Equations for the Reynolds-stresses

In order to study the dynamics of the Reynolds stresses the budget equations for these stresses are required. Since the derivation of these equations is beyond the scope of this thesis, only the result of the derivation will be given⁷. In tensor notation the budget equations for the Reynolds stresses read:

$$\begin{aligned} \frac{\partial \overline{\mathbf{u}'\mathbf{u}'}}{\partial t} &+ \underbrace{\bar{\mathbf{u}} \cdot \nabla \overline{\mathbf{u}'\mathbf{u}'}}_{\text{CT}} + \underbrace{\overline{\mathbf{u}'\mathbf{u}'} \cdot \nabla \bar{\mathbf{u}}}_{\text{PR}} + \underbrace{(\overline{\mathbf{u}'\mathbf{u}'})^T \cdot (\nabla \bar{\mathbf{u}})^T}_{\text{PR}} + \underbrace{\nabla \cdot \overline{\mathbf{u}'\mathbf{u}'\mathbf{u}'}}_{\text{TD}} \\ &= -\frac{1}{\rho} \underbrace{(\nabla \bar{p}'\mathbf{u}' + (\nabla \bar{p}'\mathbf{u}')^T)}_{\text{PD}} + \underbrace{\frac{2}{\rho} \overline{p'S'}}_{\text{PS}} + \underbrace{\nabla \cdot \nu \nabla \overline{\mathbf{u}'\mathbf{u}'}}_{\text{VD}} - \underbrace{2\nu \overline{(\nabla \mathbf{u}')^T \cdot (\nabla \mathbf{u}')}}_{\text{DS}} \end{aligned} \quad (2.10)$$

The local rate of change (RC) of $\overline{\mathbf{u}'\mathbf{u}'}$ is determined by the convective transport (CT), production (PR) and turbulent diffusion (TD) on one hand. In addition there are the pressure diffusion (PD) and the pressure strain terms (PS). The viscous terms have been split in a viscous diffusion (VD) term and a dissipation term (DS).

Some a priori statements can now be made on the dynamics of the Reynolds stresses. Production of Reynolds stress (by velocity gradients) occurs only when at least one combination of the principle axes of the stress tensor and the strain tensor have parallel components. Furthermore, the dissipation term will always be negative and thus reduces the Reynolds stress. By taking the trace of (2.10) one obtains the budget equation for the turbulent kinetic energy. For an incompressible fluid the pressure strain term becomes zero in that budget equation. Finally, in the case of isotropic turbulence the production of turbulent kinetic energy vanishes by definition, since $\text{tr}(\mathbf{I} \cdot \nabla \bar{\mathbf{u}}) = 0$ (Ferziger and Shaanan, 1976), where \mathbf{I} is the unit tensor ($\mathbf{I} = \delta_{ij} \mathbf{e}_i \mathbf{e}_j$, with δ_{ij} being the Kronecker delta).

⁷For details on the derivation of these equations the reader is referred to Stull (1988) (or to Hinze (1975) who derived rate equations for the two-point correlations which can be converted to stress budget equations by equating the two points). The main line of reasoning is to take the rate equation for \mathbf{u}' , multiply it with \mathbf{u}' to form a dyad and add this result to its transpose. The resulting equation is averaged.

2.1.5 Equations for incompressible flow in a cylindrical geometry

Since the geometry of the flow domain we aim to consider here has axial symmetry, use will be made of cylindrical coordinates throughout this study. The cylindrical coordinate system is defined by the three coordinates z , θ and r (the axial, tangential and radial coordinate, respectively). The velocity vector \mathbf{u} is decomposed into the components along these coordinate directions: u_z , u_θ and u_r , respectively.

The Reynolds averaged continuity equation (2.1) can now be expressed as:

$$\nabla \cdot \bar{\mathbf{u}} = \frac{1}{r} \frac{\partial r \bar{u}[r]}{\partial r} + \frac{1}{r} \frac{\partial \bar{u}[\theta]}{\partial \theta} + \frac{\partial \bar{u}[z]}{\partial z} \quad (2.11)$$

The next step is to derive the Reynolds averaged equations of motion, which can be found in Hinze (1975):

$$\frac{\partial \bar{u}_r}{\partial t} + (\bar{\mathbf{u}} \cdot \nabla) \bar{u}_r - \frac{\bar{u}_\theta^2}{r} = -\frac{1}{\rho} \frac{\partial \bar{p}}{\partial r} + \frac{1}{r} \frac{\partial r \tau_{rr}}{\partial r} + \frac{1}{r} \frac{\partial \tau_{r\theta}}{\partial \theta} + \frac{\partial \tau_{rz}}{\partial z} - \frac{\tau_{\theta\theta}}{r} \quad (2.12a)$$

$$\frac{\partial \bar{u}_\theta}{\partial t} + (\bar{\mathbf{u}} \cdot \nabla) \bar{u}_\theta + \frac{\bar{u}_r \bar{u}_\theta}{r} = -\frac{1}{\rho r} \frac{\partial \bar{p}}{\partial \theta} + \frac{1}{r} \frac{\partial r \tau_{r\theta}}{\partial r} + \frac{1}{r} \frac{\partial \tau_{\theta\theta}}{\partial \theta} + \frac{\partial \tau_{z\theta}}{\partial z} + \frac{\tau_{r\theta}}{r} \quad (2.12b)$$

$$\frac{\partial \bar{u}_z}{\partial t} + (\bar{\mathbf{u}} \cdot \nabla) \bar{u}_z = -\frac{1}{\rho} \frac{\partial \bar{p}}{\partial z} + \frac{1}{r} \frac{\partial r \tau_{rz}}{\partial r} + \frac{1}{r} \frac{\partial \tau_{\theta z}}{\partial \theta} + \frac{\partial \tau_{zz}}{\partial z} \quad (2.12c)$$

with

$$\tau = \bar{\sigma} - \begin{pmatrix} \overline{u_r'^2} & \overline{u_r' u_\theta'} & \overline{u_r' u_z'} \\ \overline{u_r' u_\theta'} & \overline{u_\theta'^2} & \overline{u_\theta' u_z'} \\ \overline{u_r' u_z'} & \overline{u_\theta' u_z'} & \overline{u_z'^2} \end{pmatrix} \quad (2.12d)$$

$$\bar{\sigma} = \nu \bar{\mathbf{S}} \quad (2.12e)$$

The Navier-Stokes equations in cylindrical coordinates are given in section B.1.1, whereas the budget equations for the Reynolds stresses are given in section B.1.2.

2.2 Swirl

The term ‘swirling flow’ indicates a very loosely defined class of flows. The main characteristic that all swirling flows have in common is that the flow has both an axial velocity component and a tangential velocity component (Kuroda and Ogawa, 1986). Swirling flows can be both confined (pipe flow or flow between two coaxial cylinders) and free flows (jet). Given the subject of this thesis, the emphasis in the following discussions will be on confined swirling flows.

A rough classification of swirling flows can be made, based on the shape of the tangential velocity profile (Kitoh, 1991; Steenbergen, 1995):

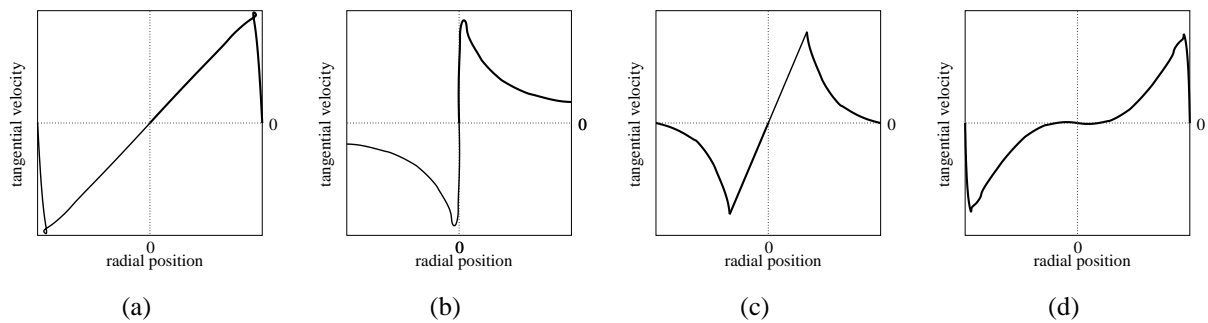


Figure 2.1: Tangential velocity profiles for a number of prototype swirling flows: forced vortex (a), free vortex (b), Rankine vortex (c) and wall jet (d).

- Forced vortex or solid-body rotation;
- Free vortex, which is irrotational;
- Rankine vortex, which is a combination of a forced vortex in the centre and a free vortex in the outer part; when the transition between from the forced vortex to the free vortex is smoother, the \bar{u}_θ -profile resembles that of a Burgers vortex (a diffusing line vortex in axial strain) after some diffusion occurred.
- Wall jet, in which the maximum tangential velocity occurs near the wall.

A sketch of the tangential velocity profiles for these prototypes is given in figure 2.1 (these sketches refer to a confined flow)⁸. The extent of the core with positive vorticity, as well as the location of the maximum vorticity depends on the type of swirl.

Swirling flows unify a number of complexities which occur in other turbulent flows as well: streamline curvature, rotation and three-dimensionality. Furthermore, the rotation may decay downstream due to friction: swirl decay. These phenomena will be the subjects of separate sections, but before discussing these topics separately, an attempt will be made to show the link between them in section 2.2.1.

2.2.1 The link between phenomena in swirling flows

The first feature of swirling flows is the non-zero mean tangential velocity. A flow without axial velocity, leads to the circular streamline pattern shown in figure 2.2(a). This streamline pattern possesses two related characteristics: streamline curvature and rotation. The effects of these phenomena on turbulence are the subject of quite distinct volumes of literature. This distinction is probably due to the difference in the origin of the interest in streamline curvature versus rotation: aerodynamics versus geophysical flows. For the current discussion, however, it is sufficient to notice that the distinction is a human invention –related to the choice of reference frame– rather than a physical reality (see for appendix C for a limited discussion on this topic).

⁸Note that in the case of a pipe flow with swirl a core with positive vorticity (in axial direction) exists in the central part, whereas near the wall a shear region with vorticity of opposite sign can be found.

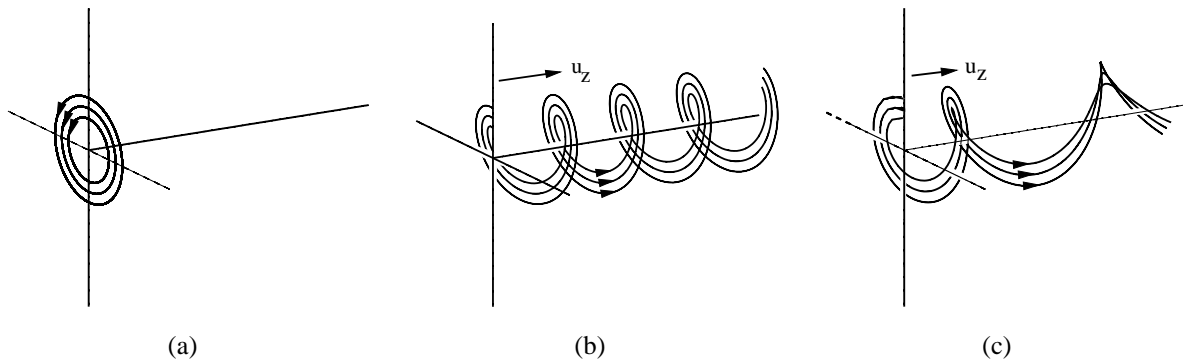


Figure 2.2: Sketches of the streamlines for rotating flows: rotation without an axial velocity component (a) (the profile of the tangential velocity is arbitrary), solid-body rotation with uniform axial velocity (b), uniform axial velocity with decaying solid-body rotation (c).

- Streamline curvature: as is obvious from figure 2.2(a) the streamlines are curved. The radius of curvature is simply equal to the radial position. Although the curvature of streamlines is present in the equations for the Reynolds stresses, the effect is usually at least an order of magnitude larger than one would expect on the basis of the magnitude of the relevant terms (Bradshaw, 1973). The effect of streamline curvature is often explained in terms of stability (and analogies between the stability effects of buoyancy and curvature are used here as well: Bradshaw (1969)). The curvature of streamlines can be viewed as an extra strain rate ('extra' relative to simple shear) if the velocities would be expressed in Cartesian coordinates rather than cylindrical coordinates.

It should be noted that the K-diffusion hypothesis, underlying the link between stress and strain, is in itself under debate, even for 'simple shear flows' (see e.g. Brouwers (2002)).

- Rotation: if the \bar{u}_θ -profile is that of a solid-body rotation ($\bar{u}_\theta = \Omega r$) the flow could as well be analysed in a rotating reference frame, with the z -axis as the rotation axis. Then $\bar{u}_\theta = 0$. To compensate for the change in reference frame, two apparent forces have to be introduced: a centrifugal force and a Coriolis force. Apart from leading to extra terms in the budget equations for the Reynolds stresses, rotation also influences the structure of the turbulence through the pressure-strain terms (Cambon and Jacquin, 1989). Real swirling flows generally do not have a pure solid-body \bar{u}_θ -profile, but in some parts of the pipe cross section the radial dependence of \bar{u}_θ is linear: $\bar{u}_\theta = \Omega r$. In the forced vortex (figure 2.1(a)) this region is large, whereas in the free vortex and Rankine vortex (figures 2.1(b) and 2.1(c)) the region of solid-body rotation is narrow. On the other hand, the wall jet lacks a region of solid-body rotation.

The next step toward a real swirling flow is the addition of a uniform axial velocity in combination with solid-body rotation⁹. This would yield the streamline pattern shown in figure 2.2(b). As in the case of pure rotation the streamlines are curved. But, they do not form a closed circular

⁹This combination has been chosen because of the relatively simple streamline pattern it produces.

path, but have become spirals. The radius of curvature now not only depends on the distance from the centre of rotation, but on the axial velocity as well (in the limit of infinite axial velocity the streamline curvature would disappear). Still, both the analysis in terms of turbulence in a rotating frame, and in terms of streamline curvature are valid. The fact that the streamlines are no longer parallel gives rise to three-dimensionality. This implies that the fluid is distorted or sheared in the cross-flow direction¹⁰.

The effects of streamline curvature, rotation and three-dimensionality are only three of a long list of ‘extra strain rates’ given by Bradshaw (1973)¹¹. Bradshaw uses the term ‘extra rate of strain’ in his qualitative discussions for ‘any departure from simple shear’. In the case of swirling pipe flow the ‘simple shear’ (or one-dimensional shear) would be $\frac{\partial}{\partial r}\bar{u}_z$. The streamline curvature is expressed in the shear $-\bar{u}_\theta/r$. Three-dimensionality is present when the shear $\frac{\partial}{\partial r}\bar{u}_\theta$ is not proportional to $\frac{\partial}{\partial r}\bar{u}_z$.

A final aspect of swirling flows is the decay of swirl: the total amount of tangential momentum decreases due to wall friction. Figure 2.2(c) shows the streamlines in the idealised case of uniform axial velocity and a decaying solid-body rotation. In terms of extra rates of strain, the decay of swirl introduces two new complications: the axial changes in \bar{u}_z and \bar{u}_θ give rise to extra shears: $\frac{\partial}{\partial z}\bar{u}_z$ and $\frac{\partial}{\partial z}\bar{u}_\theta$. However, it should be noted that the decay of swirl is a slow process in most cases, and then the axial derivatives will generally be negligible, compared to other extra strains or shears (which are due to streamline curvature and three-dimensionality).

The phenomena in swirling flows summarised above will be the subject of the forthcoming sections.

2.2.2 Streamline curvature and stability

For a thorough review of the research until the early 1970’s on the effects of streamline curvature the reader is referred to Bradshaw (1973). More recent reviews can be found in Bradshaw (1990) and Holloway and Tavoularis (1992). A detailed overview of linear stability analysis can be found in Schlichting (1979).

Here the main emphasis will be on the influence of streamline curvature on the stability of flows. The term ‘stability’ can here be interpreted in two ways:

- The stability of a basic mean flow is analysed in terms of the growth or decay of disturbances that are added to the basic flow. These disturbances may be subject to constraints on symmetry or dimensionality. This type of —linear— stability analysis is most often used to study the *transition to turbulence*, or the formation of secondary flows;
- The stability of turbulent flows is can be analysed in terms of the growth or suppression of the turbulent kinetic energy , or in terms of the change of the anisotropy of the stress tensor, in *an already turbulent flow*.

Both interpretations of stability will be dealt with below.

¹⁰In some flows, regions may exist where $\frac{\partial}{\partial r}\bar{u}_z \sim \frac{\partial}{\partial r}\bar{u}_\theta$ (for example in the outer region of the free vortex and Rankine vortex, see figures 2.1(b) and 2.1(c)). In that case the flow could be considered to be locally two-dimensional.

¹¹The term ‘extra strain rate’ is rather inexact: the list of Bradshaw not only includes strains (= deformation) but shears (deformation and rotation) and pure rotation as well.

Stability in terms of growth of disturbances

The applicability of linear stability analysis to turbulent flows is limited since the turbulent fluctuations are usually much larger than the ‘small’ disturbances on which linear stability analysis is based. Besides, if linear stability analysis predicts the growth of a disturbance, this growth may be obscured by the turbulent fluctuations that are present already. On the other hand, if linear stability analysis predicts stability, this may be visible in a turbulent flow as a damping of fluctuations (provided of course that the flow remains turbulent: the Reynolds number remains above the critical Reynolds number).

The notion that the curvature of streamlines may have either a stabilising or a destabilising effect on fluid flow dates back at least to Rayleigh (1916). His main conclusion—based on a two-dimensional, inviscid analysis—is that the flow between two coaxial cylinders, of which at least one is rotating, is unstable when the angular momentum ($u_\theta r$) increases outward. This is the so-called centrifugal instability. The argument of Rayleigh in fact boils down to a ‘displaced particle’ argument. Various versions of the ‘displaced particle’ argument exist of which some consider the effect of solid-body rotation on a shear flow, where the rotation axis is perpendicular to the shear plane, (Tritton, 1992; Cambon *et al.*, 1994). Others consider the effect of streamline curvature in a shear flow (Rayleigh, 1916; Bradshaw, 1973; Lumley *et al.*, 1985). All these analyses have in common that they are purely two-dimensional and inviscid. The stability of flows which include an axial velocity component has been analysed by Leibovich and Stewartson (1983) in the context of vortex breakdown and by Mackrodt (1976) and Pedley (1969) for a Hagen-Poiseuille flow in a rotating pipe.

The analysis of Rayleigh (1916) of the stability of the flow between two concentric cylinders was extended by Taylor (1923) to include viscosity and three-dimensional perturbations. It appears that the presence of viscosity stabilises the flow. The instabilities that occur are the well-known Taylor vortices: counter-rotating toroidal vortices. An instability that is more closely related to swirling pipe flow (but also related to the Taylor vortices) is the instability of a boundary layer over a concavely curved surface. This instability gives rise to the the so-called Taylor-Görtler vortices (Schlichting, 1979). In the application of the above—linear and viscous—stability analyses it should be remembered that in those flows the instability occurs, *before* the flow becomes fully turbulent. Thus in fully turbulent flows the patterns predicted by the theory may be obscured by non-linear instabilities and interactions.

Stability in terms of the growth of turbulence quantities

Streamline curvature also has a profound influence on turbulence quantities. In particular attention has been paid to the effect of curvature on the shear stress in shear flows. Prandtl (1961) focuses on turbulent flows and draws an analogy between flows influenced by buoyancy and flows in which streamline curvature produces the (de-)stabilising effect. He proposes to modify the expression for the turbulent shear stress, based on his mixing-length theorem, with a factor depending on the stability, expressed in the dimensionless number S , which is defined as (not to

be confused with the swirl number or strain tensor)¹²:

$$S = \frac{\bar{u}_\theta}{r} \left(\frac{\partial \bar{u}_\theta}{\partial r} - \frac{\bar{u}_\theta}{r} \right)^{-1} \quad (2.13)$$

This S can be interpreted as the ratio between work done by (or against) the centrifugal force and the work done by the mean flow (shear) on the turbulence. In this sense it is similar to a Richardson number which describes the influence of buoyancy on the production of turbulent kinetic energy. For a profile with $\bar{u}_\theta(r) = \text{const}/r$ the curvature can be seen to have no effect., whereas for profiles with $\bar{u}_\theta(r) \sim r^n$ with $n < -1$ Prandtl predicts instability and for $n > -1$ stability. Bradshaw (1969) has investigated the analogy between the stability effects of streamline curvature and buoyancy in more depth.

As opposed to the stability analyses presented above, Holloway and Tavoularis (1998) state that the effects of mild streamline curvature on the anisotropy of the Reynolds stress tensor do not arise from a centrifugal effect. They present a geometric explanation instead. In this explanation it is assumed that a turbulent eddy *maintains* its original orientation once it has been produced. In a curved flow this implies that the axes of the eddy will *rotate* relative to the coordinates of the curved flow. The orientation of the eddies that are found at a certain position in the flow is the cumulative effect of eddies that have been convected from various positions upstream (and have decayed in the meantime).

For a review of experimental evidence for the effect of streamline curvature on turbulent (shear) the reader is referred to Holloway and Tavoularis (1992).

2.2.3 Rotation

When a turbulent flow is considered in a rotating reference frame the Reynolds averaged momentum equations have to be augmented with two apparent accelerations: the centrifugal force and the Coriolis force:

$$\frac{\partial \bar{\mathbf{u}}}{\partial t} + \nabla \cdot \bar{\mathbf{u}\mathbf{u}} + \nabla \cdot \overline{\mathbf{u}'\mathbf{u}'} = -\frac{1}{\rho} \nabla \bar{p} + \nabla \cdot \nu \bar{\mathbf{S}} + \Omega^2 \mathbf{R} - 2\boldsymbol{\Omega} \times \bar{\mathbf{u}}. \quad (2.14)$$

/see b where $\boldsymbol{\Omega}$ is the rotation vector, Ω is the magnitude of $\boldsymbol{\Omega}$, and \mathbf{R} is the distance between the point of interest and the rotation axis. The centrifugal force is balanced by an increased pressure gradient force. The Coriolis force causes an exchange of momentum between different components of the velocity vector. Another influence of the rotation enters (2.14) through the Reynolds stress, which is influenced by rotation as well (see below).

In order to gain some extra insight, the perspective of two-point statistics of the velocity field is needed, e.g. the Fourier transform of the velocity field. Jacquin *et al.* (1990) show that under certain conditions, an inertial wave regime results (see also Veronis, 1970) which

¹²In the original paper the dimensionless number was called θ . The form of the function proposed by Prandtl for the stability effect of *buoyancy* is remarkably close to relationships found experimentally in the 1960's (see Garrat (1992) for a review). But the magnitude of the effect is an order of magnitude larger than expected by Prandtl, which is in line with the statements of Bradshaw (1973). See also Bradshaw (1969) for the analogy between stability effects of curvature and buoyancy.

corresponds to ‘spring-like’ behaviour observed by Johnston *et al.* (1972) and to the ‘displaced particle analysis’ by Tritton (1992) (see section 2.2.2). One of the effects of these inertial waves is the disruption of the phase relations in turbulence, so-called phase-scrambling. This hampers the energy cascade and —since the small scales just dissipate the energy delivered by the larger scales— also diminishes the dissipation (see Zhou, 1995).

A next step is to study the *direct* effect of rotation on the budget equation for the Reynolds stress (equation (2.10)). Two extra terms occur in this equation due to the rotation:

$$RC + CT + PR + TD = PD + PS + VD + DS - 2\mathbf{\Omega} \times \overline{\mathbf{u}'\mathbf{u}'} - 2(\mathbf{\Omega} \times \overline{\mathbf{u}'\mathbf{u}'})^T \quad (2.15)$$

The effect of the extra terms is to generate an exchange between different components of the stress tensor. Or, equivalently, the principal axes of the stress tensor are rotated around the rotation axis. In section 2.1.4 (equation (2.10)) it was shown that the angle between the strain tensor and the stress tensor determines the production of Reynolds stresses (Bertoglio, 1982), so that rotation does —indirectly— influence that production. The effect of rotation on the turbulent kinetic energy can be studied by taking the trace of (2.15). It appears that the rotation terms do not have a direct contribution ($(\mathbf{\Omega} \times \mathbf{u}') \cdot \mathbf{u}' = 0$ since $\mathbf{\Omega} \times \mathbf{u}' \perp \mathbf{u}'$). However, by changing the relative magnitude of the different stress components, the rotation terms do influence the turbulent kinetic energy indirectly through the production terms.

In the analysis of (2.15) the influence of rotation on the pressure diffusion term, pressure strain term and the turbulent diffusion remains unclear. Some extra understanding can be obtained by analysing the effect of rotation on the Fourier transform of the Reynolds stress tensor, i.e. the spectral tensor Φ . In these analyses the role of a part of the pressure-strain terms can be studied. Cambon and Jacquin (1989) studied the influence of rotation on homogeneous but anisotropic turbulence. They find that rotation enhances the anisotropy of the length scales, while it diminishes the difference between the normal stress components parallel and normal to the rotation axis.

Bertoglio (1982) and Cambon *et al.* (1994) study the effect of rotation on homogeneous turbulence that includes mean shear. They analyse the flow in terms of the rotation number R :

$$R_n = \frac{2\Omega}{\overline{\omega}} \quad (2.16)$$

where $\overline{\omega}$ is the vorticity of the (ensemble) mean flow. They find that maximum destabilisation of the flow occurs at $R_n = -1/2$ or zero tilting vorticity (Cambon *et al.*, 1994)¹³. The destabilisation occurs mainly through the pressure strain terms. If $R_n > 0$ the mean rotation adds to the rotation of the shear and stabilisation occurs. Tritton (1992) arrives at the same conclusion using a simplified Reynolds stress model, and assuming that the principal axes of $\overline{\mathbf{u}'\mathbf{u}'}$ and $D\overline{\mathbf{u}'\mathbf{u}'}/Dt$ are aligned.

This section concludes with some (laboratory and numerical) experimental evidence of the influence of rotation of turbulent flows. Three similar experiments, studying the influence of rotation on grid-generated turbulence, have been performed by Traugott (1958), Wigeland (1978)

¹³Due to an unfortunate definition of the direction of the rotation vector $\mathbf{\Omega}$ in his paper, Bertoglio (1982) states that the maximum destabilisation occurs for $R_n = 1/2$, rather than $R_n = -1/2$.

and Jacquin *et al.* (1990). Although these experiments do contradict each other in some places — which may be attributed to experimental deficiencies— the main conclusions stand out clearly:

- Rotation reduces the dissipation of the turbulent kinetic energy;
- The effect of rotation on anisotropic turbulence is highly dependent on the exact form of the anisotropy;
- The length scales along the mean flow direction tend to increase with rotation, the effect being more pronounced for the length scale of the radial component.

Bardina *et al.* (1985) find in numerical simulations of rotating isotropic turbulence that the length scales become anisotropic due to rotation. All length scales grow, but the length scales of the velocity components perpendicular to the rotation axis grow more. Rotation also has a large effect on dissipation¹⁴: the vortex tubes are reordered to become more parallel to the rotation axis, which hampers the energy cascade. Bardina *et al.* interpret this modification of the energy cascade in terms of a conversion of turbulent energy into inertial waves. Mansour *et al.* (1992) have performed direct numerical simulations and EDQNM (Eddy-Damped Quasi-Normal Markovian) computations of isotropic turbulence subject to strong rotation. Their results also show a shut-off of the energy transfer from large scales to small scales. Anisotropy in the turbulent length scales is observed for intermediate rotation rates only. For strong rotation no tendency toward two-dimensionality can be observed.

2.2.4 Three-dimensionality

In case of a simple shear flow the magnitude of the mean velocity varies in a direction perpendicular to that mean velocity (in most cases this direction is normal to a wall). In the context of fluid flow three-dimensionality refers to a situation in which not only the *magnitude* of the mean velocity varies (shear) but also the *direction* of the mean velocity changes in a direction normal to the mean velocity vector (Schlichting, 1979).

Nearly all research on three-dimensionality in turbulent flows has focused on three-dimensional boundary layers. Various processes may be responsible for the occurrence of three-dimensional boundary layers. These comprise:

- the bounding surface moves laterally relative to the mean flow direction (e.g. Bissonette and Mellor, 1974);
- due to some upstream disturbance the mean velocity has a lateral component for a range of distances normal to the wall (swirling pipe flow belongs to this category);
- the presence of an obstacle in a flow over a flat surface; the obstacle will influence the pressure field upstream, which will in turn influence the velocity field (e.g. Hornung and Joubert, 1962);
- differences in downstream boundary layer development may produce a lateral pressure gradient and subsequent three-dimensionality (e.g. 'swept-wing' experiments (by e.g. van den Berg *et al.*, 1975)).

¹⁴Dissipation can be viewed as the interaction of randomly oriented vortex tubes. The tubes need to have a certain mutual orientation to be able to exchange momentum efficiently.

One of the differences between a standard shear layer and a three-dimensional boundary layer is that the directions of mean velocity (γ), shear (γ_g) and stress (γ_τ) do not need to coincide (and will not do so in general). The angles γ , γ_g , and γ_τ are defined in a plane parallel to the bounding surface. Examples can be found in literature where the difference between γ_g and γ_τ is of the order of 10 degrees. The difference between γ and γ_g is even larger (see van den Berg, 1988; Bradshaw and Pontikos, 1985; Bruns *et al.*, 1999). The implication of shear and stress not being aligned is that the eddy-viscosity is anisotropic (the component in the cross-flow direction being the smallest). The alignment of shear and stress in a simple shear flow (one-dimensional shear) is often considered to be an indication of local equilibrium between production and dissipation. On the other hand, the non-alignment in the case of a steady three-dimensional boundary layer may point at a non-local equilibrium and history effects in the flow might be important (van den Berg, 1988).

Another effect that has been observed in three-dimensional boundary layers is a general reduction in the shear stress relative to the turbulent kinetic energy (Compton and Eaton, 1997). This might be explained by so-called 'turbulent eddy toppling' (Bradshaw and Pontikos, 1985). This term refers to the process that large turbulent eddies –with sizes comparable to the boundary layer depth– are distorted and even disrupted by the cross-flow shear acting on them.

In the context of swirling flows, it should be noted that the effect of three-dimensionality in the near-wall region appears to be of minor importance. Only at distances beyond approximately $y^+ = 60$ the flow gradually becomes skewed (Kitoh, 1991).

2.2.5 Swirl decay

In a wall-bounded swirling flow, the tangential motion will decay downstream due to a tangential wall shear stress¹⁵. This tangential wall shear stress will of course have a pronounced effect on the shape of the profiles of both the mean velocities and the turbulent stresses. However, in the case of swirl decay most attention is paid to the decay of the total 'amount of swirl'. Numerous integral quantities have been devised to represent this amount of swirl. Here the swirl number (S) as given by Kitoh (1991) (see also Steenbergen and Voskamp (1998)) will be used:

$$S = 2 \int_0^R \frac{\overline{u_z \overline{u_\theta}} r^2}{U_{bulk}^2 R^3} dr \quad (2.17)$$

This swirl number is equal to the non-dimensionalised angular momentum flux (i.e. the *axial* flux of *angular* momentum).

The amount of swirl decreases downstream due to the loss of mean tangential momentum through the tangential wall shear stress. By integration of the mean momentum equation for $\overline{u_\theta}$ (multiplied by r^2), an expression for the tangential wall shear stress in terms of $\overline{u_z}$, $\overline{u_\theta}$, $\overline{u'_z u'_\theta}$ and $\frac{\partial}{\partial z} \overline{u_\theta}$ can be obtained (for axisymmetric flow):

$$\frac{\tau_{r\theta,wall}}{\rho} = \frac{1}{R^2} \int_0^R r^2 \frac{\partial}{\partial z} \left(\overline{u_z \overline{u_\theta}} + \overline{u'_z u'_\theta} - \nu \frac{\partial \overline{u_\theta}}{\partial z} \right) dr \quad (2.18)$$

¹⁵Unless it is a fbw in which the swirl is generated by the rotation of the pipe wall itself Imao *et al.* (1996); Eggels (1994).

$\overline{u_z \bar{u}_\theta}$ will be much larger than both $\overline{u'_z u'_\theta}$ and $v \frac{\partial \bar{u}_\theta}{\partial z}$. With this knowledge, and by scaling all velocities by U_{bulk} , and the axial coordinate by the pipe diameter D , (2.18) can be rewritten as:

$$\frac{\tau_{r\theta,wall}}{\frac{1}{2}\rho U_{bulk}^2} = 2 \frac{d}{d(x/D)} \int_0^R \frac{\overline{u_z \bar{u}_\theta} r^2}{U_{bulk}^2 R^3} dr = \frac{1}{2} \frac{dS}{d(x/D)} \quad (2.19)$$

Then Kitoh (1991) suggests to express $\tau_{r\theta,wall}$ as a series expansion in terms of S . For low swirl numbers one can decide to only retain the linear term, i.e. $\tau_{r\theta,wall} \sim S$. In that case an exponential decay law for S is obtained:

$$S = ae^{-\beta z/D}, \quad (2.20)$$

where a and β are fitting coefficients. The quantity a can be interpreted as a the swirl number at the axial position $z = 0$ and β is the a measure of the decay rate¹⁶. This approximate exponential decay has been confirmed experimentally for many types of swirling flows, although the decay rates (i.e. β) do depend on the type of flow and to some extent on the swirl number. Besides, there is a dependence of β on Re_D : the decay depends on the scaled tangential wall shear stress which appears to have the same dependence on Re_D as the scaled axial wall shear stress $\tau_{rz,wall}/\rho U_{bulk}^2$. The latter is related to the Re -dependence of the friction factor $\lambda = (8u_* / U_{bulk})^2$. Steenbergen (1995) finds for low initial swirl numbers (of $O(0.2)$) that $\beta = (1.49 \pm 0.07)\lambda$. Note that the friction factor used here is the λ for a fully developed pipe flow, as given by Blasius' relationship: $0.3168 Re_D^{-1/4}$. An ample review of swirl decay rates obtained in 18 other experiments is given in Steenbergen and Voskamp (1998).

Although most analyses of swirling flows are based on the assumption that the flow is axisymmetric (so that all angular momentum is present in u_θ and not in u_r), asymmetries do occur in practice. Kito (1984) concludes that small asymmetries in the inflow can result in large asymmetries further downstream. Furthermore, Kito considers the precession of the vortex core (i.e. the axial change in the location of the vortex core in the pipe cross section). He suggests that the direction of precession is always in the same direction as the swirl ($0 < S < 0.4$). However, Dellenback *et al.* (1988) show that for $0 < S < 0.15$ the precession direction is opposite to the swirl and for higher S it is in the same direction.

2.3 Axial strain

The term axial strain signifies one of many possible strain configurations, among which are plane strains and combinations of axial strain and plane strain (see Reynolds and Tucker (1975)). In an axial strain the flow is strained (in the mean) in its flow direction. This can be expressed in a mean strain rate tensor $\overline{\mathbf{S}}$ (in Cartesian coordinates) as:

$$\overline{\mathbf{S}} = \begin{bmatrix} D & 0 & 0 \\ 0 & -\frac{1}{2}D & 0 \\ 0 & 0 & -\frac{1}{2}D \end{bmatrix}, \quad (2.21)$$

¹⁶Generally, a is not equal to S at $z = 0$, since the decay process is not exponential in the initial stage.

where $D = \frac{\partial u_{x_1}}{\partial x_1}$. In a wall bounded flow an axial strain can easily be generated by means of a downstream change in the cross-sectional area of the flow domain. This change in cross-sectional area can either be a locally continuous decrease (contraction) or increase (diffuser) or decrease followed by an increase (constriction). In a contraction the flow is accelerated, whereas in a diffuser the flow is decelerated.

Two aspects will influence the strain that is realised in practice:

- The friction at the wall will locally influence the strain field;
- The way in which the cross-sectional area changes with axial position determines whether –and in which way– the strain varies with the axial position in the contraction.

In the sequel, only contractions will be considered, since that is the type of axial strain generator used in the present study. Thus the studies on flows through diffusers and constrictions will be left out (e.g. Çantrak (1981); Spencer *et al.* (1995); Desphande and Giddens (1980); Lissenburg *et al.* (1974)).

The study of the turbulent flow through pipe contractions has been motivated by different needs. On one hand, contractions, diffusers and constrictions are present in all kinds of piping systems (industrial applications, water supply systems, etc; see Bullen *et al.* (1996)). In these applications the main interest is in the pressure loss due to the presence of the change in pipe diameter, and the possible occurrence of separation (see section 2.3.1). On the other hand, the axial strain due to a change in pipe diameter also strongly influences the turbulence structure. This effect has practical applications, since some processes in industrial installations, such as mixing, do depend on the nature of the turbulent flow. But it is also of more theoretical interest, since the study of the effect of straining on turbulent fields may shed light on the internal processes in a turbulent flow (large eddies that strain small eddies). The effect of axial strain on turbulence is the subject of section 2.3.2. Finally, downstream of the axial strain the turbulent flow will be strongly deformed. It will need a certain distance to relax to an undisturbed flow, i.e. to return to a situation in which the flow is in equilibrium with its forcings (e.g. a fully developed pipe flow). Some results of the research on developing flows are treated in section 2.3.3.

2.3.1 Effect of axial strain on mean flow

The first order effect of a contraction in a pipe is that it acts as an obstruction to the flow. Consequently, an extra axial pressure gradient has to develop in order to force the fluid through the contraction. The need for the extra pressure gradient can also be understood from the fact that – due to continuity– the bulk velocity needs to be higher downstream of the contraction, compared to the upstream value. Thus the flow has to be accelerated by an extra axial pressure gradient.

Not only the bulk velocity changes due to the acceleration. Also the shape of the axial velocity profile changes: the downstream profile is flatter than the upstream profile (see e.g. Spencer *et al.* (1995); Yeh and Mattingly (1994)). The flattening of the \bar{u}_z -profile can be explained for a large part with a simple representation of what happens in the contraction. Upstream and downstream of the contraction it can be assumed that the flow is parallel, so that the mean pressure is constant in planes of constant z : iso-pressure surfaces are parallel¹⁷. Thus for a part of the region

¹⁷Within the contraction the iso-pressure surfaces will be curved rather than flat surfaces. In some parts of the

between entry and exit of the contraction the pressure gradient experienced by the flow will be independent of the radial position. As a consequence the total increase of axial velocity upon passage through the contraction will be identical for each radial position. This implies that the *relative* increase is largest in the near-wall region and smallest in the centre. The result will be a flatter profile of \bar{u}_z .

2.3.2 Effect of axial strain on turbulence

The way in which an axial strain affects a turbulent flow depends on the magnitude of the strain. The strain rate \mathbf{S} can be interpreted as the inverse of a time scale. So the larger the strain rate, the smaller its time scale. If the straining time scale is smaller than the turbulent time scale T , the strain is considered to be rapid. This implies that during the straining the geometry of the turbulence is deformed, but the turbulence does not have time to react on the deformation. On the other hand, when the straining time scale is less than T the deformation and the reaction to this deformation will take place simultaneously.

The flows in which rapid straining occurs are often studied using rapid distortion theory (RDT; the theory dates back to Batchelor and Proudman (1954) and for a review see Savill (1987)). Rapid distortion theory is based on a Lagrangian description of the deformation of the turbulent field (i.e. the turbulent fluctuations \mathbf{u}') by a mean strain. The effect of viscosity and the interaction between the turbulent field and *fluctuating* strain are ignored (assuming that these two effects have a longer time scale than the distortion). This description is made in terms of the vorticity (i.e. $\boldsymbol{\omega} = \nabla \times \mathbf{u}$) in order to eliminate the pressure from the equations of motion:

$$\frac{D\boldsymbol{\omega}'}{Dt} = \bar{\mathbf{S}} \cdot \boldsymbol{\omega}' \quad (2.22)$$

For a given strain and initial field of vorticity fluctuations equation (2.22) needs to be integrated in time. Then, at the end of the path of the fluid particle the fluctuating velocity field can be reconstructed from the vorticity field. Since the fluctuating velocity field is not known in detail but only in a statistical sense, and since the vorticity depends on the spatial structure of the field, the distortion is usually applied to the spectral tensor rather than the vorticity field. There is ample discussion in literature about the exact values connected to the conditions for the validity of the RDT approximation. But there is no discussion on the kind of conditions (see e.g. Goldstein and Durbin (1980)):

- the turbulent field upstream of the distortion should be weakly turbulent, i.e. u'/\bar{u} should be small;
- the distortion of turbulent vortex lines by mean straining is much larger than the distortion due to turbulent straining;
- the Reynolds numbers of both the mean flow and the turbulence should be large (i.e. the flow should be nearly inviscid).

contraction—where the curvature of the wall in the axial direction is non-zero—the iso-pressure surfaces will also not be parallel, since the iso-pressure surfaces have to be perpendicular to the wall to ensure impermeability. In the part of the contraction where the curvature of the wall in the z -direction is zero, the iso-pressure surfaces can be assumed to be parallel.

The RDT analysis by Batchelor and Proudman (1954) shows that for an axisymmetric, homogeneous and irrotational¹⁸ strain (with $\partial \bar{u}_z / \partial z > 0$), acting on isotropic turbulence, the fluctuations in the axial velocity will decrease and the fluctuations of the lateral components will increase (see figure 2.3):

$$\frac{(\overline{u'_z u'_z})_{ds}}{(\overline{u'_z u'_z})_{us}} = \mu_z = \frac{3}{4} c^{-2} \left(\frac{1 + \alpha^2}{2\alpha^3} \ln \frac{1 + \alpha}{1 - \alpha} - \alpha^{-2} \right) \quad (2.23)$$

$$\frac{(\overline{u'_r u'_r})_{ds}}{(\overline{u'_r u'_r})_{us}} = \mu_r = \frac{3}{4} c + \frac{3}{4} c^{-2} \left(\frac{1}{2} \alpha^{-2} - \frac{1 - \alpha^2}{4\alpha^3} \ln \frac{1 + \alpha}{1 - \alpha} \right), \quad (2.24)$$

where the subscripts *us* and *ds* signify 'upstream' and 'downstream', *c* is the strain ratio (i.e. the extension factor of a material element on the axis of symmetry or the inverse of the ratio of cross sectional areas downstream and upstream of the contraction) and $\alpha = \sqrt{1 - c^{-3}}$. Thus, assuming isotropic initial conditions, axisymmetric straining will result in an anisotropic field of velocity fluctuations. Batchelor and Proudman also show that the total turbulent kinetic energy will *increase*, but relative to the mean kinetic energy it will *decrease* due to the increase of the mean axial velocity.

Reynolds and Tucker (1975) suggest a way to incorporate the fact that the initial turbulence might not be isotropic (in terms of the components of the stress tensor). Their approach is to first find the hypothetical strain ratio (*c_h*) that would have produced the given anisotropy (e.g. from (2.24)). Subsequently they apply the product of this hypothetical strain ratio and the actual strain ratio (*c_e* = *c_h**c*) to isotropic turbulence. This will give the effect of strain under consideration on initially anisotropic turbulence. In the present context, the results of Batchelor and Proudman (1954) and Reynolds and Tucker (1975) could be compared to the downstream development of the normal stresses on the pipe axis.

Hultgren and Cheng (1983) have studied the effect of an inhomogeneous strain characteristic of the flow through an internal contraction (as is the contraction in a pipe). Their analysis provides insight into the radial dependence of the changes in the normal stresses (as well as the shear stress). Apart from a slight radial dependence of μ_z and μ_r , the results indicate that axial and radial velocity fluctuations become correlated due to the contraction. The correlation coefficient increases from zero at the symmetry axis, to between 0.02 and over 0.3 (depending on the contraction ratio, which ranged from 1.25 to 9). Another result Hultgren and Cheng is that in the stream wise one-dimensional spectrum of *u_z* the energy shifts to small scales, whereas in the spectrum for the radial component, the energy shifts to larger scales. This result is consistent with the experimental observations of Leuchter and Dupeuble.

Various authors have developed methods to extend RDT beyond the restrictions posed above (e.g. Hunt (1973); Goldstein and Durbin (1980); Tsugé (1984)) and to flows with more complex strains (see Savill (1987) for a review).

Experimental studies on the effect of a contraction on the turbulence are described in Sreenivasan (1985) (the effect of a contraction on a homogeneous shear flow), Bullen *et al.* (1996) (contractions in pipe flow), Yeh and Mattingly (1994) (flow downstream of a reducer), and Spencer *et al.* (1995).

¹⁸This excludes the effects of both shear and rotation.

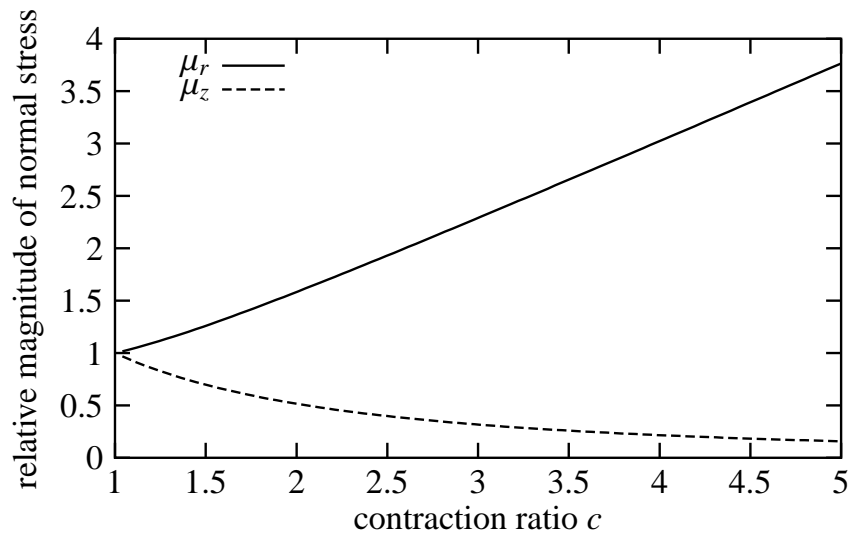


Figure 2.3: Relative magnitude of normal stresses resulting from an axisymmetric contraction with contraction ratio of c , according to Batchelor and Proudman (1954).

2.3.3 Relaxation of strained flow

The flow directly downstream of a contraction is characterised by a very flat axial velocity profile and low –relative– levels of turbulent fluctuations. These are also exactly the characteristics of the flow at a pipe entrance, i.e. developing pipe flow. The main concern in the study of developing pipe flows is how, and how quickly, the flow reaches a fully developed stage, i.e. the flow is axially homogeneous. Numerous studies, both experimental and numerical, have been performed regarding developing pipe flow (see e.g. Mizushima *et al.* (1970), Barbin and Jones (1963), Richman and Azad (1973), Reichert and Azad (1976), Klein (1981) and Laws *et al.* (1987)).

The main mechanism for a disturbed pipe flow to become fully developed is through the growth of the wall boundary layers. For a turbulent boundary layer, on a flat plate the boundary layer thickness is proportional to $z^{4/5}$, i.e. the growth rate decreases downstream (Schlichting, 1979). Thus whereas the adjustment of the profile close to the wall is rather quick, the adjustment of the entire profile is slow. Especially the shear stress near the pipe axis takes a long distance to adjust (see Barbin and Jones, 1963; Klein, 1981).

Klein (1981) provides a review of developing pipe flow experiments and focuses on the development of the shape of the axial velocity profile. The shape of the velocity profile is summarised in a measure of its peakiness, i.e. the ratio of centreline velocity and bulk velocity. Directly downstream of the pipe entrance (or contraction as in the present case) the peakiness of the profile increases. For some cases it even increases beyond the equilibrium value before reaching that equilibrium value. Thus it is not sufficient that the wall boundary layer completely fills the pipe in order to have a fully developed flow. The fully developed flow is reached only at a downstream distance of 70 pipe diameters.

2.4 Combined effect of swirl and axial strain

Only very little theoretical and experimental results regarding the combined effect of swirl and axial strain are available. A theoretical analysis that can be useful in this context –at least to understand the behaviour of the mean flow– is the inviscid analysis by Batchelor (1967) (see section 2.4.1). With respect to turbulent flows theoretical analyses have been made by means of RDT (Dupeuble and Cambon, 1994) and EDQNM (Leuchter, 1997; Leuchter and Bertoglio, 1995). The same group has also performed excellent experiments on rotating flows subject to axial strain (Leuchter and Dupeuble, 1993). The experiment of Čantrak (1981) –turbulent swirling flow through a diffuser– in principle also belongs to this section, but will not be dealt with (partly because the current subject is the flow through a contraction, partly because the results of Čantrak are difficult to interpret).

2.4.1 Inviscid analysis of simplified swirling flows subject to axial strain

Batchelor (1967) presents an analytical analysis of an inviscid flow in which both swirl and axial strain play a role (section 7.5 in his book). In this section the conclusions of his analysis will be summarised and applied to swirling pipe flow subject to axial strain.

Summary of the analysis as presented by Batchelor (1967)

For an *incompressible* axisymmetric flow mass conservation may be satisfied by expressing the velocity components in terms of a stream function $\psi(z, r)$ (see also e.g. Kundu (1990)):

$$u_z = \frac{1}{r} \frac{\partial \psi}{\partial r}, \quad u_r = -\frac{1}{r} \frac{\partial \psi}{\partial z}. \quad (2.25)$$

In the case of *steady* motion a fluid element moves along a streamline. All streamlines for a given value of ψ form a surface of revolution around the axis. So when the motion is steady, elements move on a surface defined by $\psi = \text{constant}$. Applying both Bernoulli's theorem and the conservation of angular momentum (i.e. $Dru_\theta/Dt = 0$) to a particular streamline (with given value of ψ), it follows that:

$$\frac{1}{2}(u_z^2 + u_r^2 + u_\theta^2) + \frac{p}{\rho} = H(\psi), \quad (2.26a)$$

$$ru_\theta = C(\psi), \quad (2.26b)$$

where H and C are arbitrary functions of ψ . Since ψ is constant along a streamline, $H(\psi)$ and $C(\psi)$ will be constant as well. Or: on a surface with $\psi = \text{constant}$, $(\nabla H) = 0$ and thus $\mathbf{u} \times \boldsymbol{\omega} = 0$. This is a Beltrami flow: the components of \mathbf{u} and $\boldsymbol{\omega}$ are locally parallel. Flows in which all quantities are independent of z and $u_r = 0$ are termed *cylindrical* flows, since the surfaces $\psi = \text{constant}$ are cylindrical surfaces. For those cases the radial equation of motion can be simplified to (see 2.12a):

$$\frac{1}{\rho} \frac{dp}{dr} = \frac{u_\theta^2}{r} = \frac{C^2}{r^3}. \quad (2.27)$$

This leads to a relationship between H and C for a cylindrical flow:

$$\begin{aligned} H &= \frac{1}{2}(u_z^2 + u_\theta^2) + \int \frac{C^2}{r^3} dr \\ &= \frac{1}{2}u_z^2 + \int \frac{C}{r^2} \frac{dC}{dr} dr. \end{aligned} \quad (2.28)$$

If now, for a certain region of the flow (where the flow is cylindrical), the velocity components are known (and from this ψ as a function of r) the functions $C(\psi)$ and $H(\psi)$ are known. Then velocities can be calculated at any other position in the flow.

Application to swirling strained pipe flow

The analysis summarised above can be applied to swirling flow through a pipe of varying cross-section (which was in fact already done by Batchelor in his book). Considering the flow as a whole, quantities are a function of both z and r (axisymmetry is assumed). But in the upstream and downstream regions the flow is assumed to be cylindrical. In those parts of the flow the pipe radius is r_1 and r_2 for upstream and downstream pipe section, respectively, and there is no dependence of flow properties on z .

Only for very simple flows $H(\psi)$ and $C(\psi)$ can be known. Here an upstream flow with a radially uniform axial velocity and a solid-body rotation is assumed:

$$\begin{aligned} u_z(r) &= U, \\ u_\theta(r) &= \Omega r. \end{aligned} \quad (2.29)$$

The latter implies $C = \Omega r^2$. From (2.29) and (2.28) it follows that $H = \frac{1}{2}U^2 + \Omega^2 r^2$. This in turn leads to expressions for $C(\psi)$ and $H(\psi)$.

With the use of a partial differential equation for ψ (not discussed here) and the application of appropriate boundary conditions (neither discussed here, see Batchelor (1967), page 547) Batchelor derives that at a location where the pipe radius is r_2 , the radial dependence of u_z and u_θ is:

$$\frac{u_z(r, r_1, r_2)}{U} = 1 + \left(\frac{r_1^2}{r_2^2} - 1 \right) \frac{\frac{1}{2}kr_2 J_0(kr)}{J_1(kr_2)} \quad (2.30a)$$

$$\frac{u_\theta(r, r_1, r_2)}{\Omega r} = 1 + \left(\frac{r_1^2}{r_2^2} - 1 \right) \frac{r_2 J_1(kr)}{r J_1(kr_2)}, \quad (2.30b)$$

where $k = 2\Omega/U$. Figure 2.4 shows an example of how the inviscid analysis describes the influence of axial strain on a swirling flow. It is clear that the axial velocity, which started with a uniform profile, obtains a maximum in the centre downstream of the axial strain. Furthermore, the tangential velocity changes from a solid-body rotation to a wall jet¹⁹.

For $kr_2 \ll 1$ (i.e. low swirl numbers) these expressions can be reduced, since in that case the factors involving the Bessel functions approach 1. The low swirl number approximation yields

¹⁹Note that, given the fact that this an inviscid analysis, no influence of a wall is present in the model.

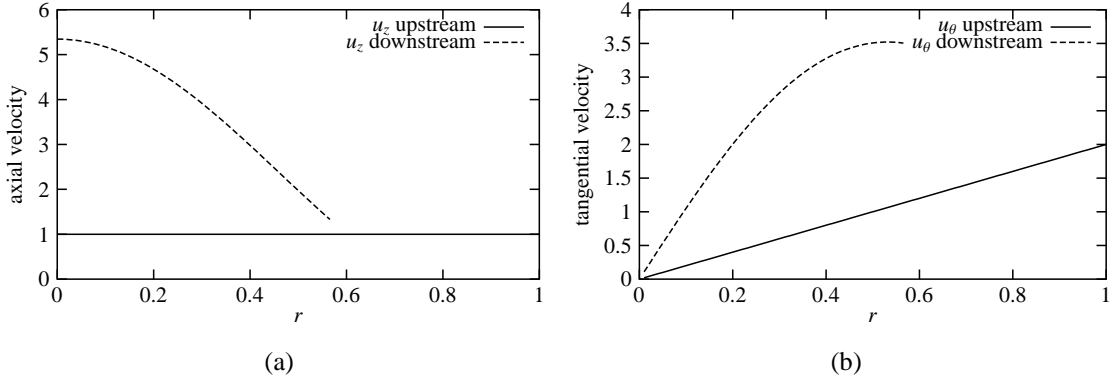


Figure 2.4: Illustration of the change in shape of the axial and tangential velocity profiles for swirling flow with axial strain (2.31). The following values for the parameters have been used: $r_1 = 1$, $r_2 = 1.75^{-1}$, $U = 1$ and $\Omega = 2$.

the following expressions for u_z and u_θ :

$$\frac{u_z(r, r_1, r_2)}{U} \approx \frac{r_1^2}{r_2^2}, \quad (2.31a)$$

$$\frac{u_\theta(r, r_1, r_2)}{\Omega r} \approx \frac{r_1^2}{r_2^2}, \quad (2.31b)$$

so that for this first approximation u_z and u_θ will just increase for the case of a contraction, without a change in the shape of the profiles. It is worth noting that in (2.31) u_z/U and $u_\theta/(\Omega r)$ have become independent of r . Thus the shape of the u_z - and u_θ -velocity profiles will not change upon passage through a contraction.

2.4.2 Turbulent flows with swirl and axial strain

All presently known references to work on the combined effect of rotation and axial strain on *turbulent* flows stem from the groups at ONERA (Office National d'Étude et de Recherches Aéropatiales) and ECL (Ecole Centrale de Lyon), both in France. This work comprises both experimental work and modelling by means of RDT (rapid distortion theory) and EDQNM (Eddy-Damped Quasi-Normal Markovian).

Experiment

Leuchter and Dupeuble (1993) have used a wind tunnel in which the air is first passed through a rotating honeycomb. In this way a turbulent flow with a uniform axial velocity and a solid-body rotation is generated. Subsequently, this air passes through a contraction. The geometry of the

contraction is designed such that the strain rate is constant and uniform, i.e.²⁰.

$$R\left(\frac{z}{L}\right) = \frac{R_0}{\sqrt{1 + \gamma \frac{z}{L}}}, \quad (2.32)$$

where L is the length of the contraction, R_0 is the upstream radius and β is the dimensionless strain rate ($\gamma = DL/u_{0,z}$). γ is related to the contraction ratio as $\gamma = c - 1$ (see page 26). D is the strain rate (see (2.21)).

The authors present results for the effect of axial strain on both a flow without and with rotation. The effect of axial strain on the mean flow in the non-rotating flow is simply an acceleration in the axial direction. The effect on the turbulence is studied in terms of the downstream development of the Reynolds stresses on the symmetry axis of the flow. From the budget equations for the normal stresses (see (2.10)) it can be deduced that –as far as the production terms are concerned– the axial normal stress should decrease and the transverse normal stress should increase (for a strain of the type produced by a contraction (2.21), see also section 2.3.2). The same conclusion could be drawn from the RDT analysis presented in section 2.3.2. However, in the experiment of Leuchter and Dupeuble both normal stresses decrease downstream. They attribute this to the influence of non-linear terms, based on the fact that the time scale of the linear distortion is of the same order as the time scale of the non-linear processes (rather than much smaller, as required for the neglect of non-linear terms). Nevertheless, the opposite effect of the axial strain on the axial and transverse normal stress component is still visible in the decrease of the stress-anisotropy (defined here as $A = (\overline{u'_z u'_z} - \overline{u'_r u'_r})$). A decreases from slightly above zero, to well below zero.

The comparison of the cases without and with rotation gives rise to a number of observations:

- The experimental results for the mean velocities are indeed in accordance with the inviscid analysis of Batchelor (1967);
- The decay of the normal stresses is reduced in the case of rotation;
- The decay of the axial normal stress is reduced more than that of the transverse component;
- As a result of the latter effect, the anisotropy of the normal stresses decreases downstream for both the rotating and the non-rotating case. This decrease is smaller for the case with rotation when compared to the case without rotation²¹;
- From an evaluation of the budget equation for the anisotropy Leuchter and Dupeuble show that the linear part of the pressure strain terms (i.e. the 'rapid part' which was obtained from the experiment as a rest term) is markedly different for the rotating and non-rotating case;

²⁰The strain is indeed constant for a flow *without* rotation. For flows *with* rotation the –radially– non-uniform change in u_z due to inviscid effects (see section 2.4.1) cause the strain to be non-constant.

²¹Leuchter and Dupeuble (1993) present their results in terms of a dimensionless anisotropy: $A^* = (\overline{u'_z u'_z} - \overline{u'_r u'_r}) / \overline{u'_i u'_i}$. The disadvantage of this approach is that the effect of rotation on the turbulent kinetic energy and the anisotropy is mixed. They show a large difference between the rotating and non-rotating case in the decay of the anisotropy (in terms of A^*). But a large part of this difference can be attributed to the different behaviour of the turbulent kinetic energy $\frac{1}{2} (\overline{u'_r u'_r} + \overline{u'_z u'_z})$.

- The effect on integral length scales was also studied. In the case of axial strain without rotation the length scale in z -direction for u_z is hardly affected, whereas the scale in the z -direction for u_r is increased beyond the length scale for u_z . In the case of axial strain *with* rotation this difference increases.

Linear and non-linear analysis

Leuchter and Dupeuble (1993) also present a linear spectral RDT analysis (see also Dupeuble and Cambon (1994)) along with their experimental results. Since non-linear effects had a large impact on the experiment (see above), a direct comparison of the results of the theoretical analysis and the experimental results is not useful. However, the RDT results do show the same trends as the experimental results. First, rotation reduces the generation of anisotropy by the axial strain. Through the budget equation for the turbulent kinetic energy this in turn reduces the growth of the turbulent kinetic energy. Secondly, the linear –rapid– pressure strain term is strongly enhanced by the rotation.

In Leuchter (1997) and Leuchter and Bertoglio (1995) a non-linear spectral EDQNM analysis is presented. The results of this analysis approaches the experimental results quite well, including the large non-linear effects observed in the experiment. Besides, two important conclusions with respect to the pressure strain terms are posed. First, it appears that the effect of rotation on the rapid pressure strain term can easily be isolated from the effect of the axisymmetric strain. This conclusion is based on the fact that –if the applied strain is split into a symmetrical part (the axial strain) and an anti-symmetrical part (the rotation)– it appears that the part of the rapid pressure strain term which is due to the symmetrical part is hardly affected by rotation. Secondly, the Rotta (1951) model for the so-called slow pressure-strain term seems to be adequate for both the rotating and non-rotating case.

2.5 To conclude

In this chapter the various aspects of a turbulent swirling flow subject to axial strain have been dealt with, i.e. turbulence, swirl and axial strain. The combination of this knowledge from past experiments and analyses leads to a qualitative picture of what may happen in the flow that is the subject of this thesis.

The flow domain can be divided into three regions: upstream, inside and downstream of the contraction.

Upstream of the contraction the flow is decaying swirling flow (section 2.2), which is dominated by non-linear processes:

- stabilising effects –near the centre– or destabilising effects –near the wall– of streamline curvature;
- reduced dissipation due to rotation;
- three-dimensionality in the near-wall region.

Then the fluid passes through the contraction, a process that combines swirl and axial strain (section 2.4). The effect of the axial strain on turbulent quantities is well described by linear

theory, but this process is strongly influenced by non-linear processes which are due to streamline curvature.

Finally, downstream of the contraction, again a stage of decaying swirling flow is entered. But since the flow has been heavily distorted by the axial strain, this stage has also the characteristics of a developing pipe flow (section 2.3.3). In the latter type of flows the turbulent quantities usually relax more quickly to their fully developed values than mean quantities. But two complications arise:

- The relaxation process might be influenced by the non-linear effects of streamline curvature;
- The flow will only attain fully developed state (i.e. with zero axial development) when the swirl has decayed completely.

The details of the different stages sketched above can only be found through laboratory experiments and numerical simulations. This will be the subject of the rest of this thesis.

3

Laser Doppler measurements

The main point of investigation in the flow under consideration is the velocity field: both the mean velocities and the turbulent fluctuations as they develop in a rotating flow under the influence of a change in cross-section. These velocities have been measured by means of a Laser Doppler Anemometry (LDA) system.

This chapter deals with the principles and techniques of Laser Doppler Anemometry. The first part, 3.1, gives an overview of the method of LDA. The second part describes the experimental set-up used in the current study.

3.1 Principles of Laser Doppler Anemometry

In principle, the determination of the velocity of a fluid using LDA consists of a number of separate processes (see figure 3.1, and details below):

- A laser beam illuminates the moving fluid.
- Particles are suspended in the fluid, and supposedly moving at the same speed as the fluid. A moving particle, when struck by the laser beam, will see light a Doppler shifted frequency. The Doppler shift depends on the component of the velocity in the direction of the laser beam.
- The laser light will be scattered by the particle in all directions. Due to the fact that the scattered light is emitted by a moving particle, the frequency of the light will again be Doppler shifted. In this case the Doppler shift depends on the component of the velocity of the particle in the direction of the detector.
- A stationary detector will detect the scattered light. Depending on the number density of scattering particles in the fluid, the scattered light will either arrive at the detector as individual bursts (low density) or as a continuous signal (high density).
- A signal processor analyses the detector signal (bursts or continuous) to determine the Doppler shift.

The idea behind Laser Doppler Anemometry dates back to the early 1960's. Since its discovery the technique has developed quickly and has become a standard technique. A number of advantages of LDA are that it is non-intrusive, both the magnitude and the direction (by using a frequency pre-shift) of the velocity can be measured, high frequency fluctuations of the velocity can be detected (depending on the sampling rate) and the spatial resolution is good (although the qualification 'good' depends on the scale of the flow and the flow domain).

A recent review of the technique of Laser Doppler Anemometry can be found in Adrian (1996). Here, some aspects of LDA are discussed qualitatively in the forthcoming sections.

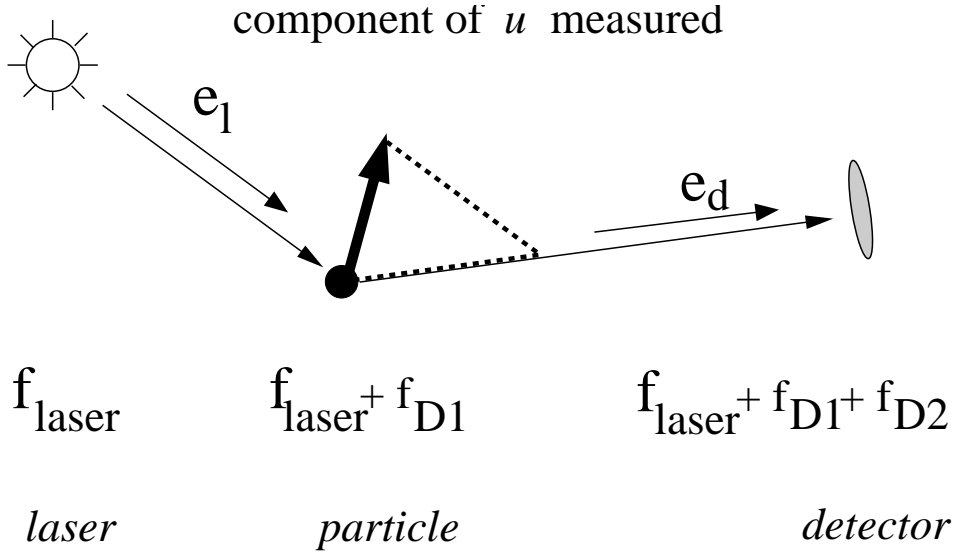


Figure 3.1: The principle processes of detecting fluid velocity with LDA: the frequency of the laser light experienced by a moving particle is Doppler shifted (D_1); the Doppler shifted light is scattered in all directions and impinges on the detector; due to the velocity of the particle relative to the detector, the light at the detector is Doppler shifted twice ($D_1 + D_2$).

3.1.1 Fundamentals

Without touching upon the details of the phase and amplitude of the electromagnetic fields involved in the theory of LDA (see e.g. Adrian (1996)), useful equations that link the Doppler shift of the detected light to the velocity of the scattering particle can be derived.

As shown in figure 3.1, suppose the direction of the incoming laser beam is given by the unit vector \mathbf{e}_l and the velocity of the scattering particle is \mathbf{u} . Furthermore, the wavelength of the laser is λ_l , the corresponding frequency is $f = \lambda/c$ or $\omega = 2\pi f$. Then the frequency of the light as seen by the particle, f_p , is:

$$f_p = f_l \left(1 - \frac{\mathbf{e}_l \cdot \mathbf{u}}{c} \right). \quad (3.1)$$

The light with frequency f_p in turn is scattered by the particle in all directions, among others in the direction of the detector, which is given by the unit vector \mathbf{e}_d . The frequency of the light observed at the detector is:

$$f_d = f_p \left(1 - \frac{\mathbf{e}_d \cdot \mathbf{u}}{c} \right)^{-1}. \quad (3.2)$$

Combination of equations 3.1 and 3.2 then gives an expression for the frequency at the detector, in terms of the frequency of the laser light:

$$\begin{aligned}
 f_d &= f_l \left(1 - \frac{\mathbf{e}_l \cdot \mathbf{u}}{c} \right) \left(1 - \frac{\mathbf{e}_d \cdot \mathbf{u}}{c} \right)^{-1} \\
 &\approx f_l \left(1 + \frac{(\mathbf{e}_d - \mathbf{e}_l) \cdot \mathbf{u}}{c} - \frac{(\mathbf{e}_d \cdot \mathbf{u})(\mathbf{e}_l \cdot \mathbf{u})}{c^2} + \dots \right)
 \end{aligned}$$

which for $|\mathbf{u}| \ll c$ reduces to:

$$\begin{aligned} &\approx f_l + f_l \left(\frac{(\mathbf{e}_d - \mathbf{e}_l) \cdot \mathbf{u}}{c} \right) \\ &= f_l + f_D, \end{aligned} \quad (3.3)$$

where f_D is the total Doppler shift ($D_1 + D_2$ in figure 3.1). In order to detect the Doppler shift f_D one needs to measure a tiny change (about 1 in 10^8) in the light frequency. Though this is possible with filters and modern electronics for high speed flows, for low-speed flows direct detection of f_D is virtually impossible. Therefore nearly all detection systems make use of so-called optical heterodyne detection. The principle of this technique is the optical mixing of light (with f_1) with a beam of different frequency, f_2 . The difference in f_1 and f_2 is either caused by the fact that only one of the two beams is Doppler-shifted, or by the fact that their Doppler-shift is different.

The mixing takes place at the photodetector. Since the detector is a square-law device, in its output only signals with frequencies $f_1 + f_2$ and $f_1 - f_2$ will be present¹. The sum frequency is much higher than the frequency response of the detectors and thus only the difference frequency remains. This difference frequency is related to the Doppler frequency –since the frequency of the light source has dropped out in subtracting both signals– and thus to the velocity of the scattering particle. The exact relationship depends on the optical configuration.

Roughly three optical configurations are used in LDA (Adrian, 1996):

- Reference beam method: one beam illuminates the particle and the scattered light is collected at the detector. There it is mixed with a beam that has not been scattered.
- Dual beam method: two beams illuminate a particle and light from both beams is scattered. At the detector the scattered light from both beams is mixed.
- Dual scatter method: one beam illuminates the particle. Light is collected at two different positions and mixed at the detector.

Since the reference beam method has been used in this study, some more details about this method are given below. More details of the setup used in this study can be found in section 3.2.2. In the reference beam method the light of the illuminating beam is scattered and Doppler shifted (see figure 3.2). If the direction of the illuminating beam is \mathbf{e}_l and the scattered light collected at the detector has direction \mathbf{e}_d (3.3) shows that the Doppler shift will be :

$$\begin{aligned} f_D &= f_l \left(\frac{(\mathbf{e}_d - \mathbf{e}_l) \cdot \mathbf{u}}{c} \right) \\ &= \frac{(\mathbf{e}_d - \mathbf{e}_l) \cdot \mathbf{u}}{\lambda} \end{aligned} \quad (3.4)$$

f_D is proportional to the velocity component parallel to the difference vector $\mathbf{e}_l - \mathbf{e}_d$. But the Doppler shift does not depend on the sign of the direction of the velocity.

¹Since the detector is a square-law device the output will be proportional to $(\sin 2\pi f_1 t + \sin 2\pi f_2 t)^2$ (ignoring possible phase differences between the signals). Given the trigonometric identities $(\sin x)^2 = \frac{1}{2}(1 - \cos 2x)$ and $\sin x \sin y = \frac{1}{2}[\cos(x - y) - \cos(x + y)]$ (with $x = 2\pi f_1 t$ and $y = 2\pi f_2 t$) the signal at the square law detector will only contain signals with frequencies $f_1 + f_2$ and $f_1 - f_2$.

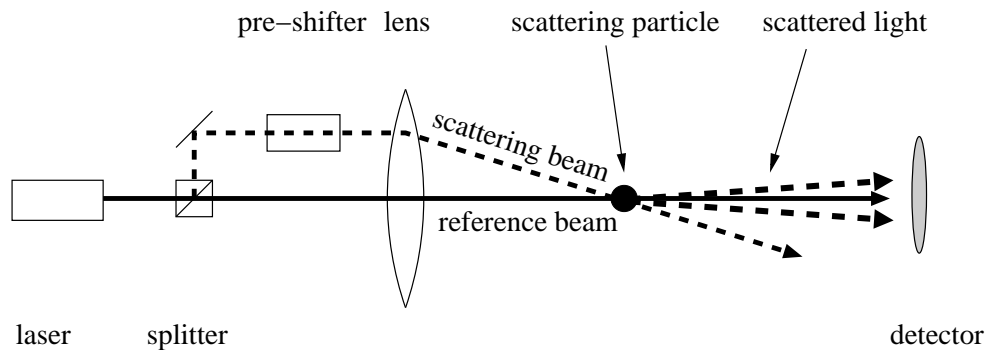


Figure 3.2: Optical configuration for the reference beam method. Light from the reference beam hits the detector directly. Light from the scattering beam (which originates from the same source as the reference beam, but has undergone a pre-shift) is scattered by the particle and the scattered light hits the detector. The light from both sources is mixed at the detector. The frequencies of light and signal at different locations is dealt with in figure 3.3.

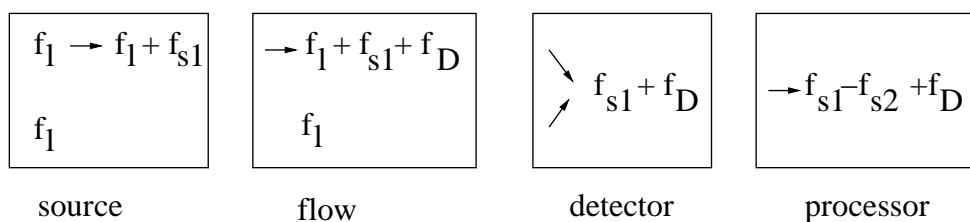


Figure 3.3: The changes in light frequency in a reference beam LDA. The light source produces two beams: a scattering beam (top) that is pre-shifted in frequency and a reference beam (bottom) with frequency f_1 . In the flow the frequency of the scattering beam is Doppler shifted (see figure 3.1). At the detector the light of scattering beam and reference beam is mixed. The resulting difference frequency ($f_{s1} + f_D$) is down-shifted by an amount f_{s2} .

In situations where the direction of the velocity vector is not known beforehand, or when velocities are close to zero, frequency shifting is used: the light of one of the two beams is shifted in frequency. Frequency shifting of light can be attained by either electro-optic cells, acousto-optic cells or with rotating diffraction gratings. The acousto-optic Bragg-cell is most commonly used and gives frequency shifts in the order of 10-80 MHz. The frequency of one of the beams is shifted by a fixed amount, f_{s1} . The total frequency at the detector will be $f_d = f_D + f_{s1}$. In low-speed flows the Doppler-shift can be much less than the pre-shift frequency. In those cases the detector signal is down-shifted by an amount f_{s2} to a level where it is more compatible with the range of the signal processor used. The various steps in the change in frequency are summarised in figure 3.3

3.1.2 Implementation

Scattering particles

The aim of LDA is to measure the velocity of the fluid under consideration. Consequently, the objects scattering the laser light should follow the fluid as well as possible; i.e. the particle inertia should be small (low density). On the other hand, the particle should have a density close to that of the surrounding fluid, in order for it not to float or sink, or to be influenced by centrifugal forces. An optical requirement is that the particles should have sufficiently large scattering cross-section (due to either size, shape or refractive index). Various seeding particles are used in practice such as plastic spheres (in water), aerosols (in air) or various types of oil.

Not only the properties of the seeding particles are important, also their concentration. This determines whether or not at every moment in time at least one particle is present in the measuring volume. If the answer is positive, a continuous Doppler signal can be obtained (i.e. the signals from individual particles can not be distinguished). In the other cases, each passing particle produces a burst of light at the detector with the Doppler frequency superimposed on it. This distinction has consequences for the type of signal processor that can be used (spectrum analysers and frequency trackers, vs. counters and burst analysers, see section on signal processing below).

Optics

The aim of an LDA system is to determine the Doppler shift generated by particles at a certain location in the flow. Ideally, one would like to determine the velocity at a point but in practice one can only determine the velocity in a volume: the measuring volume. The measuring volume is that part of the fluid from which scattered light, in combination with the light from the reference beam, will cause a Doppler shift at the detector. For measurements in flows close to a wall or with large velocity gradients, the measuring volume should be as small as possible, to make the velocity change across the measuring volume as small as possible.

One step in minimising the size of the measuring volume is the reduction of the beam diameter. The light intensity across a laser beam is not constant, but has a Gaussian radial dependence. Therefore the width of the beam is generally defined as the radial position where the intensity has decreased to e^{-2} of its centreline value. The beam produced by a laser is either diverging or converging. To minimise the size of the beam in the measuring volume, the beam must be made to converge, with the point of minimum diameter (beam waist) located in the point where measurements need to be done (measuring volume). To this end the beam first passes through a beam expander, and then through a converging lens. The beam waist will be located in the focal point of that lens. In the reference beam method this will also be the point where reference beam and scattering beam intersect (see figure 3.2). Apart from by the beam width, the size of the measuring volume is also determined by the characteristics of the detector and the signal-processor. The Doppler signal from a particle at the heart of the intersection of scattering beam and reference beam will be stronger than that from a particle at some distance from the centre. At a certain distance from the centre of the measuring volume the Doppler signal will fall below a level that is detectable by detector and signal-processor (Adrian, 1996).

Detailed analysis and experiments indicate that light scattered in a small cone around the

reference beam contributes to the Doppler signal (see figure 3.2 and Steenbergen (1995)). The cone may include light that is scattered by particles outside of the common volume of reference beam and scattering beam. The contribution of light from outside the common volume depends on the beam geometry, the scattering properties of the particles and the optics at the detector side. To reduce this contribution of light from outside the common volume, a combination of a lens and a small aperture is placed in front of the detector. The lens images the beam waist on the detector and consequently the Doppler signal will only be due to light scattered from within the reference beam (Steenbergen, 1995).

Detector

A photodetector is used to convert the variations in light intensity into variations in voltage. Two types of photodetectors are in use:

- Photo multiplier tube: photons that strike a photoemissive material cause electrons to be emitted. These electrons are collected at a dynode where for each impinging electron more than one electron is emitted. In this way the signal is amplified.
- Photo diode: a light-sensitive semiconductor. The resistance of the junction depends on the incident light flux. By applying a fixed current to the diode, a voltage proportional to the light intensity can be obtained.

Photo multipliers are used in situations where a high sensitivity is needed: under conditions of little scattered light, usually in back-scatter arrangements. Photo diodes, on the other hand, are used in conditions of high light intensity, e.g. in forward scatter. In the research photo diodes were used.

Signal processing

The final step in LDA is to derive the Doppler frequency from the voltage output by the photodetector. Various methods of signal processing have been described in the literature:

- Spectrum analysers and filter banks: the Doppler signal is fed into a (collection of) very narrow band filter(s). If a signal passes through a given filter, the velocity of the particle can be linked to the frequency of the given band filter.
- Counter: if a burst due to a scattering particle is detected, the time is determined for the signal to make a fixed number of zero-crossings.
- Frequency tracker: measures the instantaneous frequency of the signal using either a phase-locked-loop (PLL) or a frequency-locked-loop (FLL). In both cases the Doppler signal is compared with the output of an internal oscillator. The frequency of the internal oscillator is controlled by a voltage signal. The difference (in phase or frequency) between both signals adjusts this voltage such that the input signal and the internal oscillator are in phase (PLL) or have the same frequency (FLL). As a result, the voltage that controls the oscillator is proportional to the Doppler frequency.
- Burst analysers: if a burst is detected the Doppler frequency of the signal in the burst is determined either by Fourier Transformation of the signal within the burst, or by determination of the frequency of oscillations in the autocorrelation function of the burst signal.

The applicability of a signal processor to a given flow depends on two characteristics of the Doppler signal: the burst density (mean number of particles located simultaneously within the measuring volume: less than one or more than one) and the signal to noise ratio. All processors that depend on the analysis of a single burst need at most one particle within the measuring volume, and sufficient time between the arrival of individual particles. The frequency trackers, on the other hand, need a nearly continuous presence of particles within the measuring volume. Burst analysers are able to deal with slightly noisier signals than trackers (see Adrian (1996)). In the present research trackers were used.

3.1.3 Error sources

As with each measurement technique, there will be a discrepancy between the real value of an observed quantity and the value estimated from measurements. For LDA a number of groups of error sources can be identified.

Broadening effects

Since the Doppler signal varies linearly with the velocity component in a given direction, the probability distribution of the velocity and the Doppler signal should also be linearly related. Due to broadening effects, however, the distribution of f_D is broader than that of u . A number of causes of this broadening can be identified.

- If many particles are present in the measuring volume, the resulting Doppler signal will be the superposition of the signals of the individual particles. Those individual signals will have random phase and amplitude. As a consequence, the frequency (the time derivative of the instantaneous phase) of the resulting Doppler signal will have a random deviation from the Doppler frequency that is related to the velocity inside the measuring volume. This so-called ambiguity noise is an important drawback of flows with a high burst density.
- The frequency inside a burst can only be determined with limited accuracy, since it is a oscillating signal of finite length. This accuracy depends on the time it takes the particle to cross the measuring volume: transit time broadening (see Zhang and Wu (1987)).
- If a mean velocity gradient is present in the measuring volume particles that pass the measuring volume away from the centre will give extra variations in the observed Doppler frequencies (see Durst *et al.* (1995a));
- Brownian motion (negligible);
- Laser line width (negligible).

Optics and signal processing

The geometry of the various laser beams needs to be known accurately:

- In the equation that links the Doppler frequency to velocity (equation 3.4), the angle between the direction of the laser beam and the direction of detection occurs (through $\mathbf{e}_d - \mathbf{e}_l$). The accuracy with which these angles are known directly influences the accuracy of the velocity estimates.

- In a non-homogeneous flow not only the direction and magnitude of the velocity is important but also the location at which it is measured. Thus the positioning of the measuring volume is relevant.

For the set-up as used in this study, the effect of the aforementioned errors is quantified in appendix D (after Steenbergen (1995)).

When a wall-bounded flow is studied a number of difficulties, and potential error sources, arise:

- Optical access to the flow is needed. For this one needs a transparent wall. As long as this wall is flat and plane-parallel and the refractive index of the fluids on either side of the wall is equal, the geometry of the laser beams is not changed. If the refractive indices are not equal, but known, the beam geometry inside the flow can be determined from the geometry outside the flow domain. However, if the transparent wall is not flat, it will distort the beam geometry in a way that depends on the respective refractive indices and on the angle of the beams with the wall. The distortion of the beam geometry may even be so large, that the beams may even no longer cross. To overcome this problem, two solutions are possible: either make the wall as thin as possible in order to reduce the distortion to a tolerable amount (see e.g. Steenbergen (1996)), or to make sure that the wall is surrounded by fluids which have refractive index that is equal to that of the wall (refractive index matching).
- If a wall-bounded flow is studied and one wants to obtain measurements close to the wall, the material of the wall may act as a scatterer as well, thus causing a false signal with zero velocity. This can be remedied by using a clean wall, by refractive index matching (if feasible) and by the use of a combination of pre-shift and down-shift frequencies that excludes a zero velocity.

A final error that may be introduced by the signal-processing equipment is the accuracy of frequency shifts. If the light of one or more beams is pre-shifted (with a Bragg-cell for example) and down-shifted again, the accuracy of those shift frequencies influences the accuracy of the velocity estimates.

Statistical errors in estimates of flow statistics

The aim of LDA measurements is to obtain statistical properties of the flow. These are defined in terms of an ensemble average. In practice, however, the only averaging method available is a time average over a limited amount of time. This will introduce a difference between the true statistical property and the estimate of it, as derived from LDA measurements. These errors are dealt with in appendix A.

3.2 Experimental set-up

This section describes the set-up as used for the laboratory experiments in this thesis. Before all the details of the experimental set-up, first a short overview is given.

The experimental set-up is a closed system in which water is circulated. The flow is driven by gravity; i.e. water flows from a reservoir well above the experimental test section. At the

inflow of the horizontal experimental section an adjustable swirl generator (with guide vanes) is installed so that flows with different types and intensities of swirl can be generated. The experimental section is made of brass pipe sections and optical access to the flow is obtained by means of a special measurement sections. Pipes of two diameters are available, as well as a contraction so that both the flow through a straight pipe and flow with axial strain can be generated. A sketch (to scale) of the configuration used in this study was given in figure 1.5 on page 5. LDA measurements are done with a two-component reference-beam system with diode-detectors and trackers as signal processors.

For *details* on the pipe system and the LDA equipment, the reader is referred to Steenbergen (1995), Steenbergen and Voskamp (1998) and Steenbergen (1996).

3.2.1 Pipe system

Generation of flow

The pipe system is shown schematically in figure 3.4. It roughly consists of three parts:

- an experimental section of nearly 20m (between two rubber bellows);
- a reservoir about 10m above the experimental section; the water level in this reservoir is kept constant; the hydrostatic pressure due the height difference between reservoir and experimental section drives the flow;
- a reservoir in the basement is used as the main storage of water.

The pumps are used to keep the water level in the upper tank constant (within about 5cm). The flow rate is primarily controlled by operating valve 2. The use of a submerged valve (valve 2 rather than valve 1) proved to be advantageous with respect to cavitation within the valve. Valve 1, downstream of the test section, is used only occasionally for fine tuning of the flow rate. In the given configuration the maximum attainable flow rate is of the order of 60 m³/hr (which corresponds to a bulk velocity of 4.3ms⁻¹ for a pipe with inner diameter 70mm).

Four pumps are available to pump the water from the storage tank in the basement to the reservoir on the roof. The pumps are switched on automatically when the water level in the upper reservoir has dropped below a prescribed level (the upper and lower level of the water surface differ by about 5 cm, which leads to a variation in the bulk velocity of roughly 2.5 ‰).

To generate swirling pipe flow a swirl generator (see figure 3.5) is installed at the inflow end of the horizontal pipe section ('S' in figure 3.4). The swirl generator consists of a contraction from a diameter of 160 mm to 70 mm around an inner body. The generation of swirl is achieved by tangential inflow along guide vanes, which can be adjusted to change the strength of the swirl. The type of swirl can be adjusted by changing the configuration of the central channel, by means of allowing more or less flow through this central channel. The configuration of the swirl generator as used in the current study is shown in figure 3.5.

Pipe sections

The pipe sections used for the measurements consists of brass pipe with a wall thickness of 5 mm. The inner diameter is either 40 ± 0.1 mm or 70 ± 0.1 mm, where the uncertainties are better than those required by the DIN standard (the uncertainties have been measured at the ends of the pipe

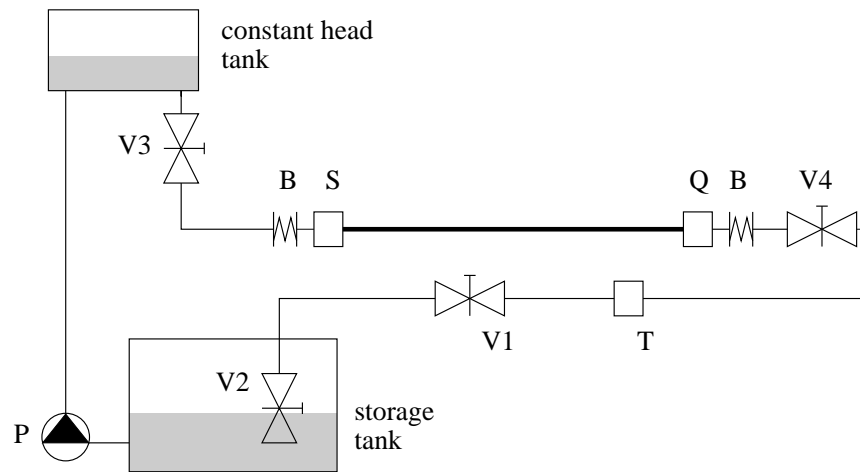


Figure 3.4: Schematic overview of pipe system (after Steenbergen (1995)). S: swirl generator; Q: flow meter; T: temperature sensor; V1, V2, V3 and V4: valves; B: rubber bellows; P: four pumps.

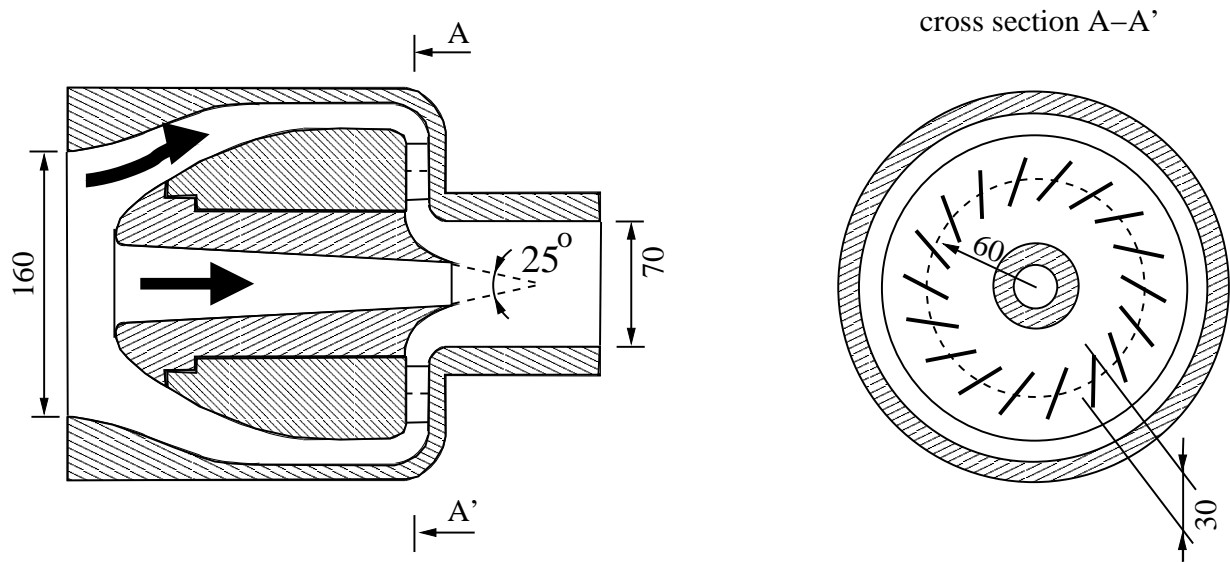


Figure 3.5: Swirl generator side view (left) and front view in direction opposite of flow direction (right). All sizes are in mm (after Steenbergen (1995)).

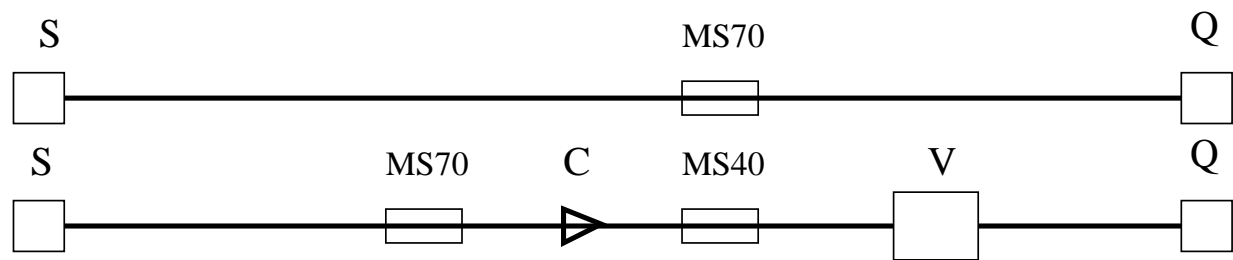


Figure 3.6: Two configurations of horizontal pipe section: straight pipe with a diameter of 70 mm (top) or varying pipe diameter: 70mm \rightarrow 40mm \rightarrow 70mm (bottom). S: swirl generator; Q: flow meter; C: contraction; MS40 and MS70: measurement sections with internal diameter 40mm and 70mm respectively; V: expansion vessel. Note that drawing is not to scale.

sections). The pipe sections are connected by specially designed couplings (see Steenbergen (1995)). These couplings ensure that pipe walls of two coupled pipes are aligned within 0.05 mm. Two flow configurations can be studied: a straight pipe with one diameter or a pipe with a change in pipe diameter. Both configurations are shown schematically in figure 3.6.

The measurement section (see figures 3.7 and 3.8) with internal diameter 70mm has three chambers with optical access (each 140mm apart), whereas the 40mm measurement section has two chambers (with the centres 320mm apart). The outer glass wall are made of high quality plane parallel glass of 5 mm thickness (DESAG highly transparent glass, B-270). The chambers can be rotated around the pipe axis in order to permit measurements under different angles (see section 3.2.2). In the chambers the brass pipe wall has been replaced by a thin polyester film (of 85 μm thickness). The space between the foil and chamber wall is filled with water that has a slightly lower pressure than the water within the pipe to ensure that the film is tight and stable (see also Steenbergen (1996)). The film is birefringent with refractive indices for the ordinary and the extra-ordinary rays are 1.27 and 1.47, respectively (Steenbergen, 1995).

Since the outflow of the pipe system has an inner diameter of 70 mm an expansion from a diameter of 40 mm to 70 mm is needed. This is done in an expansion vessel of PVC pipe with an inner diameter of 235mm and a length of 830mm. Apart from providing a transition in pipe diameter, the purpose of the expansion vessel is also to decouple the section of the pipe where the swirling flow is studied from the outflow of the pipe. The vessel should provide an approximation of free outflow into stagnant fluid.

Figure 3.9 shows the shape and dimensions of the pipe contraction used in the experiments on strained turbulence. The shape of the contraction is based on circle arcs and straight lines. This was done to ease manufacturing and to ensure a smooth transition from the straight pipe sections to the contraction (this in contrast to a contraction with a constant strain rate which would have a discontinuity in the first derivative). The latter is both important in the laboratory experiment itself (prevention of cavitation) and in the numerical experiment ².

²It was realised afterward –too late to redo the experiments– that this configuration has a discontinuity in the second derivative of the pipe diameter. This drawback (especially relevant for the numerical simulations) could have been prevented by using a polynomial of order 5 or higher. On the other hand, the shape of the contraction used here very can well be represented with a 5-th order polynomial (within 5% of the local diameter).

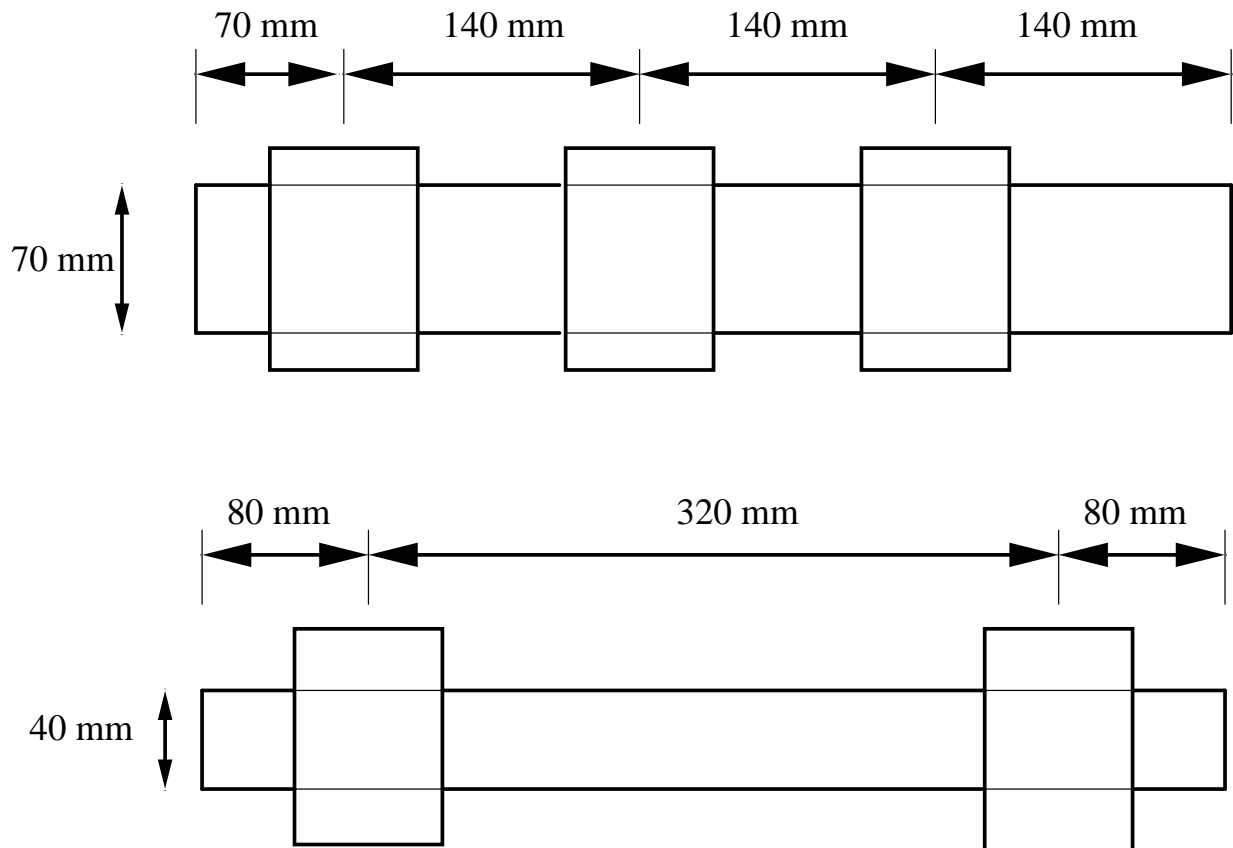


Figure 3.7: A sketch of both measurement sections: section with internal pipe diameter of 70mm, having three chambers (top) and the section with internal diameter 40mm having two chambers (bottom). The length of both measurement sections is not to scale.

3.2.2 LDA system: optics, positioning and data processing

In this section we describe the hardware that is used to perform the measurements. On one hand this comprises the LDA optics and electronics and the data logging equipment needed to store the data. The LDA optics is positioned relative to the pipe with help of a traversing mechanism. Finally, the miscellaneous measurements needed to characterise the flow are described.

The control of most components of the experimental set-up, as well as the data-logging is performed by means of the PHYDAS system (Voskamp *et al.*, 1989).

Optical configuration

The LDA method used in this study is the reference-beam method (as described in sections 3.1.1 and 3.1.2). The optical system is a two-component system with two reference beams in a plane parallel to the pipe axis and a scattering beam that is oblique to that plane (see figure 3.10). With equation (3.4) the resulting Doppler shift can be described, albeit with a number of modifications:

- The speed of light in water should be used, rather than that in air (or vacuum). Thus the

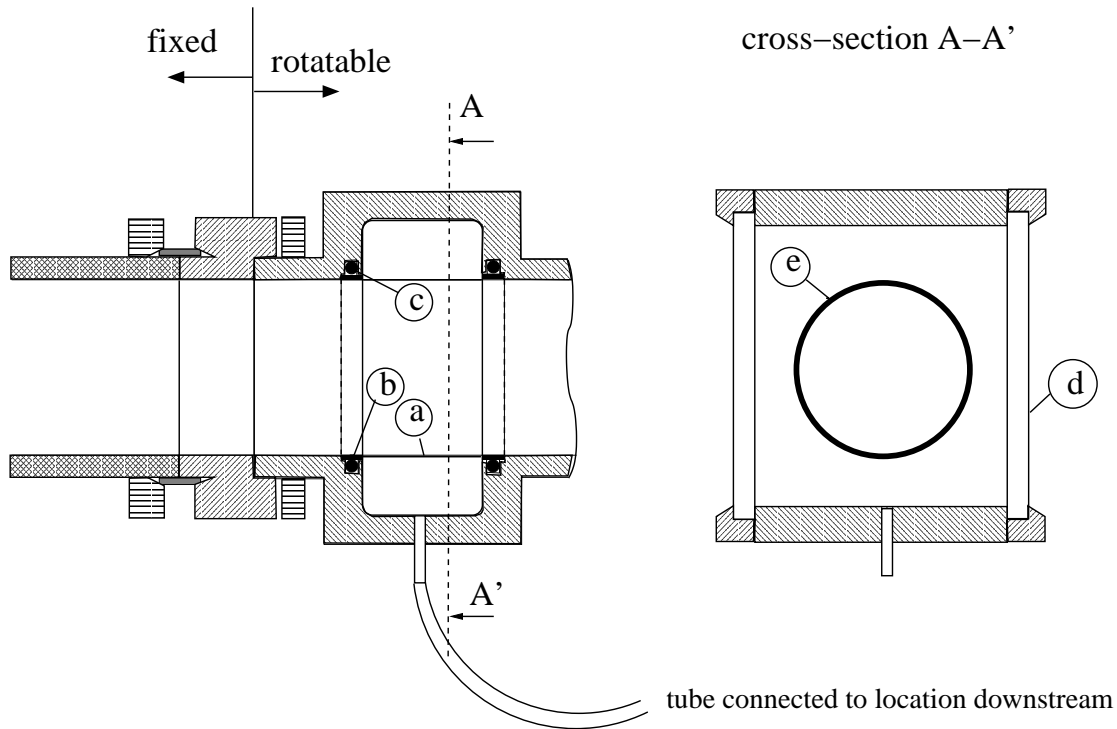


Figure 3.8: One chamber of the measurement section: side view (left) and view in direction of pipe axis (right). a: transparent film replacing pipe wall; b: brass ring to which film is glued; c: rubber O-ring; d: glass wall (high quality, plan-parallel).

factor $\frac{1}{\lambda}$ becomes $\frac{n_w}{\lambda}$.

- The unit vectors that give the direction of the beams (\mathbf{e}_l), as well as the direction of detection (\mathbf{e}_d), are different in water than in air. Using Snell's law, the direction vectors \mathbf{e}_l and \mathbf{e}_d can be translated. Since the glass walls of the measurement section are plane parallel, the direction of the beams is identical on both sides of the glass wall.
- When the reference beam and the scattering beam intersect, the direction of detection coincides with the direction of the reference beam (see page 40).

This results in:

$$f_{D, is} = n_w \frac{(\mathbf{e}_i - \mathbf{e}_s) \cdot \mathbf{u}}{\lambda} \quad \text{with } i = 1, 2 \text{ (reference beam 1 or 2), } s = \text{scattering beam,} \quad (3.5)$$

which can be summarised in matrix notation as:

$$\begin{pmatrix} f_{D, 1s} \\ f_{D, 2s} \end{pmatrix} = \begin{pmatrix} a_{1, 1s} & a_{2, 1s} & a_{3, 1s} \\ a_{1, 2s} & a_{2, 2s} & a_{3, 2s} \end{pmatrix} \begin{pmatrix} u_1 \\ u_2 \\ u_3 \end{pmatrix}, \quad (3.6)$$

where the direction 1 is in the direction of the pipe axis, direction 2 is perpendicular to the plane through the pipe axis and the optical axis and direction 3 is perpendicular to both 1 and 2. If the optics between laser and front lens (the lens in figure 3.10) are well aligned, the coefficients

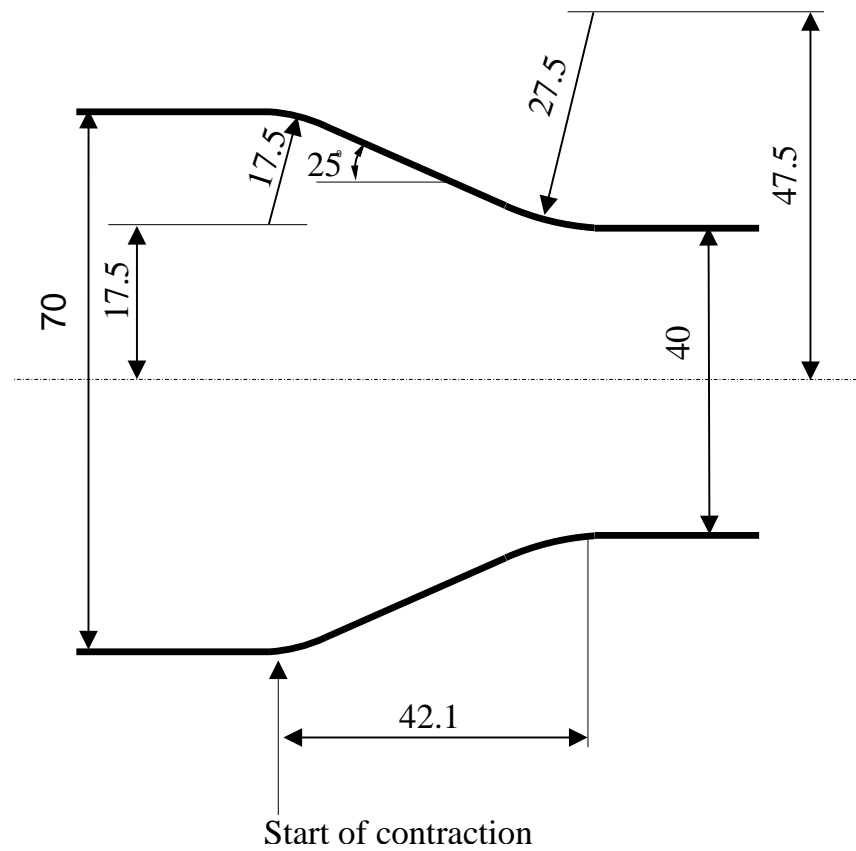


Figure 3.9: Dimensions of the pipe contraction (sizes are in mm)

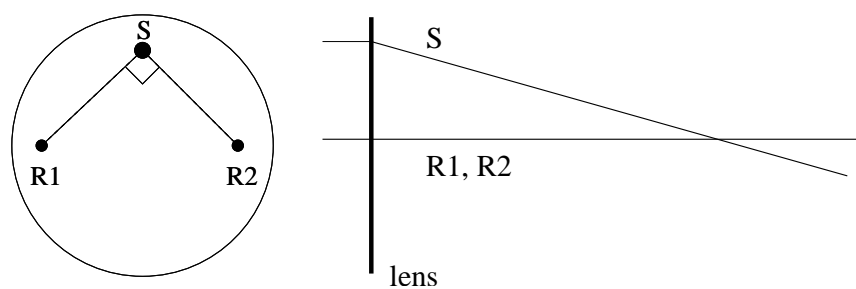


Figure 3.10: Configuration of the laser beams, front view (left), side view (right): S denotes the scattering beam and R1 and R2 are the two reference beams.

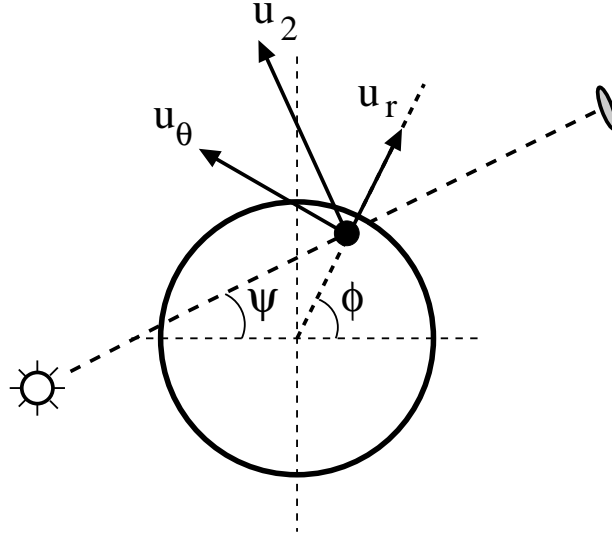


Figure 3.11: Relationship between velocity component u_2 in LDA coordinate system and u_θ and u_r in cylindrical coordinate system.

$a_{3,1s}$ and $a_{3,2s}$ are about four orders of magnitude smaller than the other coefficients and can thus be neglected. In that case (3.6) reduces to a set of two equations, with two unknowns (u_1 and u_2). However, one is not interested in the velocity components defined in the coordinate system of the LDA optics, but in those in the cylindrical coordinate system of the pipe, i.e. u_z , u_r and u_θ . If the optical axis of the LDA optics passes through the axis of symmetry of the cylindrical coordinate system, u_1 corresponds to u_z and u_2 to u_θ . More generally, the following relationship can be given:

$$u_1 = u_z \quad (3.7a)$$

$$u_2 = u_\theta \cos(\phi - \psi) + u_r \sin(\phi - \psi), \quad (3.7b)$$

where ψ is the inclination of the LDA optics and ϕ is the inclination of the line through the measuring volume and pipe axis (see figure 3.11). Relationship (3.7b) holds as well for the mean velocities. The relationship between covariances in both coordinate systems is given by

$$\overline{u'_1 u'_1} = \overline{u'_z u'_z} \quad (3.8a)$$

$$\overline{u'_2 u'_2} = \sin^2(\phi - \psi) \overline{u'_r u'_r} + \sin 2(\phi - \psi) \overline{u'_r u'_\theta} + \cos^2(\phi - \psi) \overline{u'_\theta u'_\theta} \quad (3.8b)$$

$$\overline{u'_1 u'_2} = \cos(\phi - \psi) \overline{u'_z u'_\theta} + \sin(\phi - \psi) \overline{u'_r u'_z} \quad (3.8c)$$

In order to obtain all three mean velocities as well as all six components of the Reynolds stress tensor at a given point in space, the LDA measurements need to be made under three different angles ψ (two angles would be sufficient to obtain the mean velocity components only). The sensitivity of $\overline{u_r}$, $\overline{u_\theta}$, $\overline{u'_r u'_z}$, and $\overline{u'_z u'_\theta}$, to inaccuracies in the tilting angles ψ (see appendix D) is minimum when ψ equal -45, 0 and 45 degrees. To reduce errors in $\overline{u'_r u'_r}$, $\overline{u'_\theta u'_\theta}$, and $\overline{u'_r u'_\theta}$ due to

inaccuracies in ψ , the angles should be -60, 0 and 60 degrees. However, the latter combination is not permitted by the traversing system, and hence tilting angles ψ of -45, 0 and 45 degrees are used (Steenbergen, 1995).

The procedure to obtain mean velocities and Reynolds stresses is the following:

- \bar{u}_z is obtained by averaging the \bar{u}_1 for all three angles;
- \bar{u}_r and \bar{u}_θ can be computed from the combination of \bar{u}_2 measured for two different angles ψ (see (3.7b)); with three available angles, three combinations can be made; the three resulting values for \bar{u}_r and \bar{u}_θ are averaged;
- $\overline{u'_z u'_z}$ is computed as the average of the three available values for $\overline{u'_1 u'_1}$;
- from the combination of $\overline{u'_2 u'_2}$ for three different angles $\overline{u'_r u'_r}$, $\overline{u'_r u'_\theta}$ and $\overline{u'_\theta u'_\theta}$ can be computed (see (3.8c));
- with equation (3.8c) $\overline{u'_z u'_\theta}$ and $\overline{u'_r u'_z}$ can be computed by combining measurements under three different angles; with three available angles, three different combinations of two angles can be made; the resulting values for $\overline{u'_r u'_z}$ and $\overline{u'_z u'_\theta}$ are averaged.

Laser and signal processing

The velocity measurements are made using an LDA system of Dantec. The system is based on the reference beam principle (using forward scattered light). The laser that is used is a 15 mW He-Ne laser manufactured by Uniphase. The optics mounted before the laser provide two reference beams and one scattering beam (see figure 3.10 and 3.12). The scattering beam is shifted in frequency (40MHz) by a Bragg-cell (the Bragg cell is driven by a signal from one of the frequency shifters Dantec 55N10). Two different front lenses can be mounted on the optics: one with a focal length (f) of 160mm and one with $f = 80$ mm. The beams pass through the measurement section and the light of the reference beams and the light scattered in the direction of the reference beams is collected by lenses with a focal length of 60mm. Subsequently, it passes through a pinhole and finally hits the photo diode (the pinhole is part of the housing of the diode Dantec 55L11). In the shifter the signal from the diode is shifted back by a frequency which is the sum of the 40MHz pre-shift of the Bragg-cell and a (positive or negative) frequency needed for an optimal use of the range of the tracker. From the shifter the signal is passed to the Dantec tracker 55N21 where the high frequency information is converted to a voltage (between 0 and 10 V). The selection of the frequency range of the tracker (out of seven) and the shift frequency if the shifter (54 available) depends on the Doppler shifts that are generated by the flow. The choice of range and shift is always such that measurements in one traverse ($-1 < r/R < 1$) can be made with one combination of range and shift.

The analog signal from the tracker is digitised using the parallel sampler (PARSAM) developed by 'Technical Laboratory Automation Group' at TUE (see Smeets and van Nijmweegen (1993)). Since the PARSAM has an input voltage range of -10 V to 10 V, a programmable amplifier³ is used to re-scale the signal from the tracker. The output signal of the lock indicator of the tracker is fed directly to the PARSAM. The PARSAM uses a 12bit analog-to-digital converter (ADC). The choice to use a PARSAM in this experiment (rather than a conventional ADC) is

³Built by Jan Niessen.

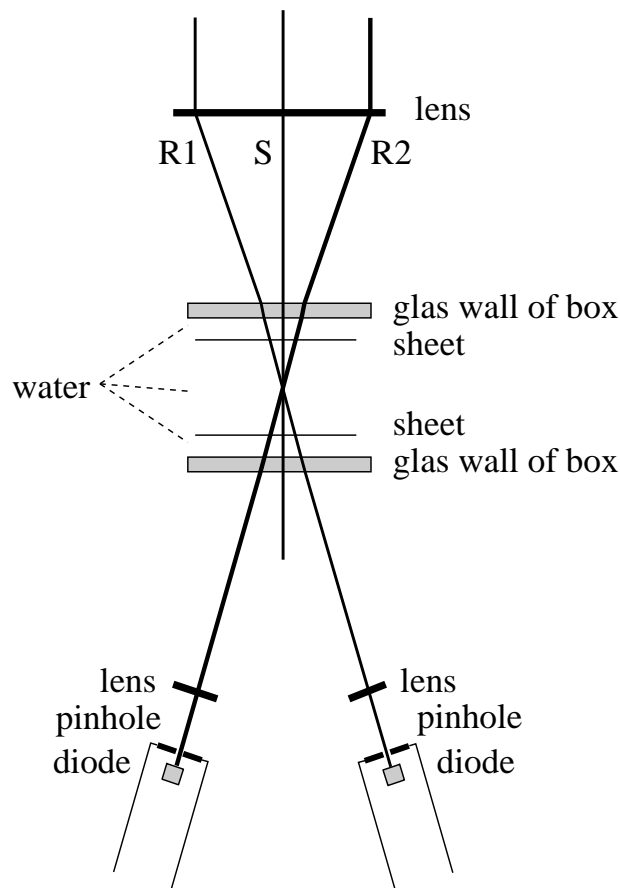


Figure 3.12: Top view of the path of the laser beams: from front lens of the sending optics, through the measurement section (glass walls and sheet) toward the diode optics

based on two considerations:

- the PARSAM allows high sampling rates (up to 25 *kHz* per channel);
- two memory buffers (512 *kB* each) allow continuous operation, so that large amounts of data can be gathered continuously;

These two latter characteristics are mainly important when information on the temporal structure of the signal is required (such as spectra).

Steenbergen (1995) observed that the response of the trackers used in this study was not linear and that this non-linearity was mainly linked to the ambient temperature. Therefore the trackers need to be calibrated daily using a second order polynomial. For this calibration a Philips PM5138 function generator is used.

Traversing system

The traversing system to move around the LDA optics is shown in figure 3.13. The coordinates of this traversing system are defined as follows:

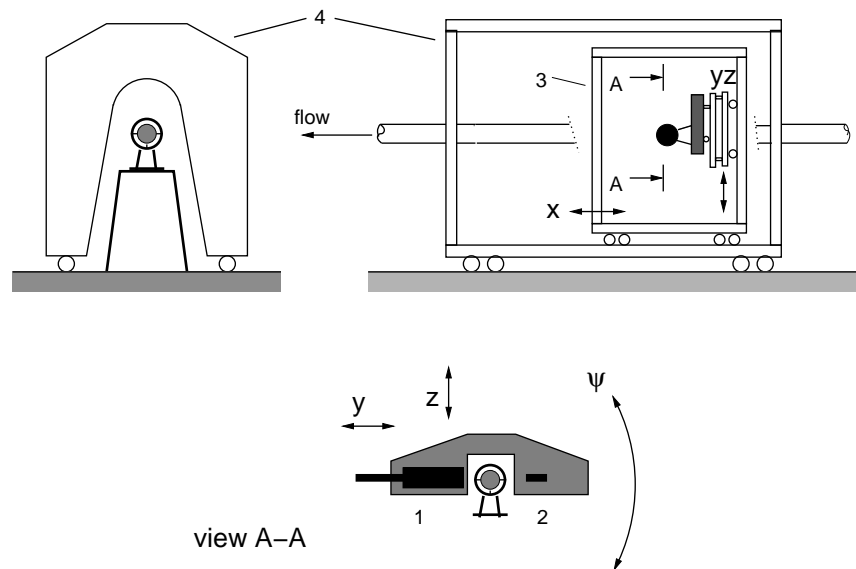


Figure 3.13: Traversing mechanism (figure from Steenbergen (1995)): view in the direction of the flow (top left), side view (top right) and the rotatable plate to which the optics are mounted (bottom); 1: transmitting optics; 2: photo-detectors; 3: rigid frame; 4: frame standing on floor; x -direction is flow direction, y is horizontal perpendicular to flow direction, z is vertical.

- x is the direction parallel to the pipe axis.
- y is the direction perpendicular to the pipe axis and perpendicular to the vertical defined by gravitation.
- z is the direction perpendicular to the pipe axis and parallel to the vertical defined by gravitation.

The plate to which the LDA optics ('1' and '2') are mounted can be turned around an axis that is parallel to the pipe over an angle of -50° to 50° . This rotation mechanism in turn is mounted on a plate that can be moved horizontally (y) and the latter plate is mounted to a plate that can be moved vertically (z). This vertical movement is relative to a rigid frame ('3' in figure 3.13) that can be moved horizontally (in a direction parallel to the pipe) within the outer rigid frame ('4'). The latter is standing on the floor of the laboratory. For the y and z movement use is made of stepper motors that allow movements with a step of 0.02mm to be made. The number of steps is checked by position encoders connected to the shafts of the stepper motors. End-switches are used to restrict the movement of the plate with optics to a bounded region. For the vertical movement counter weights are used in order to drastically reduce the amount of power needed to traverse the optics vertically.

Miscellaneous measurements

Besides the velocity measurement by means of the LDA, some additional quantities are measured: water temperature and flow rate.

The water temperature is monitored with the help of a thermal diode of which the signal is converted to a voltage signal with a Laumann temperature display (which also displays the temperature). The flow rate is measured by an Altometer magnetic flow meter (SC 80 AS), which has a current output proportional to the flow rate. This current is converted to a voltage by passing the current through a resistor of $470\Omega \pm 1\%$. The temperature and flow rate signal are digitised using a 12 bit ADC.

Incidentally measurements of pressure drop between difference axial positions have been done. To this purpose pressure taps (with a diameter of 0.5mm) are present in the pipe wall. These taps can be connected to one of the two pressure transducers, Validyne DP15-30 or DP45-16, which have a range of $|\Delta p| \leq 880$ and $35\text{mmH}_2\text{O}$, respectively. The signal of these pressure transducers is passed through an amplifier to a 12 bit ADC.

Alignment and calibration

A number of angles in the geometry of the beams and the flow need to be known or set accurately. Details of these calibrations and alignments can be found in Steenbergen (1995). Here only the main points are given.

- The geometry of the three beams has been determined with a theodolite (for the procedure see Steenbergen (1995)). For a large part of the experiments the calibration done by Steenbergen has been used. After a disruption of the alignment by a careless window-cleaner this calibration had to be redone.
- The entire pipe (including the measurement section) is made level in the axial direction with an accurate water level.
- The traversing system should be level, both in the directions parallel and perpendicular to the pipe axes. This is checked with an accurate water level.
- Inclination ψ for measurement section: the (windows of the) measurement section is set to the correct inclination angle ψ with the help of an accurate water level. For $\psi = 0$ the water level is placed directly on the measurement section, whereas for $\psi = \pm 45^\circ$ a metal wedge of exactly 45° is used.
- u_z in direction of pipe axis: the optical axis of the LDA system is set perpendicular to the pipe axis: by rotating the LDA system is rotated around its optical axis such that the plane through the reference beams is *vertical*; then the traversing system is turned (around its vertical axis) until the reflected reference beams (reflected in the window of the measurement section) fall within the plane of the reference beams themselves.
- Inclination ψ for LDA optics: the optical axis of the LDA system set to the correct inclination ψ horizontal by first turning the LDA system around its optical axis such that the plane through the reference beams is *horizontal*; then the plate on which the optics are mounted (see figure 3.13, is turned until the reflected reference beams (reflected in the window of the measurement section) fall within the plane of the reference beams themselves.
- Rotation of LDA around its optical axis: the LDA system is aligned such that a motion in the direction of the pipe axis gives a zero vertical velocity according to the LDA. To this end a transparent plate is used as a scatterer. This plate is slid on top of the measurement section, parallel to the pipe axes and its velocity in x and z direction is measured with the

LDA. The LDA optics is rotated around its optical axis until u_x and u_z given by the LDA indicate that the motion is purely horizontal within 0.1 degree.

- The coordinate system of the traversing system needs to be tied to the coordinate system of the pipe. This is done by measuring (with a telescope which is translated parallel to the pipe axes) the distance between the intersections of the two reference beams with the pipe wall. This distance is determined three times. Twice with the LDA optics placed such that the measuring volume is near the pipe axes (the distance between the beam-wall intersection is measured at both sides of the pipe: at the pipe wall closest to the laser and at the opposite side). And once with the LDA optics placed off-axis. From these three measurements, the distance between the origin of the coordinate system of the traversing system and the pipe axis can be determined, as well as the pipe diameter. If the latter is within 0.1mm of its nominal value (either 35mm or 20mm) the alignment is accepted.

The effect of inaccuracies in the above procedures have been analysed by Steenbergen (1995). His results are reproduced in appendix D.

3.3 Measurement strategy

3.3.1 Flow types

The geometry of the flow domain is a circular pipe containing a contraction; the diameter of the pipe upstream of the contraction $D_u \equiv D = 70\text{mm}$, whereas downstream the diameter is $D_d = 40\text{mm}$.

Two types of flow have been studied: developed turbulent pipe flow and turbulent pipe flow with swirl. For the measurements without swirl the contraction was situated at $82D$ downstream of the swirl generator (which had a vane angle of zero degrees, producing zero swirl) so that in the inflow of the contraction a fully developed pipe flow could be assumed. For the measurements with swirl the contraction was placed only $14D$ downstream of the swirl generator (closer to the swirl generator in order to have a higher swirl number at the entrance of the contraction). In that case the angle of the vanes relative to the radial direction was 45 degrees;

Both flows have been studied at two values of Re_D (where D is the diameter *upstream* of the contraction, i.e. the larger diameter): $2 \cdot 10^4$ and 10^5 , respectively. During the measurements, the Reynolds number was required to remain within 1% of its nominal value (where both variations in flow rate and temperature were taken into account).

For the two types of flow measurements have been performed, at both Reynolds numbers, at six axial positions. Two of these positions were situated upstream of the contraction ($x/D = -5.8$ and -1.8) and four downstream: $x/D = 2.4, 6.9, 11.4$ and 25.2 . Here the origin of the axial coordinate is located at the point of the contraction where the radius starts to diminish (indicated in figure 3.9) and all axial positions have been scaled with the *upstream* pipe diameter.

At each axial measuring position a number of measurements have been made, as will be detailed in section 3.3.2 and 3.3.3.

Reynolds number	Sampling frequency	
	$D = 40\text{mm}$	$D = 70\text{mm}$
20000	100	50
100000	500	200

Table 3.1: Sampling frequency (Hz) for measurements at different bulk Reynolds numbers and in pipe sections with different diameters.

3.3.2 Processed data

The main part of the data gathered, are data to determine the mean velocity and Reynolds stresses at the *axial* positions mentioned in the previous section and at a large number of *radial* positions. Data were gathered at 47 radial positions ranging from $-0.99R$ to $0.99R$ with a higher concentration of point near the wall than near the pipe centre. These data are processed before being stored⁴. To determine all components of the mean velocity and the Reynolds stress, the measurements need to be repeated under three different angles ψ . The traverse along the r -direction (pipe coordinates) was made horizontally (i.e. the y -direction in the coordinate system of the traversing system). The sampling frequency is set such that the individual samples (of the continuous tracker signal) are supposed to be independent (see table 3.1). The number of samples is based on a rough estimate of the required error in variances and covariances and is set to a nominal value of 50000.

For each of the radial positions the strategy is as follows:

- The control program moves the measurement volume to the radial position under consideration.
- The control program determines the quality of the signal:
 - A limited number of samples is taken.
 - If for less than 75% of these samples the tracker was locked, the number of samples to be taken is increased in order to retain the originally requested number of samples. If this final number of samples is more than twice the nominal number of samples the position is skipped for further measurements.
 - If for more than 75% of the samples the tracker was locked, the original number of samples will be gathered.
- If the position is not skipped because of a lack of locking of the tracker, the measurements will be made. The quality of the data will be assessed again (the program requires the tracker to have locked for more than 75% of the samples). If the data quality is sufficient the samples of the velocity signal will be processed and stored to file.

Thus the actual number of samples used for the processing may be between 75% and 100%

⁴At the moment that this project started, storage capacity was a serious problem, so that storage of all individual samples seemed not feasible.

of 50000. Depending on the signal quality data may be not present for some of the 47 radial positions. Especially the radial positions closest to the wall prove to have a low signal quality.

3.3.3 Raw data

Apart from the data that are gathered and processed on-line (previous section), raw velocity data are gathered and stored for later processing. This is done only for a limited number of radial positions (because of the limitations in data storage). For each flowtype (swirl or no swirl), at each axial position, and each Reynolds number, two traverses are made to obtain raw data: a horizontal traverse to obtain u_z and u_θ and a vertical traverse for u_z and u_r . Each traverse consists of only nine radial positions ranging from $r/R = 0$ to $r/R = 0.97$. The sampling frequency depends on the cut-off frequency of the low pass filter of the tracker for the range used⁵. The number of samples is $2 \cdot 10^5$. Together with the velocity data, also the lock information for both channels is stored. In the post-processing, samples for which the tracker does not lock are replaced by linearly interpolated values.

⁵Only after completion of the experiment it turned out that the filter in the tracker was not very sharp (first order only). As a consequence, for some combinations of range and sampling frequency the sampling frequency was too low and aliasing occurred. This mainly affects spectra of the measurements at $Re_D = 2 \cdot 10^4$.

4

Numerical simulation of turbulence

Three fundamentally different approaches to the numerical modelling of turbulent flows can be distinguished: Direct Numerical Simulation (DNS), Large Eddy Simulation (LES) and ensemble averaged modelling¹.

In section 2.1.2 it was shown that the ranges of length and time scales present in a turbulent flow depend on the Reynolds number. From (2.6) it can be deduced that even for a moderate (macroscale) Reynolds number of 10^4 the range of length scales comprises three orders of magnitude and the range of time scales one order of magnitude. This large separation between the smallest and the largest scales forms a challenge to the three major approaches in turbulence modelling.

In DNS discretized versions of the Navier-Stokes equations (and possibly additional conservation equations for scalars) are solved and integrated in time. Due to the large range in scales one needs a high spatial and temporal resolution. Both increase with Reynolds number. The information one can obtain from a DNS are both instantaneous realisations of the flow and statistical quantities which are obtained from computing statistics in the homogeneous dimensions, be it spatial and/or temporal.

In LES, the problem of the enormous range of scales in a turbulent flow is tackled by spatially filtering the governing equations with a filter with characteristic size² l_f (see section 4.1.1). In that way the range of length scales is reduced to L/l_f . The filtering operation results in extra terms in the governing equations, which describe the influence of the flow at scales smaller than l_f on the flow at scales above the filter size. These terms have the form of the divergence of stresses and these stresses need to be modelled (see section 4.1.3). These stresses are commonly—but incorrectly—called 'subgrid-scale stresses' (SGS-stresses), whereas in principle they should be named *subfilter*-scale-stresses. The SGS-stresses provide the communication between the resolved scales (grid scale, or GS) and the dissipation scales. As in the case of DNS, the information one can obtain from LES are instantaneous fields and statistical quantities.

The third approach to the modelling turbulent flows is ensemble averaged modelling. This approach comprises two steps: Reynolds decomposition of all variables in the Navier-Stokes equations (see section 2.1.3) and ensemble averaging of those equations (see (2.9)). These steps produce additional terms which contain the so-called Reynolds stresses. In order to *close* the

¹Numerous reviews on these subjects are available: for DNS see Moin and Mahesh (1998), for LES see Reynolds (1989), Lesieur and Méttais (1996) or Mason (1994) and concerning ensemble average models see Launder (1990) or Speziale (1989).

²Filtering can both be done in the spatial and the spectral domain. In the latter case a parameterisation is sought for the spectral transfer across the wavenumber at which the equations were filtered. From here onward only spatial filtering will be considered.

equations, one needs a model for Reynolds stresses. Various approaches to the modelling of the stresses exist (see Stull, 1988; Wilcox, 1993, for an overview), ranging from first-order closure (Reynolds stresses are estimated from mean quantities), through two-equation models (Speziale *et al.*, 1992; Speziale, 1987; Wilcox, 1988) to algebraic stress models (Rodi, ????) and second-order closure or Reynolds-stress models (Launder *et al.*, 1975; Launder, 1990).

Section 4.1 describes the principles and the techniques used in Large Eddy Simulation of turbulent flows. In 4.2 the model used in the present study is described.

4.1 Principles of Large Eddy Simulation

4.1.1 Filtering the governing equations

The equations that are solved in an LES model are filtered versions of the Navier-Stokes equations. Formally, the filtering operation involved in the development of the governing equations in LES can be defined as:

$$\widehat{\phi}(\mathbf{x}, t) = \int \phi(\mathbf{x}', t) F(\mathbf{x} - \mathbf{x}') d\mathbf{x}' \quad (4.1)$$

where $F(\mathbf{x} - \mathbf{x}')$ is the filtering function and $\widehat{\phi}$ is the filtered variable (see Aldama (1990) for a discussion on filtering)³. The filter function F is non-zero within a distance of the order of l_f from \mathbf{x} and zero elsewhere. The actual field can be interpreted as a filtered field plus a sub-filter deviation:

$$\phi = \widehat{\phi} + \phi^* \quad (4.2)$$

Although this expression appears to be similar to the Reynolds decomposition, there are important differences to note. A *spatial filter* does not necessarily possess all the properties of an *ensemble average* (see (A.7)). In particular, the following differences should be mentioned (Reynolds, 1989; Boris *et al.*, 1992):

- Depending on the filter used, the filtering operation may not fulfil the condition that $\widehat{\widehat{\phi}} = \widehat{\phi}$. A spectral sharp cutoff filter *does* obey $\widehat{\widehat{\phi}} = \widehat{\phi}$, whereas a Gaussian filter does not. For a tophat filter generally $\widehat{\widehat{\phi}} \neq \widehat{\phi}$, unless the filtered variables are defined only at discrete locations in space and the filter length equals the spatial spacing (see Schumann, 1975b);
- Filtering and differentiation do not commute in general: $\widehat{\frac{\partial}{\partial x} \phi} \neq \frac{\partial}{\partial x} \widehat{\phi}$ (where x is either a space or time coordinate); only when the filter is constant in space and time (e.g. a convolution filter like equation (4.1)) do filtering and differentiation commute. Non-constant filters might be useful when the size of the energy containing eddies varies within the flow domain. Besides, the presence of solid boundaries makes filters vary in space (e.g. van der Ven, 1995).

³Note that in (4.1) the filtered variable $\widehat{\phi}$ is not necessarily a continuous variable in space or time (see Schumann, 1975b).

Application of the filtering operation to the continuity equation yields (under the assumption that filtering and differentiation commute):

$$\nabla \cdot \widehat{\mathbf{u}} = 0, \quad (4.3)$$

and the momentum equation becomes:

$$\frac{\partial \widehat{\mathbf{u}}}{\partial t} + \nabla \cdot \widehat{\mathbf{u}\mathbf{u}} = -\frac{1}{\rho} \nabla \widehat{p} + \nabla \cdot \nu \widehat{\mathbf{S}} - \nabla \cdot \boldsymbol{\tau}, \quad (4.4)$$

where $\boldsymbol{\tau}$ is a stress-like tensor resulting from the filtering operation applied to the nonlinear advection term. In view of the derivation of models for $\boldsymbol{\tau}$ (see section 4.1.3) it is important to note that this stress is a quantity that varies in space and time. In the sequel, the combination of equations (4.3) and (4.4) will be called the 'LES-equations'⁴.

The full expression for this sub-filter scale tensor, $\boldsymbol{\tau}$, is:

$$\boldsymbol{\tau} \equiv \widehat{\mathbf{u}\mathbf{u}} - \widehat{\mathbf{u}}\widehat{\mathbf{u}} = \left(\widehat{\mathbf{u}\mathbf{u}} - \widehat{\mathbf{u}}\widehat{\mathbf{u}} \right) + \left(\widehat{\mathbf{u}\mathbf{u}^*} + \widehat{\mathbf{u}^*\mathbf{u}} \right) + \widehat{\mathbf{u}^*\mathbf{u}^*}, \quad (4.5)$$

where the three terms at the right-hand-side are the Leonard stresses, the cross-stresses and the SGS-stresses, respectively. The SGS tensor $\boldsymbol{\tau}$ contains unknown quantities and needs to be modelled (see 4.1.3). It depends on the type of filter used which of these terms are non-zero. Various approaches to the treatment of these terms can be followed (Aldama, 1990).

The Leonard terms could be lumped with the advective term and the resulting advective term ($\widehat{\nabla \mathbf{u}\mathbf{u}}$) could be obtained by explicit filtering (see e.g. Piomelli and Ferziger, 1988). Alternatively the doubly filtered term in the Leonard stress could be approximated with a series expansion around $\widehat{\mathbf{u}\mathbf{u}}$ (Leonard, 1974; Aldama, 1990; Vreman *et al.*, 1997). In the latter approach one needs to take into account that the expansion depends on the filter used, and that the expansion will result in a third-order term in the filtered Navier-Stokes equation. It will depend on the accuracy of the numerical method whether it makes sense to compute this term. Other researchers have just lumped the Leonard term in the parametrisation of the SGS-stress, where it should be kept in mind that the Leonard stresses are dissipative in general (according to the analytical approximation by Leonard (1974)).

Although the cross stresses and the SGS-stresses both involve SGS velocities, they are of a completely different nature. Whereas the SGS-stresses describe the net dissipative effect of the SGS fluctuations on the resolved field, the cross terms describe the random interaction between resolved and SGS scale velocity fields (Aldama, 1990). This difference can also be explained in terms of the direction in which transfer of energy takes place: either from GS to SGS, or from SGS to GS. The cross-terms may transfer energy in either direction, both locally (and instantaneously) and in the mean. On the other hand, the SGS-stresses will –in the mean– transfer energy from the GS to the SGS. Locally, however, the direction of energy transfer might be reversed:

⁴The LES-equations do not contain an independent equation for the pressure. However, this can be constructed by taking the divergence of (4.4) which yields, together with the constraint of incompressibility, a Poisson equation for the pressure: $\frac{1}{\rho} \nabla^2 \widehat{p} = \nabla \cdot \left(-\nabla \cdot \widehat{\mathbf{u}\mathbf{u}} + \nabla \cdot \nu \widehat{\mathbf{S}} - \nabla \cdot \boldsymbol{\tau} \right)$

backscatter occurs (Kraichnan, 1976; Vreman *et al.*, 1997; Mason and Thomson, 1992). Despite this difference between the SGS-stress and the cross-terms, the latter are often lumped with the SGS-stresses and parameterised simultaneously by one model.

Before proceeding with the discussion on SGS-stress modelling, it should be noted that generally, SGS-stress models are used to model only the *anisotropic* part of the SGS-stress tensor. The *isotropic* part is subtracted from the SGS-stress and added to the dynamic pressure:

$$\boldsymbol{\tau}' = \boldsymbol{\tau} - \frac{1}{3} \text{tr}(\boldsymbol{\tau})\boldsymbol{\delta} \quad (4.6)$$

$$p' = p + \frac{1}{3} \text{tr}(\boldsymbol{\tau})\boldsymbol{\delta}, \quad (4.7)$$

where $\text{tr}(\boldsymbol{\tau})$ is twice the sub-grid scale turbulence kinetic energy, and $\boldsymbol{\delta}$ is the identity tensor (Kronecker delta).

4.1.2 The relationship between filtering and the SGS-model

Although the SGS-stresses appear naturally from the filtering operation, different views exist with respect to the exact link between filtering and SGS-stress (model). In short the debate boils down to the question whether the SGS-stress (model) is the consequence of an explicit filtering operation or is the filtering operation the implicit result of the SGS-stress model used?

- Schumann (1975b) uses the finite volume method to spatially discretise the momentum equations: the equations are integrated over finite subvolumes of the entire flow domain. In terms of the filtering approach, this method could be interpreted as the application of a filter (see (4.1)) that is fixed in space, i.e. fixed to the grid: the tophat filter is non-zero *only* if \boldsymbol{x} coincides with the gridpoint of the variable under consideration and \boldsymbol{x}' lies within the grid volume. The grid value of a variable represents the mean value averaged over the grid volume and the SGS-stresses are actual *stresses* acting on the cell faces, rather than stresses that exist in the entire cell volume. One of the effects of this way of filtering is that the Leonard term and the cross-stresses are non-existent in the approach of Schumann. Schumann calls his method the "volume balance method".
- Mason and Thomson (1992) state that the form of the filter seen by the resolved motions is determined by the subgrid model and not by any particular assumed form or type of the filter. This statement is true as long as there is no explicit reference to the type and size of the filter in the governing equations (as in (4.3) and (4.4)). The view of Mason and Thomson also implies that a SGS-stress model should not be judged as to how well it represents some –assumed– SGS-stresses. Rather the resulting resolved flow should be evaluated, i.e. the *effect* of the SGS-stress model on the resolved scales.
- Piomelli and Ferziger (1988) investigate the relationship between the filter type and the SGS-stress model in an *a posteriori* test. They show that the resulting flow statistics for a particular SGS-stress model *do* depend on the filter used (they investigate filters in the spectral domain only) as opposed to the claim of Mason and Thomson (1992), cited above. The difference in view can be attributed to the fact that the filtered Navier-Stokes equation used by Piomelli and Ferziger contains a doubly filtered term: they have a term $\nabla \widehat{\widehat{\boldsymbol{u}}}$ on

the left-hand side of (4.4) whereas Mason and Thomson have $\nabla \widehat{\mathbf{u}} \widehat{\mathbf{u}}$ ⁵. This implies that the version of (4.4) used by Piomelli and Ferziger not only contains a term that depends on the SGS-model, but also on a characteristic of the filter, viz. to what extent does $\widehat{\widehat{\mathbf{u}} \widehat{\mathbf{u}}}$ differ from $\widehat{\mathbf{u}} \widehat{\mathbf{u}}$ (see section 4.1.1).

A discussion of some aspects of the relationship between SGS-stress models and spatial discretisation, in particular the grid used, can be found in section 4.1.4.

4.1.3 Subgrid scale-stress modelling

Subgrid-scale models are available in roughly three variations, viz. eddy-viscosity models, models based on rate-equations for the SGS-stresses (second-order closure) and models that depend on an extra level of filtering (the dynamic models and scale-similarity models). Since the LES model used in the present study uses an eddy-viscosity SGS-stress model, emphasis will be on this type of SGS-stress parameterisation. The other two types will be discussed at the end of this section.

Derivation of eddy-viscosity models

The origin of eddy-viscosity models lies in the early days of numerical weather prediction (NWP) (Smagorinsky, 1993). As in the case of LES, NWP models needed to assure that the large – resolved– scale motions communicated correctly with the viscous subrange of the spectrum of atmospheric motion.

The first step is to postulate that the SGS tensor $\boldsymbol{\tau}'$ (the anisotropic part of $\boldsymbol{\tau}$) can be linked to the rate of strain tensor of the filtered field $\widehat{\mathbf{S}}$:

$$\boldsymbol{\tau}' = -\boldsymbol{\nu}_t : \widehat{\mathbf{S}}, \quad (4.8)$$

where $\boldsymbol{\nu}_t$ is in general a fourth-rank tensor⁶. Based on necessary reflective symmetries and optional other types of symmetry the number of independent components of $\boldsymbol{\nu}_t$ can be reduced.

In order to arrive at the classical Smagorinsky SGS stress model a number of assumptions need to be made (Canuto and Cheng, 1997):

- The eddy-viscosity tensor $\boldsymbol{\nu}_t$ can be replaced by a scalar eddy viscosity ν_t . This corresponds to the assumption that the SGS-stress tensor and the strain tensor are always aligned.
- Next the assumption of local equilibrium between production ($\approx -\boldsymbol{\tau}' : \widehat{\mathbf{S}}$)⁷ and dissipation (ϵ) of SGS-kinetic energy is made:

$$\epsilon = -\boldsymbol{\tau}' : \widehat{\mathbf{S}} = \nu_t \widehat{\mathbf{S}} : \widehat{\mathbf{S}} \quad (4.9)$$

⁵Piomelli and Ferziger deal with the Leonard term explicitly, whereas Mason and Thomson lump this term with the other SGS terms. Or, put differently, the former have $\boldsymbol{\tau} = \widehat{\mathbf{u}} \widehat{\mathbf{u}} - \widehat{\widehat{\mathbf{u}} \widehat{\mathbf{u}}}$ whereas the latter have $\boldsymbol{\tau} = \widehat{\mathbf{u}} \widehat{\mathbf{u}} - \widehat{\widehat{\mathbf{u}} \widehat{\mathbf{u}}}$.

⁶Note that the minus in front of $\boldsymbol{\nu}_t$ depends on both the definition of $\boldsymbol{\tau}$ and the sign in front of the term $-\nabla \cdot \boldsymbol{\tau}$ in (4.4).

⁷In general, the expression for the production of SGS kinetic energy will depend on the properties of the filter. For a sharp cut-off filter the expression $-\boldsymbol{\tau}' : \widehat{\mathbf{S}}$ is an exact representation of the SGS kinetic energy production.

- Finally it is assumed that the separation between GS and SGS motion is located within the inertial subrange of homogeneous isotropic turbulence so that the energy spectrum is a Kolmogorov spectrum at the GS-SGS separation:

$$E(k) = \alpha_K \epsilon^{2/3} k^{-5/3}, \quad (4.10)$$

where α_K is the Kolmogorov constant. When the filter is characterised by a cutoff wavenumber $k_f = \frac{2\pi}{l_f}$ and it is assumed that the Kolmogorov spectrum extends down to $k = 0$, the mean square rate of strain ($\widehat{S}^2 = \widehat{\mathbf{S}}:\widehat{\mathbf{S}}$), and the sub-grid kinetic energy, E_{SGS} , can be written as:

$$\widehat{S}^2 = \int_0^{k_f} k^2 E(k) dk = \frac{3}{2} \alpha_K \epsilon^{2/3} k_f^{4/3} \quad (4.11)$$

$$E_{SGS} = \int_{k_f}^{\infty} E(k) dk = \frac{3}{2} \alpha_K \epsilon^{2/3} k_f^{-2/3} \quad (4.12)$$

respectively. From (4.11) it can be deduced that $\epsilon \sim (\widehat{S}^2)^{3/2}$ and, with (4.9) and (4.11):

$$\nu_t = \left(\frac{3}{2} \alpha_K\right)^{-3/2} \left(\frac{l_f}{2\pi}\right)^2 |\widehat{\mathbf{S}}| = l^2 |\widehat{\mathbf{S}}| \quad (4.13)$$

where $|\widehat{\mathbf{S}}| = \sqrt{\widehat{S}^2}$. Since the derivation is based on the assumption of a Kolmogorov type inertial subrange spectrum (which is based on an ensemble average of flows and not valid for an instantaneous turbulent field), (4.13) is valid only in the ensemble mean. Equation 4.12 can be reduced to

$$E_{SGS} = \frac{1}{0.27} l^2 |\widehat{\mathbf{S}}|^2, \quad (4.14)$$

by combination of (4.9), and (4.13), and with $\alpha_K = 1.6$

In the early days of the eddy-viscosity model, filtering was done implicitly by the spatial discretisation. Thus the filter length was linked to the grid spacing. Since the smallest scale resolvable on a grid with typical spacing Δ^* is $2\Delta^*$ (i.e. $l_f = 2\Delta^*$) it follows from (4.13) that the link between grid spacing and length scale l is:

$$l = \frac{l_f}{2\pi} \left(\frac{3}{2} \alpha_K\right)^{-3/4} = \frac{\Delta^*}{\pi} \left(\frac{3}{2} \alpha_K\right)^{-3/4} \quad (4.15a)$$

$$\equiv C_s \Delta^*, \quad (4.15b)$$

where C_s is the Smagorinsky constant. The combination of equations (4.13) and (4.15b) is the classical Smagorinsky model. (4.15b) leads to a theoretical value for C_s between 0.17 and 0.28, with α_K ranging between 1.6 and 0.8, (see Smagorinsky (1993) for a review). Note that this

derivation for C_s —under the assumptions given— only holds for a sharp spectral cutoff filter⁸ and isotropic turbulence. In general C_s will depend on the exact properties of the filter and on the validity of the assumptions made in the derivation of (4.13). With reference to the type of flow, various values for C_s have been reported, ranging from 0.1 for shear driven turbulence up to 0.23 for isotropic turbulence (see Mason and Callen (1986); Smagorinsky (1993)). Canuto and Cheng (1997) show that the lower value needed in the case of shear flows can be explained by the invalidity of the assumptions underlying the original derivation of the Smagorinsky model (viz. linear relationship between stress and strain, Kolmogorov type inertial subrange spectrum and local equilibrium of production and dissipation). The reported maximum of 0.23 is less than the theoretical upper bound of 0.28.

Apart from the above *derivation* one could also *postulate* forms for ν_t on dimensional grounds. Referring to (4.13) ν_t is interpreted as the product of a lengthscale squared and an inverse time scale (the strain rate) leading to (4.16a).

$$\nu_t \sim \mathcal{L}^2 \mathcal{T}^{-1}, \quad (4.16a)$$

Or one uses the notion that the SGS-stress is linked to the dissipation of turbulent kinetic energy: ν_t can be written in terms of the dissipation and a length scale. This can be compared to (2.5) with ν replaced by ν_t (see also Leslie and Quarini (1979)):

$$\nu_t \sim \epsilon^{\frac{1}{3}} \mathcal{L}^{\frac{4}{3}}, \quad (4.16b)$$

A final option is to link the SGS-stress to some velocity scale of the SGS field, for instance —the square root of— the SGS kinetic energy and combined with a length scale, as in (4.16c) (Schumann, 1975b) or a time scale, as in (4.16d) (Horiuti, 1993).

$$\nu_t \sim \mathcal{L} \mathcal{U}, \quad (4.16c)$$

$$\nu_t \sim \mathcal{T} \mathcal{U}^2. \quad (4.16d)$$

Modifications to eddy-viscosity models

Generally, the derivations of eddy-viscosity SGS-stress models are valid only for isotropic homogeneous turbulence. Thus anisotropy or inhomogeneity of the flow may invalidate the derivation and will necessitate modifications of the model. In the present context the main points of concern are the effect of the pipe wall and the effect of rotation.

Pipe wall The presence of the pipe wall will both induce inhomogeneity and anisotropy in the flow: mean and fluctuating properties of the flow will become dependent on the distance from the wall and fluctuations of the normal-to-the-wall velocity component will be damped relative

⁸One should be cautious in the translation of results obtained under the assumption of a sharp spectral cutoff filter to other (spatial) filters. Kraichnan (1976) shows a sharp increase of the eddy viscosity as the wavenumber from which energy should be drained approaches the wavenumber of the spectral cutoff. On the other hand, results from Leslie and Quarini (1979) for a Gaussian filter show an eddy viscosity that is mostly constant for wavenumbers below the filtering wavenumber and that rapidly *decreases* as the filter size is approached (see also Mason, 1994).

to the other fluctuations of the other velocity components. Roughly three approaches are used to take into account the presence of a wall:

- The distance to the wall is taken into account explicitly in the length scale in (4.16a). \mathcal{L} is adjusted (reduced) close to the wall (van Driest, 1956; Schumann, 1975b).
- Use is made of the sensitivity of some of the properties of the resolved flow field to the presence of the wall (measures of anisotropy, shear or vorticity for instance). One or more of the scales used in (4.16) are chosen such that it depends on such a property⁹.
- Deardorff (1972) suggests to remove the mean shear from the flow field before computing the strain used in (4.13). In his simulation of a neutrally stratified planetary boundary layer this resulted in useful simulations with a value of C_s of about 0.2 in the entire domain.

The standard way to take the distance to the wall into account is the first approach, the method of van Driest (1956):

$$l = C_s \Delta^* \left(1 - \exp\left(-\frac{y^+}{A^+}\right) \right), \quad (4.17)$$

where y^+ is the distance from the wall in viscous wall units ($y^+ = yu_*/\nu$, with u_* the friction velocity: $u_* = \sqrt{\tau/\rho}$) and A^+ is a dimensionless constant with an empirical value of 26. The application of (4.17) only makes sense if both the wall shear stress and the distance to the wall are well-defined.

An example of the second approach is the work of Horiuti (1993) who uses an expression for ν_t according to (4.16d). His time scale and velocity scale are:

$$\mathcal{T} = \frac{E_{SGS}}{\epsilon}, \quad (4.18a)$$

$$\mathcal{U} = \sqrt{E_{SGS}}, \quad (4.18b)$$

where E_{SGS} is the SGS kinetic energy (see equation 4.12). The crucial step made by Horiuti is to replace the velocity scale in (4.18b) by $\frac{3}{2}$ of the component of the SGS-stress that is normal to the wall, here denoted by E_{SGS}^\perp ¹⁰, which leads to:

$$\nu_t \sim \Delta^{*2} \frac{3}{2} \frac{E_{SGS}^\perp}{|\widehat{\mathbf{S}}|} \sim \Delta^{*2} \frac{3}{2} \frac{E_{SGS}^\perp}{E_{SGS}} |\widehat{\mathbf{S}}| \quad (4.19)$$

This model for ν_t can be interpreted as the standard Smagorinsky model with a damping function for the length scale (compare to (4.17)):

$$l = C_s \Delta^* \sqrt{\frac{3}{2} \frac{E_{SGS}^\perp}{E_{SGS}}} \quad (4.20)$$

⁹The model of Canuto and Cheng (1997) could also be thought to belong to this category, since their model is also sensitive to both shear *and* vorticity. Besides, they neither impose a Kolmogorov type inertial subrange spectrum, nor do they impose local equilibrium between production and dissipation.

¹⁰In the case of isotropic turbulence $\frac{3}{2}E_{SGS}^\perp = E_{SGS}$.

Yakhot *et al.* (1990) and Eggels (1994)¹¹ use the fraction $\frac{E_{GS}^\perp}{E_{GS}}$ rather than $\frac{E_{SGS}^\perp}{E_{SGS}}$:

$$l = C_s \Delta^* \sqrt{\frac{3 E_{GS}^\perp}{2 E_{GS}}} \quad (4.21)$$

This can be justified by the fact that the main contribution to E_{SGS}^\perp and E_{SGS} comes from the largest sub-filter scales¹². The anisotropy in the components of the turbulent kinetic energy at those scales might be comparable to that of the filtered field. Although the approach of Horiuti (1993)—or equivalently Yakhot *et al.* (1990) and Eggels (1994)—eliminates both the reference to the wall shear stress (which is implicit in the method of van Driest) and the distance to the wall, the specification of the direction perpendicular to the wall still remains non-trivial except for the case of flow over a flat wall.

Rotation With respect to the influence of rotation on the SGS-stress model two remarks can be made. Firstly, Ferziger (1993) discusses the applicability of SGS-stress models to flows in which extra strains act. He states that as long as the extra strains mainly affect the large-scale phenomena in a flow, the standard SGS-stress models should remain applicable. On the other hand, the material presented in section 2.2 shows that one of the effects of rotation may be the reduction of dissipation of turbulent kinetic energy. This suggests that the dissipative action of an eddy-viscosity model should be reduced when mean rotation is present. The results of Canuto and Cheng (1997), who included vorticity in their SGS-model, indeed show a reduction in the eddy-viscosity if the vorticity is non-zero (although in their case vorticity was a result of the mean shear, rather than mean rotation).

Other types of SGS-models

Other types of SGS models used in LES in physical space will be treated only very shortly in the next sections.

Second-order closure and algebraic stress models As in the case of Reynolds-stress modelling, one can derive the rate equations for the elements of the SGS-stress tensor (similar to (2.10)). Some of the terms in such equations are dependent on GS quantities and SGS-stresses and can be computed explicitly. Other terms need parametrisation. Some authors have performed LES with such second-order closure models for the SGS-stresses (Deardorff, 1974). Others have simplified the differential equations for the SGS-stresses to an algebraic stress model (Schmidt

¹¹Eggels (1994) arrives at a damping factor which would give $l = C_s \Delta^* \left(\frac{3 E_{SGS}^\perp}{2 E_{SGS}} \right)^{1/4}$ rather than the expression given in (4.20). The effect of this is that the expression of Eggels gives less damping than that of Horiuti. The origin of the difference between the two authors lies in the choice of the scales used to define ν_t . Whereas Horiuti starts out from (4.16d) (using a time scale and a squared velocity scale), Eggels uses (4.16c) (a length scale and a velocity scale).

¹²In order to estimate the E_{GS}^\perp and E_{GS} one needs some dimension in which the flow is homogeneous: one needs to be able to compute both $\langle u^{\perp\prime\prime} u^{\perp\prime\prime} \rangle$ and $\frac{1}{2} \langle \mathbf{u}'' \cdot \mathbf{u}'' \rangle$, respectively (where $\langle \phi \rangle$ signifies the spatial average of variable ϕ , and ϕ'' is the deviation from that spatial average).

and Schumann, 1989). A variant that lies between the second-order closure and eddy-viscosity models is to use a prognostic equation for the SGS kinetic energy E_{SGS} and to use E_{SGS} in the estimation of ν_t . According to (4.16c) $\sqrt{E_{SGS}}$ can then be used as a velocity scale (Deardorff, 1980; Schumann, 1975b).

Structure function model The SGS-viscosity in the Smagorinsky model, as given by (4.13), is a function of the resolved strain rate. However, assuming isotropic turbulence, this may also be written in terms of $E(k)$:

$$\nu_t(\mathbf{x}) \sim \alpha_K^{-3/2} \left(\frac{E_x(k_f)}{k_f} \right), \quad (4.22)$$

where $E_x(k)$ is a *local* energy spectrum, rather than some global, ensemble averaged, spectrum. This local energy spectrum can be estimated from the second-order structure function of the resolved field, which is given by (for separations r equal to the grid spacing Δx):

$$F_2(\mathbf{x}, \Delta x) = \langle (\widehat{\mathbf{u}}(\mathbf{x}) - \widehat{\mathbf{u}}(\mathbf{x} + \mathbf{r}))^2 \rangle_{|\mathbf{r}|=\Delta x}, \quad (4.23)$$

where $\langle \phi \rangle$ signifies the spatial average (in one or more homogeneous directions) of variable ϕ . F_2 can be obtained from the resolved field. For isotropic turbulence, and assuming a Kolmogorov spectrum (in terms of the k -dependence of $E(k)$) it can be deduced that (4.22) can be approximated as (using the link between F_2 and $E_x(k)$):

$$\nu_t \sim \alpha_K^{-3/2} \Delta x \sqrt{F_2(\mathbf{x}, \Delta x)} \quad (4.24)$$

For a more elaborate description of the structure function model, see Lesieur and Métais (1996) and Silveira Neto *et al.* (1993).

Similarity model and mixed model The scale-similarity model (Bardina *et al.*, 1981) models the cross-terms (see (4.5)). The model is based on the assumption that the main interaction between sub-filter scale motion and resolved motion takes place between the smallest resolved scales and the largest sub-filter scales (Piomelli and Ferziger, 1988). Since no information is available on the largest sub-filter scales, this information is generated by filtering the velocity field twice (i.e. $\widehat{\widehat{\mathbf{u}}}$). This yields an estimate for the SGS-stress:

$$\widehat{\mathbf{u}\mathbf{u}^*} + \widehat{\mathbf{u}^*\mathbf{u}} = C_B \left(\widehat{\mathbf{u}\mathbf{u}} - \widehat{\widehat{\mathbf{u}}\widehat{\mathbf{u}}} \right), \quad (4.25)$$

where C_B is an empirical constant. This model is usually used in simulations where the Leonard terms are calculated explicitly and the standard Smagorinsky model is used for the SGS-stress ($\widehat{\mathbf{u}^*\mathbf{u}^*}$). For this total model for τ' to be Galilean invariant, C_B should be 1 (Speziale, 1985).

Dynamic model In the dynamic model, information from the resolved scales is used to determine the model constant(s) for the SGS-stress model (see for more information: Germano (1992); Piomelli (1993)). Where the SGS-stress tensor is the result of filtering the non-linear term in the Navier-Stokes equations with a filter of length l_f , one could subsequently apply a second filter with a larger length scale (the test-filter, with length l_{f2}) to obtain another stress (compare to (4.5)):

$$\mathbf{T} \equiv \widetilde{\widetilde{\mathbf{u}\mathbf{u}}} - \widetilde{\mathbf{u}}\widetilde{\mathbf{u}} \quad (4.26)$$

This \mathbf{T} is the SGS-stress to be used in the doubly filtered Navier-Stokes equations. The difference between \mathbf{T} and $\widetilde{\mathbf{u}}\widetilde{\mathbf{u}}$ is the contribution of the resolved scales to \mathbf{T} , i.e. the part of the SGS-stress carried by motions smaller than the l_{f2} but larger than l_f . This contribution can be obtained from the resolved field:

$$\begin{aligned} \mathbf{L} &\equiv \mathbf{T} - \widetilde{\mathbf{u}}\widetilde{\mathbf{u}} \\ &= \left(\widetilde{\widetilde{\mathbf{u}\mathbf{u}}} - \widetilde{\mathbf{u}}\widetilde{\mathbf{u}} \right) - \left(\widetilde{\mathbf{u}\mathbf{u}} - \widetilde{\mathbf{u}}\widetilde{\mathbf{u}} \right) \\ &= \widetilde{\widetilde{\mathbf{u}\mathbf{u}}} - \widetilde{\mathbf{u}}\widetilde{\mathbf{u}} \end{aligned} \quad (4.27)$$

If the Smagorinsky model is used for the parametrisation of the SGS-stresses, the *anisotropic* part of \mathbf{L} (i.e. \mathbf{L}') equals:

$$\mathbf{L}' = C\mathbf{M} = C \left(l_{f2}^2 \widetilde{\widetilde{\mathbf{S}}} \widetilde{\widetilde{\mathbf{S}}} - l_f^2 \widetilde{\mathbf{S}} \widetilde{\mathbf{S}} \right), \quad (4.28)$$

with $C = C_s^2$. Through combination of (4.28) and the anisotropic part of (4.27) a set of equations for C is obtained in terms of quantities related to the resolved field. One way to obtain *one* value for C is to contract both equations with $\widetilde{\mathbf{S}}$ (Germano, 1992) or \mathbf{M} (Lilly, 1992). The result is a spatially and temporarily varying field of the model constant C , including negative values for C (i.e. backscatter). In order to prevent numerical instabilities due to excessive backscatter, the resulting C -field is usually filtered or averaged in some way.

Concluding remarks on SGS-stress models

To conclude the discussion on SGS-stress models, two remarks are in place.

Firstly, the main function of a SGS-stress model is to drain sufficient turbulent kinetic energy from the grid-scale to the sub-grid scale. This drain should take place at wavelengths just above or at the filter scale. And the drain of energy should not only be sufficient in magnitude but should also affect the correct components of the stress tensor.

Secondly, the range of scales resolved in a LES depends on the ratio of the largest scales in the flow and the smallest resolved scales. The first depends on the domain size, which is in the present situation the pipe diameter D . On the other hand, the smallest resolved scales depend on the filter length. Thus the range of scales could be estimated as $N_L = D/l_f$. But given the fact that in the present implementation of the Smagorinsky model l_f is directly linked to the grid size Δ^* , a more direct estimate would be $\tilde{N}_L = D/\Delta^*$.

4.1.4 **Solution of the Navier-Stokes equations: some numerical issues**

Since the equations that govern LES, i.e. the Navier-Stokes equations and the SGS-stress model, cannot be solved analytically the only route that remains is numerical solution of discretized versions of those equations.

This entails the choice of the location of variables in space and time (grid) and a method to approximate the different derivatives occurring in the equations under consideration. The discretisation will yield a set of four algebraic equations for the four variables (p' , u_r , u_θ and u_z) at all discrete positions in space and time. To complete this set of algebraic equations appropriate boundary conditions have to be specified. In the three spatial dimensions these comprise boundary conditions in both the positive and negative directions, whereas in the time dimension only initial conditions need to be supplied, since there is no information that travels backward in time.

Whereas the discussion of topics concerning spatial and temporal discretisation is beyond the scope of this thesis¹³ there is one important point with respect to the spatial discretisation that does need to be discussed: the size and shape of the filters used in LES is in most cases closely coupled to the *grid* used. Another issue of importance is the specification of boundary conditions (both in space and time), which is not as straightforward as it seems.

SGS-model and spatial discretisation

When variables are discretized on a regular, rectangular grid the situation is rather simple: the size of the filter is constant in space. However, there are two reasons to employ a grid that is irregular –or at least not uniform– in space:

- The geometry of the flow may dictate that the grid is distorted in some way as to fit some imposed boundaries. In the present case of flow through an axisymmetric domain this is accomplished by using cylindrical coordinates. In cylindrical coordinates the tangential grid spacing varies proportionally with r . In order for the grid boxes to have nearly the same *aspect ratio* –i.e. an isotropic filter– throughout the domain, the radial spacing should also vary with r . However, this would imply that the size of the boxes, and consequently the *size* of the filter would vary wildly through the domain. If on the other hand the size, in terms of volume, would be kept nearly constant, the aspect ratio would vary (see figure 4.1).
- The size of eddies one would like to resolve may vary through the flow domain, requiring a varying filtersize. Furthermore, the properties of the flow, such as strong gradients, may dictate a special grid spacing in certain regions of the domain. This also results –when the filter size is linked to the grid size– in a varying filter size. For the pipe flow under consideration this is the case for the radial grid spacing which is reduced in the region near the wall, in order to resolve the large shear due to wall friction. In terms of the sketches given in figure 4.1 this will lead to a grid like the one depicted in the right figure.

¹³The reader is referred to textbooks like Ferziger and Perić (1996) and Hirsch (1990a) for more information on the different types of spatial and temporal discretisation.

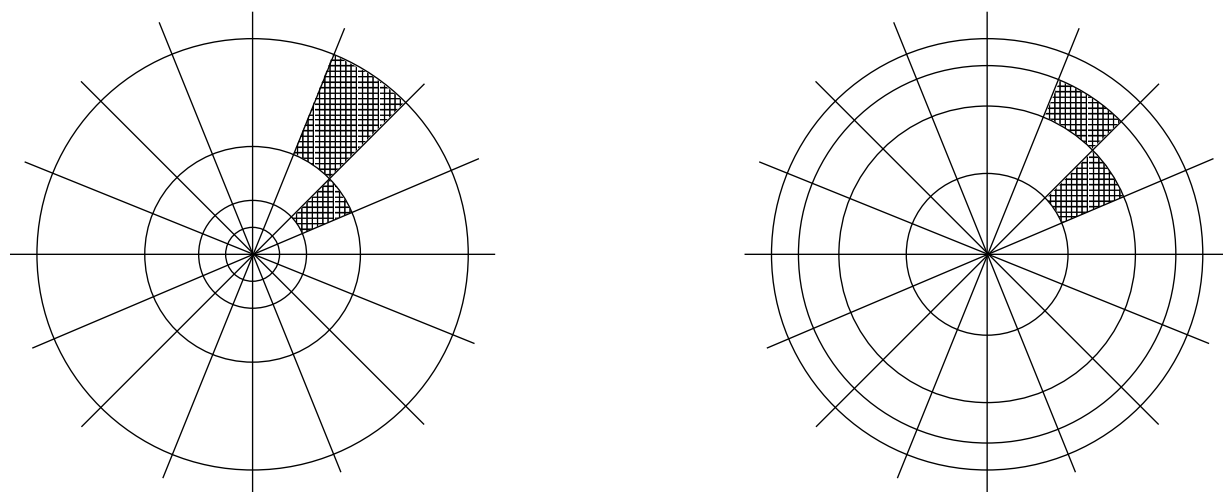


Figure 4.1: Sketch of cylindrical coordinates with grid cells of either constant aspect ratio (left) or constant volume (right).

The use of cylindrical coordinates with a radial grid spacing decreasing outward has two consequences: the filter size varies in space and the filter is anisotropic.

A consequence of the use of a filter that is variable in space is that differentiation and filtering no longer commute, i.e. $\widehat{\nabla\phi} \neq \nabla\widehat{\phi}$. This implies that the filtered Navier Stokes equations (4.3) and (4.4) are not exactly valid. However, Ghosal and Moin (1995) show that the error due to the omission of the extra terms resulting from a non-uniform filter are second-order in the filter width. Thus they are of the same order as the discretisation error when a second-order spatial discretisation is used. Ghosal and Moin (1995) also showed that the error due to a non-constant filter size is dissipative. Thus this error can just be added to errors due to the SGS-stress model, which is dissipative as well (at least in the mean). It could even be seen as support for the claim of Mason and Thomson (1992) that the form of the filter as experienced by the resolved field is determined by the subgrid model, rather than any assumed form of the filter (see section 4.1.2): the resolved field experiences the dissipation offered by the SGS-stress model. That dissipation might or might not include the dissipation due to the spatially varying filter size.

The anisotropy of the grid and the consequent anisotropy of the filter has been dealt with by Schumann (1975b), Scotti *et al.* (1993) and Scotti *et al.* (1997): the first two authors included these effects in terms of a Smagorinsky-like SGS-stress model, whereas the latter focus on the dynamic model. In the 'volume-balancing method' of Schumann (1975b) (see also section 4.1.2) the SGS-stresses are surface forces, which are proportional to the area of the grid-face on which they work. This proportionality is incorporated in the SGS-viscosity, thus Schumann's viscosity becomes anisotropic when the grid is anisotropic. Scotti *et al.* (1993) on the other hand, translate the anisotropy of the grid into an adaptation of the length scale in the definition of the SGS-viscosity. Thus the viscosity itself remains a scalar. In the analysis of Scotti *et al.* (1993) the derivation of the Smagorinsky model, given here in section 4.1.3, is redone, taking into account that the filter cut-off wavenumber is not equal in all directions (see (4.11), where k_f is the

filtering wavenumber): the smaller the filter length in a given direction, the higher the filtering wavenumber. In the end their analysis yields an expression for the length scale l in equation (4.15b) that not only depends on the grid spacing Δ^* , but also on the aspect ratio of the grid.

Another consequence of the use of an anisotropic grid may be that the smallest structures that can be represented on that grid are anisotropic, solely due to the shape of the grid.

Initial and boundary conditions

Since turbulent *flows* are highly sensitive to initial conditions one can not expect a numerical *simulation* of such a flow to give a faithful representation of the actual temporal development (Lesieur, 1993). Therefore, the initial conditions are immaterial, and in most cases the simulation is started with a random field, where the mean values and the magnitude of the fluctuations are chosen based on prior knowledge of the flow. Starting from this –non-physical– initial field the simulation will –after a number of turbulent time scales– produce a turbulent field that is consistent with the boundary conditions and external forcings¹⁴.

With respect to the specification of spatial boundary conditions three cases can be identified: the boundary may be a solid wall, a fluid with exactly identical properties as the fluid simulated, or a fluid with different properties, i.e. a free surface (the third case is not dealt with here). The specification of solid wall boundary conditions is straightforward in principle. But for the discretized equations complications will occur when spatial discretisation of order three and higher are used. Furthermore, when explicit filtering is used in the LES, special care has to be taken near the wall: the filter length should approach zero near the wall.

With respect to boundary conditions within the fluid roughly three options are available:

- When the flow is homogeneous in a given direction, periodic boundary conditions are usually employed. One should ensure that the domain is sufficiently large that the resulting flow at one end of the domain is uncorrelated to the flow half way the domain (the flow at both ends of the domain will be perfectly correlated of course). Numerous examples of this approach are available, e.g. Moin and Kim (1982), Eggels *et al.* (1994) and Nieuwstadt *et al.* (1993).
- If the flow is not homogeneous in a given direction and there is a net flow in that direction, inflow/outflow boundary conditions can be used. At the inflow plane a turbulent field must be specified and at the outflow plane the fluid should be allowed to flow out freely (without backward flow and without reflections). The inflow field may be a field derived from a separate simulation, or a random field, possibly with appropriate spatial and temporal correlation (e.g. Arnal and Friedrich (1993) and Silveira Neto *et al.* (1993)).
- In the case of an inhomogeneous direction without a mean flow in that direction, some non-reflecting boundary condition should be devised that allows local inflow and outflow, but implies a net zero outflow through the boundary. This situation occurs for instance in the

¹⁴In case of simulations with unsteady boundary conditions or mean values, e.g. a convective planetary boundary layer, one would like to reach the state of fully developed turbulence as quickly as possible. The 'start-up' process might be helped by using either a turbulent field from a previous simulation or a random field that has been filtered to give at least the correct spatial correlations for the different variables.

vertical direction in the case of flow over a flat plate or the flow in the planetary boundary layer (Nieuwstadt *et al.*, 1993).

4.1.5 Comparison between LES results and laboratory experiments

In order to validate the results of an LES, a comparison should be made to results of either a physical experiment or to another numerical, but more credible, simulation. One practical obstacle is that it is nearly impossible to exactly match the LES and experiment to which it should be compared in terms of dimensions and external parameters. Furthermore, due to the chaotic nature of turbulence (extreme sensitivity to initial conditions) LES results and physical experiments can be compared only in a statistical sense. A more fundamental problem is that results from an LES represent a different view of –ideally– the same experiment. Whereas LES results provide a –spatially– filtered four-dimensional (space and time) view of the ‘true’ velocity and scalar field, point observations in physical experiments only reflect the temporal behaviour of the non-filtered velocity or scalar field. Two approaches are possible to reconcile LES results and physical experiments:

- The physical observations can be filtered in a way that is compatible with the filter used in the LES model. Wyngaard and Peltier (1996) briefly discuss the possibility of spatially filtering observations from one point in space (through Taylor’s frozen turbulence hypothesis) to obtain a signal that would be compatible with the resolved scales in an LES. Subsequently, statistical quantities of the LES fields and the filtered observations can be compared.
- The SGS contributions to the statistical quantity under consideration (in particular Reynolds stresses) have to be added to the resolved part before the LES results can be compared to the full observations.

In the case that Reynolds stresses are the statistical quantities to be compared, the second approach is followed most often, since the SGS contributions to the Reynolds stresses is available (or can be estimated in a consistent way) from the LES. Since the SGS contribution relies on the SGS-stress model directly, it is good practice to show this contribution separately (apart from the sum of resolved stress and SGS-stress). A situation in which one would choose for the first option is when spectral quantities (including correlation functions) are considered. Since in an LES the smallest scales present in those quantities are limited to twice the filter scale, it is most practical to remove all fluctuations at smaller scales from the results of the physical experiment.

4.1.6 Sources of error in LES

In order to judge the results from a simulation vis-a-vis experimental results, one should have an indication of the error that is inherent to the results of the simulations as well as the error in the experimental results. For there will always be a difference between the results from the simulation and the experiment. Only when the ranges in which both results are known to be located –i.e. the observed value plus and minus the possible error– do not overlap there is reason to reject the simulation results.

Three fundamentally different sources of error can be identified in relationship to LES results:

- The SGS-stress model is an approximation to the true SGS-stresses. In fact it is usually this factor that one aims to test when LES results are validated against observations. Therefore it is not necessary to take this error into account into the error estimate.
- The equations that are actually solved in an LES model are the discretized approximations to the true, continuous equations. (Kravchenko and Moin, 1997) discuss both aliasing errors and truncation errors, of which the latter are most important for the type of discretisation used in the present work. A general approach to determine the errors due to discretisation is to repeat a given simulation for different grid sizes. Mason (1994) suggests a range of four orders of magnitude in the grid size. The ultimate aim is to show grid-independence of the solution at a given resolution. A disadvantage of this method in the context of LES is that the influence of the SGS-stress model also decreases upon grid-refinement¹⁵, and so does the absolute value of the contribution of the SGS-model to the total error. Furthermore, the order of the discretisation method used *does* give information on the rate at which discretisation errors decrease upon refinement of the grid. However, it does not give information on the actual size of the error.
- Since the turbulence simulated with an LES is a stochastic process, the statistical quantities derived from LES results are also stochastic variables. Therefore there will be a difference between the LES-derived statistical quantities and their ensemble average values (or expected values). The estimation of this difference is rather straightforward and frequently applied to experimental data (Lumley and Panofsky, 1964; Lenschow *et al.*, 1994) but hardly ever used in the context of LES results. Michels (personal communication) developed extended the work of Lenschow *et al.* (1994) for turbulent data with an arbitrary number of dimensions (incl. 4-D LES data). A summary of her method is given in section A.3.

4.2 An LES model for pipe fbw with swirl and axial strain

In section 4.1 various aspects of large eddy simulation were discussed. The present section deals with the specific implementation of an LES model as used for this study of the combined effect of swirl and axial strain on turbulent pipe flow.

The model used in this study is based on the model developed by Eggels (1994) and Pourquié (1994) with some modifications by B.J. Boersma (1994-1995) at TUD. The characteristics of the *original* model can be summarised as:

- Coordinate system: cylindrical coordinates with grid refinement in the radial direction (smaller grid cells near the wall);
- Spatial discretisation: finite volume method;
- Temporal discretisation: second-order Adams-Bashforth method, except for advection and diffusion terms that contain derivatives in the tangential direction. The latter are approximated with the implicit second-order Crank-Nicholson method.

¹⁵Unless the filter size is not varied with the grid size (see Mason and Callen (1986)).

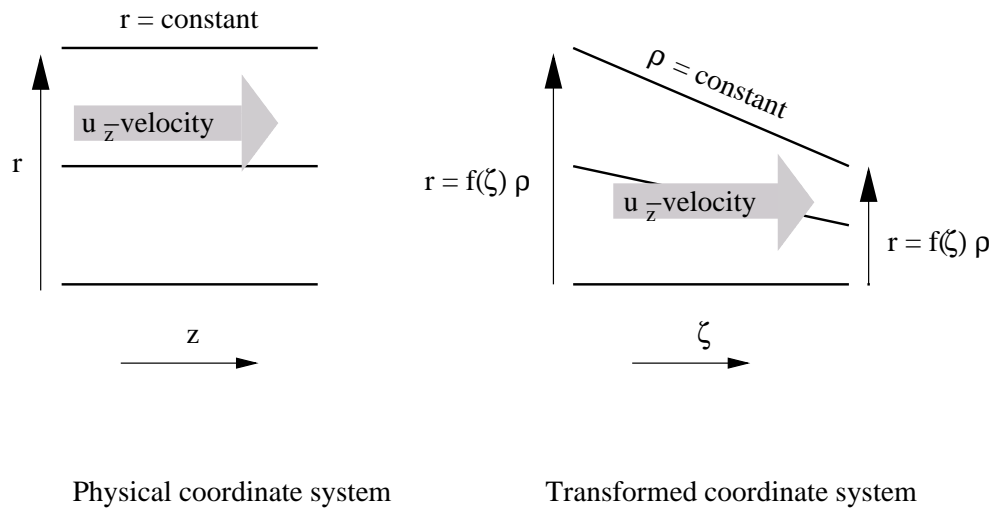


Figure 4.2: Relationship between the (cylindrical) physical coordinate system and the transformed system.

- Sub-grid scale stresses: Smagorinsky model. Wall-damping of the sub-grid scale stresses is provided with the Van Driest damping function.
- Boundary conditions: periodic in tangential and axial direction. In the radial direction the boundary conditions at the wall are Dirichlet conditions for all velocity components and Von Neumann conditions for u_r and p' .

All lengths in the model are made dimensionless by the pipe diameter D , whereas the velocities and pressure are non-dimensionalised by the friction velocity u_* .

In order to simulate the flow through a pipe contraction, as is required in this study, modifications need to be made to the original model on all points mentioned above. The implementation of the new model is discussed in the next sections:

- The coordinate system needs to be modified, leading to new governing equations in that system (section 4.2.1);
- The spatial discretisation needs to be adjusted to the new coordinate system (section 4.2.2);
- The temporal discretisation needs to be changed, as well as the method to solve the equation for the pressure (section 4.2.3).
- The subgrid-stress model needs to be adapted to the new geometry (section 4.2.4);
- The new geometry requires different boundary conditions (section 4.2.5).

A sketch (to scale) of the domain of the model as related to the configuration in the laboratory experiment can be found in figure 1.5 on page 5. The computational domain is also shown in figure 4.4.

4.2.1 Coordinate system

The original model is based on the Navier-Stokes equations in cylindrical coordinates (see B.1). In order to make simulations of the flow through a contraction, the cylindrical coordinate system

needs to be replaced by a transformed coordinate system.

In the sequel, two coordinate systems will be used (see figure 4.2). One is the cylindrical coordinate system in physical space, denoted by (r, θ, z) . The second is the system in computational space (ρ, ϕ, ζ) . The computational coordinate system is constructed such, that ρ remains constant when following the pipe wall in the axial direction. The link between physical space and computational space is as follows:

$$\begin{aligned} r &= f(\zeta)\rho \\ \theta &= \phi \\ z &= \zeta \end{aligned} \tag{4.29}$$

Derivatives are converted from physical to computational space in the following way:

$$\begin{aligned} \frac{\partial}{\partial r} &= \frac{1}{f(\zeta)} \frac{\partial}{\partial \rho} \\ \frac{\partial}{\partial \theta} &= \frac{\partial}{\partial \phi} \\ \frac{\partial}{\partial z} &= \frac{\partial \zeta}{\partial z} \frac{\partial}{\partial \zeta} + \frac{\partial \rho}{\partial z} \frac{\partial}{\partial \rho} = \frac{\partial}{\partial \zeta} - \left(\frac{\rho}{f(\zeta)} \frac{\partial f(\zeta)}{\partial \zeta} \right) \frac{\partial}{\partial \rho} \end{aligned} \tag{4.30}$$

Note that this coordinate system is non-orthogonal. Unlike the coordinate system, the velocities are not transformed. Thus, the axial velocity is no longer parallel to the corresponding grid lines. Although this is not the most logical construction if one considers the model as a step towards an LES in general coordinates, it was the most logical choice in order to re-use as much ideas as possible from the original model. Section E.2 in appendix E shows some examples of the consequences of this coordinate transformation.

4.2.2 Spatial discretisation

In the present model a staggered grid is used (Harlow and Welch, 1965), which implies that the pressure and the three velocity components are defined at different positions in space. The pressure is defined at the centre of a grid cell, whereas the velocity components are displaced to the grid cell face in the direction of the velocity component considered. The grid cells are indicated with three indices i , j , and k , denoting the positions in radial, tangential and axial direction, respectively. The total number of grid volumes is N_r , N_θ and N_z for the three respective directions (in terms of the model $imax$, $jmax$ and $kmax$, respectively).

A number of coordinate variables are used. The radial positions of the radial velocities are denoted by ρ_i^u , whereas the radial position of the other variables is given by ρ_i^p . The tangential position of the tangential velocities is given by ϕ_j and the axial positions of the axial velocities by ζ_k . Thus a grid cell with index (i, j, k) , is defined by

$$\rho_i^u < \rho < \rho_{i-1}^u, \phi_j < \phi < \phi_{j-1}, \zeta_k < \zeta < \zeta_{k-1}$$

In the model, ϕ_j and ζ_k are equidistant, whereas ρ_i^p and ρ_i^u are not. ρ_i^u is defined such that the pipe axis and the pipe wall are given by $\rho_0^u = 0$ and $\rho_{imax}^u = 0.5$, respectively. The radial positions in between are defined with a hyperbolic tangent (for details see E.4).

For the factor f that describes the axial variation of the radius, two variables are employed. f_k^w gives the value of f at $\zeta = \zeta_k$, whereas f_k^p gives f at the pressure point ($\zeta = \zeta_k - \frac{1}{2}d\zeta$; $f_k^p = \frac{1}{2}(f_k^w + f_{k-1}^w)$). Furthermore, the axial derivative of f at the same positions is used, denoted by df_k^w and df_k^p , respectively.

The equations are discretized by integrating them over the relevant grid volume, of which the edges depend on the variable under consideration. This method is similar to the "volume balance method" of Schumann (1975b), though his SGS-stress model is quite different. Whenever values of variables are needed at positions where they are not defined, interpolation with a mid-point rule is used (for a detailed discussion on the accuracy see Eggels (1994) and Pourquié (1994)). As an example of the discretisation procedure, the derivation of the discretized divergence is given in appendix E.

4.2.3 Temporal discretisation and pressure solution

For the time discretisation a fractional step method is used (Ferziger and Perić, 1996; Kim and Moin, 1985, see). This implies that each time step is split into two steps. The first step (from time level t^n to an intermediate –undefined– level t^*) comprises the tendencies due to advection and diffusion terms only (see equation 2.2). The second step (from time level t^* to t^{n+1}) solely includes the tendency due to the pressure gradient term.

First step

For the time discretisation of most terms the second order Adams-Bashforth method is used (see e.g. Ferziger and Perić (1996)):

$$\widehat{\mathbf{u}}^{n+1} \approx \widehat{\mathbf{u}}^n + \frac{dt}{2} \left(3 \frac{\partial \widehat{\mathbf{u}}^n}{\partial t} - \frac{\partial \widehat{\mathbf{u}}^{n-1}}{\partial t} \right) \quad (4.31)$$

where the superscript n denotes the moment in time, and $\partial \widehat{\mathbf{u}}^n / \partial t$ is the estimate of the time derivative, based on variables at time step n . These time derivatives only include the advection and diffusion terms. In order to study both the stability of the time discretisation one needs an expression of the maximum permissible time step.

From Schumann (1975a) it can be concluded that the maximum permissible time step is¹⁶

$$dt_{max} \leq \beta \left(m_\rho \frac{|\widehat{u}_r^{i,j,k}|}{f_k^p (\rho_{i+1}^p - \rho_i^p)} + m_\phi \frac{|\widehat{u}_\theta^{i,j,k}|}{f_k^p \rho_i^p d\phi} + m_\zeta \frac{|\widehat{u}_z^{i,j,k}|}{d\zeta} + 2(\nu + \nu_t) \left(m_\rho \frac{1}{f_k^{p2} d\rho_i^2} + m_\phi \frac{1}{f_k^{p2} \rho_i^{p2} d\phi^2} + m_\zeta \frac{1}{d\zeta^2} \right) \right)^{-1} \quad (4.32)$$

where m_ρ , m_ϕ and m_ζ are indicators whether the term should be included ($m = 1$) or not ($m = 0$). If all terms in the advection and diffusion terms are treated explicitly, m_ρ , m_ϕ and m_ζ are all equal

¹⁶More general expressions for the stability limits of different time stepping methods can be found in Wesseling (1996).

to 1. β is a safety factor to account for non-linear effects (in the current study it appears that β needs to be set to 0.35, which is lower than the values reported by Schumann (1975a) and Eggels (1994) for rectangular and cylindrical grids, respectively.).

Two regions can be distinguished in which the time step can be severely limited:

- Downstream of a contraction the shear near the wall can be significant, resulting in a large v_t ; in combination with the small values of $d\rho_i^p$ or $d\rho_i^u$ due to grid refinement near the wall. This results in a severe reduction of the time step for the diffusion terms with derivatives in the radial direction;
- Near the pipe centre, $f_k^p \rho_i^p d\phi$ becomes very small.

In order to circumvent these time step limitations, it was decided to treat some terms implicitly:

- in the region $\frac{1}{4}imax < i < imax$ the diffusion and advection terms containing derivatives in the radial direction are treated implicitly;
- in the region $0 < i \leq \frac{1}{4}imax$ the diffusion and advection terms containing derivatives in the tangential direction are treated implicitly;

These terms are advanced in time with the Crank-Nicholson method, which can be summarised as:

$$\widehat{\mathbf{u}}^{n+1} \approx \widehat{\mathbf{u}}^n + \frac{dt}{2} \left(\frac{\partial \widehat{\mathbf{u}}^n}{\partial t} + \frac{\partial \widehat{\mathbf{u}}^{n+1}}{\partial t} \right) \quad (4.33)$$

The Crank-Nicholson method is unconditionally stable, so the terms no longer pose a stability limit on the time step. For the inner region (4.32) applies with $n_\rho = 1$, $n_\phi = 0$ and $n_\zeta = 1$ whereas the time step limit for the outer region follows from (4.32) with $n_\rho = 0$, $n_\phi = 1$ and $n_\zeta = 1$.

The final product of the first step is an intermediate field $\widehat{\mathbf{u}}^*$ computed from the tendencies due to diffusion (diff) and advection (adv):

$$\widehat{\mathbf{u}}^* = \widehat{\mathbf{u}}^n + dt \left(\frac{3}{2} \text{diff}_{expl}^n - \frac{1}{2} \text{diff}_{expl}^{n-1} + \frac{1}{2} \text{diff}_{impl}^n + \frac{1}{2} \text{diff}_{impl}^* + \frac{3}{2} \text{adv}_{expl}^n - \frac{1}{2} \text{adv}_{expl}^{n-1} \right) \quad (4.34)$$

Second step

In an incompressible flow the pressure is not a dynamic variable but is completely coupled to the velocity field. This coupling is such that the pressure field makes the velocity field obey the continuity equation.

In this second step, the pressure field is determined such that application of the pressure gradient term to the velocity field at time level t^* will yield a divergence-free velocity field at time level t^{n+1} . Thus the step:

$$\frac{\widehat{\mathbf{u}}^{n+1} - \widehat{\mathbf{u}}^*}{dt} = -\nabla \widehat{p}' \quad (4.35)$$

should result in $\nabla \cdot \widehat{\mathbf{u}}^{n+1} = 0$. The pressure field which will lead to this, can be determined from the following Poisson equation:

$$\nabla^2 \widehat{p}' = \frac{\nabla \cdot \widehat{\mathbf{u}}^*}{dt} \quad (4.36)$$

In order to ensure that the *discretized* divergence of the velocity field is zero, the discretized version of (4.36) is obtained by the application of the discrete divergence operator to the discrete pressure gradient (rather than by discretising (4.36) directly).

The principle of the solution method for this Poisson equation is rather standard, but the implementation is complicated by the fact that the coefficients in the Poisson equation vary both in the radial direction and in the axial direction. The first step in the solution of this discrete Poisson equation is to Fourier transform it in the ϕ -direction. This is possible due to two facts

- the coefficients for the pressure in the discretized Poisson equation are independent of j (i.e. proportional to 1, -2 and 1 for pressures at $j - 1$, j and $j + 1$, but independent of i and k);
- the boundary conditions in the tangential direction are periodic by definition;

The result of this Fourier transform is a collection of N_θ independent sets of $N_r \times N_z$ equations (one set for each Fourier mode). The second step in the solution of the Poisson equation is that these systems of equations are solved with an iterative solver, which is based on the GMRES (Generalised Minimal Residual) method with block incomplete LU preconditioning¹⁷. The final step is that the solution of the aforementioned equations is then Fourier transformed backward to obtain the pressure field.

The pressure found from the solution of (4.36) is used to determine the pressure gradient contribution to the momentum equations. This yields the velocity field at time step $n + 1$.

4.2.4 Sub-grid scale model

In the present model the sub-grid scale tensor $\boldsymbol{\tau}'$ is parameterised using the Smagorinsky model in combination with the modification due to Horiuti, i.e. the combination of (4.8) with (4.15b) and (4.21).

The characteristic grid-spacing Δ^* , needed in (4.15b) is defined here in the same way as in Eggels (1994), except for the modifications due to the transformed grid:

$$\Delta^* = \sqrt{\frac{(f_k^u d\rho_i^u)^2 + (f_k^p d\rho_i^u d\phi)^2 + d\zeta^2}{3}}. \quad (4.37)$$

For the damping defined in (4.21), the normal-to-the-wall velocity component is needed. However, in the model used in this study there is in general no velocity component that is perpendicular to the wall. Therefore the normal-to-the-wall component of the GS kinetic energy, E_{GS}^\perp

¹⁷Use is made of the NSPCG (Non-Symmetric Preconditioned Conjugate Gradient) library which provides a number highly configurable solvers. The sparse matrix was stored in diagonal sparse format, which is optimise for vectorisation and efficient use of cache.

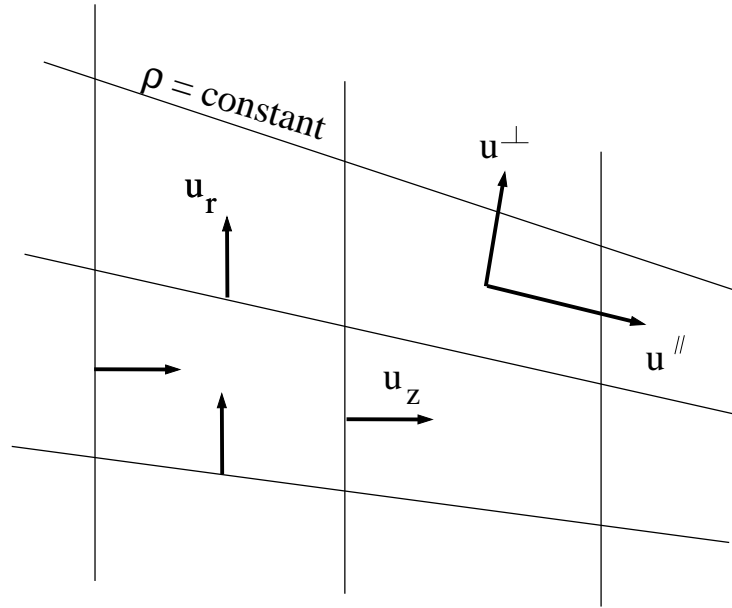


Figure 4.3: Construction of velocity components u^\perp and u^\parallel . The orientation of these components depends on the local slope of the $\rho = \text{constant}$ lines. The components u^\perp and u^\parallel are constructed at the pressure point in the staggered grid, by linear combination of the u_r and u_z velocity components.

should be constructed from the other velocity components. This is done by determining three new velocity components that are perpendicular and parallel to the local lines of equal ρ (see figure 4.3). Thus the orientation of these new velocity components changes with position. These velocity components are constructed by linear combination of the u_r , u_θ and u_z velocity components. One of the attractive properties of defining u^\perp in this way that the u^\perp is continuous across the centreline: there the component u^\perp is perpendicular to the pipe axis.

To estimate the GS kinetic energy, as well as the contribution of the normal-to-the wall velocity component to it, means and fluctuations of the velocity components need to be defined. To this end, averaging takes place in the tangential direction, being the only homogeneous direction in this particular flow (see footnote 12).

4.2.5 Boundary conditions

The boundary conditions in the tangential direction are straightforward, since these are periodic by definition. Therefore, the discussion will focus on the boundary conditions in radial and axial direction.

Boundary conditions in radial direction

Boundary conditions for \widehat{u}_r : At the pipe axis u_r has a grid value (on a gridbox face with zero surface area). This value is obtained by interpolation between $\widehat{u}_r^{1,j,k}$ and $\widehat{u}_r^{1,j+\text{max}/2,k}$. For a discussion about this procedure the reader is referred to Eggels (1994). At the pipe wall ($i =$

$imax$) the radial velocity is zero. For the u_r -point, beyond the wall (at $i = imax + 1$) the divergence is used. Since $\frac{\partial}{\partial \phi} u_\theta = 0$ and $\frac{\partial}{\partial \zeta} u_z = 0$ at the pipe wall, the remaining terms in the divergence are:

$$\frac{1}{\rho f(\zeta)} \frac{\partial \rho \widehat{u}_r}{\partial \rho} - \frac{\rho}{f(\zeta)} \frac{\partial f(\zeta)}{\partial \zeta} \frac{\partial \widehat{u}_z}{\partial \rho} = 0 \quad (4.38)$$

Details on the implementation can be found in appendix E.3.1.

Boundary conditions for \widehat{u}_θ : At the pipe axis, the boundary condition is obtained from the grid point for $i = 1$ at the opposite side of the pipe axis. Minus the value of \widehat{u}_θ at that point is taken as the value for \widehat{u}_θ at $i = 0$. For the boundary condition at the pipe wall a no-slip condition is used: $u_\theta = 0$.

Boundary conditions for u_z : The boundary conditions for \widehat{u}_z are similar to those of \widehat{u}_θ : At the pipe axis: the value is derived from a mirror point at the opposite side of the axis. At the pipe wall a no-slip boundary condition is applied.

Boundary conditions for p' : For the pressure p' , the boundary conditions are as follows. Both at the pipe axis and the pipe wall a Von Neumann boundary condition is used for the pressure. At the pipe axis $\partial p' / \partial n$ (where n is the direction normal to the pipe axis) can simply be implemented. However, at the wall boundary, the situation is more complicated. Since the line between the pressure points on either side of the pipe wall is not at right angles with that pipe wall, the pressure gradient normal to the wall –which should be zero– has to be approximated. This is done by interpolating the pressure both inside and outside the pipe wall to points that are locate on a line that is perpendicular to the pipe wall. Details can be found in E.3.2.

Boundary conditions in axial direction: infbw

Boundary conditions for velocities: At the inflow plane prescribed values for the velocities are used. The inflow boundary conditions for the velocities are generated with a separate LES model with periodic boundary conditions and parallel walls. The discretisation and the SGS-model in that model are identical to those in the model with the contraction. The forcing of the axial velocity is done with a pressure gradient that is constant in space and time, and which has a non-dimensional magnitude of 4. This value can be derived from the following force balance (see (2.12c)):

$$0 = \frac{\pi}{4} D^2 \Delta p + (\pi D L) \rho u_*^2, \quad (4.39)$$

where L is the domain length and Δp is the pressure drop over the total domain (here, ρ is density). This leads to a dimensionless pressure drop $D / (\rho u_*^2) \frac{\partial}{\partial z} p = 4$.

For the simulations *with* swirl, the non-zero tangential velocity has to be introduced somehow. Two options are discussed here. The two methods have in common that the exact shape of the forcing depends on the swirling flow one desires to simulate.

One possibility is to apply an artificial force that depends on the difference between the actual mean tangential velocity and the \bar{u}_θ -profile of the flow to be simulated. This method has been used by van Haarlem (1995). The artificial force is an integrator of the deviation of the simulated \widehat{u}_θ -profile from the target profile, and is formulated as:

$$f_\theta^{n+1} = f_\theta^n + \alpha ((\bar{u}_\theta)_{meas} - \langle u_\theta \rangle^n) \quad (4.40)$$

where n is an indicator of the time step, $\langle \widehat{u}_\theta \rangle$ is the tangential velocity averaged in the homogeneous directions (i.e. axial and tangential) and $(\bar{u}_\theta)_{meas}$ is the measured mean tangential velocity. van Haarlem (1995) reports that the relaxation factor α should be set to 1. Since f_θ accumulates deviations of $\langle \widehat{u}_\theta \rangle$ from $(\bar{u}_\theta)_{meas}$, the risk exists that the forcing is non-zero, while $(\bar{u}_\theta)_{meas} - \langle u_\theta \rangle$ equals zero, which in turn might lead to oscillations around the target \widehat{u}_θ . To prevent this, in the first stage of the simulation $(\bar{u}_\theta)_{meas}$ is increased gradually to its final value:

$$f_\theta^{n+1} = f_\theta^n + \alpha \left(\frac{t^{n+1}}{t_r} (\bar{u}_\theta)_{meas} - \langle \widehat{u}_\theta \rangle^n \right) \quad (4.41)$$

where t_r is the time in which the target profile is relaxed from zero to its final value. Thus 4.40 holds for $t \geq t_r$ and 4.41 for $t < t_r$. The disadvantage of this forcing is that it is not constant in time and care has to be taken to prevent oscillations. On the other hand this forcing will yield a correct \bar{u}_θ -profile.

Another possibility is to introduce an artificial force that is constant in time as well as in the axial direction, but varies in the radial direction. Integrated over the pipe cross section, the tangential forcing f_θ will act to oppose the tangential wall shear stress $\tau_{\theta,wall}$. In fact, this f_θ acts as if it is a tangential pressure gradient. From (2.12b) it can be deduced, under the assumptions of stationarity, axisymmetry, axial homogeneity and $\bar{u}_r = 0$ (and without making the equations dimensionless):

$$\begin{aligned} 0 &= f_\theta + \frac{1}{r} \frac{\partial r \tau_{r\theta}}{\partial r} + \frac{\tau_{r\theta}}{r} \\ &= f_\theta + \frac{1}{r^2} \frac{\partial}{\partial r} (r^2 \tau_{r\theta}) \\ &= f_\theta - \frac{1}{r^2} \frac{\partial}{\partial r} \left(r^2 \overline{u'_r u'_\theta} - r^2 \nu \left\{ \frac{\partial \bar{u}_\theta}{\partial r} - \frac{\bar{u}_\theta}{r} \right\} \right). \end{aligned} \quad (4.42)$$

This forcing f_θ will be dependent on the radial coordinate and it can be derived from measurements of turbulent stresses and the mean u_θ velocity profile. The advantage of this forcing method is that the forcing is constant in time and that the $\overline{u'_r u'_\theta}$ -profile will be correct in the simulation. There is no guarantee, however, that the \bar{u}_θ -profile will be correct.

Boundary conditions for pressure: At the inflow plane a zero-gradient boundary condition is used.

Boundary conditions in axial direction: outflow

Boundary conditions for velocities: In the case of outflow boundary conditions a convective boundary condition (see Ferziger and Perić (1996)) is used. This implies that first the convective terms in the momentum equation are applied at the outflow boundary, with the convecting velocity replaced with its mean value (where *mean* signifies 'averaged in the homogeneous direction', indicated with $\langle \cdot \rangle$). Thus only the terms with derivatives in axial and tangential direction remain since $\langle \widehat{u}_r^{i,j,k} \rangle$ should be zero, but $\langle \widehat{u}_\theta^{i,j,k} \rangle$ will not be zero in a swirling flow. Since the pipe walls are parallel at the outflow plane, terms involving the derivative of the radial coordinate (i.e. $\frac{\partial f(\zeta)}{\partial \zeta}$) will vanish. Thus the momentum equations at the outflow plane reduce to:

$$\begin{aligned}\frac{\partial \widehat{u}_r}{\partial t} &= -\frac{1}{f(\zeta)\rho} \frac{\partial \widehat{u}_r \langle \widehat{u}_\theta \rangle}{\partial \phi} - \frac{\partial \widehat{u}_r \langle \widehat{u}_z \rangle}{\partial \zeta} + \frac{1}{f(\zeta)} \frac{\widehat{u}_\theta \langle \widehat{u}_\theta \rangle}{\rho} \\ \frac{\partial \widehat{u}_\theta}{\partial t} &= -\frac{1}{f(\zeta)\rho} \frac{\partial \widehat{u}_\theta \langle \widehat{u}_\theta \rangle}{\partial \phi} - \frac{\partial \widehat{u}_\theta \langle \widehat{u}_z \rangle}{\partial \zeta} \\ \frac{\partial \widehat{u}_z}{\partial t} &= -\frac{1}{f(\zeta)\rho} \frac{\partial \langle \widehat{u}_\theta \rangle \widehat{u}_z}{\partial \phi} - \frac{\partial \widehat{u}_z \langle \widehat{u}_z \rangle}{\partial \zeta}\end{aligned}\quad (4.43)$$

For the mean values of the velocities (where *mean* implies averaged in the homogeneous direction) the outflow boundary conditions are a zero-gradient (Von Neumann) conditions for the radial and tangential velocity and a zero-curvature ($\partial^2 / \partial z^2 = 0$) condition for the axial velocity:

$$\begin{aligned}\langle \widehat{u}_r^{i,j,kmax+1} \rangle &= \langle \widehat{u}_r^{i,j,kmax} \rangle \\ \langle \widehat{u}_\theta^{i,j,kmax+1} \rangle &= \langle \widehat{u}_\theta^{i,j,kmax} \rangle \\ \langle \widehat{u}_z^{i,j,kmax+1} \rangle &= 2\langle \widehat{u}_z^{i,j,kmax} \rangle - \langle \widehat{u}_z^{i,j,kmax-1} \rangle\end{aligned}\quad (4.44)$$

Boundary conditions for pressure: The outflow boundary condition for the pressure is applied in two steps:

- In the Poisson solver a Von Neumann condition is used, $\frac{\partial \widehat{p}'}{\partial z} = 0$ at the outflow boundary.
- The second step involves an adjustment of the axial velocity needed to ensure equality of the volumes of inflow and outflow. This adjustment could be viewed as an extra pressure gradient force. The magnitude of the correction δ , is derived from the bulk velocities at the inflow and outflow plane ($\widehat{u}_{z,bulk}^{*,outflow}$; this is an intermediate value only, which will be changed by the correction under consideration):

$$\delta = \left(\widehat{u}_{z,bulk}^{n+1,inflow} \left(\frac{f_0^w}{f_{kmax}^w} \right)^2 - \widehat{u}_{z,bulk}^{*,outflow} \right)\quad (4.45)$$

Consequently, the total boundary condition for the pressure in the axial direction is:

$$\left(\frac{\partial \widehat{p}'}{\partial z} \right)_{outflow} = \frac{\delta}{dt}.\quad (4.46)$$

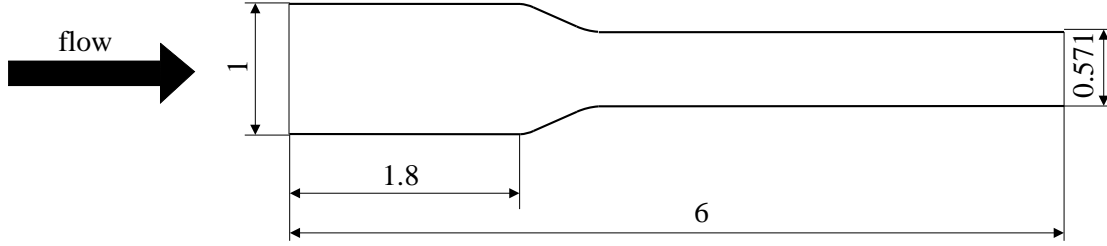


Figure 4.4: Domain of the LES model with contraction (all sizes are in expressed in upstream pipe diameters D).

4.3 Strategy of the simulations

The aim of this study is to simulate the same flow situation as described in section 3.3 of which the measurement results will be presented in chapter 5. Due to the limitations of LES, only the flow at $Re_D = 20000$ will be simulated. Since the LES model is formulated in terms of Re with u_* rather than U_{bulk} , the relationship between u_* and U_{bulk} needs to be known. For a *developed* pipe flow the relationship between u_* and U_{bulk} only depends on the Reynolds number: $u_*/U_{bulk} = 0.199 \cdot Re_D^{-\frac{1}{8}}$ (Blasius, 1908). From this it follows that Re should be approximately 1150. For a swirling flow u_*/U_{bulk} will be different, but also for the simulations of swirling pipe flow $Re = 1150$ will be used.

Two domain sizes need to be defined: for the straight pipe model and for the model including a contraction. For the straight pipe model a length of 5 will be used (since the length is non-dimensionalised with D , this corresponds with $5D$ in the physical experiment). According to Eggels (1994) this should be sufficient –at least for the non-swirling flow– not to be bothered by artificial axial correlation due to the periodic boundary conditions. For the model of the contraction the total domain has a length of 6, where the start of the contraction (i.e. the point where the diameter starts to decrease) is located at 1.8 downstream of the inflow plane. This corresponds to the laboratory experiment where the measurement section just upstream of the contraction is located $1.8D$ upstream of the start of the contraction as well. The domain of the contraction model is shown in figure 4.4

The spatial resolution to be used is shown in tables 4.1, together with some other key parameters. The relatively high resolution in the tangential direction has been chosen based on trial runs (see appendix F). It turns out that for a good representation of the u_θ -fluctuations in the near wall region a high resolution in the tangential direction is needed. Given the streaky nature of turbulence in the near wall region, where elongated vortices are moving in the streamwise direction, one would expect the spatial extent of u_r -fluctuations and u_θ -fluctuations to be comparable. Hence for a faithful representation one would need a comparable resolution in the r and θ direction (see also the remarks in section 4.1.4). The total number of grid points is based on the test for grid-independence given in appendix F.

quantity	straight pipe	contraction
N_r	50	50
N_θ	224	224
N_z	224	269
C_s	0.1	0.1
$Re = \frac{u_* D}{\nu}$	1150	1150 (upstream)
constant for non-uniform grid (see E.4 page 194)	0.97	0.97

Table 4.1: Overview of the most important parameters for simulations per model: the straight pipe model used to generate infbw and the contraction model to do the actual simulation.

5

Analysis of laboratory measurements

In this chapter the results of the laboratory experiments will be presented and discussed. The experiments have been performed with the set-up as presented in section 3.2. This chapter is organised as follows: in section 5.1 the data on the mean flow and Reynolds stresses are presented (both for the swirling and non-swirling flow) with only a minimum of interpretation and explanation. Further analyses of these data are made in section 5.2. These analyses comprise an attempt to explain and interpret the observations presented in 5.1. Points of attention are the axial development of the swirl number, the development of the stress anisotropy tensor and a comparison to predictions following from RDT. Subsequently, in section 5.3.1 quantities derived from the time series such as spectra and correlation functions are presented.

5.1 Mean flow and Reynolds stresses: data

This section will be devoted primarily to the mere presentation of experimental data on mean flow and Reynolds stresses. Explanations of observed phenomena, further analysis and comparison to other experiments is postponed to the next section.

5.1.1 A note on the presentation of data

Before unveiling the data, first some remarks on the presentation should be made:

- The data are presented for all six axial positions in one figure, with the vertical axis shifted upward for each position (the downstream direction in the experiment is upward in the figure, see for example figure 5.1). The axial positions to which the data refer are noted in the centre column, between the two sets of graphs. These axial positions z have been scaled with the pipe diameter upstream of the contraction. As discussed in section 3.2 the origin of the axial coordinate lies at the start of the transition from the large diameter pipe to the smaller diameter (see figure 3.9 at page 48). Thus axial positions upstream of the contraction are indicated by a negative value for z/D .
- The mean velocities are normalised with the bulk velocity U_{bulk} based on the *local* pipe diameter, whereas the turbulent stresses are normalised with U_{bulk}^2 . The radial position is normalised with the *local* pipe radius, so that the data always cover the range $-1 < r/R < 1$. These normalisations have been chosen to optimally use the space within the graphs. Besides, the local bulk velocity bears some relationship to the local wall shear stress, so that the scaling with U_{bulk} can easily be converted to a scaling with u_* ¹.

¹For a *developed* pipe flow the relationship between u_* and U_{bulk} only depends on the Reynolds number:

- The figures also show estimates of the errors in the presented quantities. These error estimates comprise both the statistical error (see appendix A) and the errors due to imperfect alignment (see appendix D). The error bars given in the figures span a range of $\pm 2\sigma_{error}$ (σ_{error} is the error variance) which would represent a 95% confidence interval if the errors would have a Gaussian distribution.
- The data points are given by symbols. For reasons of presentation these symbols are connected by line segments to clarify the relationship between the points (especially for the graphs in which two quantities are plotted);
- The velocity components are expressed in cylindrical coordinates; however, for the ease of interpretation of the graphs u_r and u_θ will be replaced by $-u_r$ and $-u_\theta$ for $r < 0$ (both for the mean flow and for the Reynolds stresses); this arrangement is especially useful in the case of non-axisymmetry.

5.1.2 Flow with axial strain and no swirl

This section deals with the measurements of the flow without swirl. Data on the mean flow, normal Reynolds stresses and Reynolds shear stresses will be presented successively.

Before discussing the actual data, it should be pointed out that the error bars are hardly discernible in all figures presented in this section. For the mean velocity \bar{u}_z the errors are less than 1%. The errors in the normal stresses are generally less than 4%, except for $\overline{u'_r u'_r}$, for which the errors are somewhat larger at some stations (but less than 10% in the majority of cases). The shear stress $\overline{u'_r u'_z}$ has an error of less than 10%.

Figure 5.1 shows the profiles of the mean axial velocity for bulk Reynolds numbers ² $Re_D = 2 \cdot 10^4$ and 10^5 . A first thing to note is that the profiles are perfectly symmetric (this holds for turbulent quantities as well: see other figures). Apart from a proof of the suitability of the experimental set-up this observed axisymmetry can also be interpreted as an indication of the correctness of the results.

The negative axial pressure gradient due to the contraction (additional to the regular pressure gradient that balances the wall shear stress) results in a flattened profile of the axial velocity ($z/D = 2.4$). Further downstream the profile again approaches the shape of the \bar{u}_z -profile of a developed pipe flow. For $Re_D = 2 \cdot 10^4$ the differences between the profiles at $z/D = -5.8$ and 25.2 is less than 1% at all radial positions. Comparison of the profiles at the same axial positions for the higher Reynolds number reveals some significant differences in the centre and near the wall (differences of at most 4%). In this comparison the effect of the Reynolds number (which increases by a factor of 1.75 between positions upstream and downstream of the contraction) on the profile of \bar{u}_z is neglected.

Figure 5.2 and 5.3 show the three normal Reynolds stresses. The main effect of the axial strain is to suppress these normal stresses. However, this is partly an effect of the normalisation chosen. If the U_{bulk} based on *one* diameter (either upstream or downstream of the contraction) had been used for all axial positions, the result would be a *suppression* of the $\overline{u'_z u'_z}$ -stress and an

$u_* / U_{bulk} = 0.199 \cdot Re_D^{-\frac{1}{8}}$ (Blasius, 1908)

²All Reynolds numbers mentioned in this chapter are –unless stated otherwise– bulk Reynolds numbers Re_D based on the pipe diameter *upstream* of the contraction.

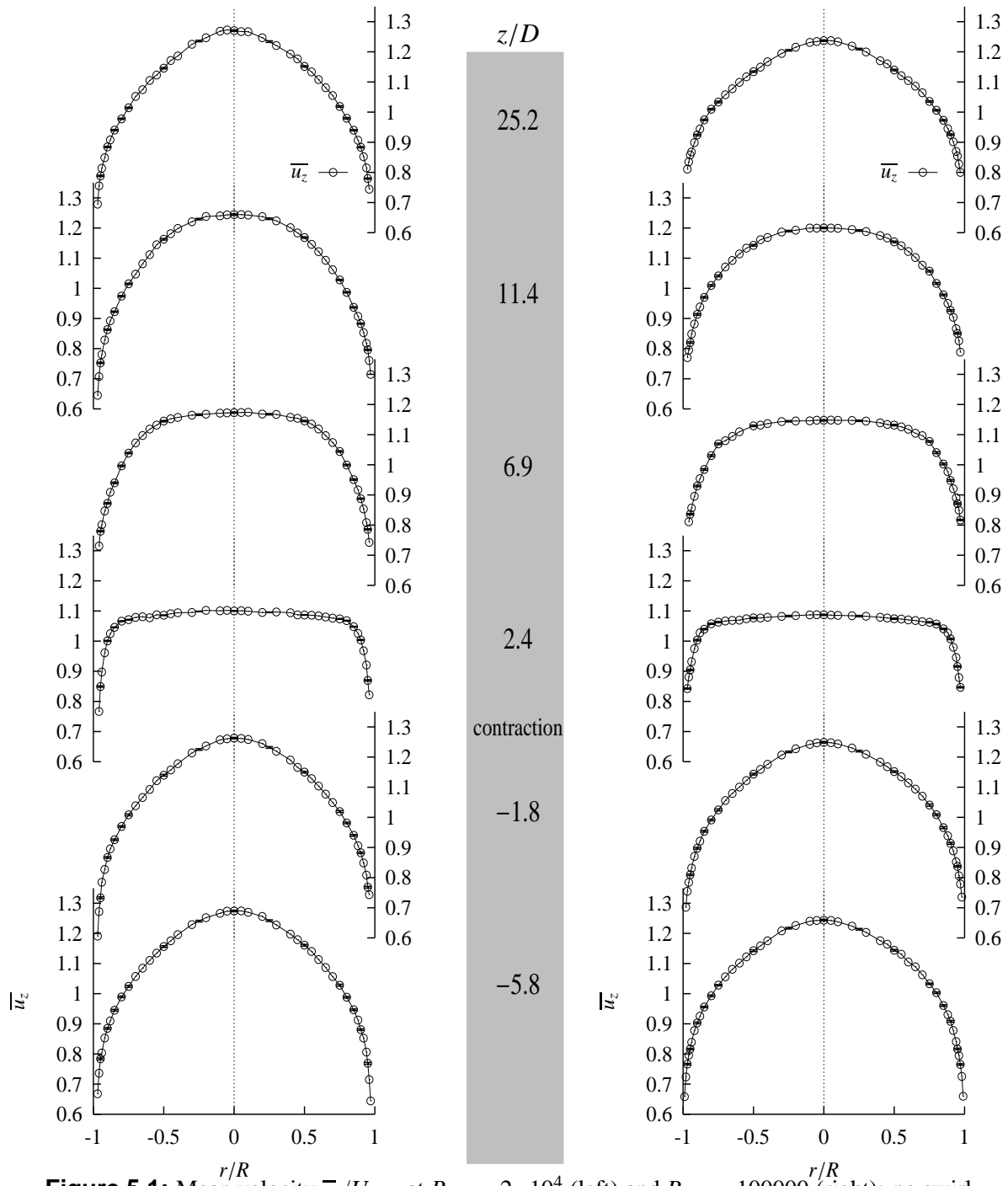


Figure 5.1: Mean velocity \bar{u}_z/U_{bulk} at $Re_D = 2 \cdot 10^4$ (left) and $Re_D = 100000$ (right): no swirl

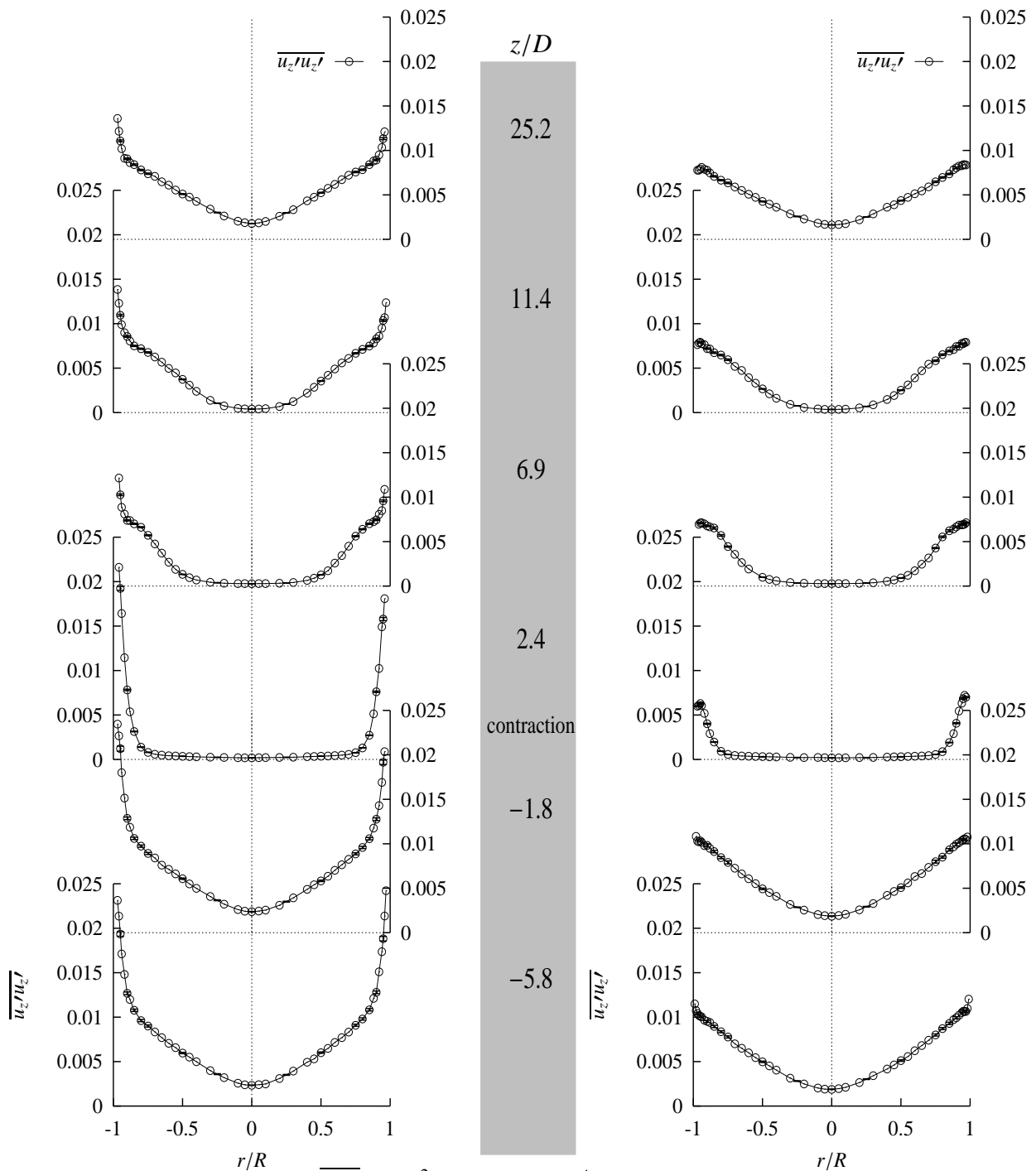


Figure 5.2: Normal stress $\overline{u'_z u'_z} / U_{bulk}^2$ at $Re_D = 2 \cdot 10^4$ (left) and $Re_D = 100000$ (right): no swirl

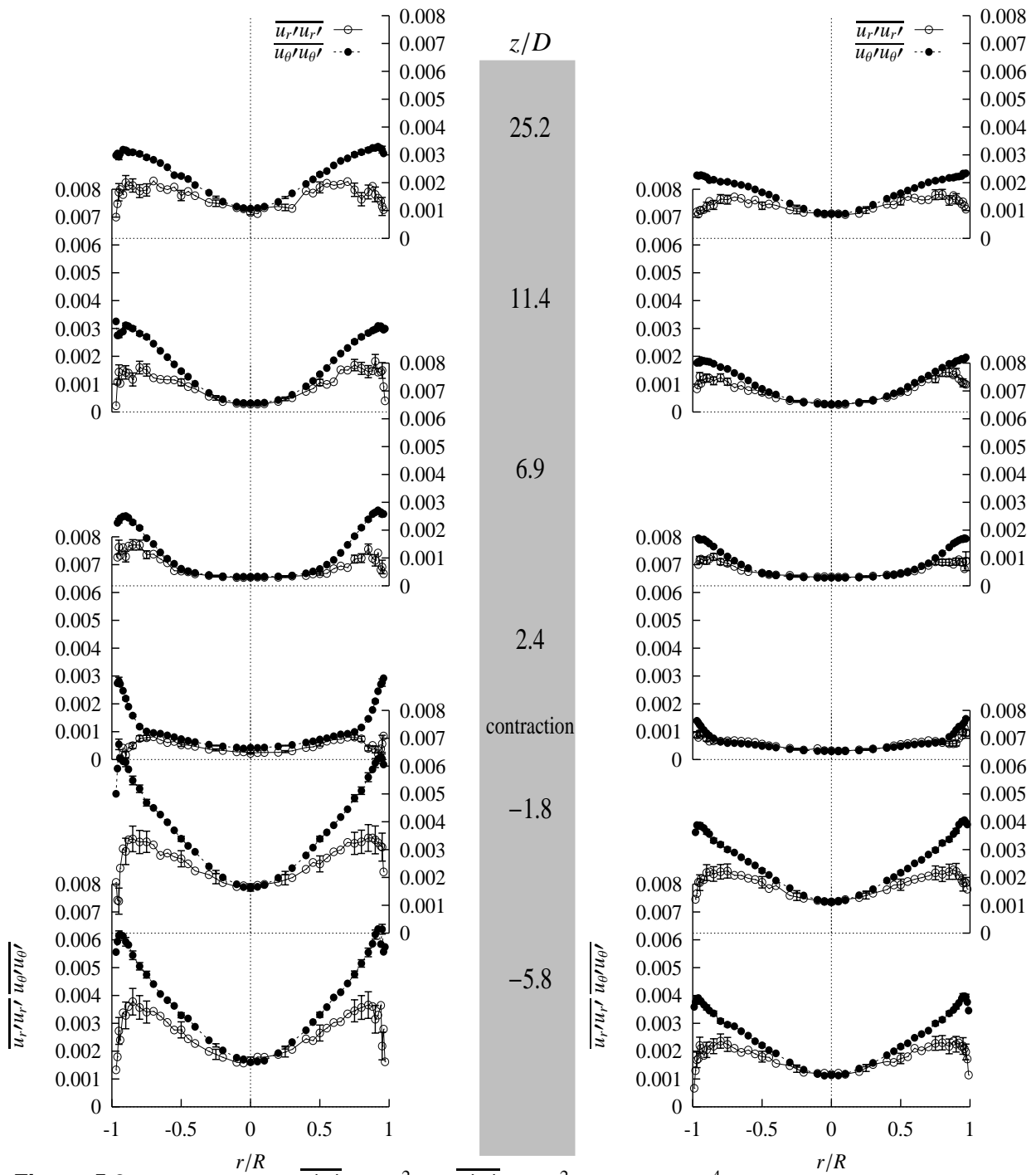


Figure 5.3: Normal stresses $\overline{u_r' u_r'}/U_{bulk}^2$ and $\overline{u_\theta' u_\theta'}/U_{bulk}^2$ at $Re_D = 2 \cdot 10^4$ (left) and $Re_D = 100000$ (right) : no swirl

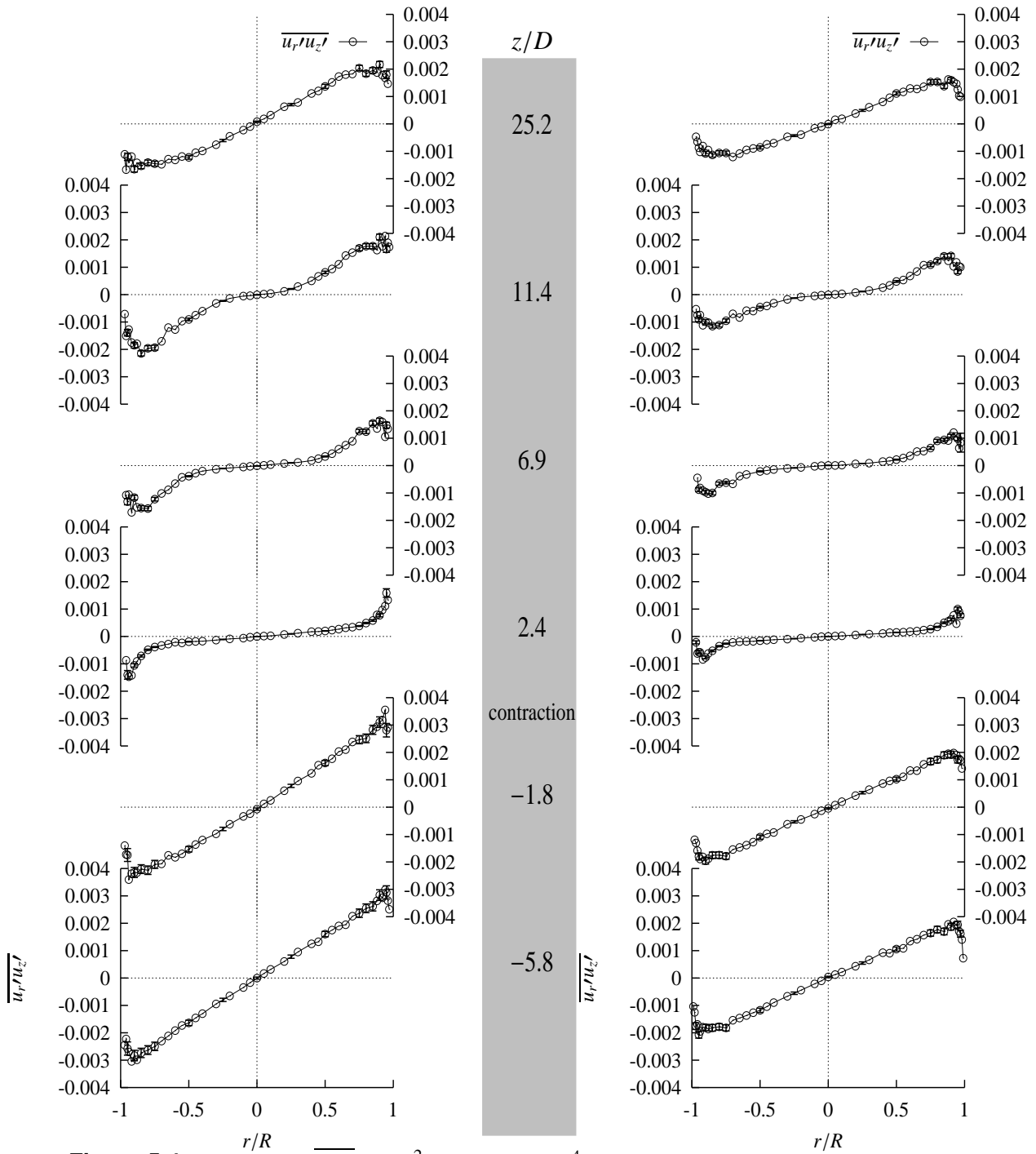


Figure 5.4: Shear stress $\overline{u_r' u_z'} / U_{bulk}^2$ at $Re_D = 2 \cdot 10^4$ (left) and $Re_D = 100000$ (right): no swirl

enhancement of the radial and tangential normal stresses. Another noteworthy feature is the fact that the region of lower $\overline{u'_z u'_z}$ -stress is eroded gradually from the wall. This low stress region has disappeared completely at $z/D = 25.2$ for both Reynolds numbers. Although the shape of the profiles of $\overline{u'_z u'_z}$ at $z/D = -5.8$ and 25.2 are similar, the values at the latter position are about 20% lower than at the former. In contrast, the $\overline{u'_r u'_r}$ and $\overline{u'_\theta u'_\theta}$ normal stresses at $z/D = 25.2$ have not yet returned to their values upstream of the contraction, neither in the centre, nor near the wall. The differences between $z/D = -5.8$ and 25.2 are of the order of 50% or more and the shape of the profiles differs as well.

In figure 5.4 the $\overline{u'_r u'_z}$ shear stress is given. The profile of $\overline{u'_r u'_z}$ is perfectly straight at $z/D = -5.8$ (as it should be for a developed pipe flow) for both Reynolds numbers. At $z/D = -1.8$ some small kinks are visible at $|r/R| \approx 0.85$ for $Re_D = 2 \cdot 10^4$. Downstream of the contraction transport of axial momentum toward the wall ($\overline{u'_r u'_z}$) is concentrated near the wall. This is in accordance with the observation above that the transformation of the flat $\overline{u_z}$ -velocity profile toward the profile of a developed pipe flow starts from the wall.

Comparison of the data for $Re_D = 2 \cdot 10^4$ and $Re_D = 10^5$, shows that for the lower Reynolds number the relaxation toward a fully developed pipe flow takes place over a shorter distance than for the high Reynolds number. This conclusion is based on the analysis of the region around the pipe axis where –downstream of the contraction– the profiles of especially $\overline{u_z}$, $\overline{u'_z u'_z}$ and $\overline{u'_r u'_z}$ persist with little change. The radial extent of this region decreases faster (i.e. over a shorter axial distance) for $Re_D = 2 \cdot 10^4$ than for $Re_D = 10^5$.

5.1.3 Flow with axial strain and swirl

Next the data for the swirling flow are considered. In figures 5.5 and 5.6 the profiles of $\overline{u_z}$, and $\overline{u_r}$ and $\overline{u_\theta}$ are shown, respectively. Compared to the data of the non-swirling flow the profiles are not as perfectly symmetric. However, the axisymmetry is better than that achieved by Steenbergen (1995). For an explanation of the (non-)axisymmetry of the flow the reader is referred to 5.2.

$\overline{u_z}$ The profiles of $\overline{u_z}$ exhibit a bump in the centre of the pipe. This region of excess velocity is larger for the data at $Re_D = 10^5$ than for the lower Reynolds number. The effect of the axial strain is to reduce the radial extent of this high velocity core and to make the velocity maximum even more pronounced (directly downstream of the contraction). When comparing the profiles of $\overline{u_z}$ at $z/D = 25.2$ for the cases *without* swirl and *with* swirl (figure 5.1 versus 5.5) the flatness of the profiles for the swirl-case is striking.

$\overline{u_\theta}$ Upstream of the contraction the profiles of $\overline{u_\theta}$ (figure 5.6) show a core that is close to a solid-body rotation, whereas the outer region has the shape of a free vortex (see figure 2.1(b)). This shape of the profile of $\overline{u_\theta}$ is representative for a Burgers vortex (see section 2.2 on page 15). Parchen and Steenbergen (1998) call this a 'distributed vortex'. The high velocity core in the $\overline{u_z}$ -profile coincides with the solid-body part of the $\overline{u_\theta}$ -profile. Or more precisely: the radial position where the $\overline{u_z}$ -profile starts to increase sharply toward its large value in the bump coincides with the maximum value of $\overline{u_\theta}$. Garg and Leibovich (1979) call this combination of a $\overline{u_\theta}$ -profile similar to that of a Burgers vortex, with an axial velocity profile with a jet-like structure, a Q-vortex. Downstream of the contraction the shape of

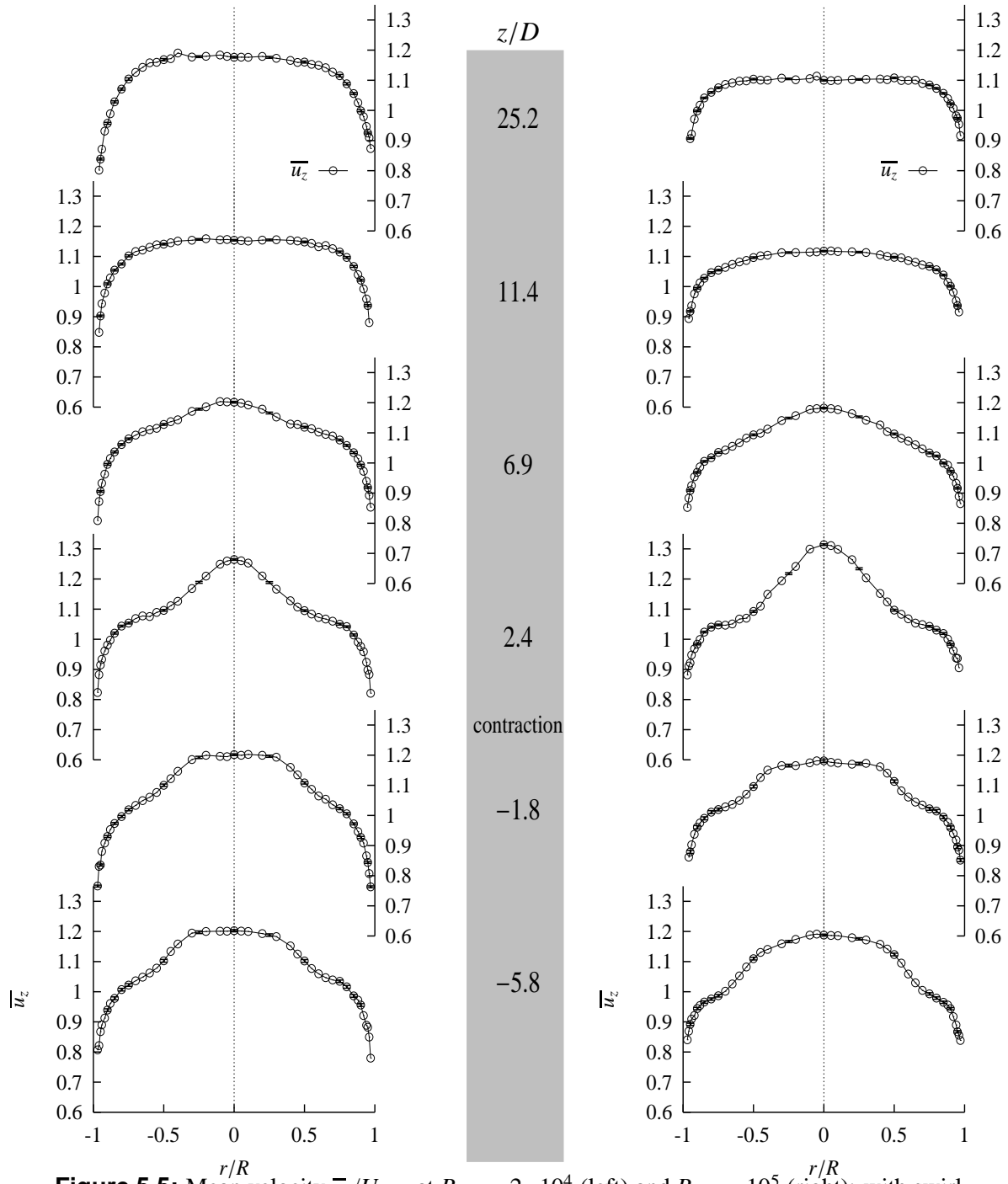


Figure 5.5: Mean velocity \bar{u}_z/U_{bulk} at $Re_D = 2 \cdot 10^4$ (left) and $Re_D = 10^5$ (right): with swirl

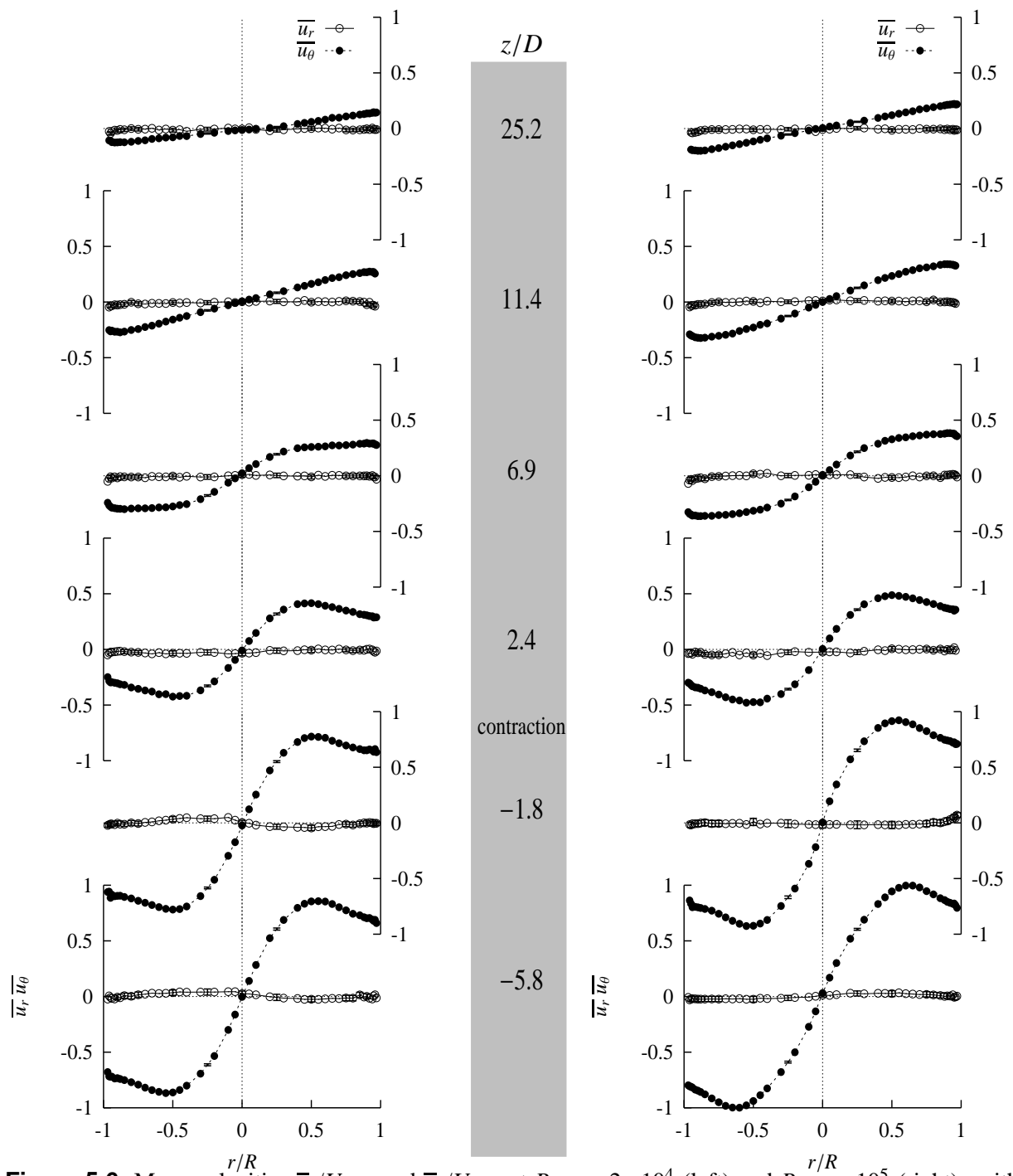


Figure 5.6: Mean velocities \overline{u}_r/U_{bulk} and $\overline{u}_\theta/U_{bulk}$ at $Re_D = 2 \cdot 10^4$ (left) and $Re_D = 10^5$ (right): with swirl

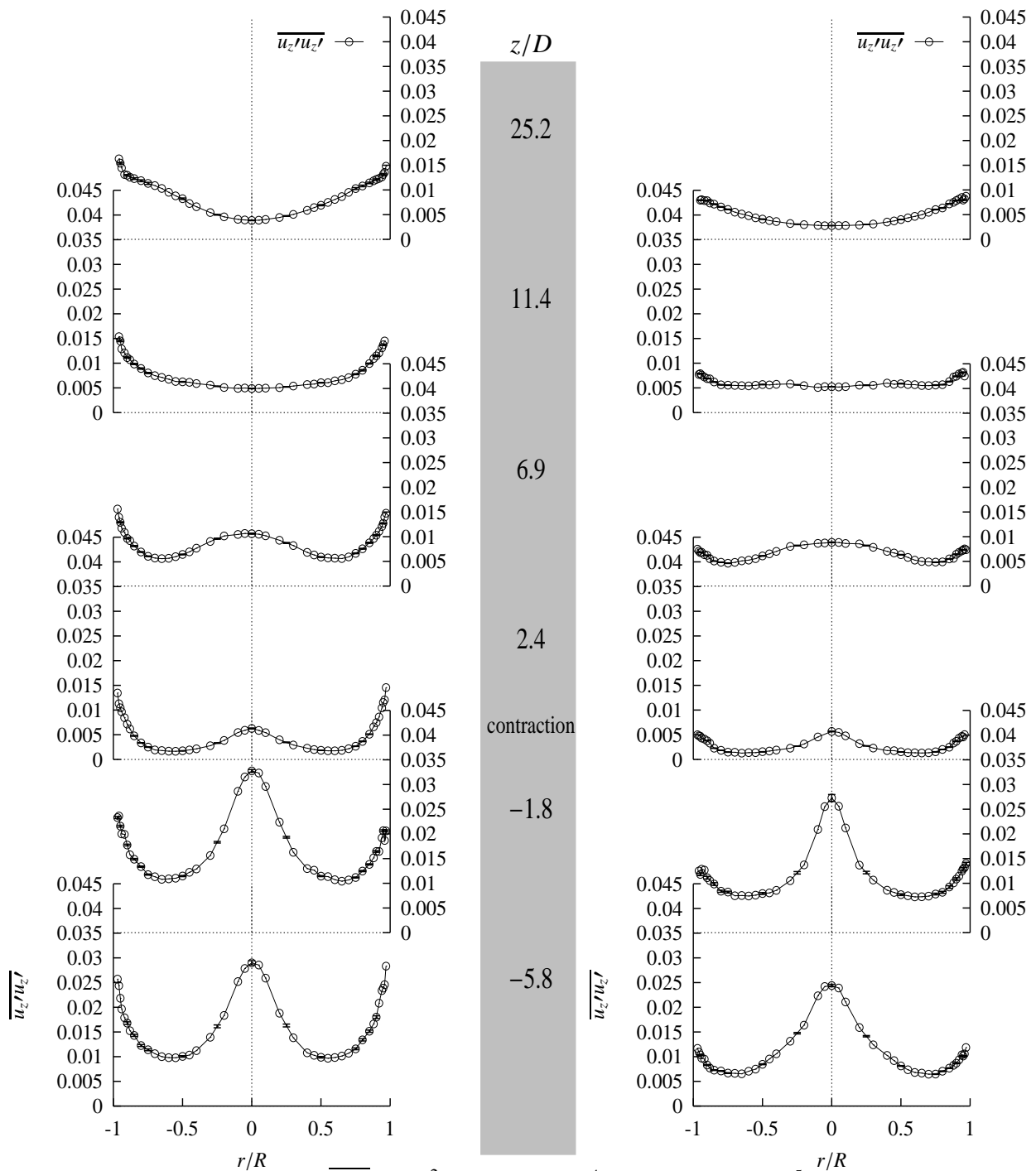


Figure 5.7: Normal stress $\overline{u'_z u'_z} / U_{bulk}^2$ at $Re_D = 2 \cdot 10^4$ (left) and $Re_D = 10^5$ (right): with swirl

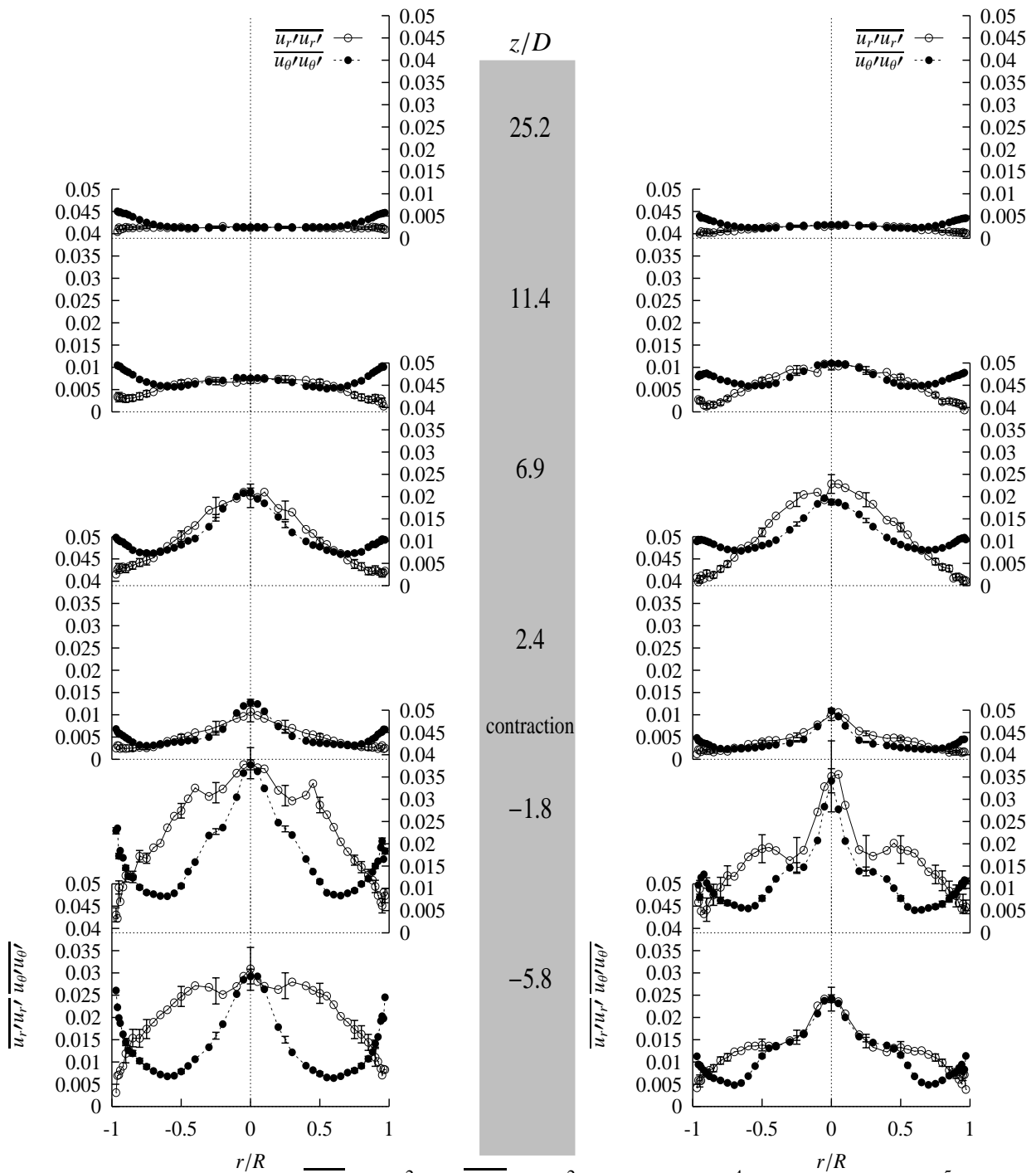


Figure 5.8: Normal stresses $\overline{u_r' u_r'}/U_{bulk}^2$ and $\overline{u_\theta' u_\theta'}/U_{bulk}^2$ at $Re_D = 2 \cdot 10^4$ (left) and $Re_D = 10^5$ (right): with swirl

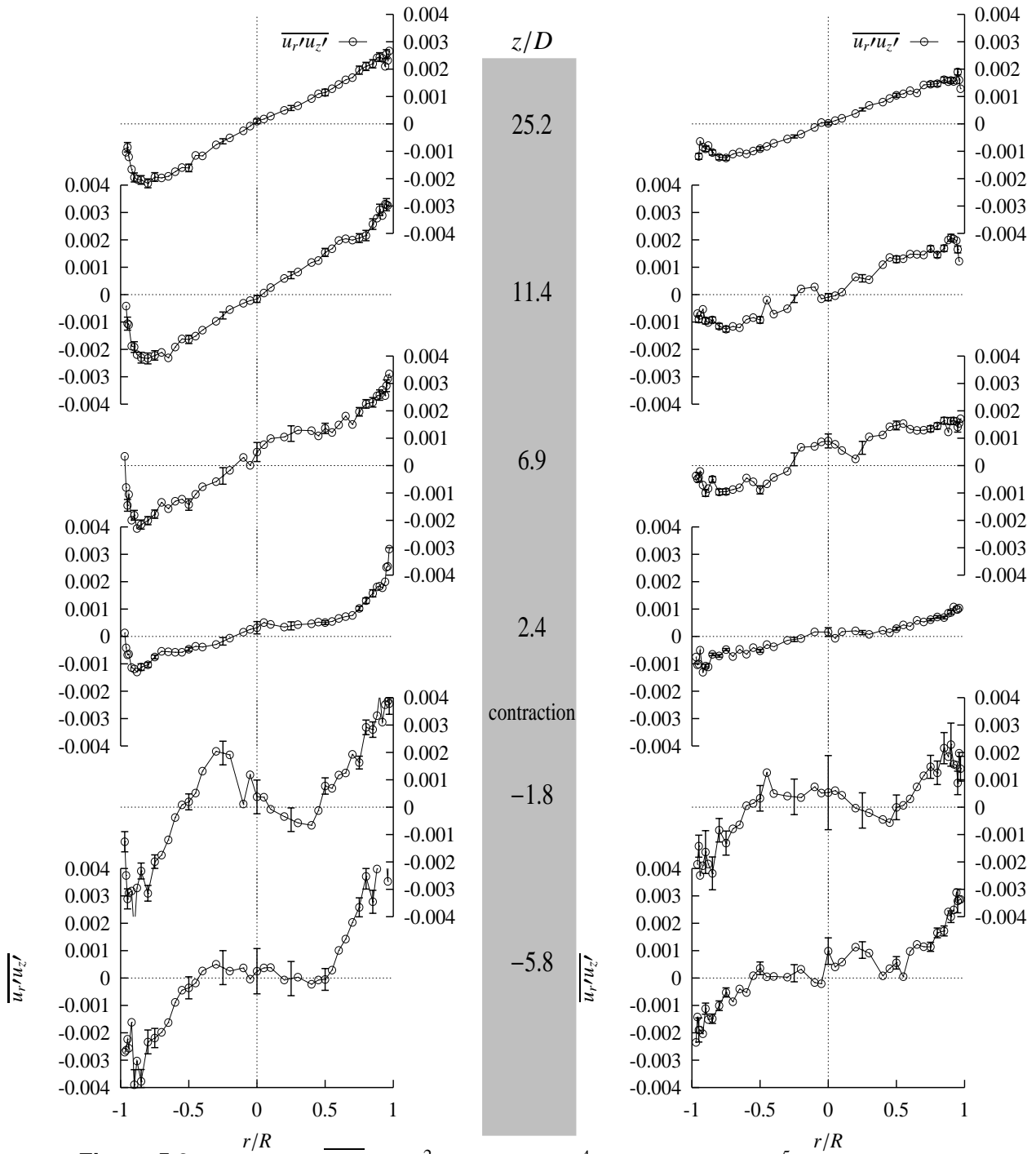


Figure 5.9: Shear stress $\overline{u_r' u_z'} / U_{bulk}^2$ at $Re_D = 2 \cdot 10^4$ (left) and $Re_D = 10^5$ (right): with swirl

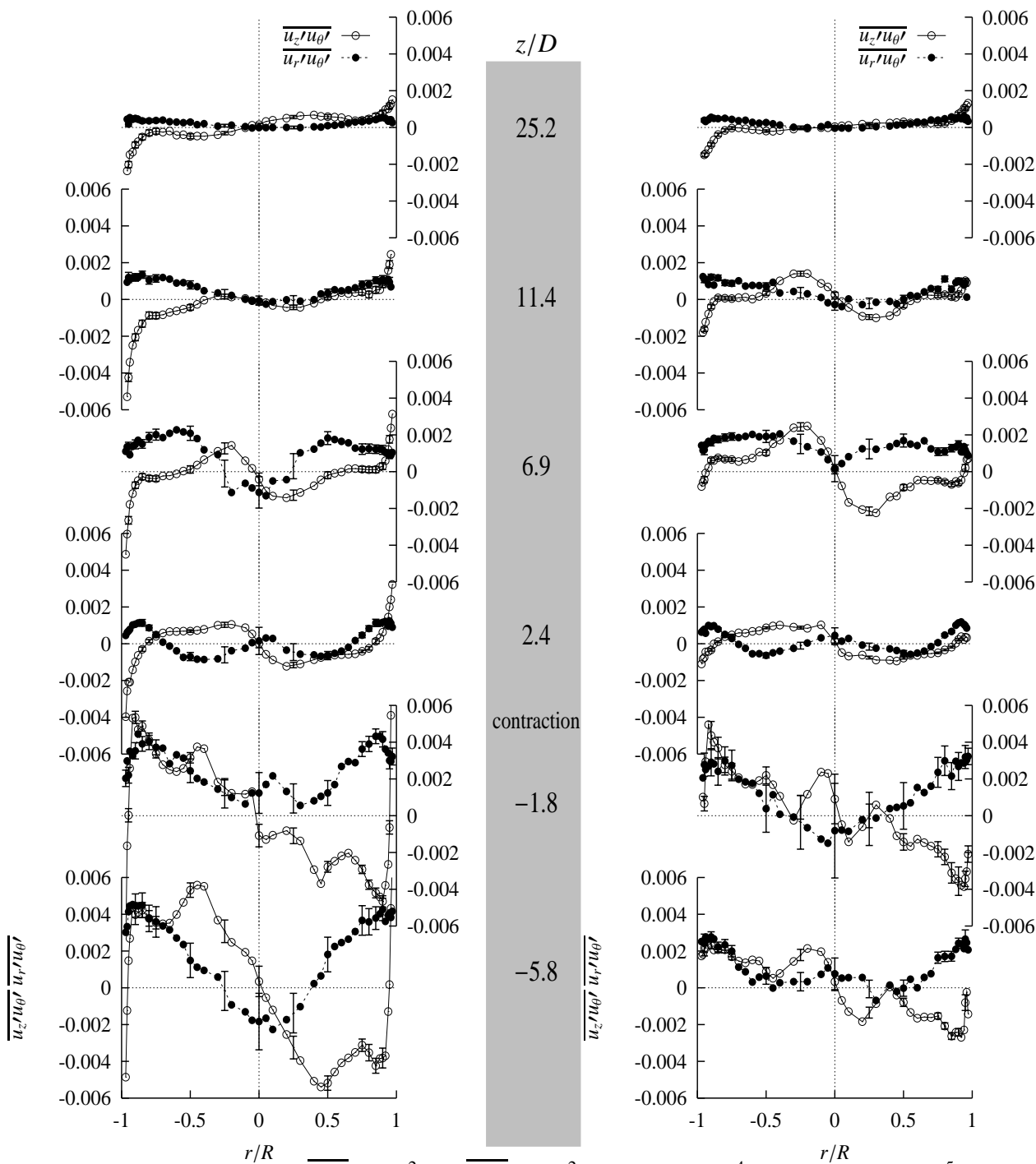


Figure 5.10: Shear stresses $\overline{u_z'u_\theta'}/U_{bulk}^2$ and $\overline{u_r'u_\theta'}/U_{bulk}^2$ at $Re_D = 2 \cdot 10^4$ (left) and $Re_D = 10^5$ (right): with swirl

the \bar{u}_θ -profile does not change much, but the maximum value shifts slightly toward the pipe centre. At $z/D = 11.4$ the local maximum in \bar{u}_θ has disappeared and so has the bump in \bar{u}_z . The fact that the value of \bar{u}_θ is lowered on passage through the contraction is perhaps counter-intuitive. However, one should remember that —apart from some swirl decay— this result is purely due to the normalisation used: conservation of angular momentum imposes that $\bar{u}_\theta \sim D^{-1}$ but $U_{bulk} \sim D^{-2}$, so that $\bar{u}_\theta/U_{bulk} \sim D$.

Figure 5.7 and 5.8 show the profiles of the normal stresses. The values for all normal stresses are an order of magnitude larger for the swirling flow than they are for the non-swirling flow (figures 5.2 and 5.3). Considering the shape of the profiles, one striking feature that can be noted for all stations between $z/D = -5.8$ and 6.9 is the bump in the profiles near the centreline. For all normal stresses an increase of the centreline value can be observed between $z/D = -5.8$ and -1.8. Downstream of the contraction the values of the normal stresses drop drastically, but this is again due to the normalisation used (U_{bulk}^2 downstream of the contraction is $(70/40)^4 \approx 9.4$ times U_{bulk}^2 upstream). The unscaled values of the normal stresses show a continuing increase with increasing z/D downstream of the contraction, until $z/D = 6.9$. For $\overline{u'_z u'_z}$ the bump in the centre has disappeared at the station $z/D = 11.4$, whereas for the other normal components of the stress only the final axial position does no longer show such a maximum value in the centre. The discussion of the normal stresses closes with a remark concerning the inequality of the centreline values of $\overline{u'_\theta u'_\theta}$ and $\overline{u'_r u'_r}$. For an axisymmetric flow these values should be equal by definition. The fact that the centreline values of $\overline{u'_\theta u'_\theta}$ and $\overline{u'_r u'_r}$ are not equal for all traverses is an indication either that the flow may not be fully axisymmetric or that the results are influenced by measurement errors (other than statistical errors and alignment errors which are included in the error bars). However, non-axisymmetry is not obvious from other quantities such as \bar{u}_r or the shear stresses involving fluctuations of the tangential velocity.

Figures 5.9 and 5.10 give the profiles of the three shear stress components $\overline{u'_r u'_z}$, $\overline{u'_z u'_\theta}$ and $\overline{u'_r u'_\theta}$:

$\overline{u'_r u'_z}$ At $z/D = -5.8$ the axial shear stress $\overline{u'_r u'_z}$ shows near-zero values for $-0.5 < r/R < 0.5$ which coincides with the vortex core (for $Re_D = 2 \cdot 10^4$ this region is somewhat smaller, as is the extent of the vortex core). For $z/D = -1.8$ the radial $\overline{u'_r u'_z}$ -stress gradient ($\frac{\partial}{\partial r} \overline{u'_r u'_z}$) even has the tendency to become negative within the core (for positive r), suggesting that the core with higher \bar{u}_z is fed from the outside. Downstream of the contraction the core with minimum $|\overline{u'_r u'_z}|$ disappears quickly. Further downstream the profile of $\overline{u'_r u'_z}$ becomes nearly straight. This happens over a shorter axial distance than in the case of the non-swirling flow, despite the fact that the mean profiles in the swirling flow are still far from fully developed.

The profiles with $Re_D = 2 \cdot 10^4$ downstream of the contraction show an asymmetry in the near-wall region. This asymmetry is not present in the data with $Re_D = 10^5$ so that a misalignment can be ruled out as the cause of the asymmetry (data at both Reynolds numbers share the same alignment, see section 3.2).

$\overline{u'_r u'_\theta}$ In general the profiles of $\overline{u'_r u'_\theta}$ show high values near the wall and low —sometimes negative— values in the centre. This picture is different for the first station downstream of the contraction ($z/D = 2.4$) where $\overline{u'_r u'_\theta}$ has a local maximum at $r = 0$. The fact that $\frac{\partial}{\partial r} \overline{u'_r u'_\theta} > 0$

(for $r > 0$) implies that tangential momentum is transported to the wall continuously: swirl decay.

$\overline{u'_z u'_\theta}$ The profiles of $\overline{u'_z u'_\theta}$ show a negative $\frac{\partial \overline{u'_z u'_\theta}}{\partial r}$ in the core region for all axial positions but the last. The fact that $\overline{u'_z u'_\theta} < 0$ (for $r > 0$) implies that tangential momentum is transported *upstream* by the turbulence. Furthermore, strong peaks in $\overline{u'_z u'_\theta}$ can be observed near the wall.

5.2 Mean fbw and Reynolds stresses: analysis

The data presented in the previous section will be analysed in a variety of ways. The first step is to find explanations for prominent features observed in the data. In this analysis frequent use will be made of the Reynolds averaged momentum equations (see equation 2.12 on page 14) and the budget equations for the Reynolds stresses (see section B.1.2). The second step will be to consider the decay of swirl (appendix 5.2.2). A third analysis relates to the Reynolds stresses which will be analysed in terms of the anisotropy tensor in section 5.2.4. The present section concludes with a comparison of rapid distortion predictions of the effect of swirl and axial strain to the observations.

5.2.1 Interpretation of the observations

Mean velocities

The first feature of the mean velocity profiles is the flattening of the \overline{u}_z -profile in the non-swirling flow. This phenomenon has been explained in section 2.3.1.

In section 5.1.2 on page 91 it was observed that the development of the flow toward a fully developed pipe flow, downstream of the contraction, takes place faster for the flow with $Re_D = 2 \cdot 10^4$ than for $Re_D = 10^5$. This difference in development speed can be understood when considering the growth of the boundary layer thickness (δ): for a flat plate the growth rate $\partial\delta/\partial z = (u_*/U_{bulk})^2$ (Hinze, 1975), and $(u_*/U_{bulk})^2 \sim Re_D^{-1/4}$ (Blasius, 1908)³. Thus the boundary layers will grow faster for the lower Reynolds number. In this context it should be noted that the *axial* positions have been scaled with the *upstream* pipe diameter. So, when comparing the rate of development with other published results (e.g. Klein (1981)) the axial positions should be multiplied with the ratio of upstream and downstream pipe diameter D_u/D_d . In this scaling the axial position of the final station becomes $z/D_d = 44.1$. According to Klein one can not yet expect the flow to be fully developed at this axial position.

The next point of interest is the shape of the mean velocity profile for the swirling flow. The combination of the jet-like structure of \overline{u}_z in the core of the swirling flow and the Burgers vortex-type profile for \overline{u}_θ is characteristic of the flow produced by swirl generators based on the radial inflow through a set of guide vanes (Leibovich, 1984). Note that, although the tangential velocity profile has the shape of a Burgers vortex, the flow under consideration is *no* Burgers vortex for two reasons. Firstly, there is no axial strain (except for that imposed by the contraction.

³Here the focus is on the Reynolds number dependence of the rate of development of a pipe fbw. According to Klein (1981) developing pipe fbw (an especially the ratio between centreline velocity and bulk velocity) is determined by more factors than flat-plate type boundary layer growth only.

Secondly, the width of the vortex core is mainly determined by the swirl generator, rather than by viscous diffusion of what was originally a line vortex. The explanation of Leibovich is that the flow passing the vanes is essentially irrotational, giving an annulus of irrotational flow between the core and the wall. The vortex core with positive vorticity, on the other hand, results from the boundary layer on the central body of the swirl generator. Leibovich explains the jet-like structure of \bar{u}_z from a low centreline pressure due to shedding of the boundary layer from the central body. The low centreline pressure would result in an extra radial inflow⁴.

Another explanation of the jet near the centre line is that in the present set-up a part of the flow passes *through* the central body, resulting in an axial jet of its own right.

The increase of the centreline value of \bar{u}_z upon passage through the contraction is –qualitatively– in accordance with the inviscid analysis of Batchelor (1967) (see section 2.4.1) in which a flow with $u_z(r) = U$ and $u_\theta(r) = \Omega r$ is passed through a contraction and the velocity profiles upstream and downstream are compared assuming the flow to be cylindrical ($\partial/\partial z = 0$ and $u_r = 0$) at both axial positions. Unfortunately it is not possible to make a quantitative comparison between the analysis of Batchelor and the present data, since the shape of the measured profiles is much more complicated than the simple flow considered by Batchelor. The same inviscid analysis predicts an increase of \bar{u}_θ proportional to D_d/D_u (i.e. conservation of angular momentum). From figure 5.11 it can be seen that the integrated angular momentum is not conserved, but decreases smoothly in the downstream direction. This is due to swirl decay. In order to remove the effect of swirl decay, the \bar{u}_θ -profiles have been replotted with \bar{u}_θ normalised with the ratio of actual angular momentum and a reference value of angular moment, i.e. at $z/D = -5.8$. The result is shown in figure 5.12. The change in the shape of the \bar{u}_θ -profile as predicted by the inviscid analysis is hardly visible in the data. In the $Re_D = 2 \cdot 10^4$ data there is a very slight steepening due to the axial strain. The data at the higher Reynolds number also show a steepening but that occurs already between $x/D = -5.8$ and -1.8 . Figure 5.12 clearly shows the way in which the profile of \bar{u}_θ changes downstream. Up to $x/D = 6.9$ there is a distinct vortex core extending to roughly $r/R = 0.5$. Further downstream the profiles tend to a solid body rotation. Another striking feature of the profiles is that –apart from the overall decrease in angular moment– the vortex core loses angular momentum and the wall region gains. The neutral point is located at $r/R = 0.7$ consistently for all profiles.

Reynolds normal stresses

For the non-swirling flow the most prominent phenomenon is the decrease of the normal stresses due the axial strain. As remarked in section 5.1.2 this decrease is partly due to the scaling (with U_{bulk}^2). The unscaled profiles would show an increase of $\overline{u'_r u'_r}$ and $\overline{u'_\theta u'_\theta}$ and a decrease in $\overline{u'_z u'_z}$. The explanation for this increase in $\overline{u'_r u'_r}$ and $\overline{u'_\theta u'_\theta}$ is as follows: the axial strain stretches vortices which have their axis in the z -direction and conservation of angular momentum requires that the vorticity ω_z increases. Vortices with their axis in the radial and tangential direction are

⁴This explanation breaks down in fbws where swirl decay plays a role: due to the decrease (in axial direction) of \bar{u}_θ , the radial pressure gradient decreases which results in $-\frac{\partial}{\partial z} p$ being smaller in the centre than near the wall. This in turn gives a minimum in \bar{u}_z in the centre and possibly reverse flow (see e.g. Parchen and Steenbergen (1998); Kitoh (1991)).

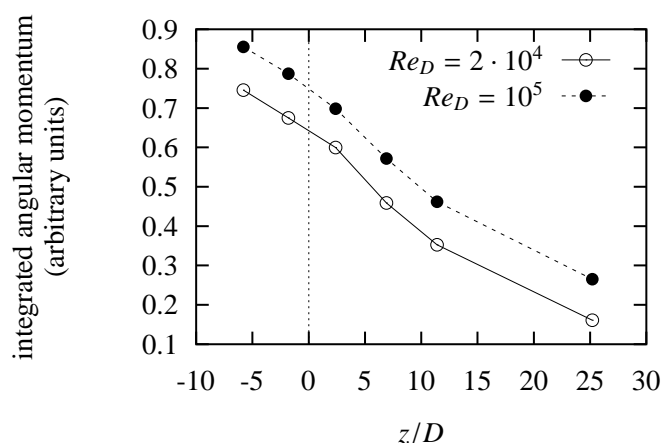


Figure 5.11: Axial development of the angular momentum integrated over the pipe cross-section. Velocities and radial positions have been normalised with U_{bulk} and R upstream of the contraction.

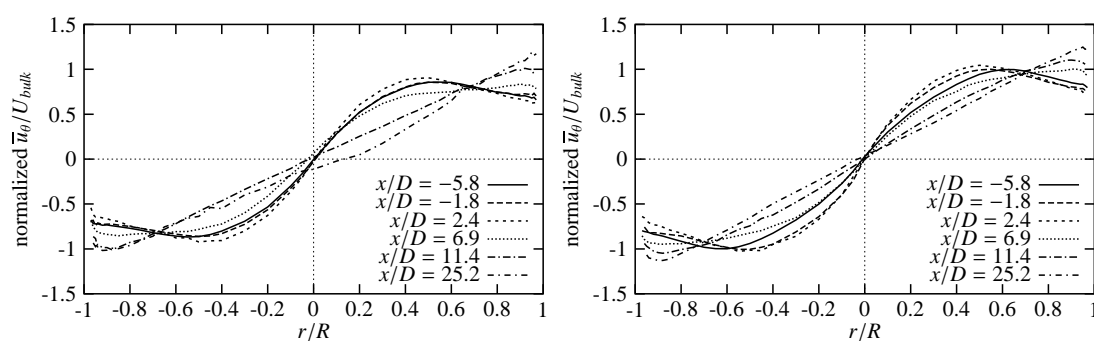


Figure 5.12: Profiles of \bar{u}_θ for all axial positions, where \bar{u}_θ has been divided by the ratio of local total angular momentum (in the \bar{u}_θ -profile) and the angular momentum at a reference point, i.e. $x/D = -5.8$. For $Re_D = 2 \cdot 10^4$ (left) and $Re_D = 10^5$ (right).

compressed and ω_θ and ω_r decrease consequently. This result is –for the data at the centreline– also in accordance with results from RDT (see Reynolds and Tucker (1975) and section 2.3).

The effect of axial strain on the normal stresses in the swirling flow can be compared qualitatively to the results presented by Leuchter (1997). As in the data of Leuchter the present data show that the decrease of $\overline{u'_z u'_z}$ and the increase of $\overline{u'_r u'_r}$ and $\overline{u'_\theta u'_\theta}$ –relative to the turbulent kinetic energy– due to the axial strain is reduced by rotation. This point will be pursued further in sections 5.2.4 and 5.2.5.

A gross comparison of the normal stresses in the non-swirling flow and the swirling flow reveals that the values for all normal stresses are an order of magnitude larger for the swirling flow. For $\overline{u'_r u'_r}$ this enhancement can be explained directly from the extra (production and convective transport) terms in the budget equations when $\bar{u}_\theta \neq 0$ and simultaneously $\overline{u'_r u'_\theta} \neq 0$. (see 2.10). For the other normal stresses no such direct explanation is possible.

Considering the shape of the profiles, one striking feature is the bump in the profiles near the centreline for all stations between $z/D = -5.8$ and 6.9 , inclusive. As far as the $\overline{u'_\theta u'_\theta}$ -stress is concerned this maximum could be the result of vortex core precession (e.g. Escudier, 1987): a small time-dependent radial displacement of the vortex core (with a large value of $\frac{\partial}{\partial r} \overline{u_\theta}$) gives a large fluctuation in u_θ . This interpretation suggests that the fluctuations in u_θ do not represent turbulent fluctuations but are –partly– the result of the meandering of the mean velocity field. Note that a bump in $\overline{u'_r u'_r}$ is a necessary consequence of the –assumed– axisymmetry of the flow in combination with a bump in $\overline{u'_\theta u'_\theta}$. To make a quantitative estimate of the vortex displacement, needed to explain the extra $\overline{u'_\theta u'_\theta}$ -stress, the profiles at $z/D = -5.8$ with $Re_D = 2 \cdot 10^4$ will be used as an example. The value of $\overline{u'_\theta u'_\theta}$ is about 0.025 above an estimated base value of 0.005 (the value at $r/R = 0.6$). Thus the extra standard deviation in u_θ , $\sigma(u_\theta)$, is 0.16. The slope of the $\overline{u_\theta}$ -profile, $\frac{\partial}{\partial r} \overline{u_\theta}$, is about $1/0.3 \approx 3.3$. Consequently, a representative value for the vortex core displacement is $\sigma(u_\theta)/\frac{\partial}{\partial r} \overline{u_\theta} \approx 0.05$. This displacement –about 10% of the core diameter– is not improbably large.

However, invocation of the possibility of vortex core precession can not explain the peak in $\overline{u'_z u'_z}$ near the centreline *directly*, since $\frac{\partial}{\partial r} \overline{u_z} = 0$ at the centreline. An explanation that links the peak in $\overline{u'_z u'_z}$ to that in $\overline{u'_\theta u'_\theta}$ is that the u_z -fluctuations may be produced through the pressure-strain correlations (see 2.10): energy present in the u_r and u_θ fluctuations is transferred to the axial velocity component.

Another explanation for the elevated levels of the normal stresses near the centreline is based on the observation that the outflow of the swirl generator can be interpreted as two coaxially co-flowing jets. The inner jet has a relatively high axial velocity and has no tangential velocity. The outer jet as a lower axial velocity and irrotational tangential velocity profile. This arrangement results in a cylindrical shear layer in which both $\frac{\partial}{\partial r} \overline{u_z}$ and $\frac{\partial}{\partial r} \overline{u_\theta}$ are non-zero and fluctuations of u_z and u_θ will be produced. This shear layer will grow radially and at a certain axial position the cylindrical shear layer will disappear. The fluctuations of u_z and u_θ produced in the shear layer will be carried downstream.

A third explanation is that fluctuations are produced at the swirl generator. According to the explanation of Leibovich (1984), the vortex core must be interpreted as the remains of the boundary layer of the central body of the swirl generator. In that boundary layer, as well as in the zone where it is shed from the central body, the normal stresses will be enhanced. Furthermore, in the current configuration of the swirl generator a part of the fluid passes through a round converging channel *through* the central body. In this channel extra u_z -fluctuations will be produced. However, it is rather improbable that such elevated levels of fluctuations persist at a downstream distance of $z/D \approx 12$ (the axial distance between swirl generator and first second measurement station).

The three possible explanations for the elevated levels of fluctuations of u_z and u_θ differ in the axial location of the production of the fluctuation: ranging from local production to production in the swirl generator.

Reynolds shear stress: $\overline{u'_r u'_z}$

For the non-swirling flow the development of $\overline{u'_r u'_z}$ is rather straightforward. Upstream of the contraction the profile of $\overline{u'_r u'_z}$ is –nearly– straight as is representative of a developed pipe flow. Downstream $\overline{u'_r u'_z}$ quickly attains its fully developed value in the near-wall region: somewhere between $z/D = 6.9$ and 11.4 . This distance appears to be in good agreement with the conclusion of Klein (1981) that the wall shear stress reaches the fully developed value after 8 to 15 diameters ($4.6 < z/D < 8.6$). Further downstream $|\overline{u'_r u'_z}|$ increases for the central part of the pipe as well.

The profiles of $\overline{u'_r u'_z}$ for the swirling flow need some closer examination. At $z/D = -5.8$ the axial shear stress $\overline{u'_r u'_z}$ shows near-zero values for $-0.5 < r/R < 0.5$, which coincides with the vortex core (for $Re_D = 2 \cdot 10^4$ this region is somewhat smaller, as is the extent of the vortex core). These low values of $|\overline{u'_r u'_z}|$ may be an indication of the stabilising effect of rotation (see 2.2.2). Downstream of the contraction the profile of $\overline{u'_r u'_z}$ becomes nearly straight much quicker than in the non-swirl case. One reason for this may be that the production term for $\overline{u'_r u'_z}$ ($-\overline{u'_r u'_r} \frac{\partial}{\partial r} \overline{u_z}$) is nearly shut off in the non-swirl case (due to the flat profile of $\overline{u_z}$), whereas in the swirling flow both $\overline{u'_r u'_r}$ and $-\frac{\partial}{\partial r} \overline{u_z}$ are enhanced (the latter due to the bump in the $\overline{u_z}$ -profile).

Reynolds shear stress: $\overline{u'_r u'_\theta}$

Upstream of the contraction the profile of $\overline{u'_r u'_\theta}$ shows a zero radial gradient in some parts of the vortex core (for $z/D = -5.8$ at $Re_D = 10^5$ this region is largest), thus no tangential mean momentum is transported outward in the core. In the rest of the pipe $\frac{\partial}{\partial r} \overline{u'_r u'_\theta} > 0$ (for $r > 0$), indicating decay of the swirl. Directly downstream of the contraction $\frac{\partial}{\partial r} \overline{u'_r u'_\theta}$ is negative (for $r > 0$): the vortex core is fed from the outside. Negative values of $\overline{u'_r u'_\theta}$ may be explained from the fact that production and convective transport terms in the budget of $\overline{u'_r u'_\theta}$ become negative when $\overline{u'_r u'_r} > \overline{u'_\theta u'_\theta}$. This does not, however, explain the negative value for $\frac{\partial}{\partial r} \overline{u'_r u'_\theta}$.

Reynolds shear stress: $\overline{u'_z u'_\theta}$

The profiles of $\overline{u'_z u'_\theta}$ are not easily interpreted. Whereas $\overline{u'_r u'_z}$ and $\overline{u'_r u'_\theta}$ stresses have a viscous counterpart, the viscous shear stress $\sigma_{\theta z}$ will be zero (since $\frac{\partial}{\partial z} \overline{u_\theta}$ and $\frac{\partial}{\partial \theta} \overline{u_z}$ are both –nearly– zero).

Upstream of the contraction, $\overline{u'_z u'_\theta} < 0$ for positive r . This is in accordance with the fact that in the budget equation for $\overline{u'_z u'_\theta}$ both the production and convective transport terms are negative. Then, given the fact that $\overline{u'_z u'_\theta} = 0$ at some point where the swirl has decayed, $\frac{\partial}{\partial z} \overline{u'_z u'_\theta} > 0$ and thus the axial gradient of $\overline{u'_z u'_\theta}$ is a loss term in the equation for $\overline{u_\theta}$: $\overline{u'_z u'_\theta}$ appears to have a function in the decay of swirl. Near the wall $\overline{u'_z u'_\theta}$ is positive, which may be explained from the fact that in the wall region long streaks of high and low streamwise velocity exist. In a non-swirling flow this streamwise velocity is simply $\overline{u_z}$, but in a swirling flow this is a combination of $\overline{u_z}$ and $\overline{u_\theta}$. When such a streak passes, highly correlated fluctuations of u_z and u_θ will occur.

5.2.2 Development of the swirl number

In the previous sections it has been observed frequently that for the swirling flow with axial strain *two* processes produce axial variations of the flow: the axial strain exerted by the contraction and

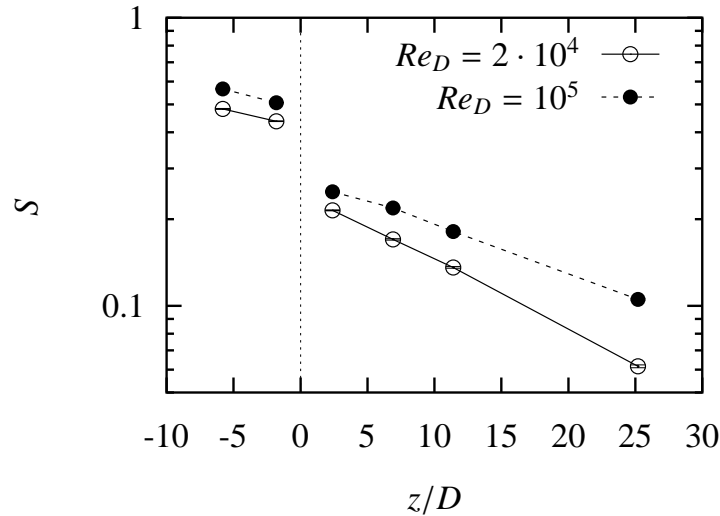


Figure 5.13: Axial development of the swirl number for $Re_D = 2 \cdot 10^4$ and 10^5 . Note that the horizontal axis shows the axial position scaled with the *upstream* pipe diameter, not the local diameter. Lines are drawn to connect points only. Error bars are drawn for the sake of completeness, but are hardly visible.

the decay of swirl due to wall friction. Numerous studies have been devoted to swirl decay in straight pipes (see section 2.2) and the aim of the present section is to see how the present experiment compares to previous results. In order to quantify the decay of swirl, some bulk measure of the 'amount of swirl' is used in those studies. In most cases this is the swirl number S , defined in equation 2.17, which will be employed here as well.

The main question is whether the axial strain has such influence on the flow that the swirl decay process *downstream* of the contraction is different from that found in straight pipes.

But first another question needs to be answered: what is the direct effect of the contraction on the swirl? This effect is twofold: on one hand the conservation of angular momentum results in an increase of the mean tangential velocity proportional to D^{-1} , whereas on the other hand the bulk velocity increases proportionally to D^{-2} . The net result on S is a decrease proportional to

Re_D	a for axial region relative to contraction		β for axial region relative to contraction	
	upstream	downstream	upstream	downstream
$2 \cdot 10^4$	0.418 ± 0.0027	0.245 ± 0.0028	0.0245 ± 0.0017	0.0307 ± 0.0008
10^5	0.483 ± 0.0022	0.274 ± 0.0039	0.0276 ± 0.0012	0.0214 ± 0.0008

Table 5.1: Fitting parameters in exponential decay of swirl (see equation 2.17) for the regions upstream and downstream of the contraction. For the downstream region a 68% confidence interval is given. The error in the upstream decay coefficient is estimated assuming maximum errors with opposite sign in the swirl numbers at $z/D = -5.8$ and -1.8 . In the exponential decay formula the *local* pipe diameter has been used to normalise the axial position x .

D^{-1} . Due to this dependence on the local pipe diameter, swirl decay needs to be studied in two separate regions: upstream and downstream of the contraction.

Figure 5.13 shows the swirl number S as a function of the axial position for both Reynolds numbers. The swirl number is higher for the higher Re_D , given the same configuration of the swirl generator. This was also found by Steenbergen (1995).

Assuming the decay is exponential in axial direction (equation 2.20), decay coefficients β have been calculated and are given in table 5.1. The first thing to be tested is whether the effect of the contraction on the swirl number indeed is a decrease proportional to D^{-1} . Since no measurements are available *directly* upstream and downstream of the contraction, and since within the contraction some swirl decay occurs as well, a trick has to be employed: the exponential decay equations for the upstream and downstream region are extrapolated to $z = 0$. At that point the swirl numbers (here $S = a$) are compared. This shows that the ratios of upstream and downstream swirl number are 1.706 ± 0.031 and 1.758 ± 0.034 for $Re_D = 2 \cdot 10^4$ and 10^5 , respectively. Taking into account the assumptions needed to arrive at these numbers, they can be considered to be very close to the ratio $D_{upstream}/D_{downstream}$.

The next step is to compare the decay coefficients to those reported elsewhere. Here only the results of Steenbergen and Voskamp (1998) and Parchen and Steenbergen (1998) will be considered, since those appear to be representative of other swirl decay data⁵. Furthermore, those experiments have been performed in the same experimental set-up as the present experiment. Finally, the swirl numbers are comparable as well: in the present experiment the swirl numbers upstream and downstream of the contraction are $O(0.45)$ and $O(0.25)$, respectively, whereas in the experiments of Parchen and Steenbergen (1998) and Steenbergen and Voskamp (1998) the swirl numbers are $O(0.5)$ and $O(0.2)$, respectively.

The decay coefficients for the region downstream of the contraction are about 10% lower than the empirical relationship given by Steenbergen and Voskamp (1998), based on their data ($0.3168Re_D^{-1/4}$ for $0 < S < 0.18$, see section 2.2.5). But the values are well within the range of results quoted in the review of Steenbergen and Voskamp. For the region upstream of the contraction the decay coefficient for the flow at $Re_D = 10^5$ is in line with relationship of Steenbergen and Voskamp. However, the value of β for $Re_D = 2 \cdot 10^4$ is *lower*, rather than higher, than that for the high Reynolds number (contrary to the assumed relationship with the friction factor, which is inversely related to Re_D). Parchen and Steenbergen (1998) report values for β of 0.0235 and 0.0284 for two flows with initial swirl numbers of about 0.65 and 0.4, respectively (at $Re_D = 5 \cdot 10^4$). When corrected for the Reynolds number dependence, these values are again higher than the decay coefficients in the region upstream of the contraction observed in the current experiment. Regarding the upstream region it should be kept in mind that the axial distance over which the decay has been determined is extremely short. Besides, it has been found before (Steenbergen (1995); Kitoh (1991)) that the initial stage of swirl decay may differ from an exponential decay.

⁵Steenbergen and Voskamp (1998) performed a thorough review of 18 experiments on swirl decay. These experiments comprised different types of swirl and swirl numbers ranging from about 0.05 to 1. When focusing on the dependence of the decay coefficient β on Re_D it is observed that the values of β cluster around a line parallel (on a log-log plot) to $\lambda(Re_D)$. Only the data with $S > 0.8$ diverge and show a more complicated dependence of β on Re_D .

5.2.3 Three-dimensionality in swirling flow

To study the possibly three-dimensional nature of the flow under consideration, the three angles γ , γ_g and γ_τ have been computed (see section 2.2.4 for their definition).

In order to reduce the scatter –particularly– in γ_g , the velocity and stress data of positive and negative r have been combined by averaging (this is warranted by axisymmetry observed in section 5.1.3). The result can be found in figure 5.14.

A number of observations can be made from this figure:

- The mean velocity profile is hardly skewed for $r/R > 0.6$ for most axial positions. Only the data at $z/D = 25.2$ show a slight increase of γ with r (i.e. decrease with $1 - r/R$).
- In the region $r/R > 0.9$ all three angles are of the same order, but differences of 10^0 to 20^0 do occur, mainly between γ and γ_τ on one hand, and γ_g on the other. However, the error γ_g can easily be 10^0 .
- The stress roughly follows (within 20^0) the shear for a larger part of the pipe cross section ($r/R > 0.5$, i.e. the region outside the vortex core) for most axial positions. Only at the station directly downstream of the contraction the relationship between shear and stress seems to be disrupted: due to the axial strain both the $\overline{u'_r u'_z}$ and $\overline{u'_r u'_\theta}$ profiles change significantly, whereas the mean velocity profiles hardly change.
- Inside the vortex core the shears are rather small (a flat $\overline{u_z}$ -profile and near-solid body rotation for $\overline{u_\theta}$). Still the shear angle γ_g seems to be well-defined, but the shear and the stress are not well aligned, which indicates the shear stresses are determined more by the flow upstream than by local processes.

It can be concluded that in this flow does not exhibit strong three-dimensionality in the sense of a skewed (or twisted) mean velocity profile in the wall-bounded part of the cross-section ($r/R > 0.5$). The shear and stress, however, are not aligned exactly, which indicates history effects or the absence of local equilibrium.

5.2.4 Comparison of stress-anisotropy between non-swirling and swirling flow

One of the problems in the comparison of the Reynolds stress data of the flows without and with swirl is the order of magnitude difference in their values. It is therefore more practical to present the data in terms of the normalised anisotropy tensor, \mathbf{a}/k :

$$\mathbf{a} = \overline{\mathbf{u}'\mathbf{u}'} - \frac{2}{3}\delta k, \quad (5.1)$$

where k is the turbulent kinetic energy. In the subsequent analysis the tensor \mathbf{a} will be represented in cylindrical coordinates. The shear components of \mathbf{a} will not be dealt with.

In figures 5.15 and 5.16 the normalised stress anisotropies are shown for $Re_D = 2 \cdot 10^4$ and $Re_D = 10^5$, respectively. When starting at the stations upstream of the contraction, it is manifest that the flows with and without swirl are different. Whereas $a_{zz} > 0$ for the non-swirl flow, the swirling flow shows a nearly isotropic stress tensor in the centre, and $a_{zz} < 0$ in a large part of

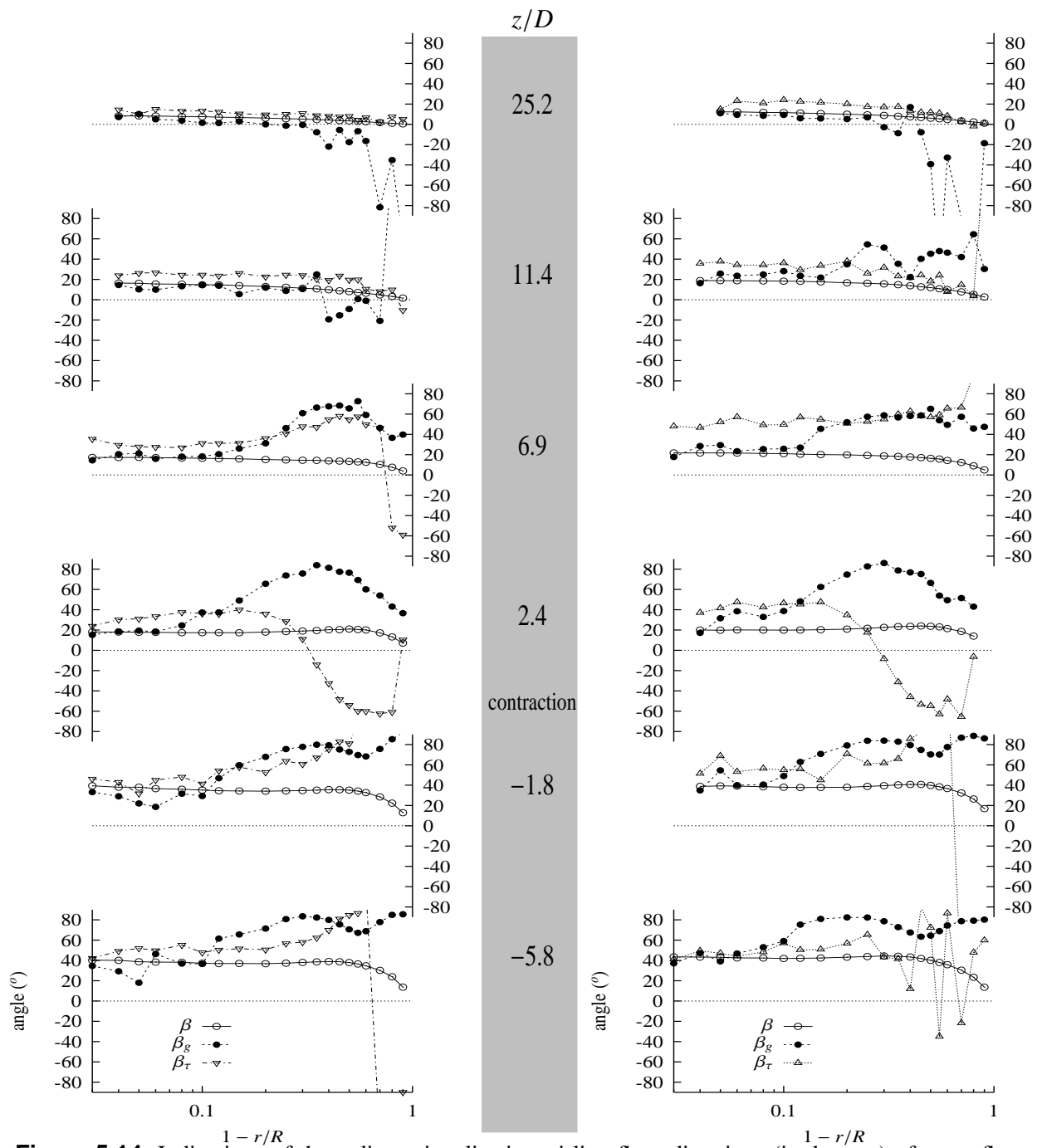


Figure 5.14: Indications of three-dimensionality in swirling flow: directions (in degrees) of mean flow (γ), shear (γ_g) and stress (γ_τ): $Re_D = 2 \cdot 10^4$ (left) and $Re_D = 10^5$ (right). Assuming axisymmetry the data for positive and negative r have been combined by averaging. Note that the horizontal axis gives the distance to the wall $1 - r/R$.

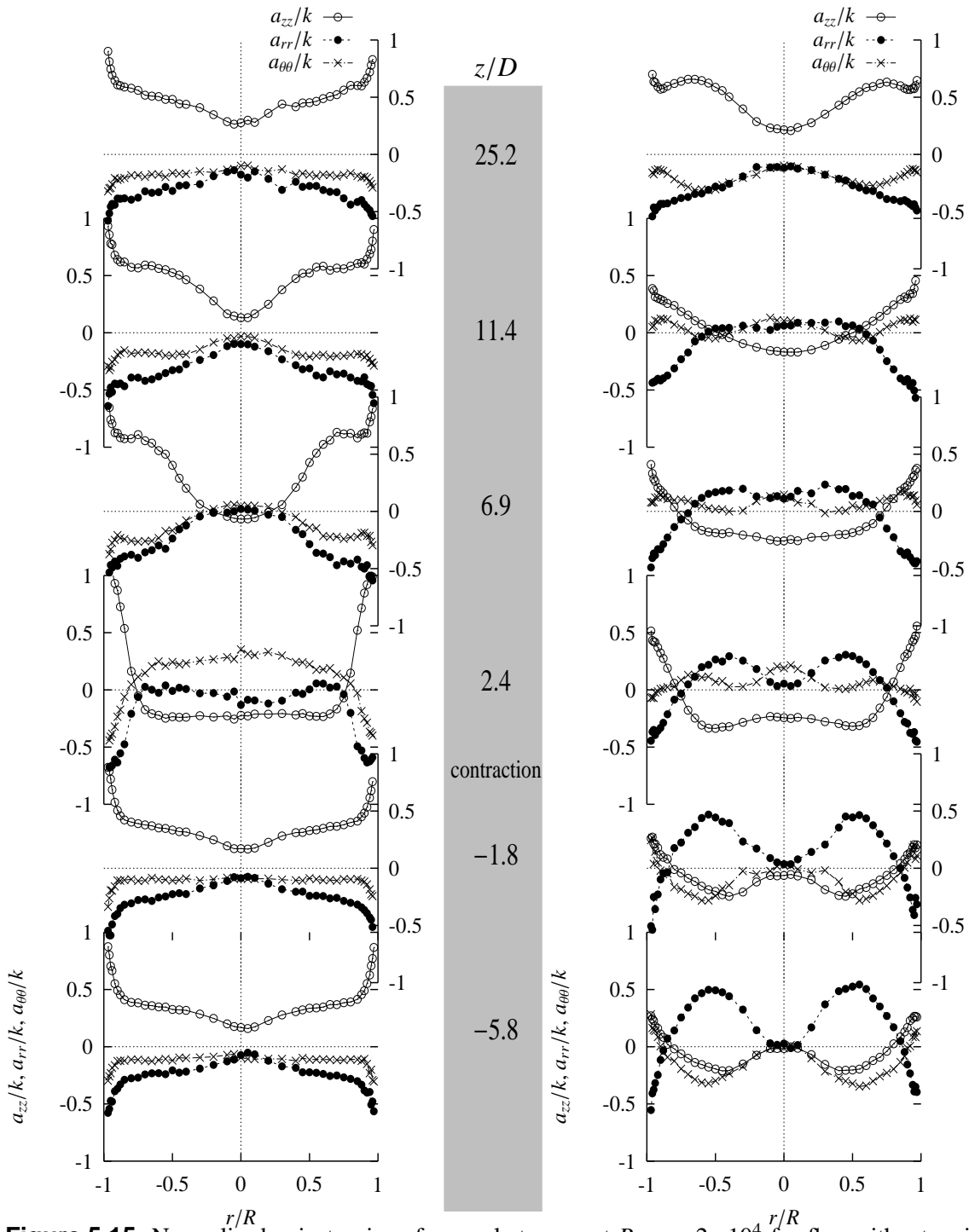


Figure 5.15: Normalised anisotropies of normal stresses at $Re_D = 2 \cdot 10^4$ for fbw without swirl (left) and with swirl (right)

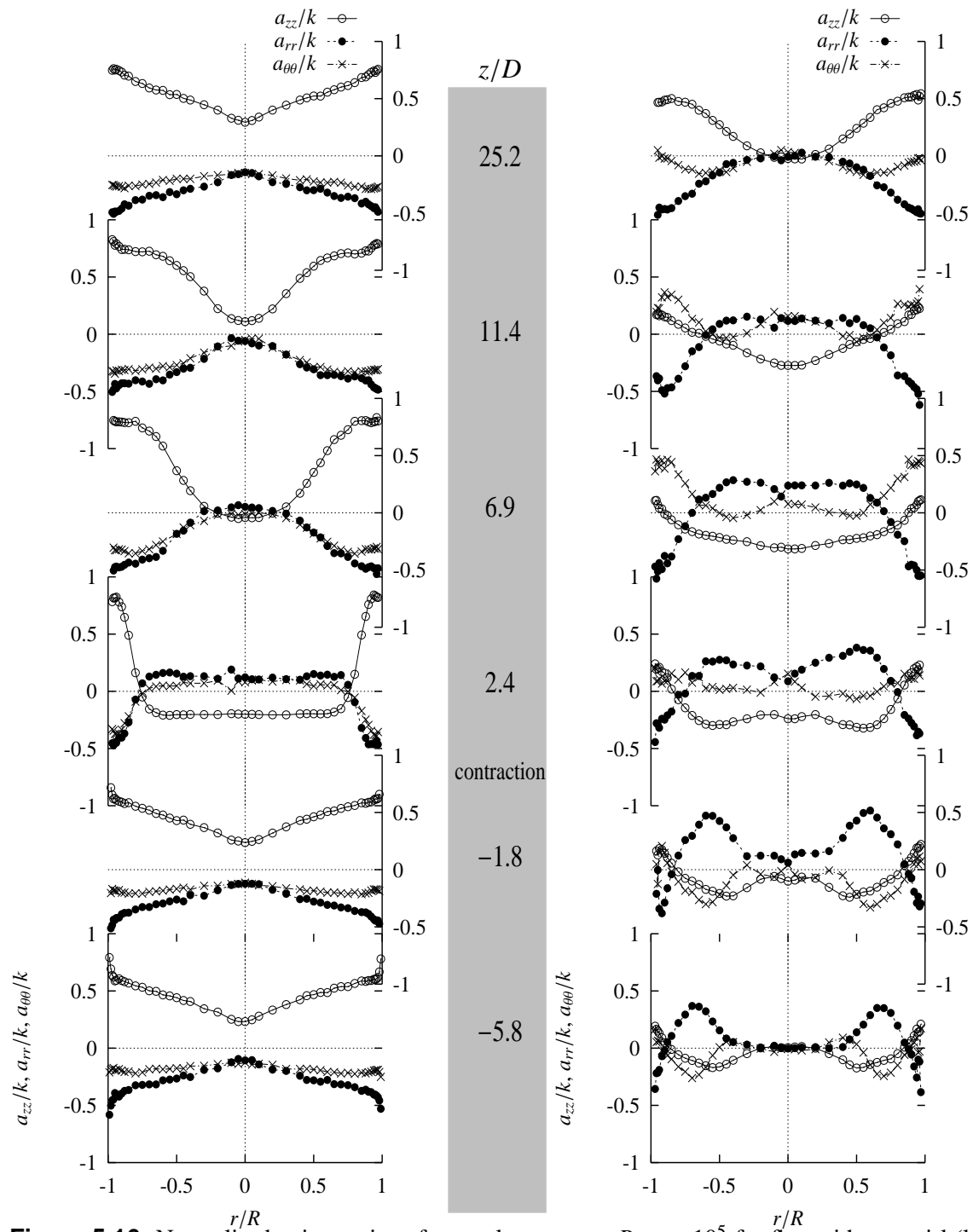


Figure 5.16: Normalised anisotropies of normal stresses at $Re_D = 10^5$ for flow without swirl (left) and with swirl (right)

the pipe cross-section. In the swirling flow the radial component of \mathbf{a} dominates and a_{zz} and $a_{\theta\theta}$ behave much alike. Directly downstream of the contraction ($z/D = 2.4$) this picture has changed dramatically. The flows with and without swirl have very similar profiles of the normal components of \mathbf{a} (especially for $Re_D = 2 \cdot 10^4$): a_{zz} has become negative and a_{rr} and $a_{\theta\theta}$ are slightly positive for $|r/R| < 0.8$ ($a_{rr} \neq a_{\theta\theta}$ at the centreline for some stations, which is incorrect if axisymmetry is assumed). In the region $0.8 < |r/R| < 1$ $a_{\theta\theta}$ follows a_{rr} for the non-swirl case. Furthermore, the profile of a_{rr} for the swirling flow is similar to that of the non-swirling flow. On the other hand, $a_{\theta\theta}$ in the swirling flow shows a deviant behaviour. This results from the fact that the mean streamwise direction in the swirling flow has a θ -component as well, whereas in the non-swirling flow the mean flow is in the z -direction. Thus one should compare the sum of $a_{\theta\theta}$ and a_{zz} . This comparison shows that indeed the swirl case and the non-swirl case behave similarly (not shown). Another indication that this explanation is correct is the observation (see section 5.2.3) that in the wall region the flow is hardly three-dimensional: mean flow and stresses are aligned.

The change in anisotropy due to the axial strain is less for the swirl flow than for the non-swirling flow, since the initial anisotropies are smaller for the first case. Leuchter (1997) shows that this can be attributed to a rotation-induced enhancement of the linear (so-called 'rapid') pressure strain term.

Focusing on the downstream development of \mathbf{a} , downstream of the contraction, it is clear that the relaxation from the effects of the axial strain is much quicker for the non-swirling flow than for the swirling flow. At the centreline of the swirling flow a_{zz} attains a zero value (which is the value upstream of the contraction) only at $z/D = 25.2$ for $Re_D = 2 \cdot 10^4$ and somewhere between $z/D = 11.4$ and 25.2 for $Re_D = 10^5$. In the non-swirling flow, however, a_{zz} changes sign at the centreline near $z/D = 6.9$. The slow relaxation of the swirling flow suggests that the pressure-strain correlations (see (2.10)), which are the main mechanism to exchange energy between normal stresses, are suppressed by the rotation. Given the fact that Leuchter (1997) shows that the linear part of the pressure strain terms is enhanced by rotation, it is probably the nonlinear part that is reduced (and the linear part is of minor importance when the large-scale strain is no longer applied).

In order to focus on the downstream development of the stress-anisotropy, figures 5.17 and 5.18 show the axial development of \mathbf{a} at the centreline for $Re_D = 2 \cdot 10^4$ and 10^5 , respectively. It appears that the change in \mathbf{a} due to the axial strain is less dramatic for the swirling flow than it is for the non-swirling flow. This is in accordance with the findings of Leuchter (1997). Another notable feature is that for the flow without swirl there is only a minor difference between the two Reynolds numbers. However, the swirling flow at $Re_D = 2 \cdot 10^4$ at axial position $z/D = 25.2$ shows values of \mathbf{a} much alike the non-swirling flow, whereas the flow at $Re_D = 10^5$ at the same position has only arrived at the pre-contraction values of \mathbf{a} . One should keep in mind that the downstream development of the swirling flow is complicated by the simultaneous swirl decay (see the previous section): the swirl number decreases between $z/D = 2.4$ and 25.2 by 71% and 57% for $Re_D = 2 \cdot 10^4$ and 10^5 , respectively.

Another way to view the anisotropy of the Reynolds stresses is by using the stress tensor

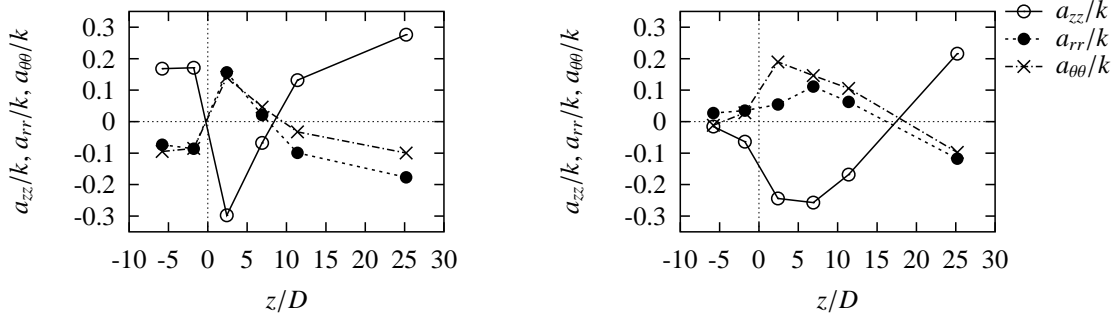


Figure 5.17: Axial development of the stress anisotropies at the centreline at $Re_D = 2 \cdot 10^4$: non-swirl case (left) and swirling flow (right). Note that the lines only serve to connect the observations.

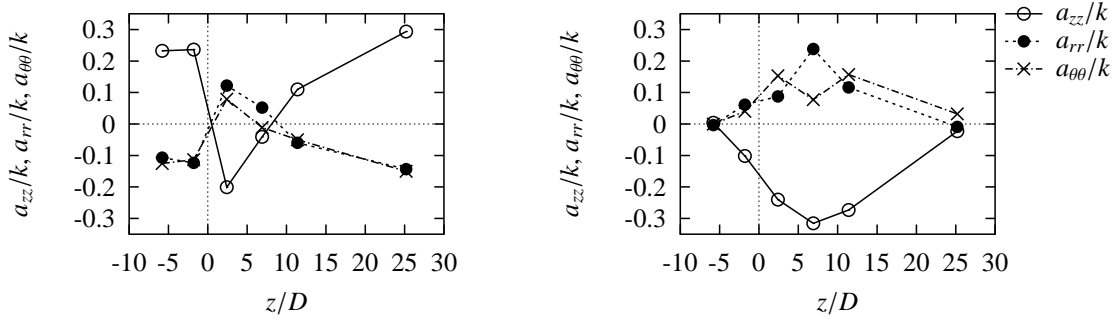


Figure 5.18: Axial development of the stress anisotropies at the centreline at $Re_D = 10^5$: non-swirl case (left) and swirling flow (right).

invariants. Usually the invariants of the anisotropy tensor (see equation 5.1) are used:

$$II = -\frac{1}{2}a_{ij}a_{ji} \quad (5.2)$$

$$III = \frac{1}{3}a_{ij}a_{jk}a_{ki} \quad (5.3)$$

van Dijk (1999) points out that the disadvantage of II is that it depends quadratically on a linear change –due to distortion– in the eigenvalues of the stress tensor. He proposes the following modified invariants:

$$II^* = 6\sqrt{\frac{III}{2}} \quad (5.4)$$

$$III^* = 3\sqrt{-II} \quad (5.5)$$

Due to conditions of realisability not all combinations of II^* and III^* are physically possible. A sketch of the domain of II^* and III^* is given in figure 5.19 along with interpretations of the

limits. The only possible combinations of II^* and III^* are within the triangular shape. In the origin the stress tensor is fully isotropic. Both straight lines starting at the origin are the limits of axisymmetric turbulence. To the left of $III^* = 0$ the stress tensor has two major axes and one minor axis (pancake), whereas to the right there is one major axis and two minor axes (cigar). The upper limit of the area of realisable stress tensors is the limit of 2-component turbulence (sometimes called two-dimensional). The idea of plotting II and III in such a diagram comes from Lumley (1978), the modified Lumley triangle is due to van Dijk (1999).

Figure 5.20 the modified Lumley-diagram is shown with data from the non-swirling flow and the swirling flow, both for $Re_D = 10^5$. Each symbol in the plot represents one radial position. The data are split into a core region $|r|/R < 0.7$ and a wall region $|r|/R > 0.7$. The limits are based on the observed indifference to swirl decay of the \bar{u}_θ -profile normalised with the total angular momentum (see figure 5.12).

In the non-swirling flow the turbulence is nearly axisymmetric for all axial positions: the stress tensor has one major axis (i.e. cigar-type anisotropy). The stress tensor is more isotropic near the pipe axis than near the wall. Only directly downstream of the contraction, the turbulence becomes non-axisymmetric for some radial positions. Furthermore, in the region $|r|/R < 0.7$ the anisotropy is of pancake type (i.e. two major axes). At $z/D = 6.9$ the flow already has recovered from this disturbance, although the stress tensor is more isotropic near the centre here than in the flow *upstream* of the contraction.

For the swirling flow the situation is less clear. For all axial positions there are (radial) points where the turbulence is not axisymmetric. The effect of the contraction is to move more points in the direction of pancake type axisymmetry, although only the near-wall points show some axisymmetry of the turbulence. Further downstream, at $z/D = 11.4$ the turbulence is nearly axisymmetric in a large part of the pipe cross section, being of the pancake type. Between $z/D = 11.4$ and $z/D = 25.2$, however, all points move from the left side to the right side: from pancake to cigar type of axisymmetry. This is due to the fact that due to swirl decay the role of $\overline{u'_\theta u'_\theta}$ and associated shear stresses has diminished when compared to upstream positions. The flow becomes more like a developed pipe flow.

When comparing the graphs of non-swirling and swirling flow it is apparent that near the pipe axis the contraction has opposite effects. For the non-swirling flow the contraction leads to a more isotropic stress tensor, whereas in the swirling flow the contraction makes it more anisotropic. In both cases the effect of the contraction disappears further downstream.

5.2.5 Rapid distortion analysis of normal stresses at centreline

In order to see to what extent the observed development of stress anisotropies can be explained by linear effects, a simple rapid distortion calculation has been made. For the data without swirl, the analytical results of analysis of Batchelor and Proudman (1954) can be used, with the extensions of Reynolds and Tucker (1975) to take into account initial anisotropy. No analytical results are given for distortions that include rotation, however. Therefore, the rapid distortion has been computed numerically with the following procedure:

- Only the pipe axis is considered. This implies that the distortion is axisymmetric.

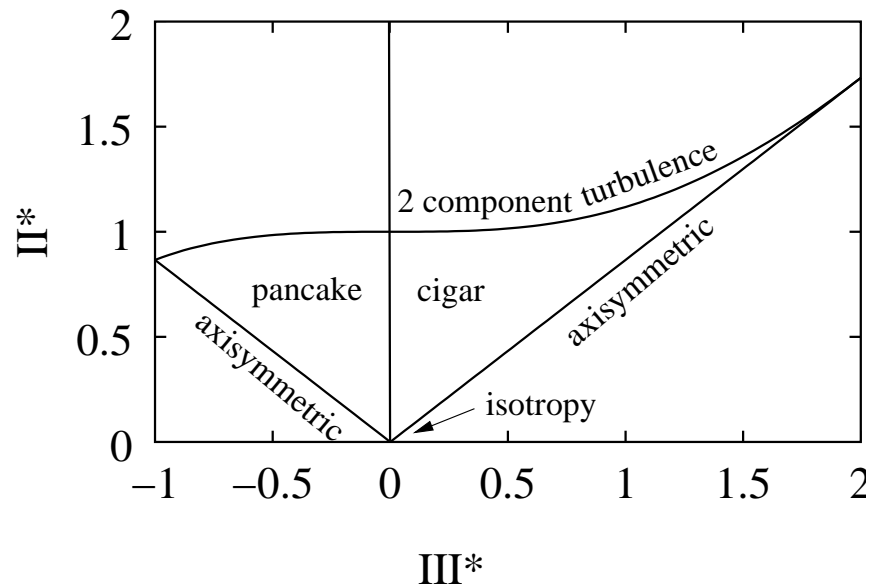


Figure 5.19: Modified Lumley-triangle (after van Dijk (1999)). The horizontal axis is a measure of elongation of the stress tensor (with isotropy at $III^* = 0$) and the vertical axis is a measure of anisotropy (with isotropy at $II^* = 0$).

- An initial isotropic spectrum is computed using the model spectrum due to Von Karman (taken from Hultgren and Cheng (1983)).
- In order to obtain anisotropic initial normal stresses, an initially isotropic spectrum is subject to an axial strain until the stresses exhibit the required anisotropy. This method was also used by Cambon and Jacquin (1989) and is similar to the trick used by Reynolds and Tucker (1975).
- The initial anisotropy is taken from the data of the station directly upstream of the contraction (i.e. 1.8 diameters upstream).
- Since the strain is not constant inside the contraction, the strain is applied step-by-step. After each small time-step the strain is recalculated given the pipe diameter for that axial position.
- For the axial strain without rotation, the strain is determined assuming a uniform axial velocity that is proportional to D^{-2} . For the flow with axial strain and rotation, the axial strain is computed identically. The tangential velocity profile is determined assuming a solid-body rotation, of which the angular velocity is proportional to D^{-1} . The initial angular velocity is taken from the observed $\frac{\partial}{\partial r}\bar{u}_\theta$ at the centre, upstream of the contraction.
- The normal stresses of which the anisotropy is studied are obtained by integration of the spectrum.
- The RDT calculations have been started at the start of the contraction ($z/D = 0$) using observed anisotropies from ($z/D = -1.8$) and continued arbitrarily until the axial position of the first observations downstream of the contraction ($z/D = 2.4$).

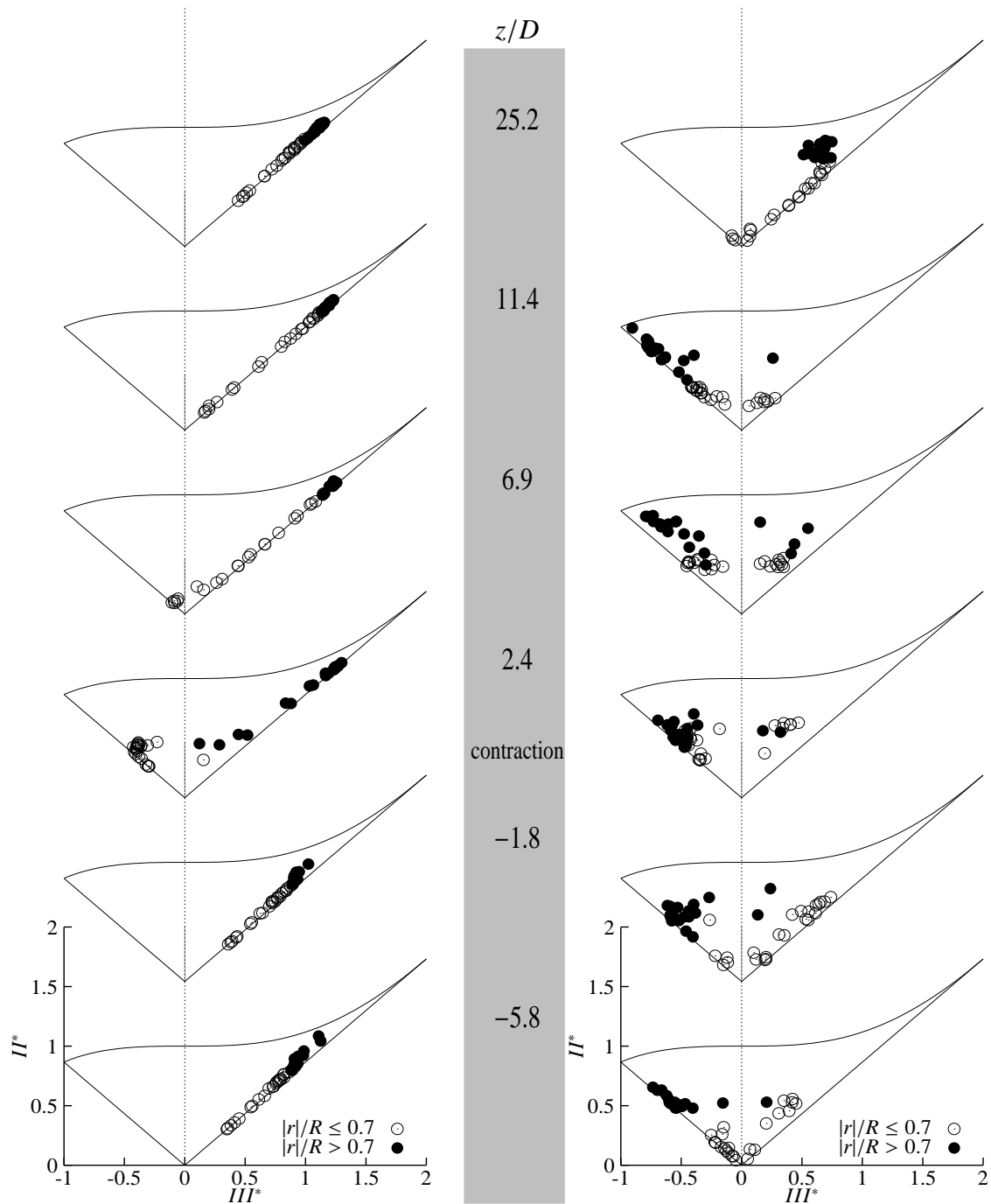


Figure 5.20: Modified Lumley plots for flow without swirl (left) and with swirl (right). $Re_D = 10^5$. Each symbol represents one radial position.

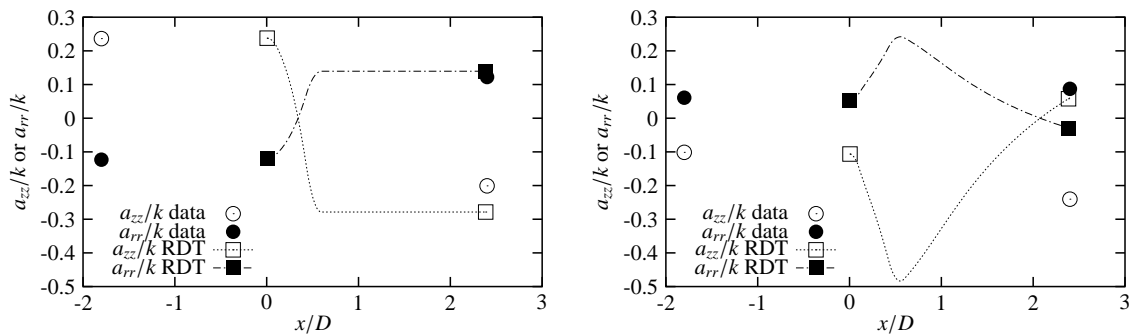


Figure 5.21: Comparison of stress anisotropies at the axis as predicted by RDT, as well as observed values. The observations are indicated by single symbols, whereas the RDT results are indicated with a line, labeled with symbols at start and end. Observations are for $Re_D = 10^5$. The RDT calculations have been started at the start of the contraction ($z/D = 0$) and continued arbitrarily until the axial position of the first observations downstream of the contraction ($z/D = 2.4$). The contraction is located at $0 < z/D < 0.6$.

Figure 5.21 shows the results of the RDT analysis together with the observed stress anisotropies for $Re_D = 10^5$. For the non-swirl case the observations at $z/D = -1.8$ and $z/D = 2.4$ can be assumed to be representative for those at the entrance and exit of the contraction, since in the regions upstream and downstream no strain acts on the turbulence. Then RDT appears to give a good prediction of the anisotropy for the non-swirl case. The RDT analysis clearly shows a_{zz} and a_{rr} change sign due to the axial strain.

For the flow with swirl the situation is more complicated, since then also in the regions upstream and downstream of the contraction a strain is present (due to the swirl). The effect of this strain can be seen clearly in the RDT results downstream of the contraction ($z/D > 0.6$) where the anisotropies continue to change, but in a direction opposite to that *inside* the contraction: there is a tendency to a return to a more isotropic situation. This linear effect of rotation on the anisotropy will certainly be present outside the contraction. However, over distances much larger than the length of the contraction, nonlinear effects will mask this linear effect of rotation. Given the distance of about two pipe diameters between the upstream observations and the entrance, as well as between the exit of the contraction and the downstream observations, the RDT results can be compared to the observations only qualitatively. The effect of the addition of rotation to the axial strain is to slightly diminish the change in anisotropy inside the contraction, when compared to the non-swirl case. This is in accordance with the data of (Leuchter and Dupeuble, 1993). The present data, however, suggest a very strong reduction in the change in anisotropy. This may be attributed to the linear effect of rotation in the region *outside* the contraction (possibly both upstream and downstream). When taking into account the observations downstream of $z/D = 2.4$ however, it becomes clear that downstream of the contraction the linear effect of rotation must be overwhelmed by nonlinear effects: up to $z/D = 6.9$ the anisotropies increase (in an absolute sense), rather than decrease as suggested by the RDT results.

5.3 Analysis of time series data

In this sections two quantities will be discussed that give information about the spatial structure of the turbulence: the one-dimensional spectra and the integral scales.

5.3.1 Spectra

The analysis of the experimental data concludes with a look at the spatial structure of the turbulent velocity field by means of one-dimensional spectra and integral length scales. These spectra have been determined from the raw data gathered (see section 3.3). Only data for $Re_D = 10^5$ will be shown, since the data for Re_D do not show a clear inertial subrange and appear to suffer from ambiguity noise (see 3.1.3) and aliasing (due to deficiencies in the low-pass filter in the trackers, see section 3.3.3).

Figure 5.22 shows the axial development of power spectra at the pipe axis: the one-dimensional u_z -spectrum and u_r -spectrum. The flows without swirl and with swirl will be discussed separately. Although according to Tennekes and Lumley (1972) no inertial subrange is to be expected at this modest Reynolds number, the data suggest that for most stations a region with a slope of the order of $k^{-5/3}$ exists above $kD = 5$. For the non-swirling flow the effect of the contraction is mainly that u_z fluctuations are suppressed at large scales (small k) and fluctuations in u_r are enhanced at large scales, while being suppressed at small scales. These effects of the contraction have disappeared again at $z/D = 25.2$. Furthermore, between $z/D = -1.8$ and $z/D = 2.4$, the values of F_{zz} at the origin decreases whereas the value of F_{rr} increases. Since $F_{ii}/\overline{u'_i u'_i}$ is proportional to the integral length scale L (Tennekes and Lumley, 1972), L_{rr} increases and L_{zz} decreases (see 2.3.2 on page 26).

For the data of the swirling flow the spectra upstream of the contraction exhibit a slope steeper than $-5/3$, even suggesting the two-dimensional limit of k^{-3} . Downstream of the contraction the data suggest a $-5/3$ slope. Another feature of the downstream spectra is that the large-scale part of the spectrum has shifted to smaller wave numbers. A related phenomenon is that the values for F_{ii} at the origin are larger than those for the non-swirling flow. Thus L will be larger for the swirling flow compared to the non-swirling flow (see below). A final remark is that the exchange of energy between $\overline{u'_z u'_z}$ (minus) and $\overline{u'_r u'_r}$ (plus) as observed in the non-swirling flow is not clearly present in the swirling flow.

Figure 5.23 shows the one-dimensional spectra at the radial location $r/R = 0.9$ for u_z , u_r and u_θ . Again the non-swirling and swirling flow will be dealt with separately. The non-swirling data show a clearer inertial subrange than for the pipe-axis data in figure 5.22 but above a higher wavenumber ($kD > 20$ upstream of the contraction, $kD > 5$ downstream). The effect of the contraction is similar for all three spectra: small scales are suppressed and large scales are enhanced. The effect is strongest for u_θ . At the axial position $z/D = 11.4$ the spectra have recovered already from the disturbance of the contraction.

The swirling flow spectra do not show a region with a spectral slope of -3 , but rather have an inertial subrange with $k^{-5/3}$. This suggests that at $r/R = 0.9$ is not so much influenced by rotation but rather behaves as a normal shear flow. The effect of the contraction on enhancement of large scales, relative to small scales is similar as for the non-swirling case, and again the effect of the u_θ spectrum is largest. The shift of the large-scale part of the spectrum to smaller wave numbers

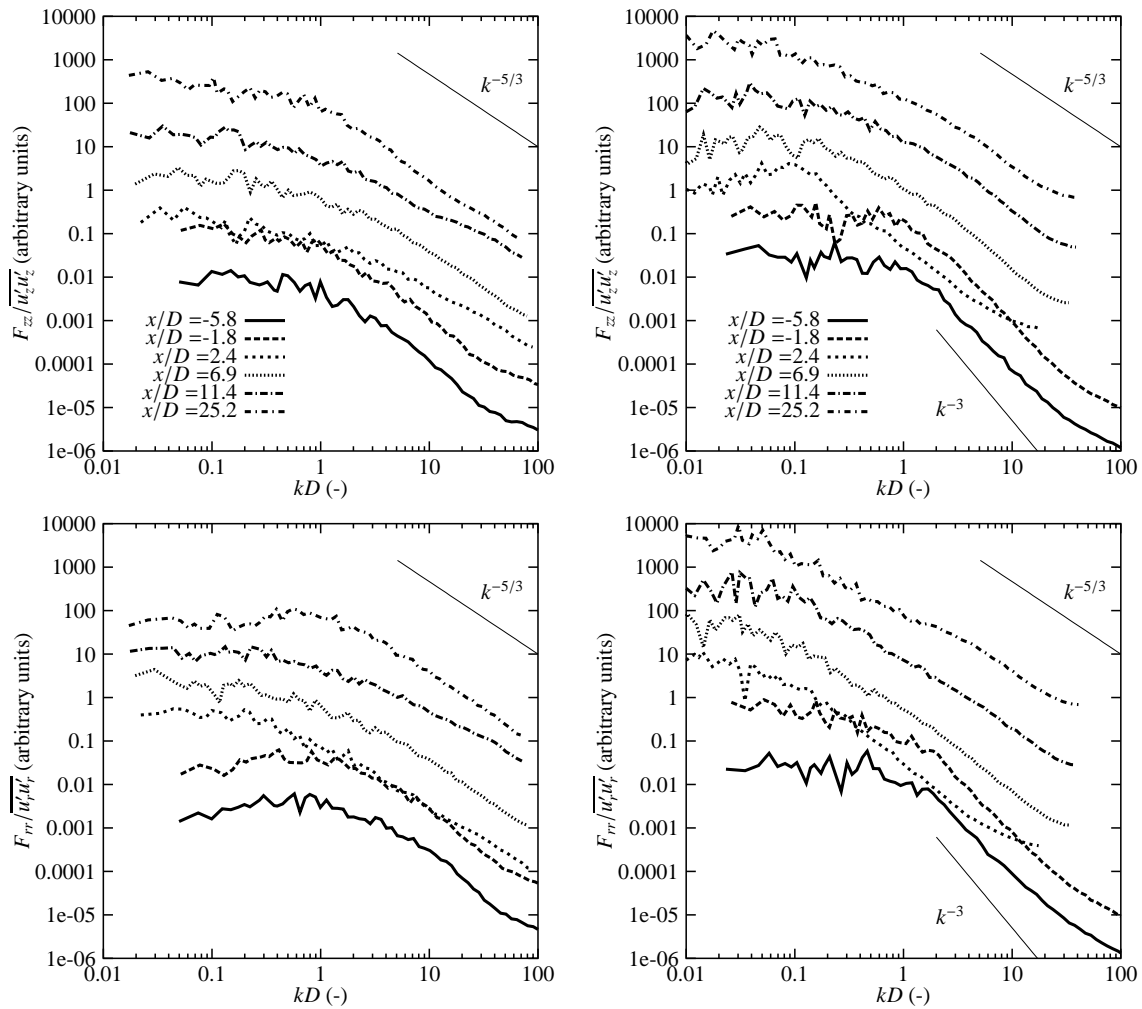


Figure 5.22: One-dimensional spectra at the pipe centreline: u_z -spectrum (top) and u_r spectrum (bottom), without swirl (left) and with swirl (right). Only data for Re_D are shown. The spectra for axial positions $z/D > -5.8$ are shifted upward by a factor of 10 for each axial position. The wavenumber has been determined from the frequency and the mean axial velocity. Normalisation of k has been done with the local pipe diameter. The spectra have been averaged over logarithmically spaced bins.

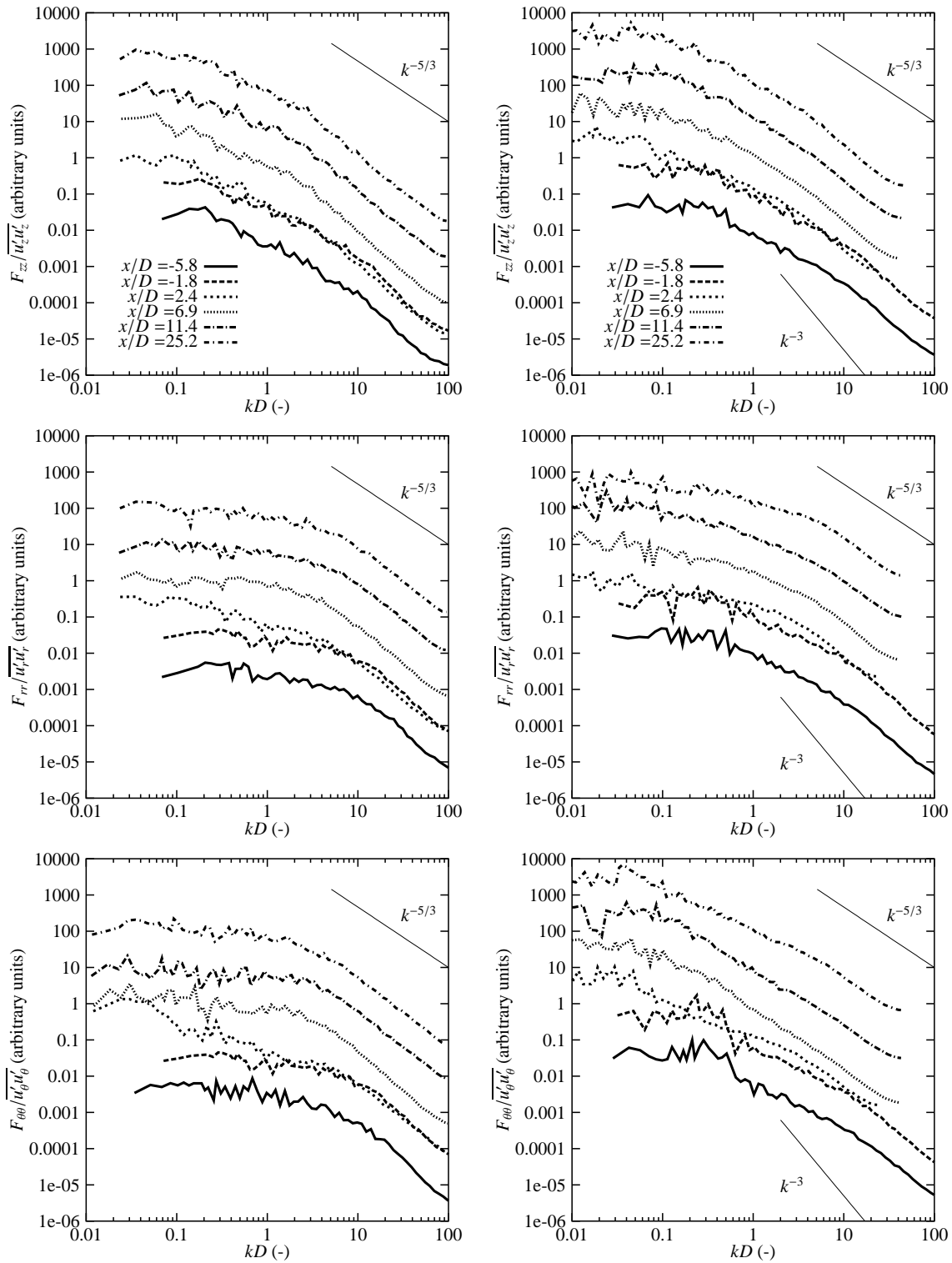


Figure 5.23: One dimensional spectra $r/R = 0.9$: u_z -spectrum (top) and u_r -spectrum (middle) and u_θ -spectrum (bottom), without swirl (left) and with swirl (right). The u_z and u_r spectra have been obtained with the LDA optics displaced vertically from the pipe axis, whereas the u_θ have been measured with the LDA displaced horizontally (along its optical axis). For further information see caption of figure 5.22.

is similar to what happens in the swirling flow spectra at the pipe axis.

A difficulty in the interpretation of the swirling flow spectra in figure 5.23 is that the spectra of u_z and u_θ are a combination of longitudinal and transverse spectra: the longitudinal direction is along the mean flow direction, whereas the velocity components are parallel and perpendicular to the pipe axis. The angle between mean flow direction and axial direction ranges from 40° to 20° at $r/R = 0.9$ (see figure 5.14). Therefore, the spectra have been recomputed with velocity components rotated in the direction of the mean flow. The results, however, hardly differ from the spectra shown in figure 5.23 and are not shown therefore.

5.3.2 Integral scales

Another measure of the spatial structure of the turbulent field is the integral length scale, L , of a given velocity component (or scalar, if applicable).

Formally the integral length scale equals the integral of the autocorrelation function⁶. It is a measure of the largest scales present in the turbulence. When using one-point measurements one can only determine the integral length scale in the direction of the mean flow. In a non-swirling flow the integral length scale for u_z will be a longitudinal length scale, whereas the scale for u_r and u_θ will be a transverse length scale. In case of swirl the situation is less clear. Then only the integral scale for u_r will be a real transverse scale, whereas the integral scales for u_z and u_θ will be a mix of longitudinal and transverse. Here, the integral length scale will be estimated from the integral time scale by converting the time lag into a spatial lag using the mean *axial* (not *streamwise*) velocity.

Figure 5.24 shows the axial development of the integral length scales at the pipe axis. The effect of the contraction is to decrease L_{zz} and to enhance the two transverse length scales. This is in accordance with results from rapid distortion theory. The length scales recover surprisingly quickly from the distortion due to the contraction. For the swirling flow the length scales upstream of the contraction are nearly isotropic (as are the Reynolds stresses as observed earlier). The effect of the contraction on L_{rr} and $L_{\theta\theta}$ is much larger than in the non-swirling case. The length scales have grown up to 1.8 times the pipe diameter. Furthermore, L_{zz} increases rather than decreases.

In figure 5.25 the length scales are shown for a radial position $r/R = 0.9$. For the non-swirling flow L_{rr} and $L_{\theta\theta}$ behave qualitatively the same as at $r/R = 0$. On the other hand, L_{zz} *increases* due to the contraction whereas it *decreases* at the centreline. For the swirling flow however, $L_{\theta\theta}$ and L_{zz} are similar in the near wall region. This can be understood from the fact that both \bar{u}_z and \bar{u}_θ exhibit strong shear in the near-wall region. This also explains the fact that the axial development of both $L_{\theta\theta}$ and L_{zz} in the swirling flow is similar to the development of L_{zz} in the non-swirling flow. The similarity between $L_{\theta\theta}$ and L_{zz} might also be due to the method of analysis: the length scale is in the direction of the mean flow, whereas the velocity components are not exactly in streamwise and cross-stream direction. However, in the discussion of spectra in the previous section it was observed that this is a small effect.

⁶By definition, however, the autocorrelation function in one-point measurements integrates to zero, resulting in zero integral length scale. Therefore the autocorrelation function is integrated between zero time-lag and the smallest time-lag until where the autocorrelation function changes sign.

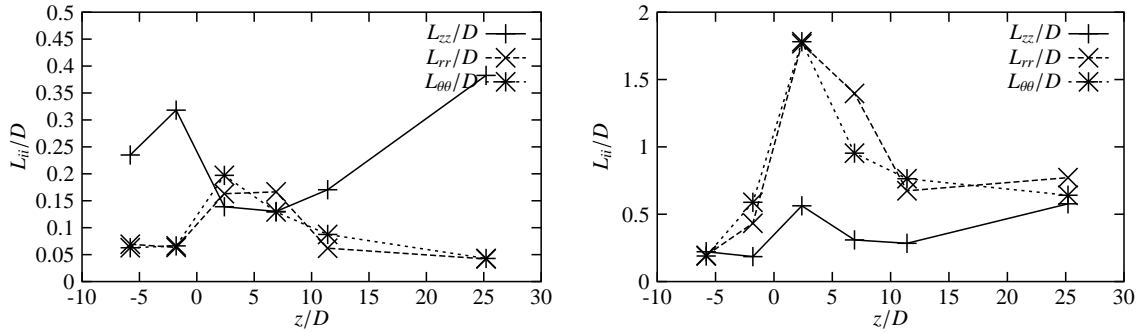


Figure 5.24: Axial development of integral length scales of the normal stresses for $Re_D = 10^5$: non-swirling flow (left) and swirling flow (right). The data refer to $r/R = 0$. The length scales have been scaled with the *upstream* pipe diameter. Note the difference in vertical scale between the two plots. The lines are drawn only to clarify the relationship between different points.

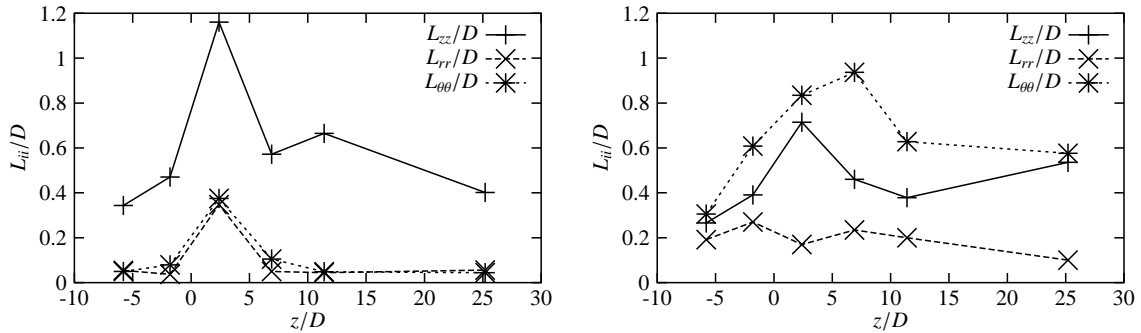


Figure 5.25: Axial development of integral length scales of the normal stresses for $Re_D = 10^5$: non-swirling flow (left) and swirling flow (right). The data refer to $r/R = 0.9$. The lines are drawn only to clarify the relationship between different points.

5.4 To conclude

In the previous sections the experimental data have been analysed in a variety of ways and it is well possible to get lost in the overwhelming amount of results. Here an attempt will be made to assemble a clear picture of the flow under consideration. The results for the flow without swirl and with swirl will be discussed separately.

5.4.1 Axial strain without swirl

The mean axial velocity is transformed from a profile representative of fully developed pipe flow to a flat profile as in the entrance region of a pipe. Also the normal stresses are nearly uniform across the pipe cross-section, and the shear stress $\overline{u'_r u'_z}$ is small except near the walls. The effect of the axial strain on the anisotropy of the normal stresses is to reverse the signs of the anisotropies of $\overline{u'_z u'_z}$ on one hand and $\overline{u'_r u'_r}$ and $\overline{u'_\theta u'_\theta}$ on the other. This effects is well described by linear theory

(RDT).

Approximately 40 pipe diameters downstream of the contraction (downstream pipe diameters) the profiles of the mean velocity and the normal stress have returned to their fully developed shape. The shear stress $\overline{u'_r u'_z}$ has not yet completely relaxed at that axial position, however. The relaxation toward the fully developed profiles occurs first near the wall. Further downstream, the region of the pipe cross-section affected by this development grows toward the pipe axis.

5.4.2 Axial strain with swirl

The effect of the axial strain on the profiles of \overline{u}_z and \overline{u}_θ near the pipe axis is in accordance with the inviscid analysis of Batchelor (1967): \overline{u}_z develops a bump and \overline{u}_θ becomes slightly curved rather than straight. The swirl decay rate seems not to change dramatically by the axial strain. The swirling flow is not skewed for large part of the near-wall region, so there are no indications for a three-dimensional boundary layer.

Upstream of the contraction the Reynolds stress tensor (at the pipe axis) in the swirling flow is more isotropic than that in the non-swirling flow. The effect of the axial strain on the stress anisotropy is weaker than for the non-swirling flow. This is –qualitatively– predicted by RDT theory. Directly downstream the anisotropies of the stress tensor are very similar for the swirling and non-swirling flow, but further downstream they diverge again. At the position, furthest downstream from the contraction, there is a clear distinction between the two Reynolds numbers: for the lower Reynolds number, the stress anisotropy is close to that for the non-swirling flow, whereas for the high Reynolds number, there is a large difference between swirling and non-swirling flow. This may have two reasons: the swirl decays faster for the lower Reynolds number, and the travel time from the contraction is a factor of 5 longer for the lower Reynolds number. The character of the stress tensor throughout the pipe cross section differs considerably between the non-swirling and swirling flow. In the non-swirling flow the turbulence is nearly axisymmetric at the vast majority of axial and radial positions: the stress tensor has one *major* axis. In the swirling flow, the turbulence is not axisymmetric at most locations. Near the wall, the tensor is pancake-shaped (two major axes), near the pipe axis there is one major axis.

The effect of axial strain on the structure of the turbulence is that in the swirling flow much energy is transferred to larger scales, especially for u_r and u_θ . This translates into large integral length scales.

All results for the swirling flow suggest that a clear distinction can be made between a core region (roughly $r/R < 0.7$) and an outer region. In the core rotational effects play an important role. On the other hand, the near wall region behaves like a normal shear flow, despite the large angle between mean flow and axial direction.

6

Results of numerical simulations

In this chapter the results of the simulations will first be compared with the measured data. Besides, additional analyses will be made, focusing on the terms in the budgets of Reynolds stresses and on what happens *within* the contraction. Details on the setup of the simulations can be found in section 4.3.

6.1 Validation of the LES results

In this section the LES results will be confronted with the results from the laboratory experiment, discussed in chapter 5. The results for the flow without and with swirl will be dealt with separately. Two measurement stations of the experimental setup fall within the domain of the simulation, viz. those at $z/D = -1.8$ and 2.4 . The data at those two locations will be used for the model validation.

6.1.1 A note on the presentation of results

In the intercomparison of laboratory data and simulation results a number of discrepancies need to be resolved:

- For the laboratory measurements, the radial coordinate is made dimensionless with the pipe radius, whereas in the model the pipe diameter is used. In the present chapter all radial coordinates will be normalised with the *local* pipe radius.
- The velocities in the laboratory measurements are originally normalised with the local bulk velocity (see previous chapter), whereas in the model the friction velocity of the pipe section upstream of the contraction is used. In the presentation of the data, all velocities will be normalised with the *local* friction velocity. Since no friction velocity data are available for the laboratory data, the ratio between bulk velocity and friction velocity from the simulation is used. This implies that an error in the ratio U_{bulk}/u_* in the simulation, results in an incorrect representation of the LDA data. In fact, the normalisation used here is equivalent to a normalisation of both simulation results and LDA data with the bulk velocity (obtained from the present presentation by multiplying velocities with the ratio u_*/U_{bulk} from the simulation). At both axial positions the velocities and stresses are normalised with the *local* model friction velocity.
- In order to make laboratory data and measurements comparable, the simulation results of Reynolds stresses include both the resolved and the sub-grid scale stresses. To show the contribution of the subgrid stress to the total stress, the subgrid contribution is also shown separately. The sub-grid contribution to the normal stresses consists of the anisotropic part

of the stress (taken into account by the sub-grid scale stress model) and the isotropic part. The latter is non-existent in the model, since it has been lumped with the dynamic pressure (see equation 4.6). For the presentation of the normal stresses, the isotropic part has been determined from the sub-grid kinetic energy (E_{SGS}), using equation 4.14.

- Since the simulation data are averaged over a full circumference of the pipe, only data for $0 < r/R < 1$ are available. Therefore the measurement data are plotted against $|r/R|$, rather than r/R . As a consequence, two datapoints will appear for each radial position $|r/R|$, viz. one for $r < 0$ and one for $r > 0$.
- The experimental data are accompanied by estimates of the error (or tolerance) in the data (although in some cases the error bars are hardly visible). For the simulation data a similar error analysis has been made. The resulting range is indicated by plotting two lines: one that gives the upper bound of the simulated value and one that gives the lower bound (95% tolerances are used). In many cases the three lines can not be discerned. For details on the error estimates see appendix A.
- The LES data for $z/D = -1.8$ are obtained from the model with periodic boundary conditions and constant radius, whereas the data downstream of the contraction ($z/D = 2.4$) are taken from the model with varying pipe diameter, as described in section 4.2. The model domain extended from over $-1.8D < z < 4.2D$. Consequently, of all the experimental data presented in chapter 5, only the data at $z = -1.8D$ and $z = 2.4D$ can be used for validation.

6.1.2 Flow with axial strain

In this section the results of the LES of the flow with axial strain but without swirl will be presented. Table 6.1 summarises the key features of the simulation. Some noteworthy facts are:

- The bulk velocity attained upstream of the contraction (and consequently downstream) is very close to the value of the laboratory experiment.
- The turbulent Reynolds number increases strongly downstream of the contraction due to the large increase in the wall friction (and thus u_*). Since the flow is an axially inhomogeneous flow, the value quoted is valid only for the given axial location ($z/D = 2.4$) in the model domain (and will probably decrease further downstream).
- Due to the increase in u_* , the resolution in terms of viscous wall units decreases (i.e. becomes coarser). Thus, despite the fact that downstream of the contraction the gridcells are smaller, effectively the resolution decreases.

The results for the mean flow, as well as the turbulent stresses are shown in figures 6.1 to 6.6. The simulated profiles of the mean axial velocity match the measurements very closely (i.e. are indistinguishable) upstream of the contraction (figures 6.1 and 6.2). Downstream of the contraction the match is close, but the tolerance intervals do not overlap. Upstream of the contraction the turbulent stresses are well represented by the model. The only exception is the slight underprediction of $\overline{u'_\theta u'_\theta}$ for $r/R > 0.9$. This near-wall discrepancy in $\overline{u'_\theta u'_\theta}$ seems to be attributable both to the grid size and the grid aspect ratio (see appendix F). The stress profiles downstream of the contraction are less favourable. $\overline{u'_r u'_r}$ is overpredicted over the entire cross-

Table 6.1: Features of the simulation of flow through contraction without swirl.

quantity	straight	contraction	
		$z/D = -1.8$	$z/D = 2.4$
$\langle u_* \rangle$	1.00	1.00	3.00 ^a
$\langle U_{bulk} \rangle$	17.00	17.00	52.06
Re	1150	1150	3450 ^b
Re_{bulk}	19550	19550	34052
time between fields	0.1	0.05	idem
number of fields	50	100	idem
average timestep ^c	1.210^{-4}	0.7910^{-4}	idem
y_{min}^+	0.91	0.91	1.56 ^d
Δr^+ (r -spacing in wall units)	1.84-24.4	1.84-24.4	3.15-41.8 ^d
$\left(\frac{1}{2}D\Delta\theta\right)^+$ (θ -spacing in wall units)	16.1	16.1	27.6 ^d
Δz^+ (z -spacing in wall units)	25.7	25.7	77.1 ^d
\tilde{N}_L (see section 4.1.3)	118	118	73.3 ^e

^aIn terms of quantities upstream of contraction. Thus, $u_*(z = 2.4D) = 3.00u_*(z = -1.8D)$.

^bThis is a *local* turbulent Reynolds number, u_*D/ν with *local* u_* and D .

^cIn $t^* = tu_*/D$.

^dUsing the *local* u_* .

^e \tilde{N}_L is effective number of eddies of smallest scale that are resolved (see page 67). Using the local macro length scale which is the local pipe diameter. And using Δz , the average Δr and $\left(\frac{1}{4}D\Delta\theta\right)$ in 4.37 to determine the effective grid spacings.

section (see figure 6.4). For $r/R < 0.8$ the LES results and the data are nearly within each others tolerances, but for $r/R > 0.8$ the model significantly overpredicts $\overline{u'_r u'_r}$. The $\overline{u'_\theta u'_\theta}$ stress (figure 6.5) is well represented by the LES model, again except for the near wall region where $\overline{u'_\theta u'_\theta}$ is too low. Furthermore, there is a local maximum near the pipe axis, which is absent in the data. This local maximum is purely due to the subgrid stress. This maximum in the subgrid contribution is also present in the $\overline{u'_r u'_r}$ stress and to a lesser extent in $\overline{u'_\theta u'_\theta}$. Upon closer examination, it appears that this large sub-grid contribution only occurs downstream of the contraction, and is solely due to the *isotropic* part of the normal SGS-stresses. This isotropic contribution is *estimated* diagnostically using equation 4.14. In figure 6.3 it can be seen that the LES model shows high levels of axial velocity fluctuations too far from the wall, which is equivalent to a too thick wall layer (although the $\overline{u_z}$ -profile gives no reason for this suspicion). Finally, the $\overline{u'_r u'_z}$ shear stress (figure 6.6) is described well by the LES model at the upstream position. For the downstream position the stress is overpredicted for $r/R > 0.8$, which is consistent with the too high values for $\overline{u'_z u'_z}$ and $\overline{u'_r u'_r}$.

The temporal spectra at the centreline of model and laboratory flow are compared in figures 6.7 and 6.8 (in fact the lab measurements have been taken *at* the pipe axis, whereas the LES results refer to the grid point *closest* to the pipe axis). The frequencies have been normalised with $D/\overline{u_z}$ and the spectral densities have been normalised with the relevant velocity variance.

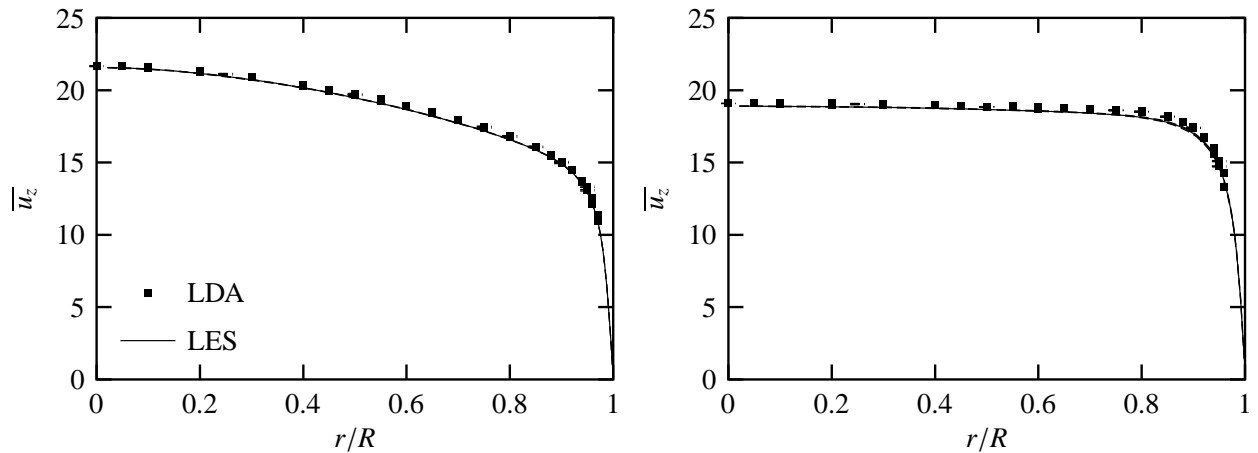


Figure 6.1: Mean axial velocity at $z = -1.8D$ (left) and $z = 2.4D$ (right) for flow without swirl. The velocities have been scaled with the local friction velocity. The radial position has been normalised with the local pipe radius.

The experimental data suggest a very short inertial subrange for the u_r -spectra and u_z -spectra. This limited inertial subrange is due to the low Reynolds number. The LES spectra also show a short inertial subrange. Furthermore, the LES-spectra fall off for *higher* frequencies much more rapidly than the experimental spectra, due to the dissipation of the sub-grid model. As a result the spectral values at *lower* frequencies are somewhat higher. Downstream of the contraction the LES spectra have a steeper slope than the experimental spectra (which again have a somewhat longer inertial subrange than the LES results). This shift of energy to lower frequencies is an indication of a growth of the axial length scales (see section 2.3.2 and 2.4.2). The LES results show more clearly than the experimental data that the time scale for u_z becomes smaller than that for u_r : the peak in the spectrum occurs at $fD_{local}/\bar{u}_z = 0.4$ and 0.12 , respectively (see also 5.3.2).

6.1.3 Flow with swirl and axial strain

Table 6.2 summarises the features of the simulation of the swirling flow. Before discussing the results of the simulation *with swirl*, some features of the simulation will be discussed.

- In the simulation without swirl it was found that fields became statistically independent well within $0.1 t^*$. Therefore, the sampling interval for fields was lowered to 0.05 for the straight pipe model, and 0.025 for the contraction model (which is computationally much more expensive).
- For the simulation with swirl the average time step is smaller than for the simulation without swirl.

The first notable difference with the flow *without* swirl is that the bulk velocity is 12% lower. Apparently, the swirl introduces extra friction resulting in a lower bulk velocity at a given axial

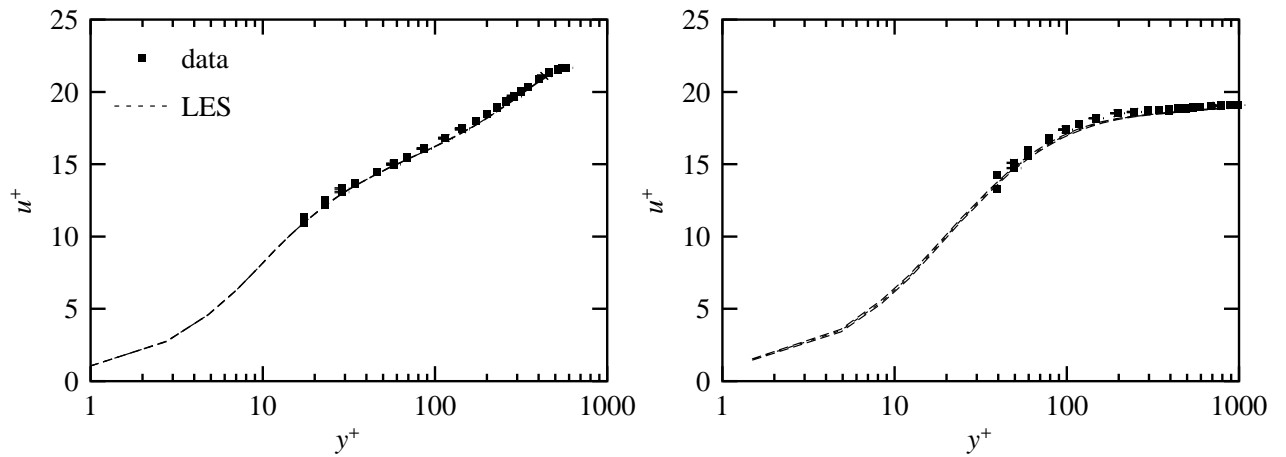


Figure 6.2: Mean axial velocity at $z = -1.8D$ (left) and $z = 2.4D$ (right) for fbw without swirl plotted in wall coordinates. The wall coordinates have been calculated with the local friction velocity.

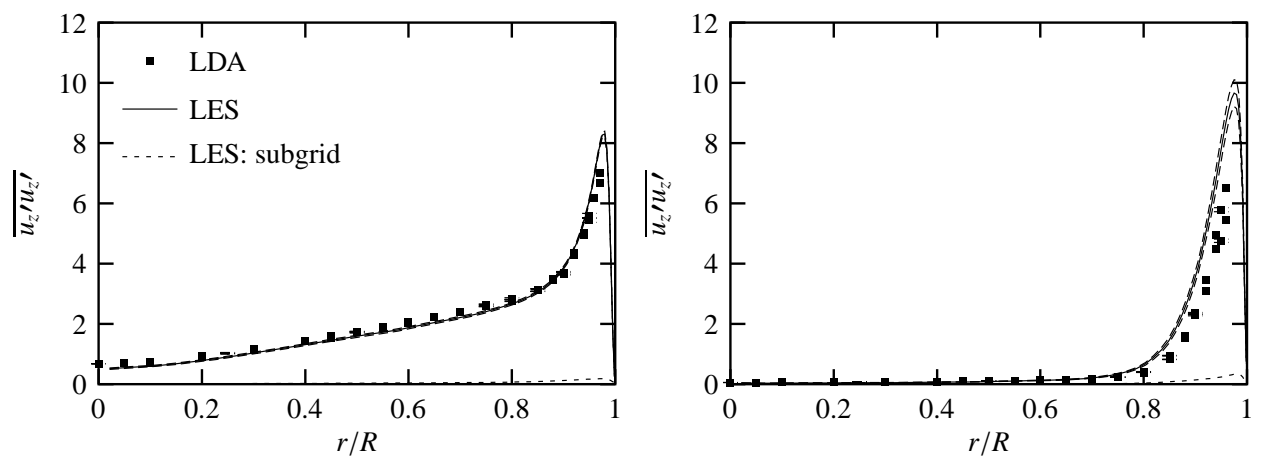


Figure 6.3: Comparison of LES-results to laboratory data for fbw without swirl: $\overline{u_z' u_z'}$ at $z = -1.8D$ (left) and $z = 2.4D$ (right). For further information, see figure 6.4.

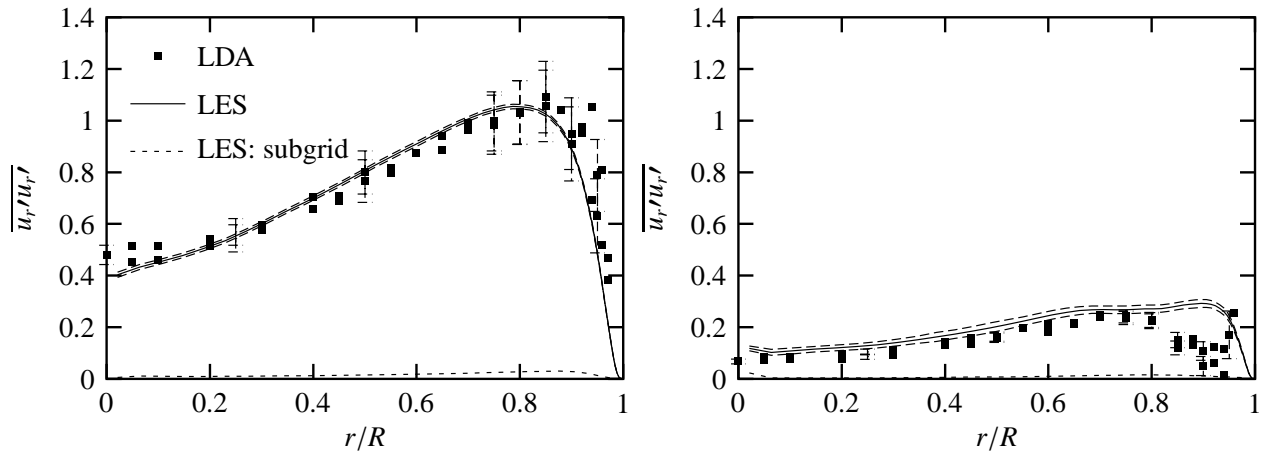


Figure 6.4: Comparison of LES-results to laboratory data for fbw without swirl: $\overline{u'_r u'_r}$ at $z = -1.8D$ (left) and $z = 2.4D$ (right). For notes on normalisation, see figure 6.1. The 'LES' result is the sum of resolved stress and subgrid stress. The subgrid contribution is also shown separately.

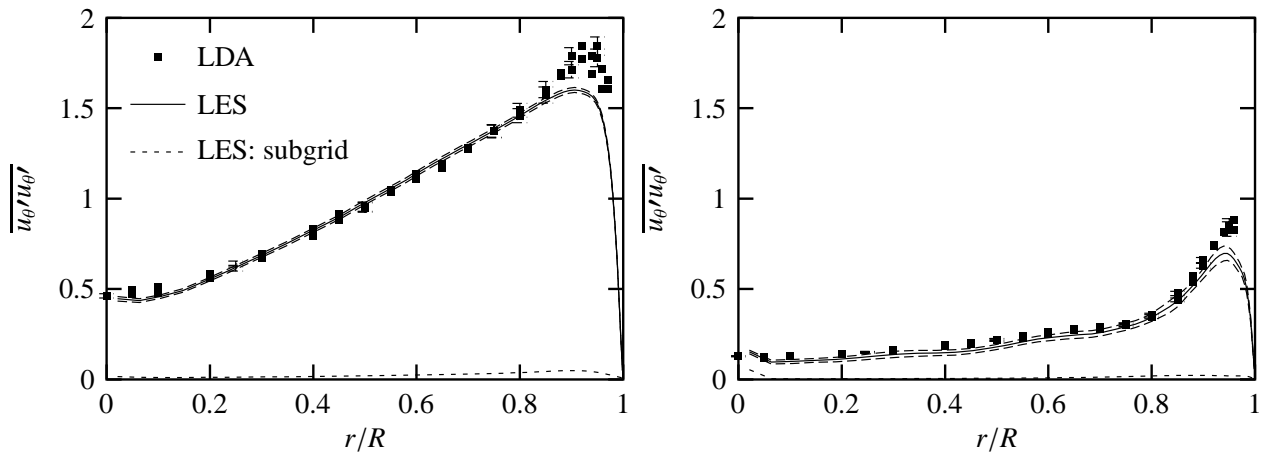


Figure 6.5: Comparison of LES-results to laboratory data for fbw without swirl: $\overline{u'_\theta u'_\theta}$ at $z = -1.8D$ (left) and $z = 2.4D$ (right). For further information, see figure 6.4.

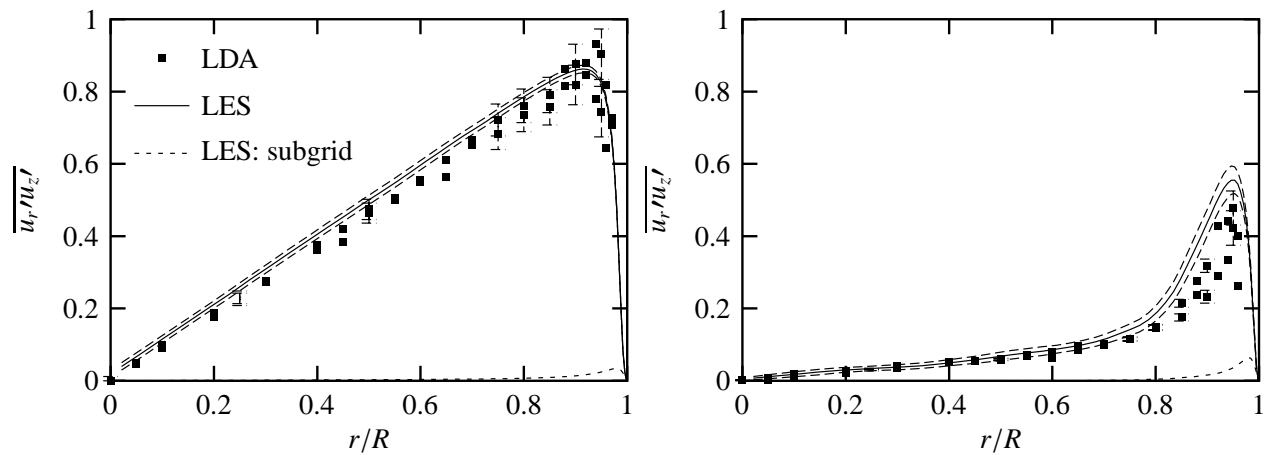


Figure 6.6: Comparison of LES-results to laboratory data for flow without swirl: $\overline{u_r' u_z'}$ at $z = -1.8D$ (left) and $z = 2.4D$ (right). For further information, see figure 6.4.

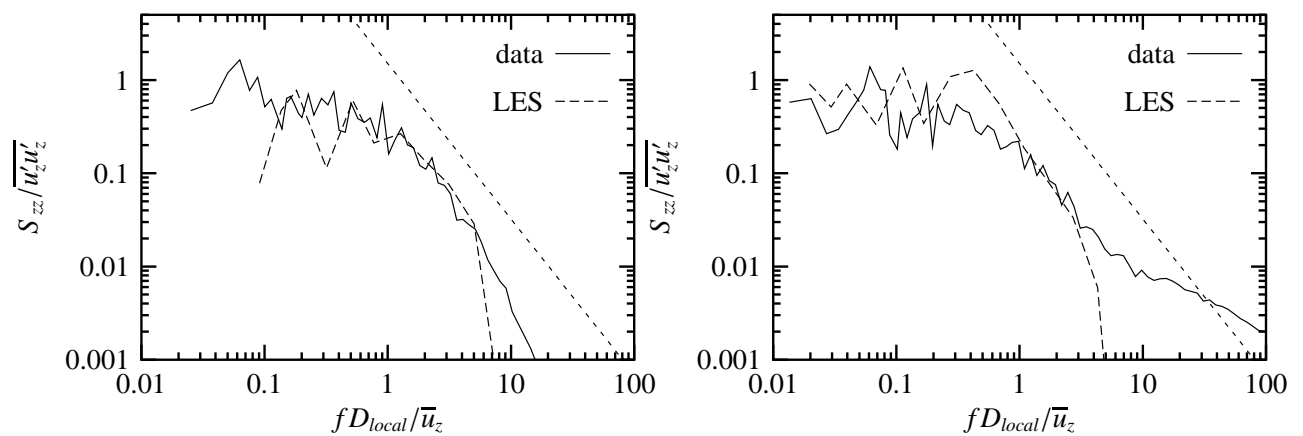


Figure 6.7: Comparison of LES-results to laboratory data for flow without swirl: Temporal power spectra of u_z at/near the pipe axis ($r/R = 0$ for lab measurements, $r/R = 0.021$ for LES) at $z = -1.8D$ (left) and $z = 2.4D$ (right). Also shown is the inertial subrange slope.

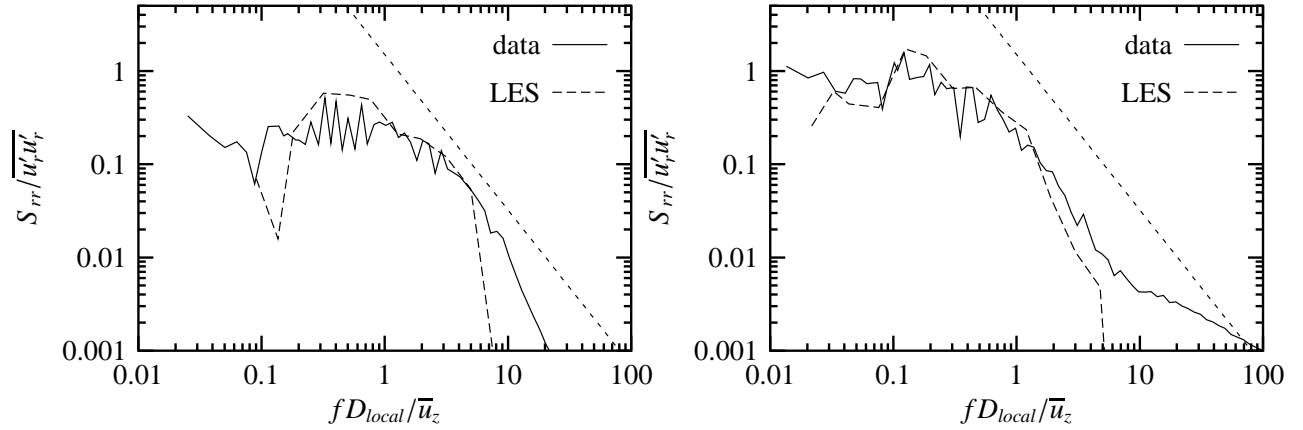


Figure 6.8: Comparison of LES-results to laboratory data for flow without swirl: Temporal power spectra of u_r at/near the pipe axis ($r/R = 0$ for lab measurements, $r/R = 0.042$ for LES) at $z = -1.8D$ (left) and $z = 2.4D$ (right). Also shown is the inertial subrange slope.

Table 6.2: Features of the simulation of flow through contraction with swirl (swirl number at inflow is 0.4). See also table 6.1 for some extra information.

quantity	straight	contraction	
		$z = -1.8D$	$z = 2.4D$
$\langle u_* \rangle$	1.00	1.00	3.13 ^a
$\langle U_{bulk} \rangle$	14.98	14.98	45.87
Re	1150	1150	3600 ^b
Re_{bulk}	17227	17227	30147
time between fields	0.05	0.025	idem
number of fields	50	100	idem
average timestep ^c	1.010^{-4}	0.510^{-4}	idem
y_{min}^+	0.91	0.91	1.63 ^d
Δr^+	1.84-24.4	1.84-24.4	3.29-43.6 ^d
$(\frac{1}{2}D\Delta\theta)^+$	16.1	16.1	28.8 ^d
Δz^+	25.7	25.7	80.4 ^d
\tilde{N}_L	118	118	73.3 ^e

^aIn terms of quantities upstream of contraction.

^bThis is a local turbulent Reynolds number, $u_* D / \nu$ with local u_* and D .

^cIn $t^* = t u_* / D$.

^dUsing the local u_* .

^e \tilde{N}_L is effective number of eddies of smallest scale that are resolved (see page 67). Using the local macro length scale which is the local pipe diameter. And using Δz , the average Δr and $(\frac{1}{4}D\Delta\theta)$ in 4.37 to determine the effective grid spacings.

forcing. Given the fact that in the simulation the Reynolds number based on u_* is prescribed, the *bulk* Reynolds number is lower than for the flow without swirl. Consequently, there is a 14% difference between the simulated bulk Reynolds number and the Reynolds number in the laboratory experiment.

Figure 6.9 and 6.10 show the profiles of the mean axial velocity. Upstream of the contraction the simulation shows a too pronounced bump near the pipe axis, whereas downstream of the contraction the results from simulation and experiment match well, with the simulation giving slightly too low values. The small bump in the measured upstream profiles is probably the result of the fluid that went through the central body of the swirl generator and remained isolated from the surrounding fluid by the strong rotation. In the simulation, however, all deviations from a smooth axial velocity profile are due to the tangential forcing.

The mean tangential velocities (figure 6.11) show a perfect agreement between experiment and simulation in the section upstream of the contraction. This agreement is of course due to the tangential forcing method used (see section 4.2.5). Downstream of the contraction, the simulated mean tangential velocity is too low by about 20%. Analysis of the swirl number decay (figure 6.43) suggests that this is due to a too high decay rate upstream of the contraction.

The results for the normal stresses are given figures 6.12 to 6.14. The general tendency for the normal stresses is that the simulation overestimates the normal stresses throughout the pipe cross-section, except for $\overline{u'_r u'_r}$, at $z = -1.8D$, where the overestimation is restricted to the vortex core. A plausible cause for this mismatch –given to reasonable match of the mean velocities– is the fact that the experimental data have been multiplied with the bulk velocity from the simulation to obtain scaling with u_* . Thus any error in U_{bulk}/u_* in the simulation is translated into a difference in the scaling between simulation results and experimental results. Since no experimental u_* data are available, the LDA data can not be normalised with the *real* u_* to check this assertion. Another point to note is that $\overline{u'_r u'_r}$ and $\overline{u'_\theta u'_\theta}$ are not equal at the centre line whereas they should be. Apparently, $\overline{u'_\theta u'_\theta}$ suffers from fluctuations (wiggles) due to the small tangential grid spacing in the centre (in the non-swirling case there was also a cusp for $z/D = 2.4$ but that was due to the SGS-term).

Finally, the results for the shear stresses will be discussed (see figures 6.15 to 6.17). The LES results for the $\overline{u'_r u'_z}$ stress do not show the negative values in the vortex core as given by the experimental data. Instead, the $\overline{u'_r u'_z}$ -profile is very similar to the straight profile in a non-swirling flow. Apparently, the $\overline{u'_r u'_z}$ -stress is mainly determined by the axial forcing which was kept independent of r , as in the case of the non-swirling flow. The profile for $z = 2.4D$ shows a similar deviation of $\overline{u'_r u'_z}$ from the experimental data. The simulation results for $\overline{u'_r u'_\theta}$ show qualitative agreement with the data, at both axial positions. At $z = -1.8D$ the LES results are too high, which seems consistent with the results for the normal stresses. At $z = 2.4D$ the tolerances are so large that data are within the tolerance interval of the LES results for a large part of the cross-section. But the simulation results themselves (i.e. the central line of the three LES-lines) do correspond quite well with the data for $r < 0.25R$ (near zero shear stress) and $r > 0.8R$ (transport of tangential momentum toward the wall). The simulation results for the $\overline{u'_z u'_\theta}$ -stress show qualitative agreement with the data for $z = -1.8D$ but even *quantitative* agreement for the station downstream of the contraction. For the upstream station only the profile in the vortex

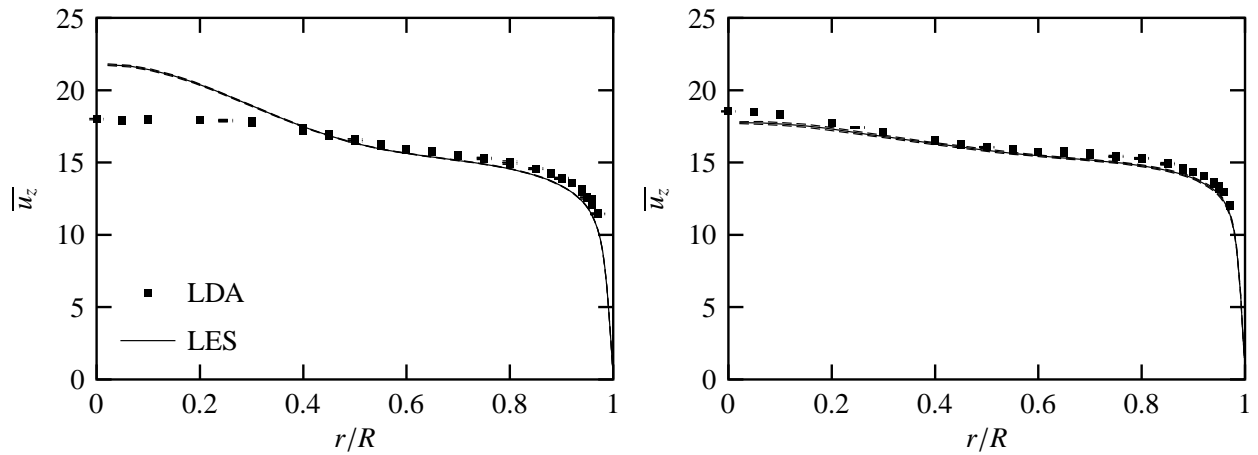


Figure 6.9: Mean axial velocity at $z = -1.8D$ (left) and $z = 2.4D$ (right) for flow with swirl. The velocities have been scaled with the local wall shear stress. The radial position has been normalised with the local pipe radius.

core is not represented correctly.

From the results for $z = -1.8D$ it can be concluded that the tangential forcing method is able to produce a swirling flow that qualitatively mimics the flow to be simulated. However, the details of the profiles of the mean axial velocity profile, as well as the shear stresses, are not correct. Especially, the negative value for $\overline{u'_r u'_z}$ for $r/R < 0.5$ is not represented in the simulation. It is not surprising that there is disagreement between model and data with respect to the details of the flow in the core. Since those details originate from the region directly downstream of the swirl generator, they can not be reproduced by a forcing that is local and axially homogeneous.

Another point to note is that the tolerance intervals for the swirling flow are larger than for the flow without swirl. This is mainly due to the increased integral time scales in the vortex core and an increase in the variance levels of the variable under consideration (see equation (A.12)). Especially for the statistics at $z = 2.4D$ the tolerances for the shear stresses become very large. The choice to reduce the sampling interval relative to the non-swirling flow has been counter-productive in this sense.

Figures 6.18 and 6.19 show a comparison between data and simulation results for the temporal power spectra for $r = 0$ (in fact the lab measurements have been taken *at* the pipe axis, whereas the LES results refer to the grid point *closest* to the pipe axis). For all velocity components and both axial positions the agreement is remarkable. The LES spectra correctly show the shift toward larger scales for the u_r and u_θ spectra (when compared to the flow without swirl). The shift to larger scales is much more pronounced in u_r than in u_z (see also section 5.3.2).

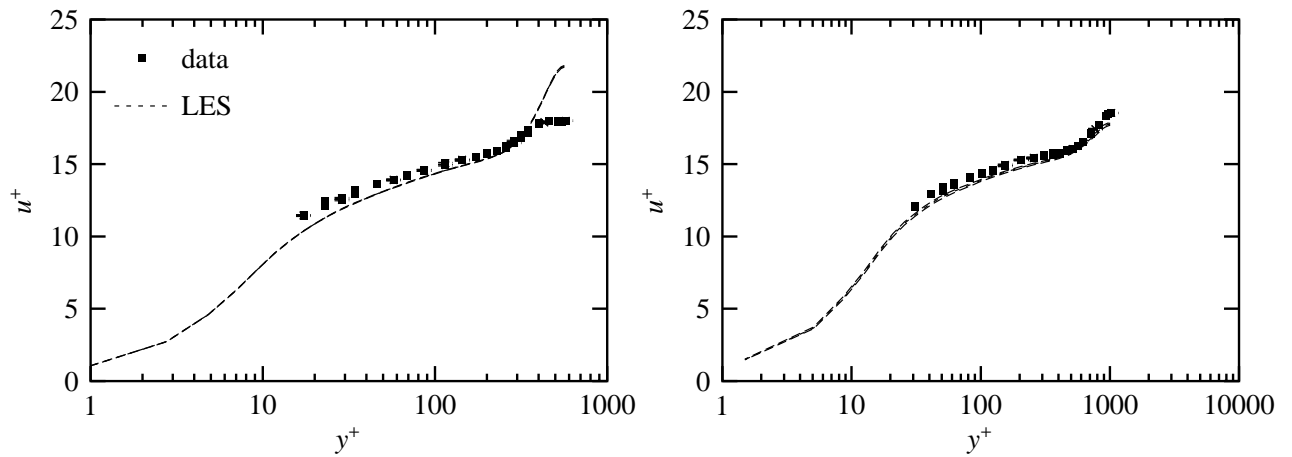


Figure 6.10: Mean axial velocity at $z = -1.8D$ (left) and $z = 2.4D$ (right) plotted in wall coordinates for fbw with swirl. The wall coordinates have been calculated with the local friction velocity.

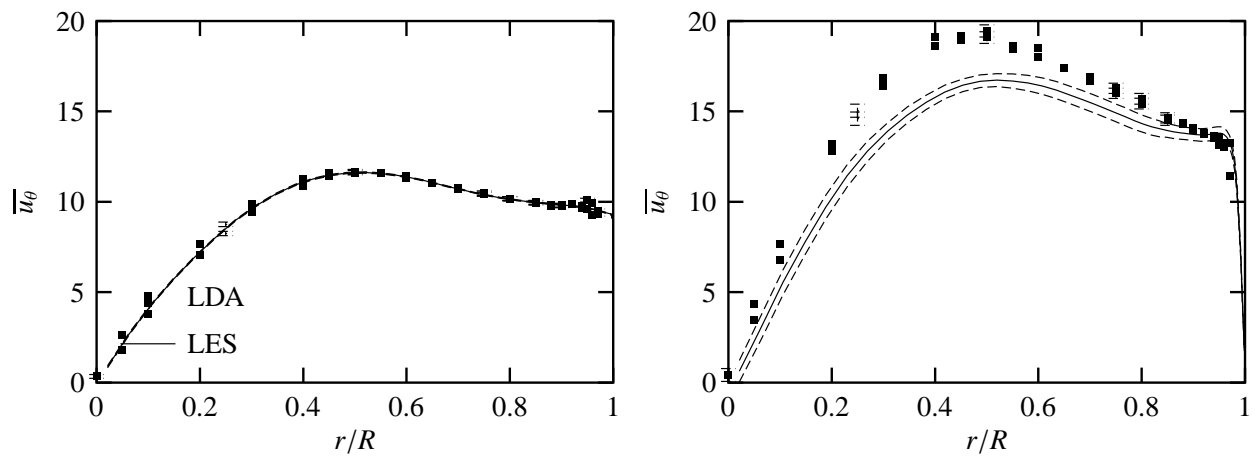


Figure 6.11: Mean tangential velocity at $z = -1.8D$ (left) and $z = 2.4D$ (right) for fbw with swirl. For notes on normalisation, see figure 6.9.

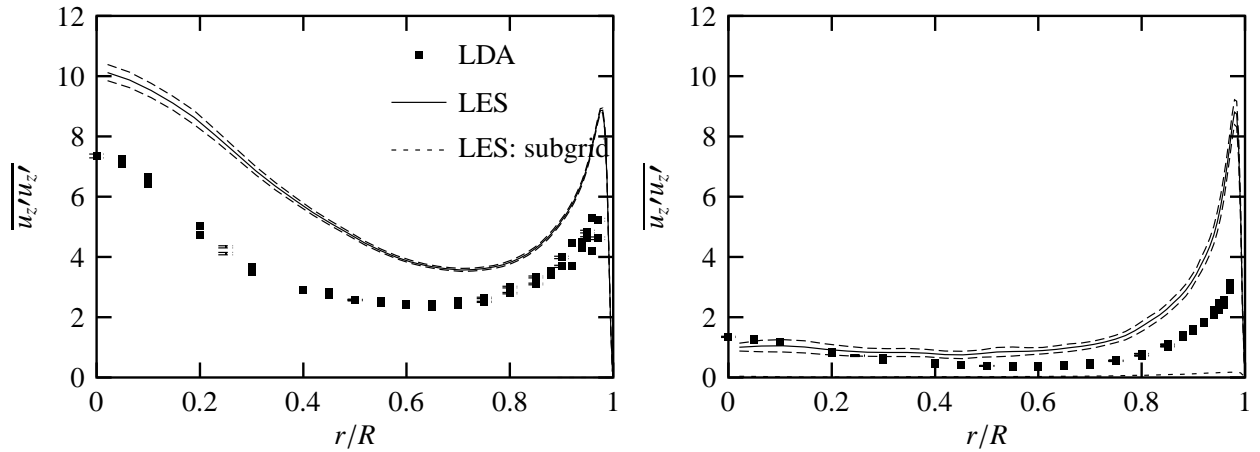


Figure 6.12: Comparison of LES-results to laboratory data for fbw with swirl: $\overline{u'_z u'_z}$ at $z = -1.8D$ (left) and $z = 2.4D$ (right). For notes on normalisation, see figure 6.9. The peak at the centreline, in the simulation results is *not* due to the SGS-model.

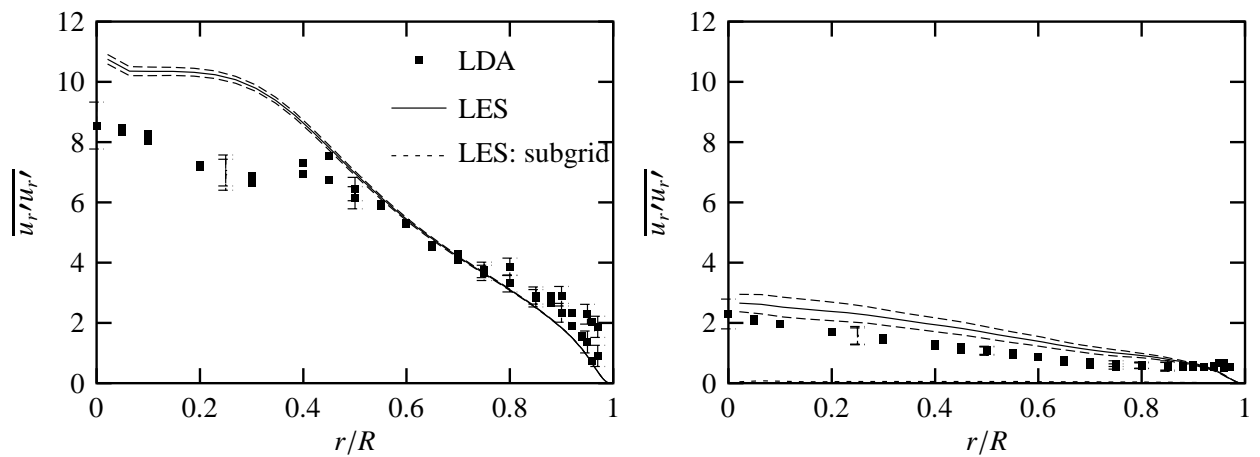


Figure 6.13: Comparison of LES-results to laboratory data for fbw with swirl: $\overline{u'_r u'_r}$ at $z = -1.8D$ (left) and $z = 2.4D$ (right). For notes on normalisation, see figure 6.9.

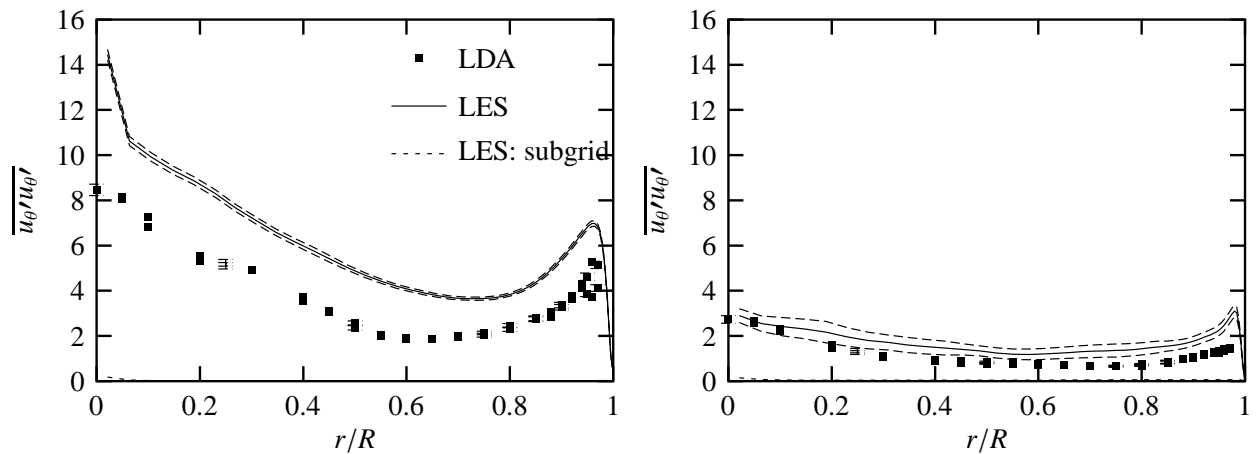


Figure 6.14: Comparison of LES-results to laboratory data for fbw with swirl: $\overline{u'_\theta u'_\theta}$ at $z = -1.8D$ (left) and $z = 2.4D$ (right). For notes on normalisation, see figure 6.9.

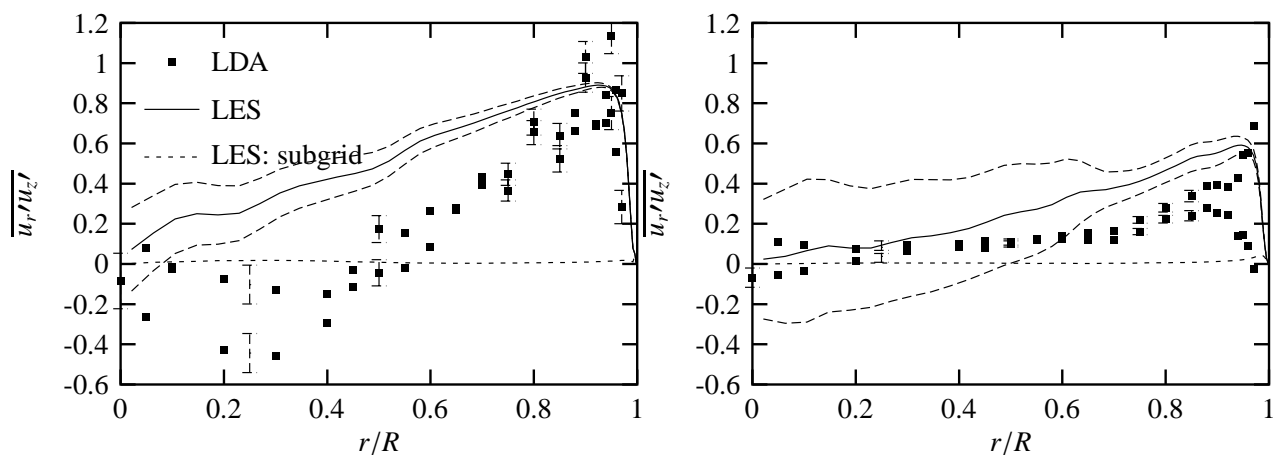


Figure 6.15: Comparison of LES-results to laboratory data for fbw with swirl: $\overline{u'_r u'_z}$ at $z = -1.8D$ (left) and $z = 2.4D$ (right). For notes on normalisation, see figure 6.9.

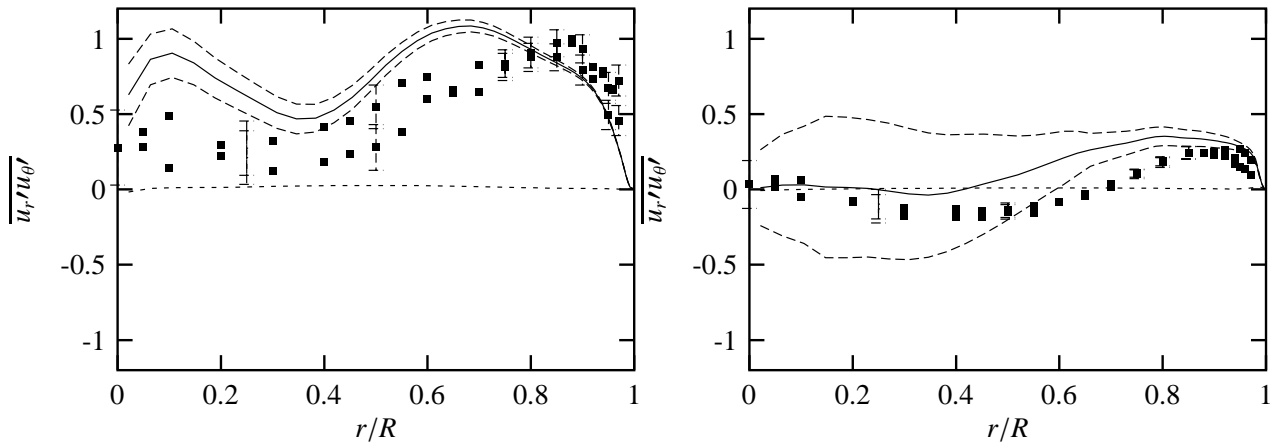


Figure 6.16: Comparison of LES-results to laboratory data for fbw with swirl: $\overline{u'_r u'_\theta}$ at $z = -1.8D$ (left) and $z = 2.4D$ (right). For notes on normalisation, see figure 6.9

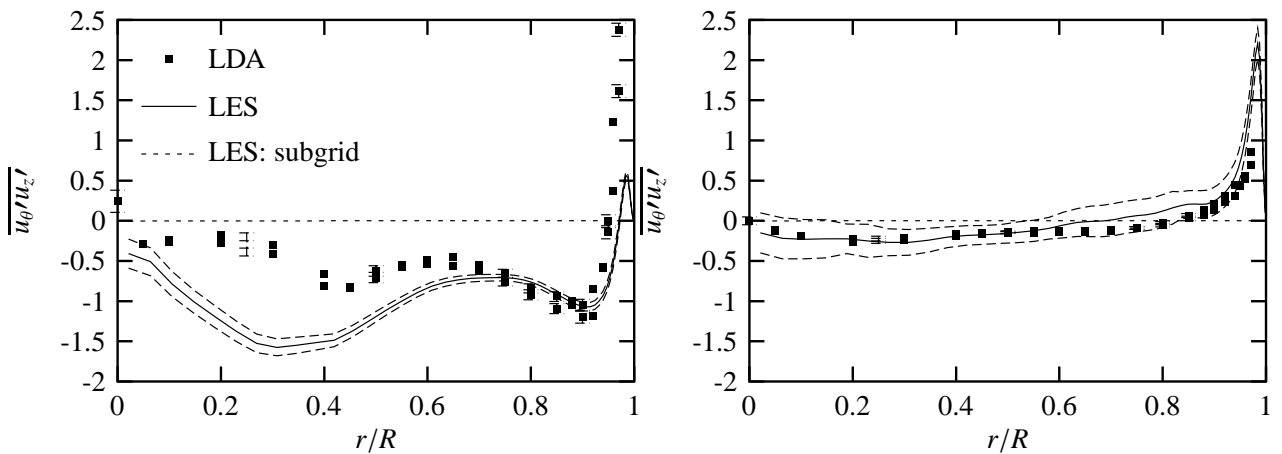


Figure 6.17: Comparison of LES-results to laboratory data for fbw with swirl: $\overline{u'_z u'_\theta}$ at $z = -1.8D$ (left) and $z = 2.4D$ (right). For notes on normalisation, see figure 6.9

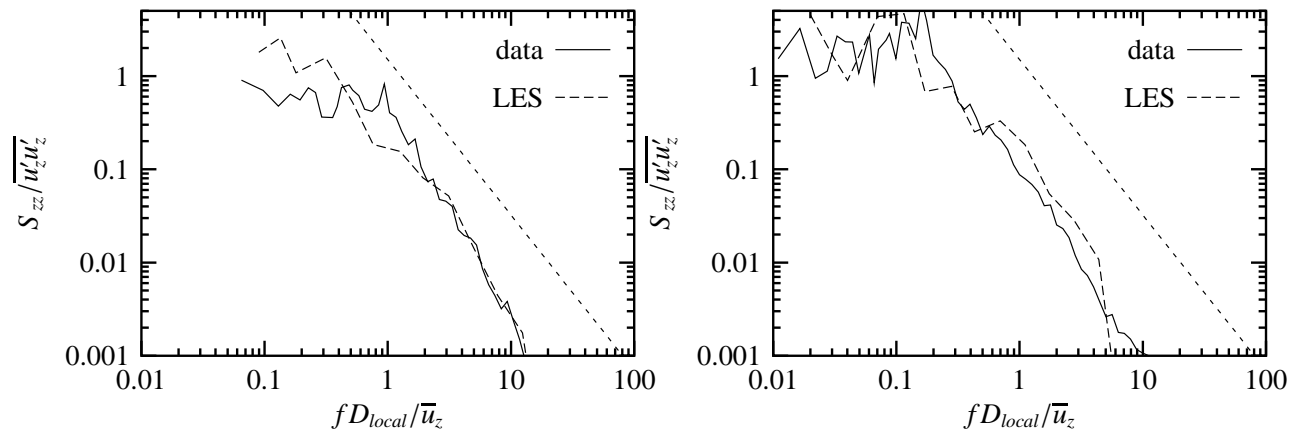


Figure 6.18: Comparison of LES-results to laboratory data for fbw with swirl: Temporal power spectra of u_z at/near the pipe axis ($r/R = 0$ for lab measurements, $r/R = 0.021$ for LES) at $z = -1.8D$ (left) and $z = 2.4D$ (right). Also shown is the inertial subrange slope.

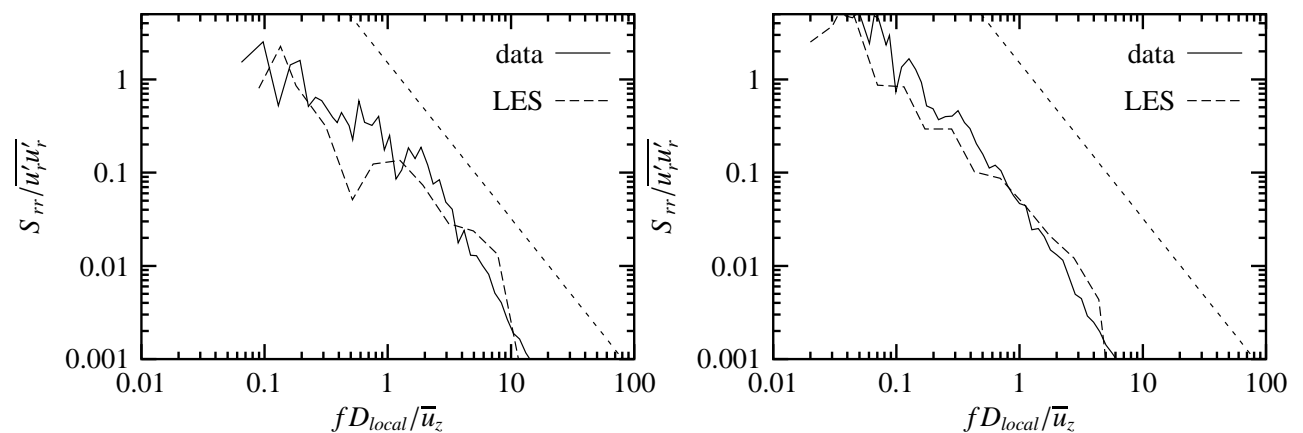


Figure 6.19: Comparison of LES-results to laboratory data for fbw with swirl: Temporal power spectra of u_r at/near the pipe axis ($r/R = 0$ for lab measurements, $r/R = 0.042$ for LES) at $z = -1.8D$ (left) and $z = 2.4D$ (right). Also shown is the inertial subrange slope.

6.2 Further analysis of LES results

In this section the results of the simulations will be analysed further. First the spatial patterns in the fields of mean velocity and turbulent stress will be discussed (section 6.2.1). Subsequently the terms of the stress budgets will be dealt with (section 6.2.2). For the locations and quantities analysed here, no experimental data is available, so that the simulation results will be presented without validation with experimental data.

6.2.1 Velocity and stress fields

Before presenting the results, first a few remarks with respect to the presentation of those results are in place:

- The fields of mean velocity and turbulent stresses are presented as grey-scale plots.
- The *mean* velocities have been normalised with the local bulk velocity, because the downstream development of the mean velocities is mainly determined by the axial acceleration. Any details of the downstream development would be lost if this acceleration would *not* be removed by scaling.
- The stresses have been scaled with the u_*^2 at the inlet as in the model. In this way the downstream development of the stresses is most apparent. Furthermore, a *direct* relationship between a turbulent stress and the wall shear stress at a given axial location is not expected.
- The values that correspond to the minimum and maximum grey-scale have been chosen such that structure of the fields is as clear as possible (i.e. the data have been clipped).

Flow without swirl

Figure 6.20 shows the fields of the mean velocities and turbulent stresses. The main conclusion that can be drawn from the figures for \bar{u}_r and \bar{u}_z is that the upstream influence of the contraction on the mean flow is limited to $z/D > -0.5$. Furthermore, \bar{u}_r is appreciably non-zero only between for $-0.5 < z/D < 1$. Further downstream, however, \bar{u}_r can not be zero exactly, since the axial velocity still develops (mass conservation implies that if $\frac{\partial}{\partial z}\bar{u}_z \neq 0$ then also $\frac{\partial}{\partial r}r\bar{u}_r \neq 0$). The axial acceleration inside the contraction mainly takes place directly at the start of the change in diameter ($z/D \approx 0$).

The figure for $\overline{u'_r u'_r}$ shows that at the downstream edge of the contraction $\overline{u'_r u'_r}$ increases sharply. Further downstream (down to $z \approx 1.5D$) the levels of $\overline{u'_r u'_r}$ decrease again. Downstream of $z \approx 2.5D$, $\overline{u'_r u'_r}$ starts to increase again, first close to the wall: the boundary layer grows. This pattern explains the profile shown in figure 6.4: maxima at $r/R = 0.7$ and 0.9 . The $\overline{u'_\theta u'_\theta}$ -stress is strongly enhanced inside the contraction, but the resulting stress decreases downstream of the contraction. Then at $r \approx 1.5D$ the $\overline{u'_\theta u'_\theta}$ -stress starts to increase again, due to the growth of the boundary layer. For $\overline{u'_z u'_z}$ the situation is different. At the entrance of the contraction a small region of enhanced $\overline{u'_z u'_z}$ occurs near the wall. At the exit $\overline{u'_z u'_z}$ starts to increase again, and due to the growth of the boundary layer, the region of higher $\overline{u'_z u'_z}$ grows –apparently linearly– with downstream distance. Finally, the shear stress $\overline{u'_r u'_z}$ is discussed. Inside the contraction, a localised region with increased $\overline{u'_r u'_z}$ exists near the wall. There, the axially accelerated flow experiences extra friction. Downstream of the contraction $\overline{u'_r u'_z}$ causes the boundary layer to

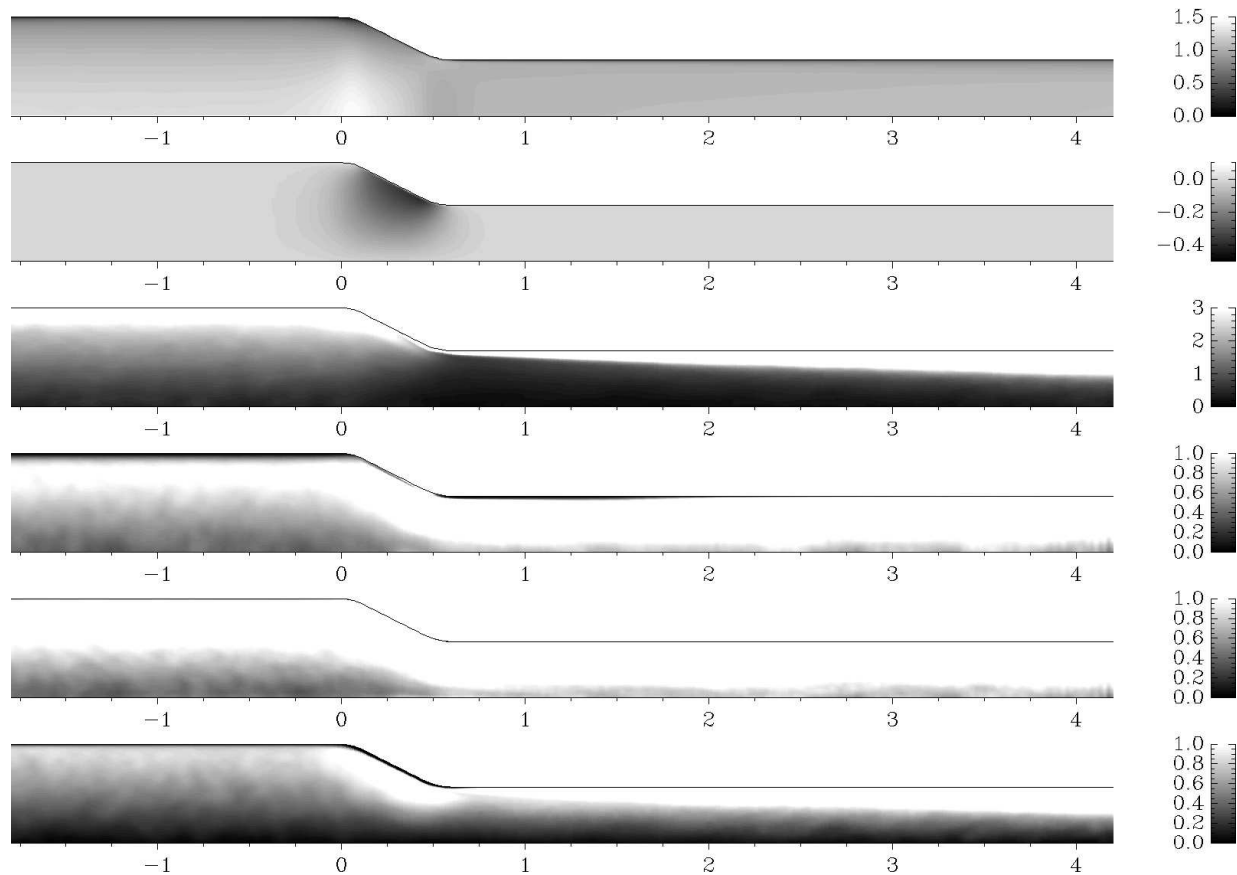


Figure 6.20: Mean velocity and stress fields for flow with axial strain, without swirl. From top to bottom: \bar{u}_z , \bar{u}_r (normalised with local U_{bulk}) $\overline{u'_z u'_z}$, $\overline{u'_r u'_r}$, $\overline{u'_\theta u'_\theta}$ and $\overline{u'_r u'_z}$ (normalised with u_* at entrance). The values have been clipped to a range that can be deduced from the scale to the right of each picture. Clipping of the values has been done to enhance features in the pictures. The stresses include the subgrid contribution.

grow. This boundary layer growth is in turn reflected in a downstream increase of the region with larger $\overline{u'_r u'_z}$.

An important conclusion that can be drawn from figure 6.20 is that upstream of the contraction the stresses are hardly affected by the presence of the contraction. Only for $\overline{u'_z u'_z}$ a slight change can be discerned for $-0.2 < z/D < 0$. Furthermore, the figure does not show any change in the downstream development of the flow as the outflow plane is approached. This gives confidence in the treatment of the outflow boundary conditions in the model.

Flow with swirl

In figure 6.21 the fields of mean velocities and stresses for the flow with swirl are shown. The figures for the mean velocities \bar{u}_z and \bar{u}_r do not differ much from those for the flow without swirl. The field of \bar{u}_z shows that the local maximum around the pipe axis has nearly disappeared at $z/D = 0$. Further downstream, the region of high \bar{u}_z inside the contraction is larger than for the

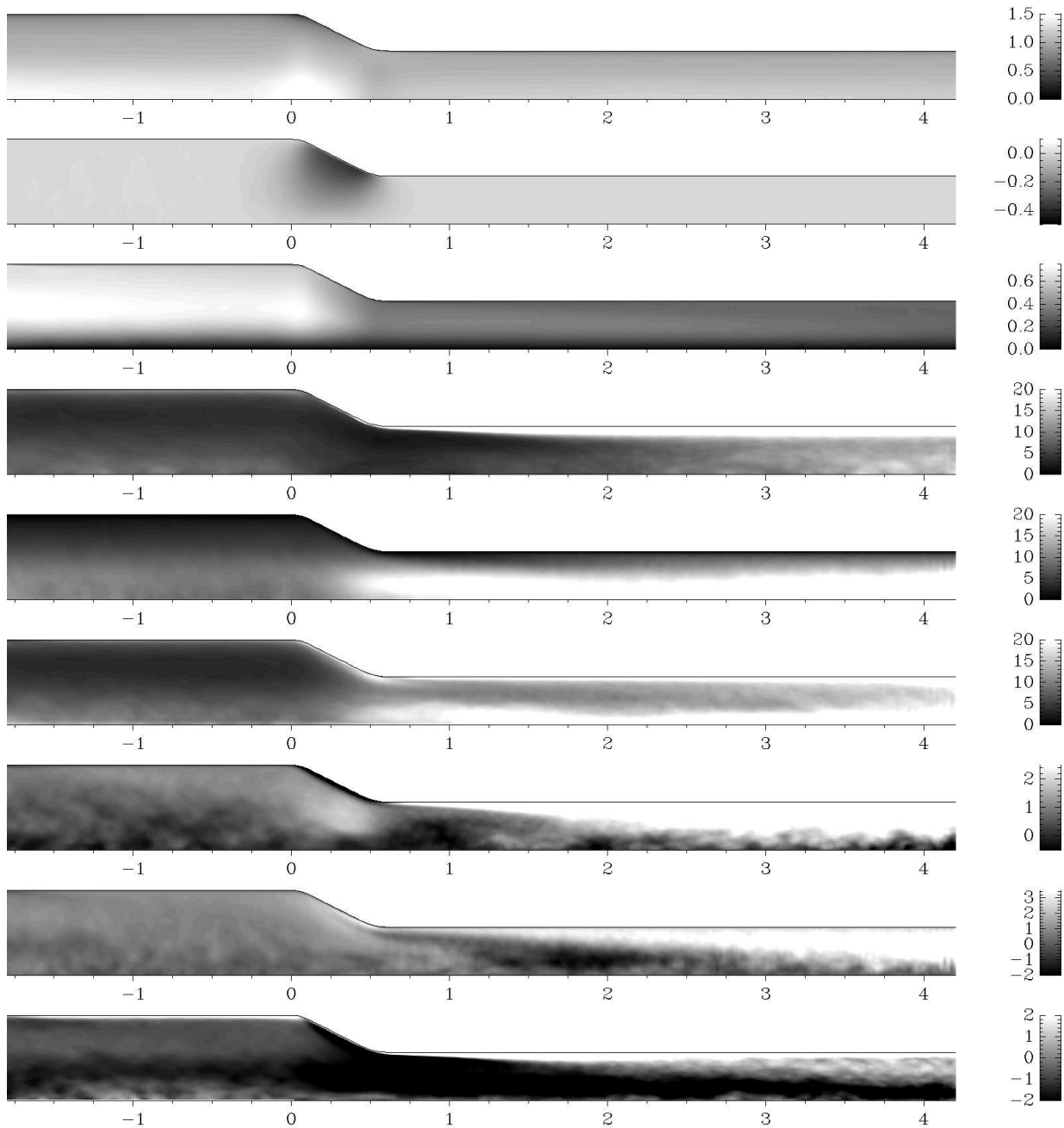


Figure 6.21: Mean velocity and stress fields for flow with axial strain, with swirl. From top to bottom: \overline{u}_z , \overline{u}_r , \overline{u}_θ (normalised with local U_{bulk}) $\overline{u'_z u'_z}$, $\overline{u'_r u'_r}$, $\overline{u'_\theta u'_\theta}$, $\overline{u'_r u'_z}$, $\overline{u'_r u'_\theta}$ and $\overline{u'_z u'_\theta}$ (normalised with u_* at entrance). The values have been clipped to a range that can be deduced from the scale to the right of each picture. Clipping of the values has been done to enhance features in the pictures. The stresses include the subgrid contribution.

flow without swirl. Downstream of the contraction, the axial development of the \bar{u}_z -profile seems to be slower than for the flow without swirl.

In the figure for \bar{u}_θ , the decay of swirl is hardly visible, due to the fact that the main change in \bar{u}_θ is due to the fact that $\bar{u}_\theta \sim D^{-1}$ whereas the velocities have been scaled with the local bulk velocity, which scales as $U_{bulk} \sim D^{-2}$. Furthermore, inside the contraction the vortex core is reduced in size, although the size relative to the pipe diameter remains the same (see also figure 5.12).

The three normal stresses, upstream of the contraction, exhibit enhanced values around the centre line. The possible origins of these higher variance was discussed in section 5.2. The effect of the contraction is that $\overline{u'_r u'_r}$ and $\overline{u'_\theta u'_\theta}$ are further increased, whereas $\overline{u'_z u'_z}$ is diminished, in accordance with the experimental data and with RDT (section 5.2.5). The peak of $\overline{u'_r u'_r}$ and $\overline{u'_\theta u'_\theta}$ around the centre remains throughout the model domain for $z > 0$. The downstream development of the normal stresses is not easily compared between flows without and with swirl due to the large difference in shape of the profiles of those stresses (see figures 5.2 and 5.7 for the full axial development).

The $\overline{u'_r u'_z}$ shear stress shows an increase within the contraction, less localised than for the non-swirling flow. In a thin layer close to the wall in the contraction $\overline{u'_r u'_z}$ is less than zero. This is due to the fact that flow is oblique to the directions of the r -velocity and z -velocity components: velocity fluctuations parallel to the wall will yield negative correlation between u_z and u_r . Directly downstream of the contraction $\overline{u'_r u'_z}$ is zero in most of the pipe cross-section. But the layer, adjacent to the wall, where $\overline{u'_r u'_z}$ is positive, grows rapidly downstream. If the shear stress $\overline{u'_r u'_z}$ is used as an indicator of the growth of the boundary layer, the rate of growth appears to be larger for the swirling flow than for the non-swirling flow. This is in accordance with the destabilising effect of concave curvature on a shear flow (see section 2.2.2). For $\overline{u'_r u'_\theta}$ the field is similar as for $\overline{u'_r u'_z}$. Upstream of the contraction there is transport of θ -momentum toward the wall, and some transport toward the pipe centre in the vortex core. Downstream of the contraction $\overline{u'_r u'_\theta}$ is negative around the pipe centre. The region of positive $\overline{u'_r u'_\theta}$ near the wall grows downstream at the same pace as the region of positive $\overline{u'_r u'_z}$. Inside the contraction, there is a positive $\overline{u'_r u'_\theta}$ near the wall (i.e. loss of θ -momentum due to friction). Finally, the field of $\overline{u'_z u'_\theta}$ is discussed. This stress is negative or near zero around the pipe centre over the total length of the domain. Upstream of the contraction a thin layer with large positive values exists close to the wall. Downstream of the contraction this layer starts to grow, but for $z > 2D$ a fuzzy transition layer starts to develop between the negative values near the pipe axis and the positive values near the wall. The growth of the layer with positive $\overline{u'_z u'_\theta}$ is different in nature than the growth of the $\overline{u'_r u'_z}$ boundary layer: due to swirl decay the angle between the velocity and the axial direction decreases and consequently $\overline{u'_z u'_\theta}$ decreases. The vortex core appears immune to swirl decay and thus $\overline{u'_z u'_\theta}$ remains virtually constant there.

6.2.2 Budgets for turbulent stresses

To understand the dynamics of the Reynolds stresses, the terms of the conservation equations for those stresses (the budget terms) need to be computed. Whereas this is (nearly) impossible to do with experimental data, from LES fields the budget terms can readily be computed. In this

section the budget terms are presented in two ways: as profiles for the axial positions $z/D = -1.8$ and 2.4 , and as fields (grey-scale pictures) for the entire model domain.

Before discussing the results of the budget terms, first some remarks will be made regarding the computation and presentation of those terms.

- The budget equations can be found in section B.1.2.
- The budget terms have not been computed using the analytical equations in B.1.2. Rather, the computation is based on the procedure used in the derivation of the budget equations: multiplication of the (discretized) conservation equation for \mathbf{u}' with \mathbf{u}' (see Stull (1988) for the procedure, Gao *et al.* (1994) for the application to LES results).
- No attempt has been made to split the pressure-gradient velocity terms into pressure-strain and pressure-diffusion terms (see appendix H for a study of the pressure strain terms in a rotating pipe). Neither has the viscous term been split into viscous dissipation and viscous diffusion. Finally, no distinction is made between the effect of molecular viscosity and the sub-grid scale viscosity. So subgrid and molecular diffusion have been added.
- For the profiles of budget terms shown in this section, the data for $z = -1.8D$ have been deduced from the fields of the straight pipe model. The data for $z = 2.4D$ have been computed with the fields from the contraction model.
- In the presentation of the *profiles* of budget terms, for the radial coordinate the distance to the wall in viscous units is used, indicated by y^+ ($= yu_*/\nu$). At both axial a local u_* has been used to determine y^+ . Furthermore, the budget terms themselves have also been scaled with the local u_*^2 . Where feasible, the profiles at both axial locations have been plotted with the same vertical scale.
- In the profiles of the budget terms, the sum of those terms is also shown. This sum should be zero if the budget is balanced exactly.
- The fields of the budget terms have been scaled differently: there the budget terms have been scaled with the local value of the stress under consideration. In that way, the fields will show the relative gain or loss due to a certain term. Consequently, the effects of large differences in the values of the stress on their budget terms are eliminated.

Flow with axial strain

Figures 6.22 to 6.29 show the profiles of the budget terms for $z = -1.8D$ and $z = 2.4D$, as well as the fields of those terms throughout the model domain. The first conclusion that can be drawn from the profiles is that there is hardly any difference in the shape of the profiles between the two axial locations, except for the fact that the budget terms are nearly zero for $y^+ > 90$ for $z = 2.4D$. Furthermore, there is some change in the relative size of the various terms. The scaling with the local u_* appears to be appropriate, given that for most stresses (except $\overline{u'_r u'_z}$ and $\overline{u'_z u'_z}$) the budget terms have equal orders of magnitude at both axial locations.

Another important conclusion is that the sum of all budget terms is very small (relative to the actual budget terms) for all budgets. This indicates that method of used in the determination of the budget terms is accurate.

The budget for $\overline{u'_z u'_z}$ does not differ much between both axial positions (figure 6.22). The budget terms are an order of magnitude larger at $z/D = 2.4$ than at the upstream location (due

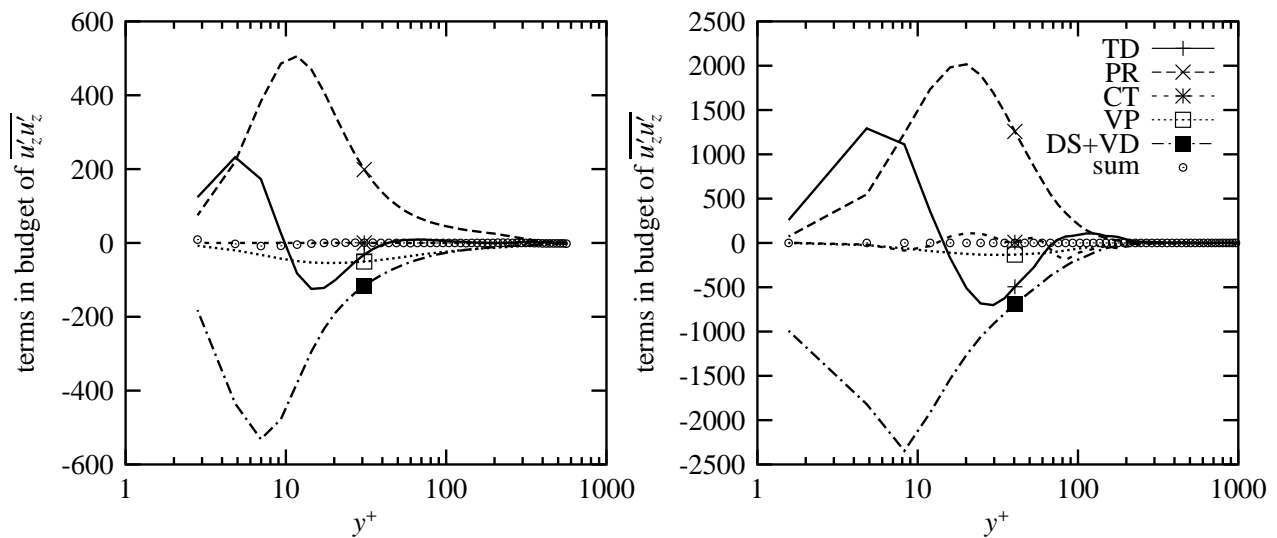


Figure 6.22: Budget terms for $\overline{u'_z u'_z}$ -budget. For fbw without swirl at $z/D = -1.8$ and $z/D = 2.4$.

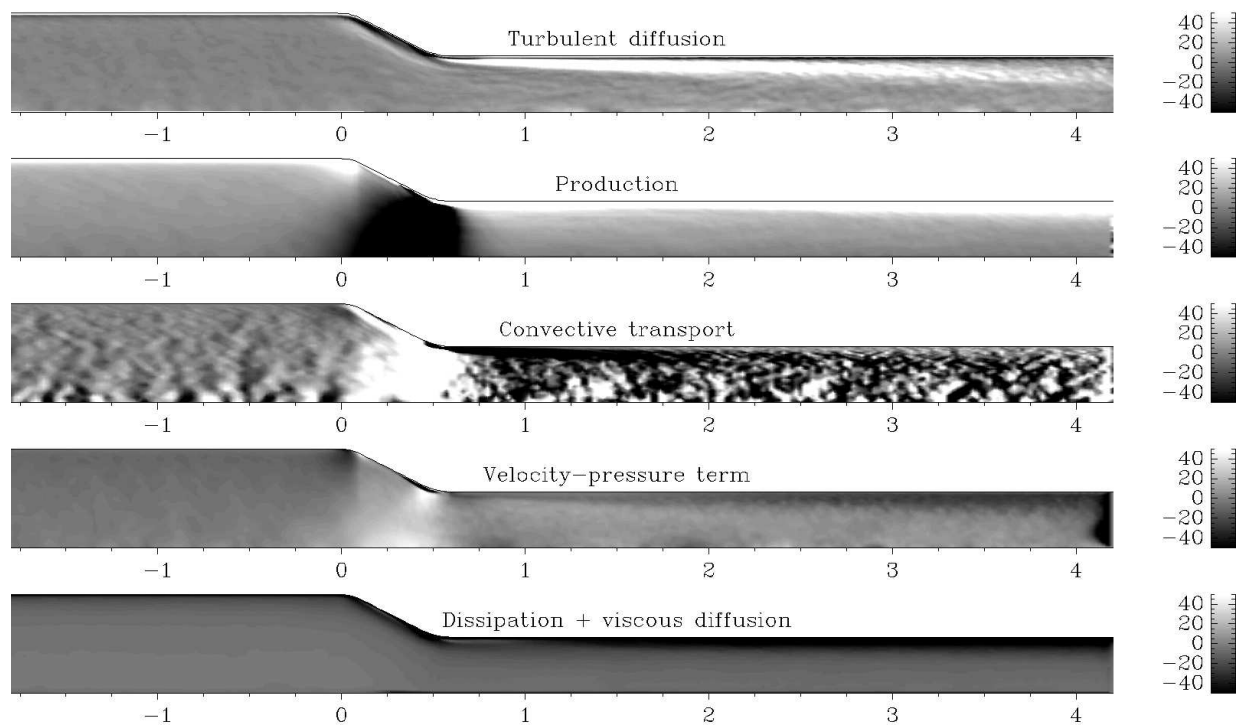


Figure 6.23: Terms in the budget of $\overline{u'_z u'_z}$ for fbw with axial strain, without swirl. From top to bottom: TD (turbulent diffusion), PR (production), CT (convective transport), VP (velocity-pressure gradient correlation term), DS+VD (dissipation + viscous diffusion). The values of the budgets have been normalised with the local value of the stress under consideration, so that the scaled budget terms indicate the relative change in the given stress. The values of the budget have been clipped in order to highlight the structure of the fields. The pipe wall is indicated with a fine black line. The horizontal axis gives the axial position z/D where D is the upstream pipe diameter.

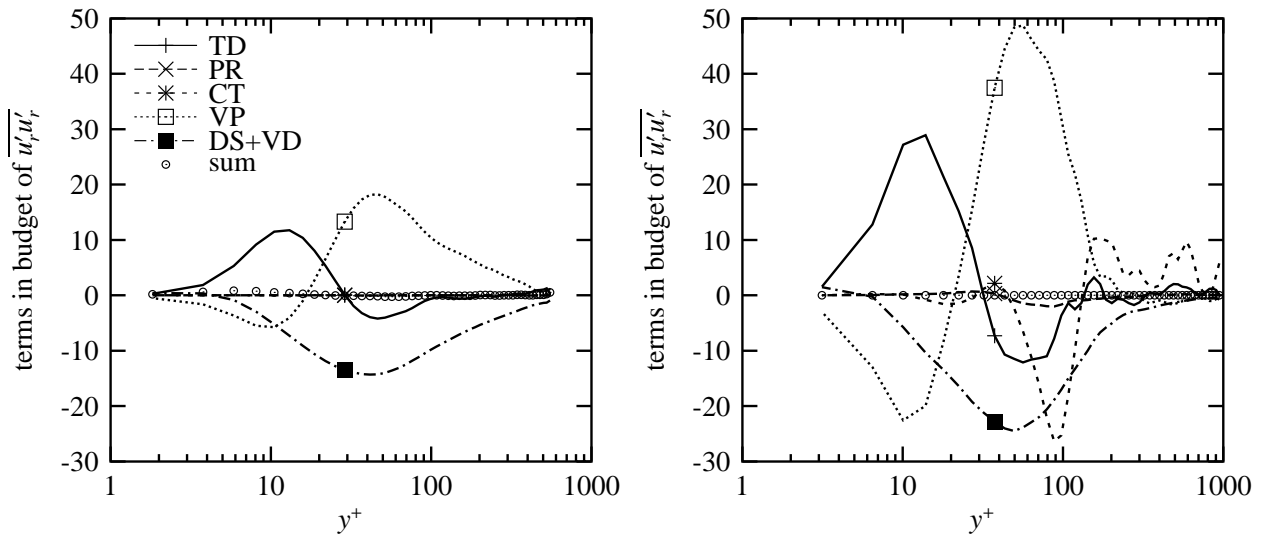


Figure 6.24: Budget terms for $\overline{u'_r u'_r}$ -budget. For fbw without swirl at $z/D = -1.8$ and $z/D = 2.4$. For notes on the normalisation: see the text.

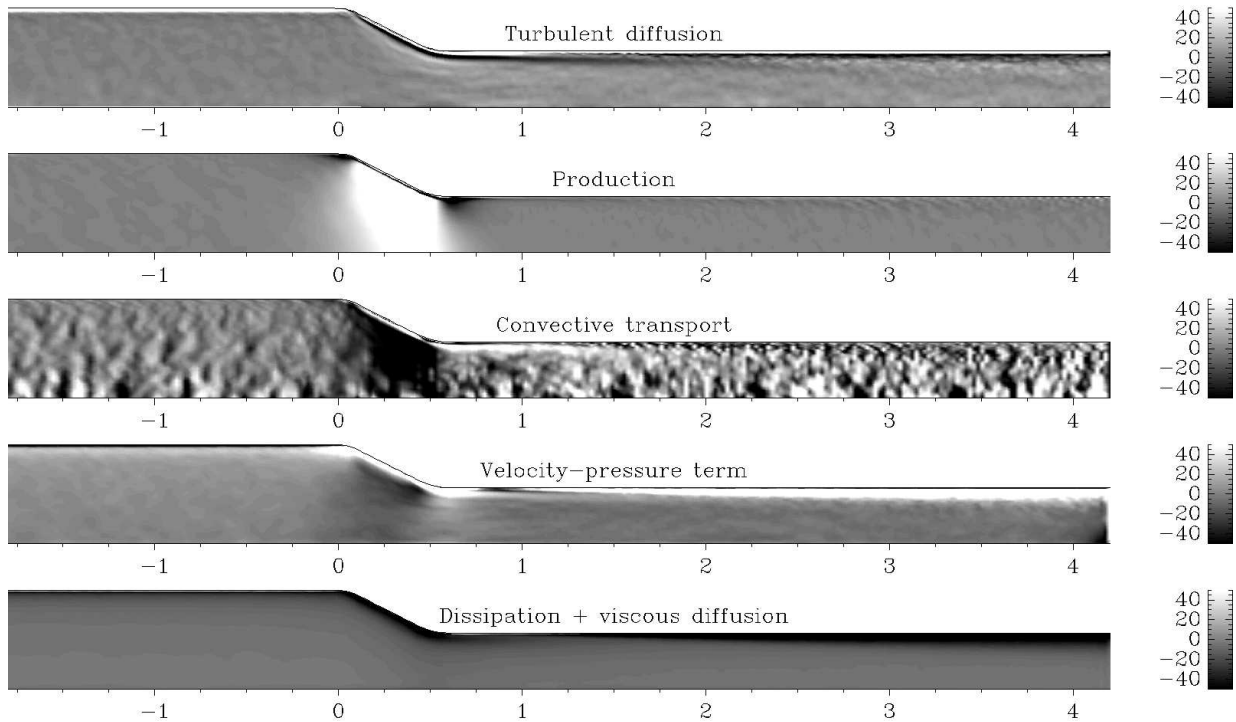


Figure 6.25: Terms in the budget of $\overline{u'_r u'_r}$ (normalised with the local $\overline{u'_r u'_r}$) for fbw with axial strain, without swirl. For more details, see figure 6.23).

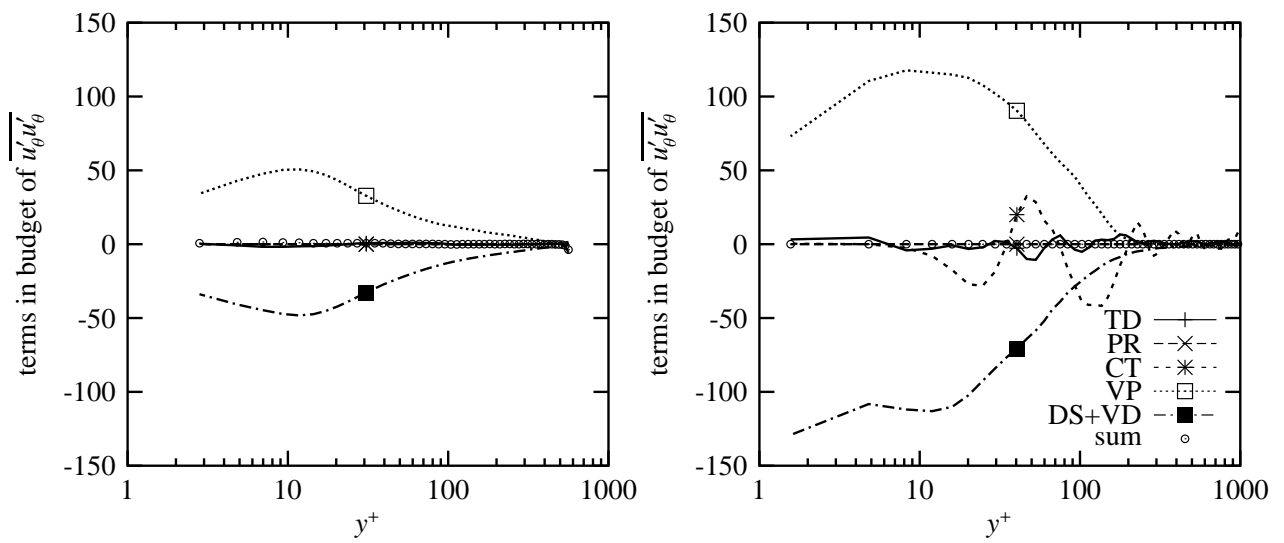


Figure 6.26: Budget terms for $\overline{u'_\theta u'_\theta}$ -budget. For fbw without swirl at $z/D = -1.8$ and $z/D = 2.4$. From top to bottom: TD, PR, CT, VP, and DS+VD.

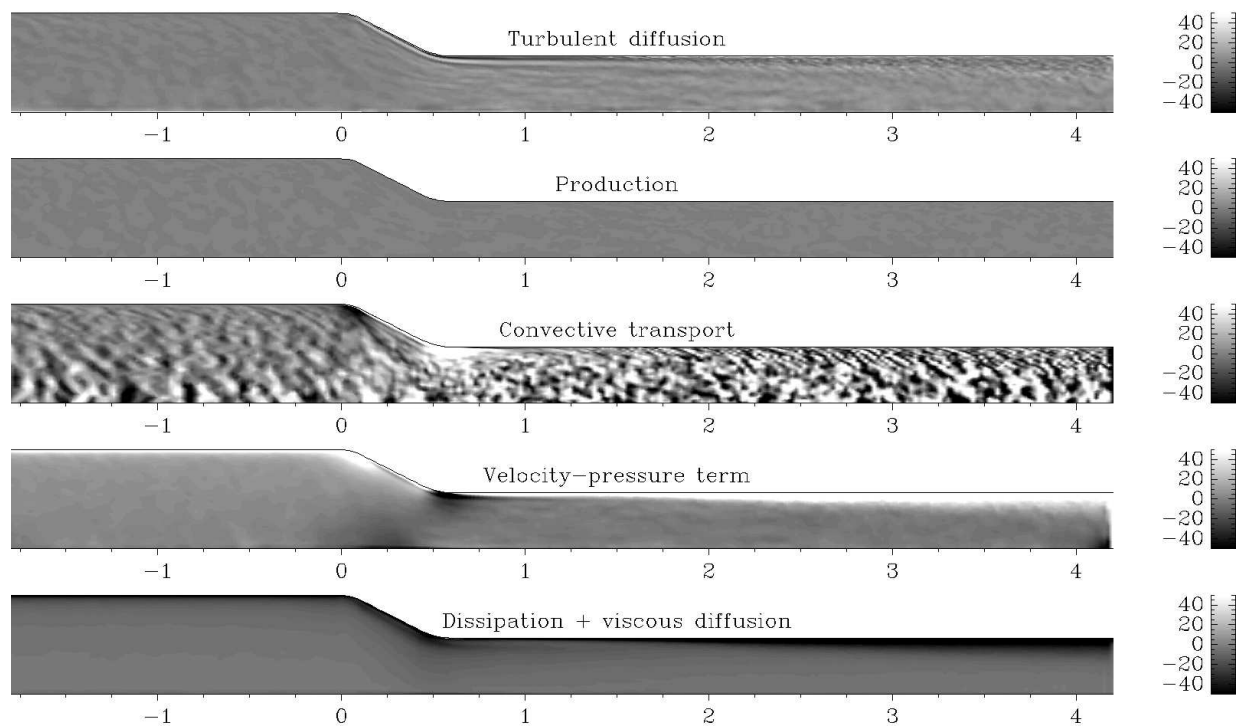


Figure 6.27: Terms in the budget of $\overline{u'_\theta u'_\theta}$ (normalised with the local $\overline{u'_\theta u'_\theta}$) for fbw with axial strain, without swirl. From top to bottom: TD, PR, CT, VP, and DS+VD. For more details, see figure 6.23).

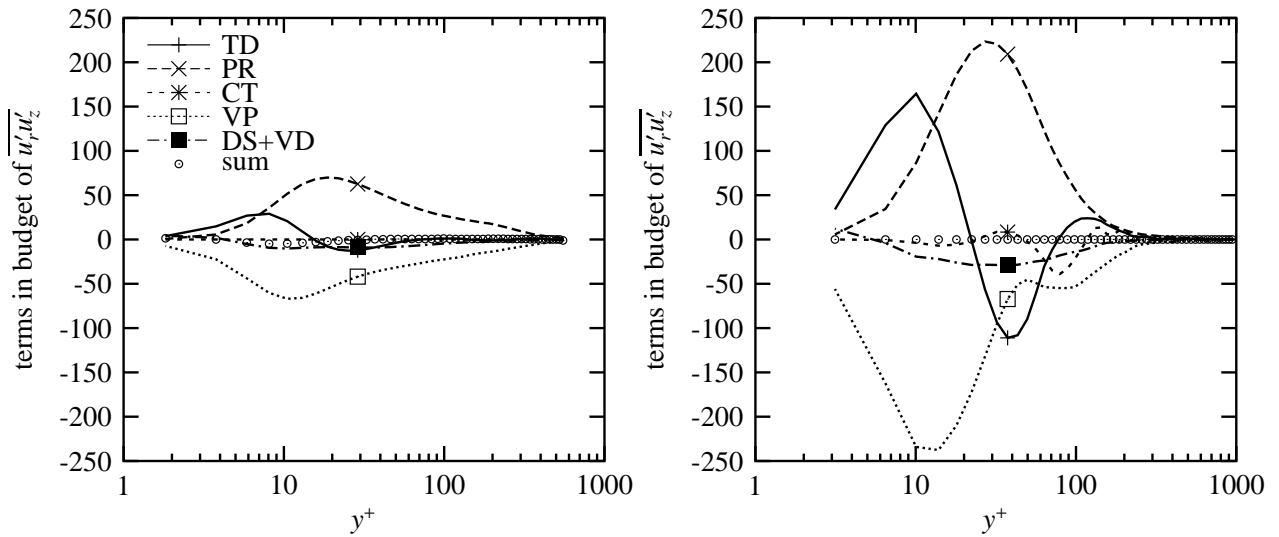


Figure 6.28: Budget terms for $\overline{u_r'u_z'}$ -budget. For fbw without swirl at $z/D = -1.8$ and $z/D = 2.4$.

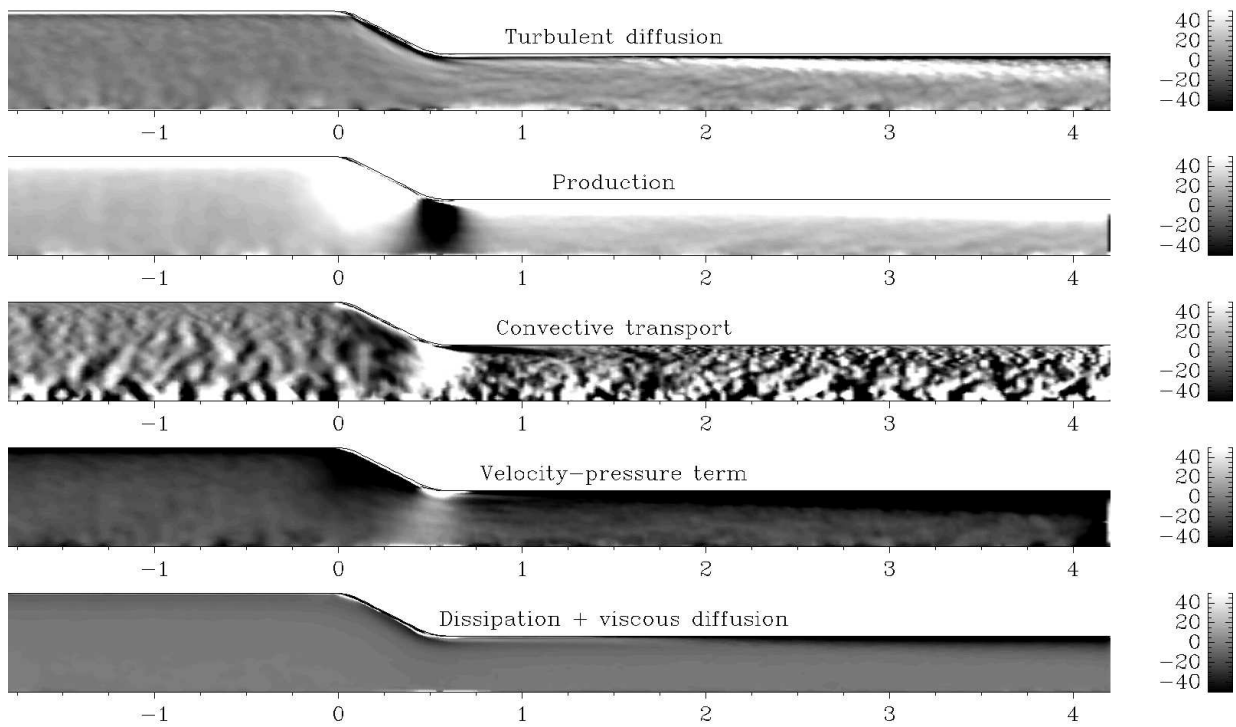


Figure 6.29: Terms in the budget of $\overline{u_r'u_z'}$ (normalised with the local $|\overline{u_r'u_z'}|$) for fbw with axial strain, without swirl. From top to bottom: TD, PR, CT, VP, and DS+VD. For more details, see figure 6.23).

to the extreme shear production). Production occurs throughout the pipe cross-section, turbulent diffusion is a gain term close to the wall but a loss term toward the pipe axis. Dissipation is a loss term, and the pressure-velocity term is a small but important loss term, since it feeds the energy the two other normal stresses. The pressure-velocity loss terms is relatively smaller at $z/D = 2.4$ than at $z/D = -1.8$. In absolute value, however, it is larger, as can also be seen from the increased magnitude of the gain from the VP-term for the other stresses.

From the fields of the $\overline{u'_z u'_z}$ -budget terms, shown in figure 6.23, it can be concluded that the budget is roughly identical both upstream and downstream of the contraction, except for the order of magnitude of the terms. Inside the contraction, however, negative production occurs, whereas convective transport is a major gain term. Furthermore, the radial transport (away from the wall) by turbulent diffusion is stronger than outside the contraction.

For $\overline{u'_r u'_r}$ the main change between the two axial positions, is that at $z = 2.4D$ the velocity-pressure correlations and the turbulent diffusion have increased, relative to the dissipation term. For both locations $\overline{u'_r u'_r}$ gains near the wall, due to turbulent diffusion, whereas further toward the pipe axis, turbulent diffusion is a loss term. Note the large fluctuations at $z = 2.4D$ in the convective transport (CT) term. This is due to statistical errors in the stresses. CT is proportional to the mean velocity in given direction and the gradient of a stress in the same direction. Especially in the axial direction (with a large mean velocity and some statistical error in the stresses) this gives rise to large statistical errors in the budget term. This feature will occur in all budgets derived from fields from the contraction model.

The fields of the $\overline{u'_r u'_r}$ -budget terms are shown in figure 6.25. As was already clear from the spatial patterns of the stresses, there are two important regions. One is inside the contraction, where $\overline{u'_r u'_r}$ is produced, and subsequently lost by convective transport. There is also some negative production at the trailing edge of the contraction. Furthermore, there is a streak, starting inside the contraction and extending to $z = 1.5D$ where the pressure-velocity term feeds the $\overline{u'_r u'_r}$ stress and turbulent diffusion is a loss term. Convective transport appears to be a gain term as well, although the noise is rather large. The second region of interest starts at $z = 2D$. Here again, there is a balance between the pressure-velocity term and dissipation, with turbulent diffusion acting as a spatial redistributor (see also figure 6.24).

The budget for $\overline{u'_\theta u'_\theta}$ is rather simple. It is a balance between the pressure-velocity correlation term and dissipation. This is the same for both axial positions. From the fields of the budget terms (figure 6.27) the following observations can be made. This budget is, near the wall, mainly a balance between the pressure-velocity term (gain) and dissipation (loss). At the trailing edge of the contraction convective transport is a gain and the pressure-velocity term is –locally– a loss term. Furthermore, in the contraction and just downstream of it, there is some spatial redistribution by turbulent diffusion (transport away from the wall).

In the $\overline{u'_z u'_z}$ -stress budget the main difference between the two axial positions is that the amplitude of the turbulent diffusion term becomes relatively large downstream of the contraction: a gain term near the wall and a loss term toward the pipe axis. In general, the magnitude of the budget terms has increased at the downstream location. The shear stress is fed through the production term and is mainly drained by the pressure-velocity term. Dissipation is only a minor term in this budget. From the fields of the budget terms (figure 6.29) it can be seen that the budget terms exhibit the same profiles over the entire length of the domain, except inside and

directly downstream of the contraction. Inside, there is positive production and negative convective transport, whereas, at the trailing edge of the contraction, the gain due to the convective transport term and the pressure-velocity term is balanced by a negative production term.

Flow with axial strain and swirl

In figures 6.30 to 6.41 the profiles of the budget terms at $z = -1.8D$ and $z = 2.4D$, as well as the fields of those terms are shown for the case with swirl.

From the profiles a difference with the non-swirling flow is immediately clear: whereas in the non-swirling flow the terms are nearly zero close to the pipe axis, they are large (and even dominate over the near-wall values) near the pipe axis.

The budget for $\overline{u'_z u'_z}$ (figures 6.30 and 6.31) is very similar to the budget for the flow without swirl. Upstream of the contraction the only difference is the occurrence of high levels of the dissipation and pressure-velocity terms near the pipe axis. Although this cusp seems unrealistic, the fact that it is not restricted to the first gridpoint off the pipe axis suggests that it is a real phenomenon. From the fields in 6.31 one can see that there are more places in the domain where patches of high, positive, values of the pressure-velocity occur. At $z = 2.4D$ the only visible difference is the fact that, in the wall region, the production is somewhat higher for the swirling flow, and that the turbulent diffusion term is smaller. Any influence of the vortex core is no longer visible. The fields of the budget terms (figure 6.31) show some more differences. In general, there is more scatter in the fields than for the flow without swirl. The negative production inside the contraction is similar to that for the flow without swirl. The pattern of the pressure-velocity term differs from that for the flow without swirl. Inside the contraction, close to the wall there is a positive contribution from VP to $\overline{u'_z u'_z}$. The gain patch of positive VP that was inside the contraction for the non-swirling flow, has shifted to a location downstream of the contraction in the swirling flow. Furthermore, there are patches of positive VP near the pipe axis that do not exist in the flow without swirl.

The budget of $\overline{u'_r u'_r}$ (shown in figures 6.32 and 6.33) is dominated by the vortex core. In that part of the cross-section, the gain due to production, convective transport and turbulent diffusion is balanced by dissipation and the pressure-velocity term. At $z = 2.4D$ the magnitude of the terms in the vortex core has diminished, relative to the near-wall values. For $y^+ < 300$ the structure of the terms is more or less identical to that at $z = -1.8D$. Inside a part of the vortex core at $z/D = 2.4$ (roughly $500 < y^+ < 800$) a sign reversal of most terms occurs: production becomes negative and the pressure-velocity term becomes positive. The fields, shown in figure 6.33, reveal that this region of sign reversal appears to originate at the trailing edge of the contraction. A similar structure appears in the flow without swirl (figure 6.25), but there the region that originates at the trailing edge of the contraction is thinner and remains close to the wall. Except for this region of sign reversal, and the high values near the pipe axis, the overall structure of the budget terms is similar for the flows without and with swirl.

The budgets of $\overline{u'_\theta u'_\theta}$ are shown in figures 6.34 and 6.35. As in the flow without swirl, the budget upstream of the contraction is dominated by the pressure-velocity term and dissipation with a small role for turbulent diffusion. Near the pipe wall the same terms are important but their values are larger. Furthermore, the production term is strongly negative near the pipe centre.

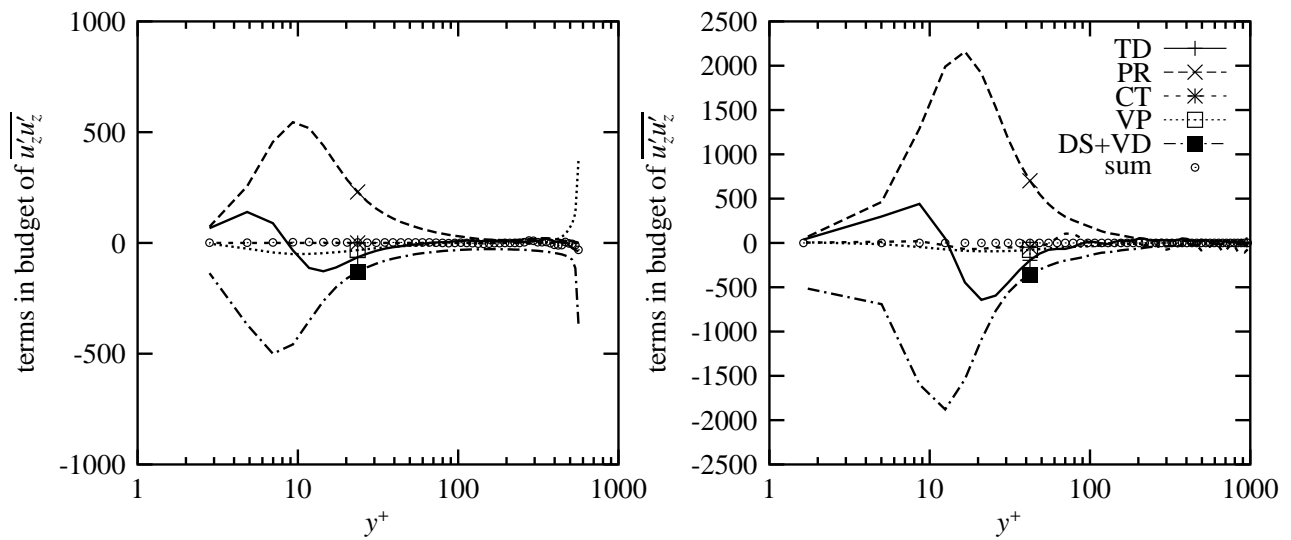


Figure 6.30: Budget terms for $\overline{u'_z u'_z}$ -budget. For flow with swirl at $z/D = -1.8$ and $z/D = 2.4$.

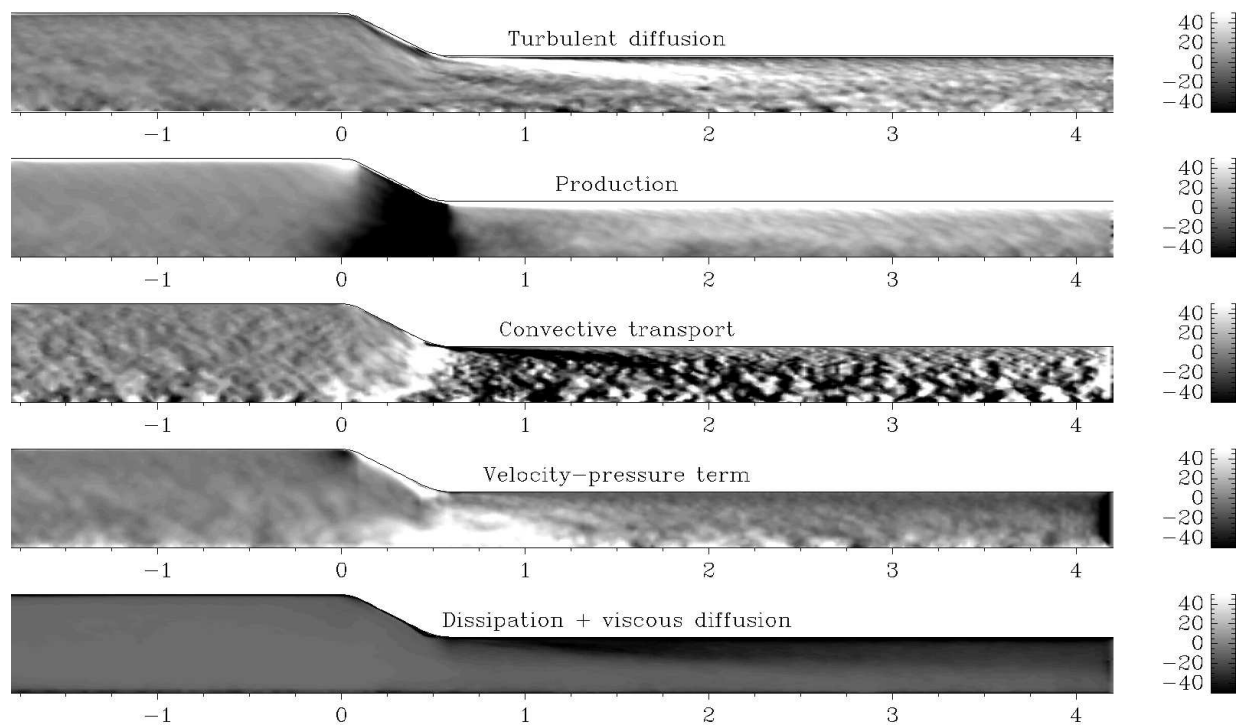


Figure 6.31: Terms in the budget of $\overline{u'_z u'_z}$ for flow with axial strain, with swirl. From top to bottom: TD (turbulent diffusion), PR (production), CT (convective transport), VP (velocity-pressure gradient correlation term), DS+VD (dissipation + viscous diffusion). The values of the budgets have been normalised with the local (absolute) value of the stress under consideration, so that the scaled budget terms indicate the relative change in the given stress. The values of the budget have been clipped in order to highlight the structure of the fields. The pipe wall is indicated with a fine black line.

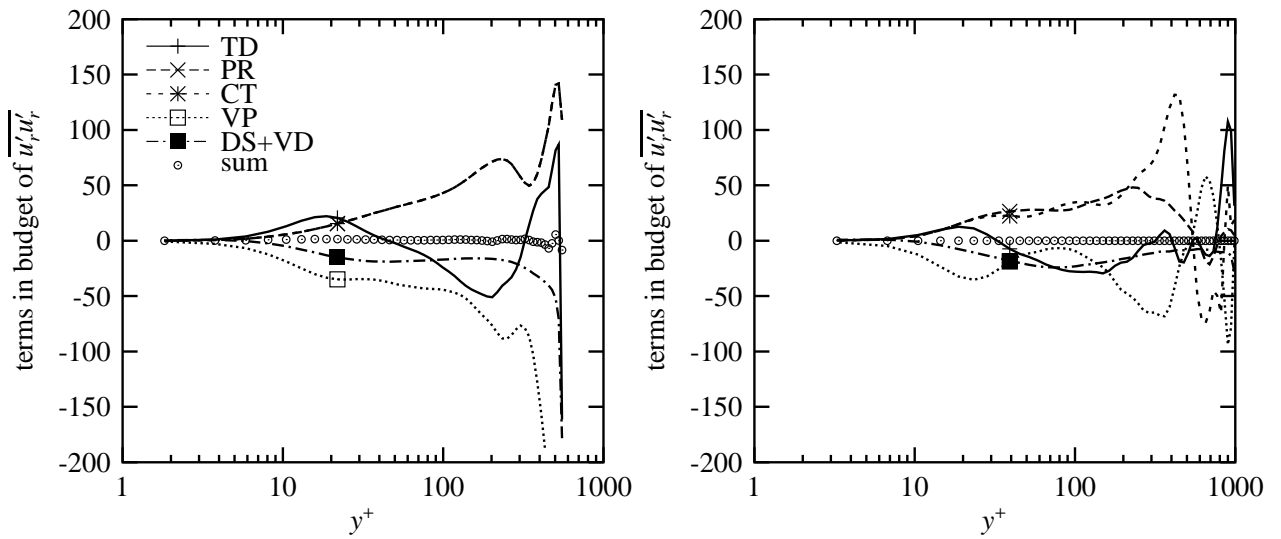


Figure 6.32: Budget terms for $\overline{u'_r u'_r}$ -budget. For flw with swirl at $z/D = -1.8$ and $z/D = 2.4$.

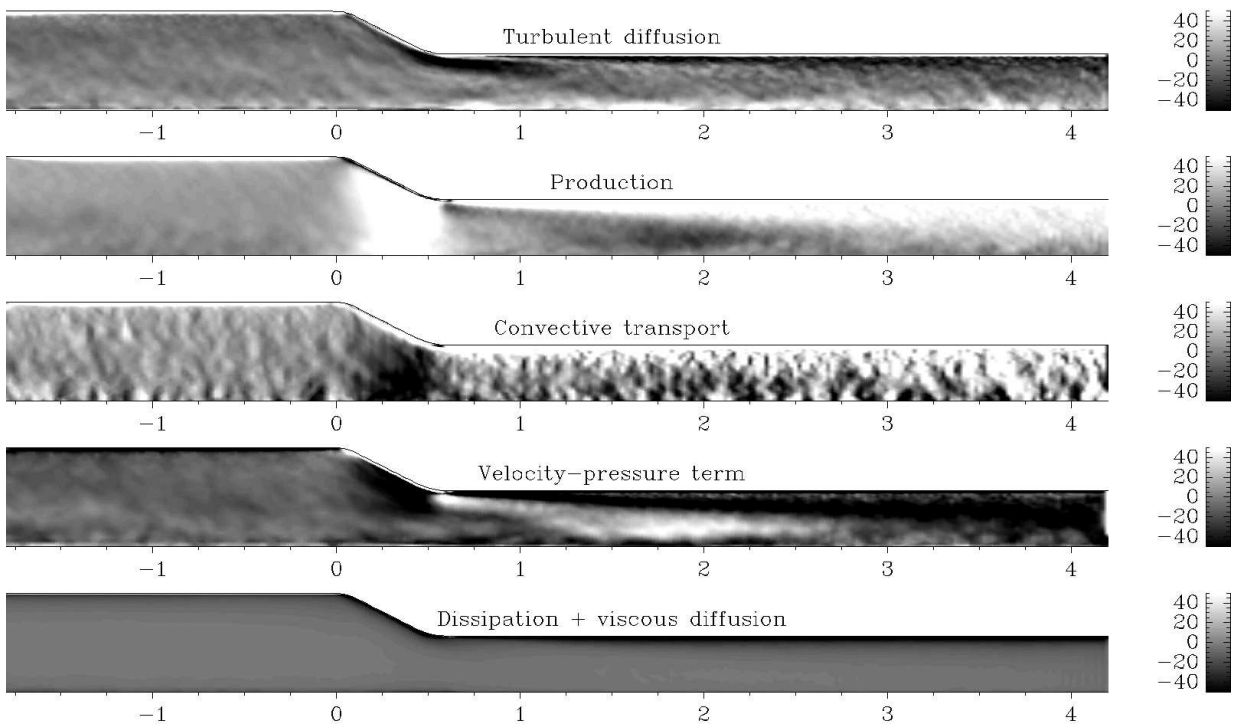


Figure 6.33: Terms in the budget of $\overline{u'_r u'_r}$ (normalised with the local $\overline{u'_r u'_r}$) for flw with axial strain, with swirl. From top to bottom: TD, PR, CT, VP, and DS+VD. For more details, see figure 6.31).

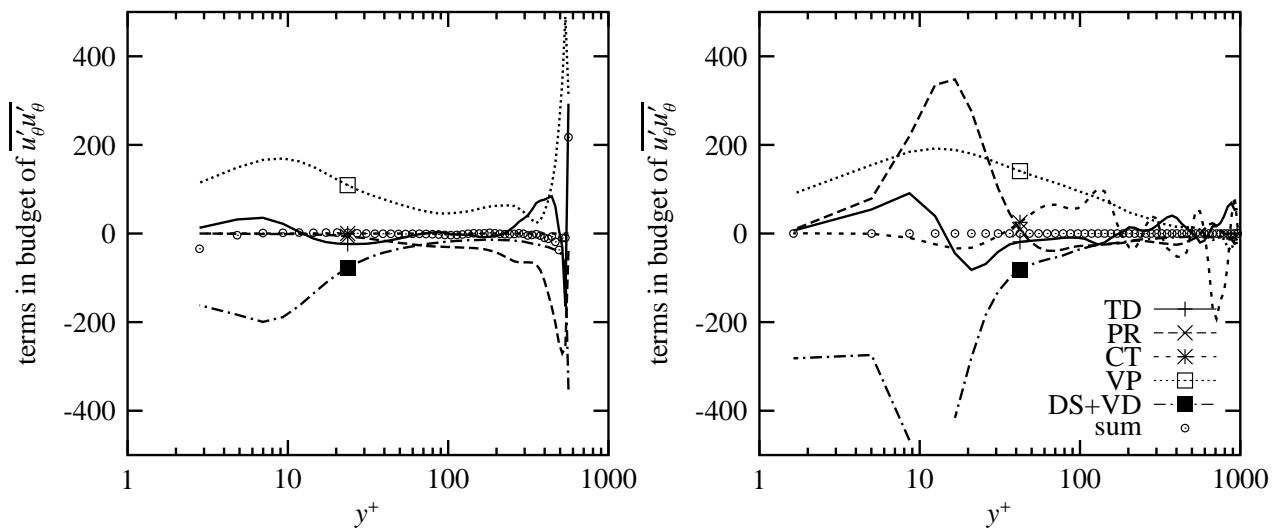


Figure 6.34: Budget terms for $\overline{u'_\theta u'_\theta}$ -budget. For flw with swirl at $z/D = -1.8$ and $z/D = 2.4$.

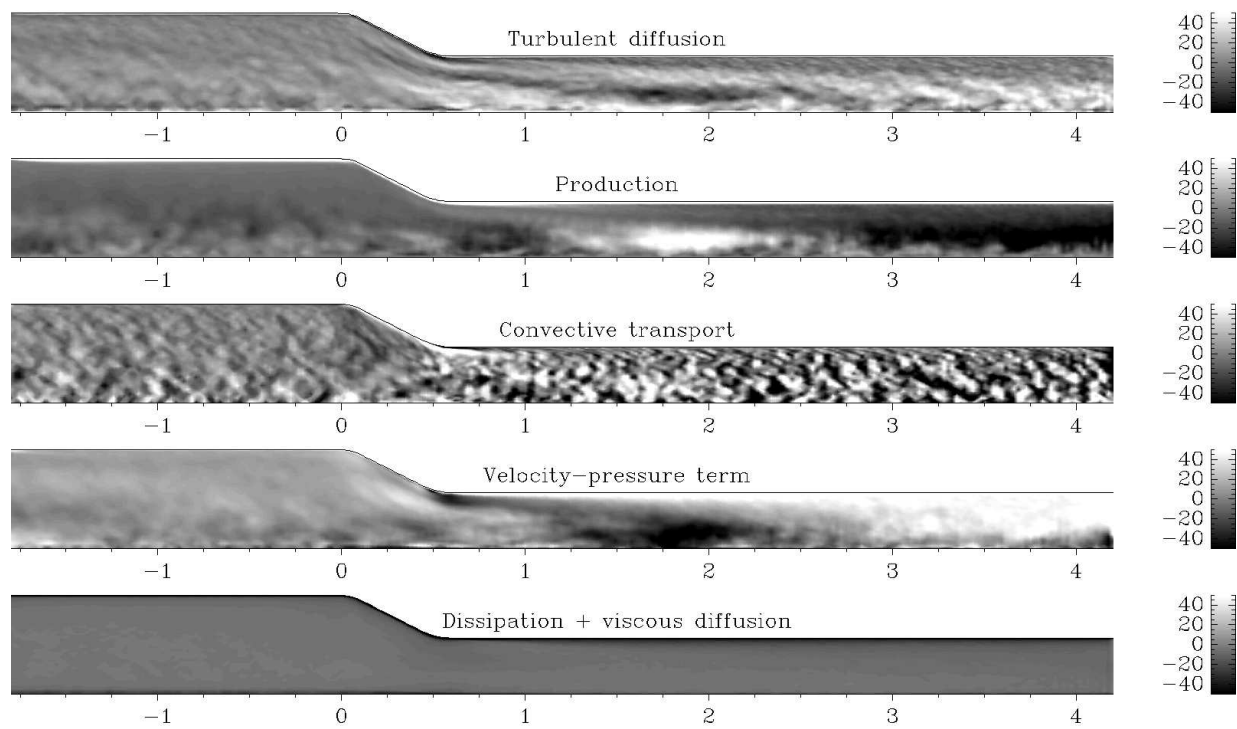


Figure 6.35: Terms in the budget of $\overline{u'_\theta u'_\theta}$ (normalised with the local $\overline{u'_\theta u'_\theta}$) for flw with axial strain, with swirl. From top to bottom: TD, PR, CT, VP, and DS+VD. For more details, see figure 6.31).

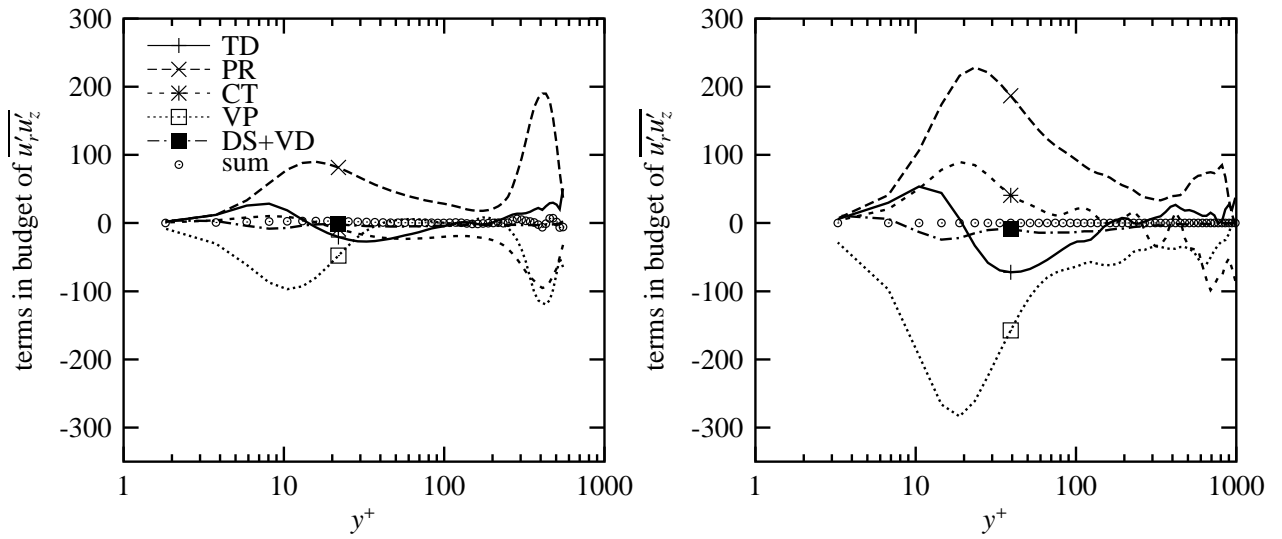


Figure 6.36: Budget terms for $\overline{u_r'u_z'}$ -budget. For fbw at $z/D = -1.8$ and $z/D = 2.4$.

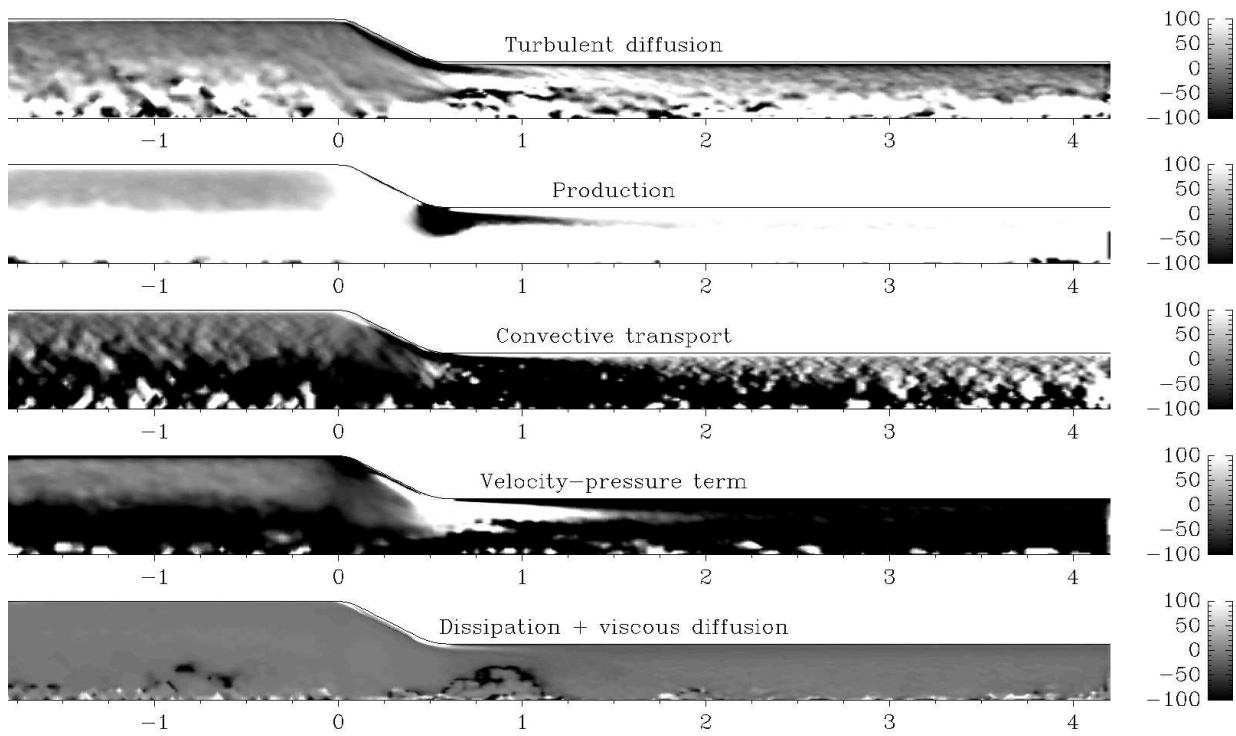


Figure 6.37: Terms in the budget of $\overline{u_r'u_z'}$ (normalised with the local $|\overline{u_r'u_z'}|$) for fbw with axial strain, with swirl. From top to bottom: TD, PR, CT, VP, and DS+VD. For more details, see figure 6.31).

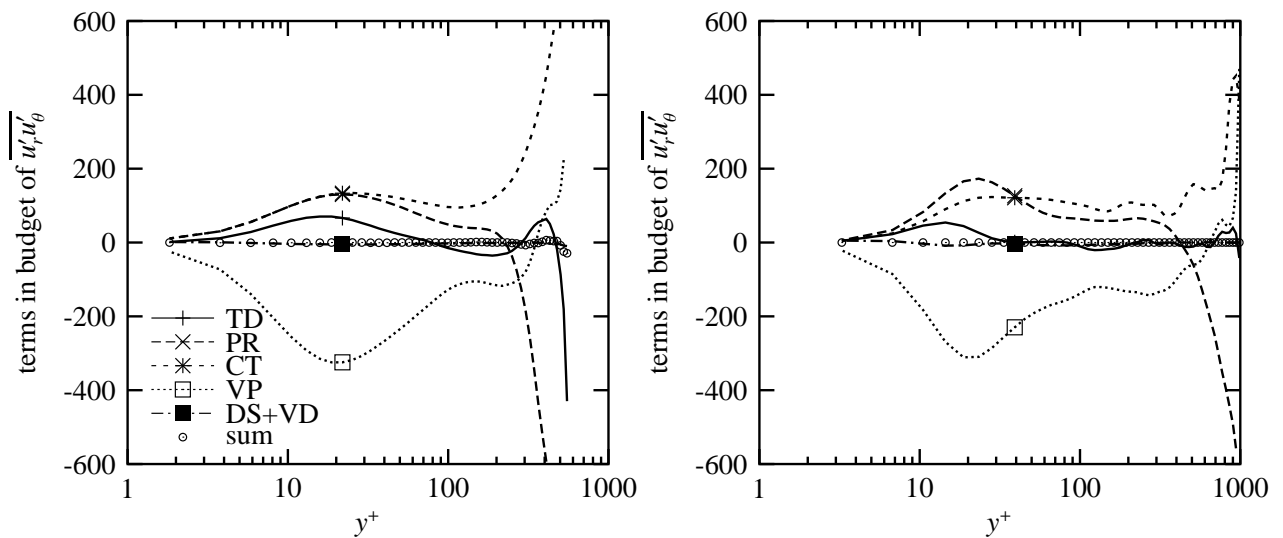


Figure 6.38: Budget terms for $\overline{u'_r u'_\theta}$ -budget. For flow with swirl at $z/D = -1.8$ and $z/D = 2.4$.

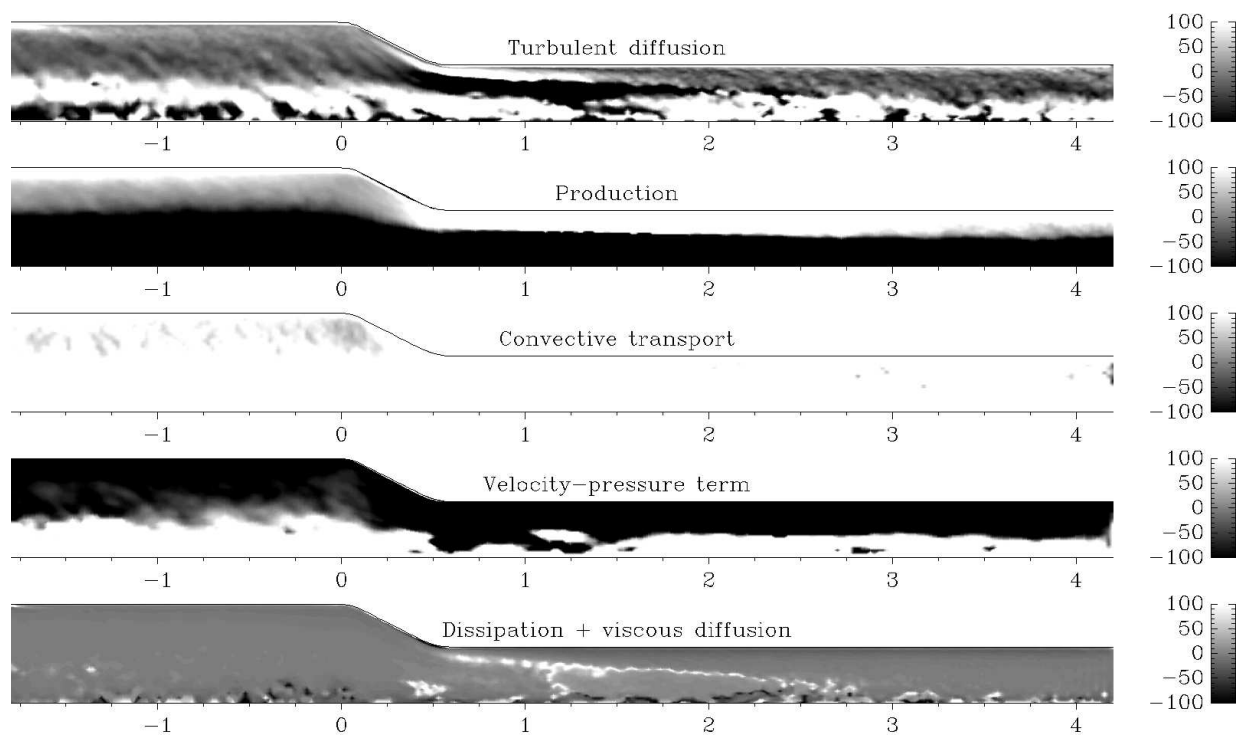


Figure 6.39: Terms in the budget of $\overline{u'_r u'_\theta}$ (normalised with the local $|\overline{u'_r u'_\theta}|$) for flow with axial strain, with swirl. From top to bottom: TD, PR, CT, VP, and DS+VD. For more details, see figure 6.31).

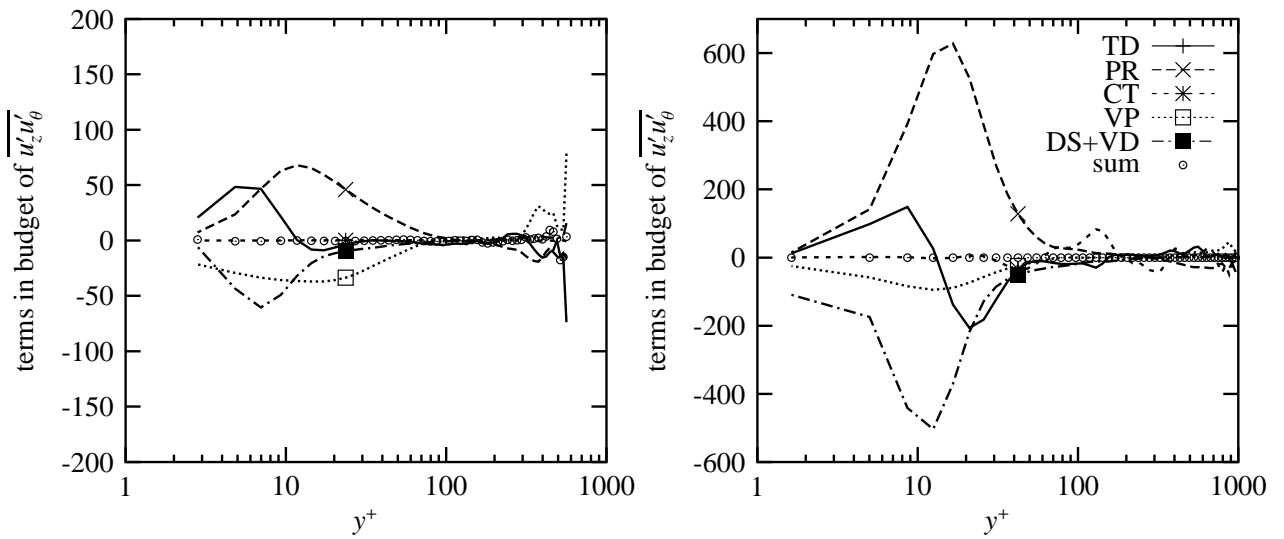


Figure 6.40: Budget terms for $\overline{u'_z u'_\theta}$ -budget. For flow with swirl at $z/D = -1.8$ and $z/D = 2.4$.

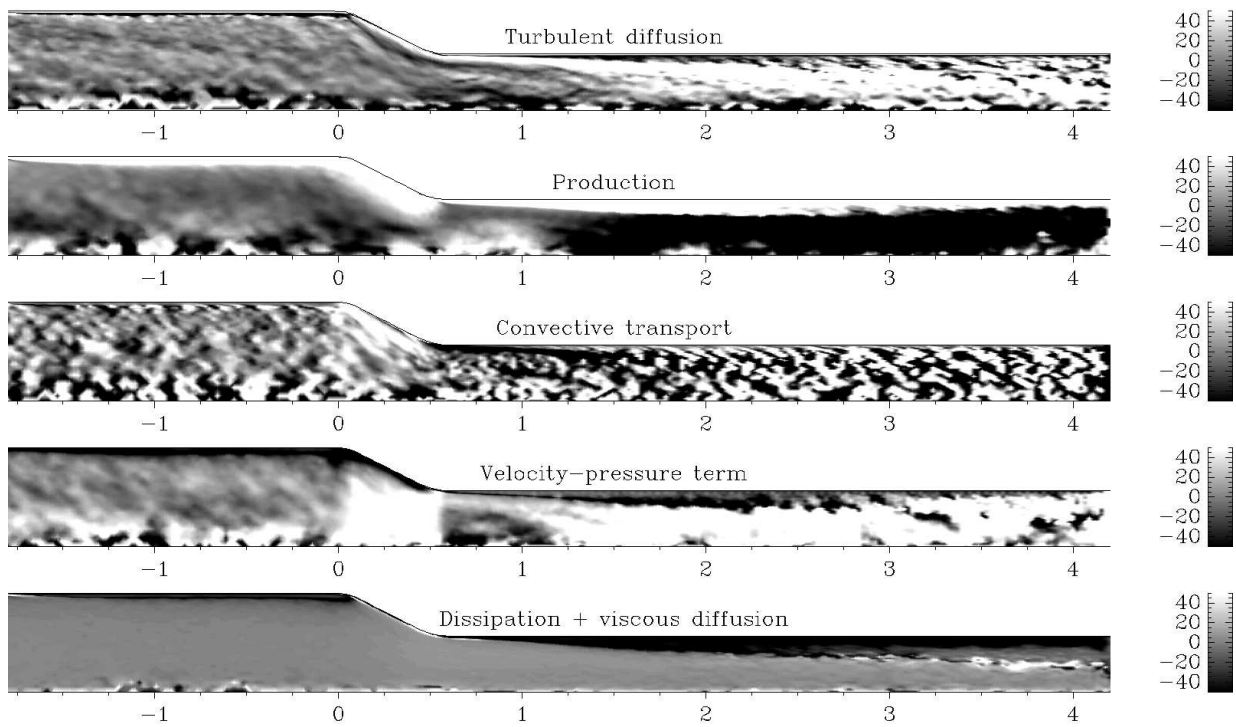


Figure 6.41: Terms in the budget of $\overline{u'_z u'_\theta}$ (normalised with the local $|\overline{u'_z u'_\theta}|$) for flow with axial strain, with swirl. From top to bottom: TD, PR, CT, VP, and DS+VD. For more details, see figure 6.31).

At $z = 2.4D$, additionally, the production term becomes important near the wall. In the fields shown in figure 6.35 the same structure occurs as in the budget of $\overline{u'_r u'_r}$: a streak originating at the trailing edge of the contraction and extending toward the pipe centre further downstream. This structure has nearly disappeared at $z/D = 2.4$. In this streak the production term is positive and the velocity-pressure term is negative. The turbulent diffusion term tends to remove $\overline{u'_\theta u'_\theta}$ away from the production zone. One would expect a positive production term near the pipe wall, given the shear in $\overline{u_\theta}$. However, the budget at $z/D = -1.8$ has been derived from the simulation of the straight pipe, in which $\overline{u_\theta}$ was forced. The forced profile had such a steep gradient of $\overline{u_\theta}$ near the wall (see figure 6.11), that the production term could not be resolved. The budget at $z/D = -1.8$, derived from the contraction model in which $\overline{u_\theta}$ is *not* forced (not shown), indeed shows a positive production term for $\overline{u'_\theta u'_\theta}$.

Figures 6.36 and 6.37 show the budgets of $\overline{u'_r u'_z}$. Upstream of the contraction, the main difference between the flow without swirl and the swirling flow occurs near the pipe axis: in the swirling flow a large production term (absent in the non-swirling case) is balanced by convective transport and the pressure-velocity term. Downstream of the contraction the same difference occurs, but the magnitude of the terms near the pipe axis is smaller relative to the near-wall values. When considering the fields of the budget terms (figure 6.37), the most striking feature is the streak of negative production and positive pressure-velocity term that originates at the trailing edge of the contraction. This structure is also visible in the shear-stress fields (see figure 6.21). Furthermore, there is mostly positive production in the rest of the pipe cross-section (as opposed to only near-wall production in the non-swirling case).

The $\overline{u'_r u'_\theta}$ budget (figures 6.38 and 6.39) is dominated by high values for most terms near the pipe axis: negative production and positive convective transport and a pressure-velocity term. In the near-wall region for $y^+ < 100$ the pressure-velocity term is a loss term and convective transport and production are positive. In figure 6.39 it can be seen that turbulent diffusion mainly plays a role inside the contraction, down to $z = 2D$, as well as around the pipe axis. The pressure velocity term is positive around the pipe axis, but directly downstream of the contraction the region of positive VP is smaller as compared to upstream of the contraction and to the region $z > 1.5D$. Finally, contrary to the budgets of other stresses, the convective transport term is important in large parts of the domain. This is due to the curvature induced terms involving $\overline{u_\theta}/r$.

The budget of $\overline{u'_z u'_\theta}$ (figures 6.40 and 6.41) mainly shows large terms in the near-wall region. There is a complicated balance between production and turbulent diffusion (mostly positive) and dissipation and the pressure-velocity term. Close to the pipe axis there is a region where the pressure-velocity term is the gain term and production and turbulent diffusion are negative. Downstream of the contraction the terms are small near the pipe axis. Near the wall there is again a balance between production (positive) and pressure-velocity and dissipation. The turbulent diffusion term is again smaller (relative to the others) than upstream of the contraction, and redistributes the stress radially. The fields of the budget terms (figures 6.41) reveal that inside the contraction production of $\overline{u'_z u'_\theta}$ occurs near the wall. Furthermore, the pressure-velocity term is a large gain term inside the contraction (except near the wall), probably due to the simultaneous occurrence of large axial pressure gradient fluctuations and large fluctuations in u_θ .

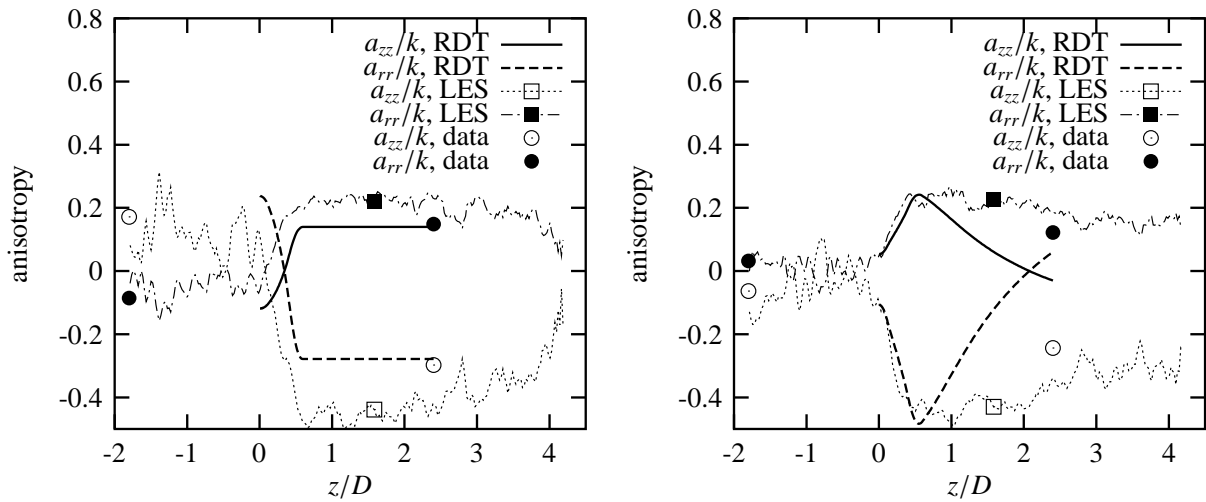


Figure 6.42: Stress anisotropy on the centre line: comparison between LES results, RDT and experimental data. Flow without swirl (left) and with swirl (right). LES and experimental results refer to a $Re_{bulk} = 2 \cdot 10^4$.

6.2.3 Stress anisotropy at the pipe axis

Analogously to the analysis in section 5.2.5, the axial development of the stress anisotropy at the pipe axis will be studied. Since in the model none of the stresses are available at the centreline, the centreline value is obtained by extrapolation of the radial profiles. To this end, quadratic extrapolation was used. The resulting axial profiles are shown in figure 6.42 for the flow without and with swirl. Apart from the LES results, also the RDT predictions (starting at $z = 0$) and the experimental data are shown. Note that the apparently random variation of the anisotropies in the LES results is due to the very limited number of independent samples available (see appendix A).

For the non-swirling flow, the anisotropies at the entrance of the domain compare well with the experimental data. Between $z = -1.8D$ and the entrance of the contraction, the anisotropy decreases somewhat. As a result, the starting values for the RDT analysis are too high, since those values were based on observations at $z = -1.8D$ (and for $Re_{bulk} = 10^5$). As a consequence of the incorrect value for the anisotropies at $z = 0$, the values at the end of the contraction are incorrect as well. However, there is a close correspondence between the change in the anisotropies, within the contraction, as given by the LES and as predicted by RDT. At $z = 2.4D$ the LES results show a higher anisotropy than both the observations and the RDT analysis. The LES results suggest that only downstream of $z = 2.5D$ the anisotropies start to diminish gradually.

For the swirling flow both the experimental data and the LES results show a smaller stress anisotropy upstream of the contraction. The change in anisotropy between $z = -1.8D$ and the entrance of the contraction is small. Consequently, the starting values for the RDT analysis correspond to both the experimental values and the LES results. The agreement between LES results and RDT analysis in the development of the anisotropy *within* the contraction is striking. However, downstream of the contraction, the RDT analysis (which is no longer valid there) predicts

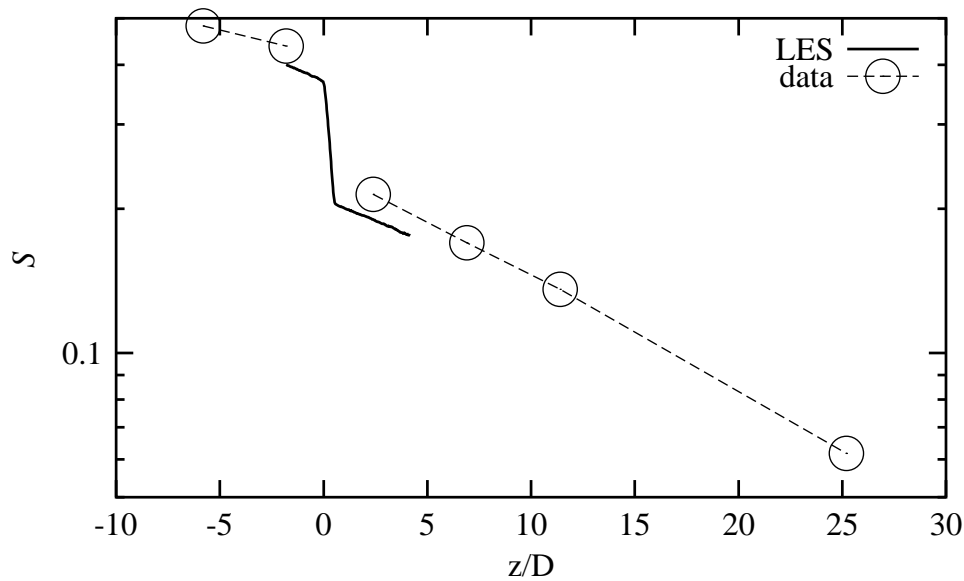


Figure 6.43: Axial development of the swirl number in the LES, compared to axial development in experimental data. The axial position has been scaled with the *upstream* pipe diameter.

a sharp decrease in anisotropy, whereas the LES results suggest that the anisotropy downstream of the contraction remains fairly constant (as in the cases of the non-swirling flow). The LDA data show a *small* decrease in anisotropy, but larger than the LES results. The experimental data at $z = 2.4D$ show a smaller anisotropy than the LES results, i.e. more change in anisotropy. The LES anisotropies start to diminish further downstream. It is not possible to tell whether this discrepancy is due to an incorrect representation of what happens inside the contraction (experimental data are not available directly downstream), or to an error in the development of the anisotropies, downstream of the contraction.

The close agreement between RDT and LES results for the anisotropy development inside the contraction suggests that RDT captures the –small– rotation induced modification of the development of the anisotropy well. Downstream of the contraction, however, the linear effect of rotation on the anisotropy becomes negligible as compared to other terms (i.e. non-linear terms like turbulent diffusion, and part of the velocity pressure interaction) and other terms neglected in RDT.

Unfortunately, the statistical error in the budget terms near the pipe axis is very large. Consequently, the changes in the anisotropy, as presented in figure 6.42, can not be traced back to the budget terms that cause those changes.

6.2.4 Axial development of the swirl number

Figure 6.43 shows the axial development of the swirl number in the large eddy simulation, compared to the swirl numbers obtained in the laboratory experiment. The first notable feature is that the swirl number in the simulation is somewhat lower than in the laboratory data. The \bar{u}_θ -profile

of the simulation matches the experimental data perfectly due to the forcing method. Therefore, the discrepancy in the swirl numbers must be attributed to the difference in the shape of the \bar{u}_z -profile. The simulation exhibits an exaggerated bump near the pipe centre. Consequently, \bar{u}_z is too low in the region outside the vortex core, where \bar{u}_r is highest. This results in a lower swirl number (see equation (2.17)). Downstream of the contraction, the role of the two velocity components is reversed: the \bar{u}_z -profile is correct, whereas \bar{u}_θ is too low. This again results in a too low swirl number.

A comparison of the swirl decay rate between data and LES is difficult, since in the simulation the decay rate needs to be determined from a very short pipe section (1.8 diameters upstream of the contraction and 3.6 diameters downstream). Upstream of the contraction, the decay of swirl appears to be higher in the simulation than in the data ($\beta = 0.0425$ for the LES, versus $\beta = 0.0245$ in the data). On the other hand, downstream of the contraction the LES shows a slower decay than the experimental data ($\beta = 0.0240$ for the LES, versus $\beta = 0.0307$ in the data). Given the observations above regarding the too low value of the swirl number, the incorrect decay rates may well be the result of an incorrect development of the \bar{u}_z -profile.

6.3 To conclude

The aim of this chapter has been twofold. The first objective is to validate the results of the LES model with experimental data. The second step is to extract information from the simulation results that can not be obtained from the experimental data. Here an attempt will be made to assemble a clear picture of the flow results that were presented. The results for the flow without swirl and with swirl will be discussed separately.

6.3.1 Axial strain without swirl

The LES model is able to simulate the flow with axial strain well. There are only some minor problems, primarily in the wall region. The most serious deviation is in $\overline{u'_r u'_r}$, downstream of the contraction. For $r/R > 0.8$ this stress is overpredicted by a factor of 2. Temporal spectra of u_z and u_r near the pipe axis show qualitatively good agreement between LES and experimental data. Given the low Reynolds number the inertial subranges are necessarily short, especially in the LES results.

The two-dimensional fields of mean velocities and stresses, derived from the LES results, give insight into the processes inside and downstream of the contraction. The most prominent feature is the region of high $\overline{u'_r u'_r}$ (and $\overline{u'_\theta u'_\theta}$) originating inside the contraction. This region is not attached to the wall, and only at $z/D = 2.5$ the wall-produced $\overline{u'_r u'_r}$ becomes more important. A possible exaggeration of this region originating in the contraction may be the cause of the over-estimation of $\overline{u'_r u'_r}$, as compared to the experimental results. Another notable feature is that the upstream influence of the contraction is limited to less than $\frac{1}{2}D$, and mainly visible in $\overline{u'_z u'_z}$. Downstream of the contraction the flow behaves as a developing pipe flow, with a boundary layer that grows downstream.

The budget of the turbulent stresses, as derived from the LES results show essentially that the upstream and downstream of the contraction the same terms are relevant for each stress, although

their absolute and relative magnitude may change. Production plays a role for $\overline{u'_z u'_z}$ and $\overline{u'_r u'_z}$. The velocity-pressure interaction term is a major term for $\overline{u'_r u'_r}$, $\overline{u'_\theta u'_\theta}$ and $\overline{u'_r u'_z}$. Turbulent diffusion is important for $\overline{u'_r u'_r}$, $\overline{u'_z u'_z}$ and $\overline{u'_r u'_z}$. The dissipation and viscous diffusion terms play a role for the normal stresses only. The role of the turbulent diffusion term is for all stresses the same: radial redistribution of the stress near the wall ($y^+ < 100$).

Apart from the axial development of the flow downstream of the contraction, the processes *inside* the contraction are of interest. In terms of the stress budgets, the most significant features appear in the $\overline{u'_r u'_r}$ and $\overline{u'_r u'_z}$ budgets: positive production for both stresses, a negative velocity pressure term for $\overline{u'_r u'_r}$ and a negative convective transport for $\overline{u'_r u'_z}$. The trailing edge of the contraction is significant in the budgets of more stresses. Here, negative production occurs for $\overline{u'_r u'_r}$, $\overline{u'_z u'_z}$ and $\overline{u'_r u'_z}$, as well as positive convective transport for *all* stresses. Furthermore, the velocity-pressure interaction term is a gain term for $\overline{u'_r u'_r}$ and $\overline{u'_r u'_z}$, and a loss term for $\overline{u'_\theta u'_\theta}$ at this location.

6.3.2 Axial strain with swirl

The first point to be addressed is the skill of the proposed method used to produce the swirl in the LES model with periodic boundary conditions. Since the method relies on minimising the difference between the simulated $\overline{u_\theta}$ -profile and the experimentally determined profile, it is not surprising that the simulated profile matches the experimental data perfectly. However, the profiles of $\overline{u_z}$ and the turbulent stresses show some (serious) deviations. The first deviation is that the structure of the vortex core is not well reproduced. This can be attributed to the fact that a part of the flow structure is not determined locally but is influence by upstream effects: the flow is axially inhomogeneous. Furthermore, the axial pressure gradient is assumed to be independent of the radial coordinate in the model, which is not necessarily true in an axially developing flow. Another discrepancy between LES results and experimental data is the fact that in the simulation the level of the turbulent stresses is generally higher than in the data. This is probably due to a difference in the ratio u_* / U_{bulk} between LES and experiment. The ratio u_* / U_{bulk} as obtained from the LES has been used to scale the experimental data.

Downstream of the contraction the agreement between LES and experimental results is of the same order as upstream. Since the vortex core is not as pronounced as upstream of the contraction, the main discrepancy is that the turbulent stresses are too high in general. Furthermore, the mean tangential velocity is too low, i.e. the swirl has decayed too quickly.

The two-dimensional fields of mean velocities and shear stresses show that *inside* the contraction the normal stresses are mainly changed in magnitude, whereas the profiles of the shear stresses are changed in shape as well. Downstream of the contraction the vortex core remains visible in the normal stress $\overline{u'_r u'_r}$ and $\overline{u'_\theta u'_\theta}$. Moreover, patches of negative $\overline{u'_r u'_z}$ and $\overline{u'_z u'_\theta}$ are present, the region $0.5 < z/D < 2.5$. If the shear stress $\overline{u'_r u'_z}$ is used as an indicator of the growth of the boundary layer, the rate of growth appears to be larger for the swirling flow than for the non-swirling flow. This is in accordance with the destabilising effect of concave curvature on a shear flow.

In the stress budgets two regions appear where gain and loss terms are large: near the wall (as in any pipe flow) and near the axis, in the vortex core. For $\overline{u'_r u'_r}$ and $\overline{u'_r u'_\theta}$ the magnitude

of the terms near the wall is even negligible. Inside the contraction, the origin of large change in the anisotropy of the normal stresses can be found: positive production of $\overline{u'_r u'_r}$ and negative production of $\overline{u'_z u'_z}$. In the region downstream of the contraction (mainly $0.5 < z/D < 3$) complicated patterns occur of production, turbulent diffusion and redistribution by the velocity-pressure terms. Convective transport mainly plays a role in the budgets of $\overline{u'_r u'_r}$ (removal of $\overline{u'_r u'_r}$ from the production zone inside the contraction) and the budget of $\overline{u'_r u'_\theta}$ (due to the curvature induced term involving $\overline{u_r}/r$).

7

Conclusion

This final chapter aims at bringing together the conclusions of previous chapters, answering the questions posed in the introduction, and providing suggestions on issues to be solved in the future.

7.1 Current knowledge

In the review of the current literature the effects of swirl and axial strain have first been considered separately. The effects of swirl can be subdivided into a number of effects, each of which is covered by a vast amount of previous research: streamline curvature (and stability effects), rotation, three-dimensionality and swirl decay. The effect of axial strain has been divided in: the effect on the mean velocity, the effect on the turbulent stresses, and the relaxation of the flow downstream of the axial strain (i.e. developing pipe flow). In combination with the limited information that is available on the *combined* effect of rotation and axial strain, a qualitative picture has emerged of what happens in the flow that is the subject of this thesis.

The flow domain can be divided into three regions: upstream, inside and downstream of the contraction. Upstream of the contraction the flow is decaying swirling flow (section 2.2), which is dominated by non-linear processes:

- stabilising effects –near the centre– or destabilising effects –near the wall– of streamline curvature;
- reduced dissipation due to rotation;
- three-dimensionality in the near-wall region.

Then the fluid passes through the contraction, a process that combines swirl and axial strain (section 2.4). The effect of the axial strain on turbulent quantities is well described by linear theory, but this process is strongly influenced by non-linear processes which are due to streamline curvature. Finally, downstream of the contraction, again a stage of decaying swirling flow is entered. But since the flow has been heavily distorted by the axial strain, this stage has also the characteristics of a developing pipe flow (section 2.3.3). In a developing pipe flow, the turbulent quantities usually relax more quickly to their fully developed values than mean quantities. But two complications arise:

- The relaxation process might be influenced by the non-linear effects of streamline curvature;
- The flow will only attain a fully developed state (i.e. with zero axial development) when the swirl has decayed completely.

7.2 Experimental results

A comprehensive laboratory experiment has been carried out to determine the characteristics of turbulent swirling pipe flow with axial strain. A closed pipe system that previously had been used to study swirling pipe flow, has been modified to include axial strain (by reduction of the pipe diameter in a part of the total length of the pipe). Data on the mean velocities and turbulent stresses have been obtained using Laser Doppler Anemometry (LDA) at six axial positions (two upstream and four downstream of the contraction). In order to identify the separate effects of swirl, axial strain and Reynolds number, the measurements have been carried out both with swirl and without swirl, and at two Reynolds numbers.

7.2.1 Axial strain without swirl

The mean axial velocity is transformed from a profile representative of fully developed pipe flow to a flat profile as in the entrance region of a pipe. Also the normal stresses are nearly uniform across the pipe cross-section, and the shear stress $\overline{u'_r u'_z}$ is small except near the walls. The effect of the axial strain on the anisotropy of the normal stresses is to reverse the signs of the anisotropies of $\overline{u'_z u'_z}$ on one hand and $\overline{u'_r u'_r}$ and $\overline{u'_\theta u'_\theta}$ on the other. This effect is well described by linear theory (RDT).

Approximately 40 pipe diameters downstream of the contraction (downstream pipe diameters) the profiles of the mean velocity and the normal stress have returned to their fully developed shape. The shear stress $\overline{u'_r u'_z}$ has not yet completely relaxed at that axial position, however. The relaxation toward the fully developed profiles occurs first near the wall. Further downstream, the region of the pipe cross-section affected by this development grows toward the pipe axis.

7.2.2 Axial strain with swirl

The effect of the axial strain on the profiles of $\overline{u_z}$ and $\overline{u_\theta}$ near the pipe axis is in accordance with the inviscid analysis of Batchelor (1967): $\overline{u_z}$ develops a bump and $\overline{u_\theta}$ becomes slightly curved rather than straight. The swirl decay rate seems not to change dramatically by the axial strain. Likewise, the shape of the $\overline{u_\theta}$ -profile is not affected by the axial strain. The swirling flow is not skewed for a large part of the near-wall region, so there are no indications for a strongly three-dimensional boundary layer.

Upstream of the contraction the Reynolds stress tensor in the swirling flow is more isotropic than that in the non-swirling flow. The effect of the axial strain on the stress anisotropy is weaker than for the non-swirling flow. This is –qualitatively– predicted by RDT theory. Directly downstream the anisotropies of the stress tensor are very similar for the swirling and non-swirling flow, but further downstream they diverge again. At the position furthest downstream from the contraction, there is a clear distinction between the two different Reynolds numbers: for the lower Reynolds number the stress anisotropy is close to that for the non-swirling flow, whereas for the high Reynolds number there is a large difference between the swirling and non-swirling flow. This may have two reasons: the swirl decays faster for the lower Reynolds number, and the travel time from the contraction is a factor of 5 longer for the lower Reynolds number. The character of the stress tensor throughout the pipe cross-section differs considerably between the

non-swirling and swirling flow. In the non-swirling flow the turbulence is nearly axisymmetric with one major axis, at the vast majority of axial and radial positions (i.e. the stress tensor has two *equal* principal components that are smaller than the other, *larger*, principal component). In the swirling flow, the turbulence is not axisymmetric at most locations. Near the wall, the tensor is pancake-shaped (two major axes), near the pipe axis there is one major axis.

The effect of axial strain on the structure of the turbulence is that in the swirling flow much energy is transferred to larger scales, especially for u_r and u_θ . This translates into large integral length scales.

All results for the swirling flow suggest that, in this particular flow, a clear distinction can be made between a core region (roughly $r/R < 0.7$) and an outer region. In the core rotational effects play an important role. On the other hand, the near wall region behaves like a normal shear flow, despite the large angle between mean flow and axial direction.

7.3 Development of LES model and validation

Below, first the main steps in the development of the LES model for swirling flow with axial strain are described, followed by the validation of modelling results with the laboratory data.

7.3.1 Development

The aim was to construct an LES model that would be able to simulate exactly the same configuration as encountered in the laboratory experiment. The model used in this study is based on the cylindrical pipe model developed by Eggels (1994) and Pourquié (1994). The main characteristics of that model are: cylindrical coordinates, finite volume spatial discretisation, partly implicit, partly explicit temporal discretisation, Smagorinsky sub-grid scale stress model with Van Driest damping function, periodic boundary conditions in axial and tangential direction.

In order to simulate a swirling pipe flow with axial strain, a number of major modifications needed to be made. These entailed the coordinate system, the temporal discretisation, the subgrid-scale stress model and the boundary conditions.

Whereas the original model used cylindrical coordinates, the new model uses cylindrical coordinates where the pipe radius is dependent on the axial position. This results in a non-orthogonal coordinate system. The velocity components have been kept orthogonal: axial, radial and tangential. Although this is not the most logical construction if one considers the model as a step toward an LES in general coordinates, it was the most logical choice in order to re-use as much ideas as possible from the original model.

In the original model, implicit time discretisation was only applied to terms with derivatives in the tangential direction (because of the small tangential grid-spacing near the pipe centre). However, due to the small grid spacing and large sub-grid scale viscosities near the wall (downstream of the contraction), the time step was severely limited as well due to terms with derivatives in the *radial* direction. Therefore, implicit time discretisation was also applied to terms with derivatives in the radial direction. This was only done in the region near the wall (the outer 75% of the grid points). The total time discretisation is a so-called fractional step method, in which first all terms but the pressure gradient terms are applied. In the second step the new pressure is computed such

that the resulting field is divergence free. The Poisson solver needed in this second step has been rewritten completely, in order to cope with the new coordinate system. Since this step is one of the most –computationally– expensive parts of an LES model, care has been taken to allow for fast convergence of the iterative solver and for optimal memory usage for both vector and scalar processors.

In the Van Driest damping function, the local distance to the wall, expressed in wall units (with the local wall shear stress) is used to determine the reduction of the sub-grid scale viscosity due to the presence of the wall. In the present model this damping has been replaced by an approach based on the reduction of the (resolved) normal-to-the-wall component of the stress tensor due to the presence of the wall (similar to, but slightly different than Horiuti (1993) and Eggels (1994)).

With respect to the boundary conditions a number of modifications needed to be made. Firstly, the boundary conditions at the wall had to be adapted to take into account the angle between the velocity components and the coordinate system inside the contraction, i.e. the radial velocity is no longer perpendicular to the wall, as is the radial pressure gradient. Furthermore, the inflow and outflow boundary conditions could no longer be periodic, since the pipe radius (and the flow) at inflow and outflow differ. At the outflow plane a convective boundary condition was used. At the inflow plane velocities are prescribed that have been derived from a separate simulation *with* periodic boundary conditions. For the flow without swirl this was simply a fully developed pipe flow. For the swirling flow simulations, a tangential forcing was introduced (based on van Haarle (1995)) that forces the mean tangential velocity to a prescribed radial profile (derived from the laboratory measurements). Another forcing method, in which a time-independent forcing derived from the measured $\overline{u'_r u'_\theta}$ -profile is used, was tested as well, but appeared to give inferior results and was not used.

7.3.2 Validation

In order to make a fair comparison of laboratory measurements and LES results possible, a method has been developed to assign an estimate of their statistical error (Moene and Michels, 2002) to both measurements *and* LES results.

The LES model is able to simulate the flow with axial strain well. There are only some minor discrepancies, primarily in the wall region. The most serious deviation is in $\overline{u'_r u'_r}$ downstream of the contraction. For $r/R > 0.8$ this stress is overpredicted by a factor of 2. Temporal spectra of u_z and u_r at the pipe axis show qualitatively good agreement between LES and experimental data. Given the low Reynolds number, the inertial subranges are necessarily short, especially in the LES results.

The results for the flow with swirl are more mixed. The first point to be addressed is the skill of the proposed method used to produce the swirl in the LES model with periodic boundary conditions. Since the method relies on minimising the difference between the simulated $\overline{u_\theta}$ -profile and the experimentally determined profile, it is not surprising that the simulated profile matches the experimental data perfectly. However, the profiles of $\overline{u_z}$ and the turbulent stresses show some (serious) deviations. The first deviation is that the structure of the vortex core is not well reproduced. This can be attributed to the fact that a part of the flow structure is not determined locally but is influenced by upstream effects: the flow is axially inhomogeneous.

Furthermore, the axial pressure gradient is assumed to be independent of the radial coordinate in the model, which is not necessarily true in an axially developing flow. Another discrepancy between LES results and experimental data is the fact that in the simulation the level of the turbulent stresses is generally higher than in the data. This is probably due to a difference in the ratio u_*/U_{bulk} between LES and experiment. The ratio u_*/U_{bulk} as obtained from the LES has been used to scale the experimental data.

Downstream of the contraction the agreement between LES and experimental results is of the same order as upstream. Since the vortex core is not as pronounced as upstream of the contraction, the main discrepancy is that the turbulent stresses are too high in general. Furthermore, the mean tangential velocity is too low, i.e. the swirl has decayed too quickly.

7.4 LES results

From the above it is clear that the validation of the LES results with laboratory measurements is satisfactory only for the flow without swirl. Therefore, the further analysis of the LES results of the simulation *with swirl* can be qualitative at best.

7.4.1 Axial strain without swirl

The two-dimensional fields of mean velocities and stresses, derived from the LES results, give insight into the processes inside and downstream of the contraction where no experimental data are available. The most prominent feature is the region of high $\overline{u'_r u'_r}$ (and $\overline{u'_\theta u'_\theta}$) originating inside the contraction. This region is not attached to the wall, and only at $z/D = 2.5$ the wall-produced $\overline{u'_r u'_r}$ becomes more important. Another notable feature is that the upstream influence of the contraction is limited to less than $\frac{1}{2}D$, and mainly visible in $\overline{u'_z u'_z}$. This limited upstream influence supports the use of a separate simulation to produce inflow boundary conditions.

The budget of the turbulent stresses, as derived from the LES results show essentially that upstream and downstream of the contraction the same terms are relevant for each stress, although their absolute and relative magnitude may change. Production plays a role for $\overline{u'_z u'_z}$ and $\overline{u'_r u'_z}$. The velocity-pressure interaction term is a major term for $\overline{u'_r u'_r}$, $\overline{u'_\theta u'_\theta}$ and $\overline{u'_r u'_z}$. Turbulent diffusion is important for $\overline{u'_r u'_r}$, $\overline{u'_z u'_z}$ and $\overline{u'_r u'_z}$. The dissipation and viscous diffusion terms play a role for the normal stresses only. The role of the turbulent diffusion term is the same for all stresses: radial redistribution of the stress near the wall ($y^+ < 100$).

Apart from the axial development of the flow downstream of the contraction, the processes *inside* the contraction are of interest. In terms of the stress budgets, the most significant features appear in the $\overline{u'_r u'_r}$ and $\overline{u'_r u'_z}$ budgets: positive production for both stresses, a negative velocity-pressure term for $\overline{u'_r u'_r}$ and a negative convective transport for $\overline{u'_r u'_z}$. The *trailing edge* of the contraction is significant in the budgets of other stresses as well.

7.4.2 Axial strain with swirl

For the flow with swirl and axial strain, the two-dimensional fields of mean velocities and stresses can be used only qualitatively, given the discrepancies with the laboratory data. The

two-dimensional fields of mean velocities and stresses show that *inside* the contraction the normal stresses are mainly changed in magnitude, whereas the profiles of the shear stresses are changed in shape as well. The changes in the normal stresses are in close accordance with Rapid Distortion Theory. Downstream of the contraction the vortex core remains visible in the normal stress $\overline{u'_r u'_r}$ and $\overline{u'_\theta u'_\theta}$. Moreover, patches of negative $\overline{u'_r u'_z}$ and $\overline{u'_z u'_\theta}$ are present in the region $0.5 < z/D < 2.5$. If the shear stress $\overline{u'_r u'_z}$ is used as an indicator of the growth of the boundary layer, the rate of growth appears to be larger for the swirling flow than for the non-swirling flow. This is in accordance with the destabilising effect of concave curvature on a shear flow.

In the stress budgets two regions appear where gain and loss terms are large: near the wall (as in any pipe flow) and near the axis, in the vortex core. For $\overline{u'_r u'_r}$ and $\overline{u'_r u'_\theta}$ the magnitude of the terms near the wall is even negligible. Inside the contraction, the origin of large change in the anisotropy of the normal stresses can be found: positive production of $\overline{u'_r u'_r}$ and negative production of $\overline{u'_z u'_z}$. In the region downstream of the contraction (mainly $0.5 < z/D < 3$) complicated patterns occur of production, turbulent diffusion and redistribution by the velocity-pressure terms. Convective transport mainly plays a role in the budgets of $\overline{u'_r u'_r}$ (removal of $\overline{u'_r u'_r}$ from the production zone inside the contraction) and the budget of $\overline{u'_r u'_\theta}$ (due to the curvature induced term involving $\overline{u_r}/r$).

7.5 Perspectives

The outlook for future work is twofold. On one hand there are results ready to be used by turbulence modellers. On the other hand improvements are needed with respect to the LES of swirling flows.

The extensive dataset of laboratory measurements of both swirling and non-swirling flow with axial strain, provides a good benchmark for turbulence models. Therefore, the dataset will be made available to the turbulence modelling community. Furthermore, the validation of the LES results of the flow *without* swirl showed that the LES model is well able to handle this flow. Therefore, the additional information that can be derived from the LES (in addition to laboratory measurements) will be valuable to turbulence modellers as well.

The LES results for the flow *with* swirl did not pass the validation well. The main reason for this, is that the flow at the entrance of the LES domain was not well represented. One could argue that the flow upstream of the contraction was too complicated, due to the fact that it was not in local equilibrium. On the other hand, this flow *does* occur, so in the end one should be able to generate it with an LES model as well. Two issues with respect to the generation of the inflow boundary condition are important. The mean tangential velocity is forced to be exactly equal to the observed tangential velocity. Especially near the wall, where $\overline{u_\theta}$ has a large radial gradient, this may be too restrictive: the model is left no room to produce an $\overline{u_\theta}$ -profile that is consistent with its turbulent stresses. Another point is that the $\overline{u_z}$ -profile is not that of a fully developed pipe flow. Consequently, the usual axial forcing (an axial pressure gradient that is independent of time and radial position) may need to be replaced by a forcing that is similar to that for the tangential velocity.

An inescapable numerical problem in the simulation of swirling pipe flow is the problem of

oscillations that occur in the near-wall region. The only real solution is to decrease the axial grid spacing without decreasing the filter size. Another numerical problem is the use of cylindrical coordinates: near the pipe axis this leads to grid-cells with an extreme aspect ratio. It is questionable how well the sub-grid stress model will be able to produce the correct sub-grid stress, as is apparent from the small bumps in SGS contribution of $\overline{u'_r u'_r}$ and $\overline{u'_\theta u'_\theta}$ near the pipe axis. The modification proposed by (Scotti *et al.*, 1993) has been tested but did not give satisfactory results. A final point is not so much related to the cylindrical coordinates as such, but rather is related to the fact that one works in an axisymmetric flow. The statistical error in the quantities derived from the LES fields is much larger near the pipe axis, due to the small number of independent samples. In a flow that is axially homogeneous this is not such a large problem, since there are three dimensions in which averaging takes place (leaving two dimensions if the tangential direction yields only few independent samples). However, in the present simulations, the flow is not axially homogeneous, so that the data near the pipe axis are effectively averaged only in the time dimension. This results in large statistical errors in the results, in particular in shear stresses and stress budget terms. This should be borne in mind in the designing of future LES experiments.

A

Statistical analysis of turbulent data

Since turbulent flows are not reproducible in detail, they can be described in a statistical sense only. In this appendix some statistical tools needed for the analysis of turbulent data will be discussed. The first section deals with various types of averages. This is an important issue, since the definition of all statistical quantities involve averaging. Section A.2 discusses a method to determine the errors in the estimation of statistical quantities. Finally it is shown how these error estimates can be applied to LDA data and LES results.

A.1 Averages

A.1.1 Reynolds decomposition

The starting point for the statistical analysis of turbulence is the Reynolds decomposition of a random variable (say u):

$$u = \bar{u} + u', \quad (\text{A.1})$$

where \bar{u} is a –yet– undefined mean value and u' is the deviation from that mean.

Apart from the mean, all other descriptors are based on u' rather than u (so-called central moments). Taking two variables u and v that are defined in four-dimensional space (space plus time), some examples of central moments are:

$$\text{variance} \quad \mu_{uu}(\mathbf{s}) = \overline{u'(\mathbf{s})u'(\mathbf{s})} \quad (\text{A.2})$$

$$3^{\text{rd}} \text{ order moment} \quad \mu_{uuu}(\mathbf{s}) = \overline{u'(\mathbf{s})u'(\mathbf{s})u'(\mathbf{s})} \quad (\text{A.3})$$

$$\text{covariance} \quad \mu_{uv}(\mathbf{s}) = \overline{u'(\mathbf{s})v'(\mathbf{s})} \quad (\text{A.4})$$

$$\text{autocovariance with separation } \mathbf{r} \quad R_{uu}(\mathbf{s}, \mathbf{s} + \mathbf{r}) = \overline{u'(\mathbf{s})u'(\mathbf{s} + \mathbf{r})} \quad (\text{A.5})$$

$$\text{cross-covariance with separation } \mathbf{r} \quad R_{uv}(\mathbf{s}, \mathbf{s} + \mathbf{r}) = \overline{u'(\mathbf{s})v'(\mathbf{s} + \mathbf{r})} \quad (\text{A.6})$$

When the fields u and v are stationary in all directions the central moments will become independent of \mathbf{s} . R_{uu} and R_{uv} will be a function of the separation only. In general an intermediate situation will exist where u and v will be stationary in some directions (e.g. time) and non-stationary in others (the space dimensions, for example).

A.1.2 Types of averages

In the previous section it was shown that all statistical quantities involve averaging. Reynolds (1895) formulated a number of conditions (the Reynolds conditions, see also Monin and Yaglom

(1971), page 207) on a 'useful' average. Monin and Yaglom state the general requirement for such a 'useful' average is that the "application of this rule to the differential equations of fluid dynamics will allow us to obtain sufficiently simple equations for the mean values of the fluid dynamic variables". They arrive at five relationships that should be satisfied:

$$\overline{u + v} = \bar{u} + \bar{v} \quad (\text{A.7a})$$

$$\overline{au} = a\bar{u} \quad \text{if } a = \text{constant} \quad (\text{A.7b})$$

$$\bar{a} = a \quad \text{if } a = \text{constant} \quad (\text{A.7c})$$

$$\frac{\partial \bar{u}}{\partial s} = \overline{\frac{\partial u}{\partial s}} \quad \text{where } s \text{ is } x_1, x_2, x_3 \text{ or } t \quad (\text{A.7d})$$

$$\overline{uv} = \bar{u}\bar{v} \quad (\text{A.7e})$$

The only average that satisfies this condition is the ensemble average. The latter is based on the existence of a hypothetical ensemble of similar flows (similar with respect to external conditions). If n is the index of a realisation of such a flow, then the ensemble average can be defined as:

$$\bar{u}(x_1, x_2, x_3, t) = \lim_{N \rightarrow \infty} \frac{1}{N} \sum_{n=1}^N u(x_1, x_2, x_3, t; n) \quad (\text{A.8})$$

In most practical cases one is not in a position to repeat an experiment a sufficient number of times to approach (A.8). Under certain conditions, however, the ensemble average can be replaced by a time or space average. Here the time average will be used as an example but the time coordinate can be replaced by any combination of time and place coordinates ¹.

The time average is defined as:

$$\bar{u}^T(x_1, x_2, x_3) = \frac{1}{T} \int_{-T/2}^{T/2} u(x_1, x_2, x_3, t) dt, \quad (\text{A.9})$$

where the dependence of u on the different components of \mathbf{s} was made explicit.

It can be shown (Monin and Yaglom, 1971, page 251) that for

$$\lim_{T \rightarrow \infty} \overline{|\bar{u}^T - \bar{u}|^2} = 0 \quad (\text{A.10a})$$

¹If averaging over more than one coordinate is performed, repeated integration is needed. E.g. averaging in t and x_2 direction would give:

$$\bar{u}^{T, L_2} = \int_{-T/2}^{T/2} \int_{-L_2/2}^{L_2/2} u(x_1, x_2, x_3, t) dx_2 dt$$

if

$$\lim_{T \rightarrow \infty} \frac{1}{T} \int_0^T R_{uu}(\tau, t) d\tau = 0 \quad (\text{A.10b})$$

A variable for which (A.10a) holds is called an ergodic variable. For stationary turbulent flows $R_{uu}(\tau)$ tends to zero as $\tau \rightarrow \infty$, thus (A.10b) is true. In practice the averaging in equation (A.9) can not be performed for $T \rightarrow \infty$, so that the time average is an estimate rather than a substitute for the ensemble average. This problem will be dealt with in the next section.

A.2 Statistical errors

Due to the fact that a time (or space) average in general is not equal to the ensemble average that it is supposed to estimate, descriptive properties describing a turbulent flow can only be estimated within a certain error. In this section estimates for this error for first and second-order (one-point) moments of one and two variables will be given. The material presented here is based on Benedict and Gould (1996), Lenschow *et al.* (1994), Monin and Yaglom (1971) and Bendat and Piersol (1986). Time t will be used as the only independent variable², but this restriction will be lifted in the next section. Only random errors will be dealt with. For a discussion on systematic errors in statistical quantities the reader is referred to Lenschow *et al.* (1994) and Bendat and Piersol (1986).

A.2.1 Statistics derived from series of independent samples

If u_i is a series of N independent samples of u , the estimate of the r -th central moment statistic m_r is

$$m_r = \frac{1}{N} \sum_{i=1}^N (u_i - \bar{u})^r . \quad (\text{A.11})$$

For a large number of samples the deviations of m_r from $\overline{(u - \bar{u})^r}$ become normally distributed and the error variance becomes (Benedict and Gould, 1996; Kendall and Stuart, 1958):

$$\text{var}(m_r) = \frac{1}{N} \left(\mu_{2r} - \mu_r^2 + r^2 \mu_{r-1}^2 \mu_2 - 2r \mu_{r+1} \mu_{r-1} \right) , \quad (\text{A.12})$$

where μ_r is the r -th central moment of u and terms of order N^{-2} have been neglected. When u is normally distributed, the higher order moments of u can be expressed in terms of the second order moment ($\mu_4 = 3\mu_2$, $\mu_6 = 15\mu_2$ and $\mu_8 = 105\mu_2$).

In the case of two series, u and v the estimate for the mixed central moment $m_{r,s}$ is:

$$m_{r,s} = \frac{1}{N} \sum_{i=1}^N (u_i - \bar{u})^r (v_i - \bar{v})^s . \quad (\text{A.13})$$

²This implies that autocovariance functions and crosscovariance functions will be functions of the separation only: $R_{uv}(\mathbf{s}, \mathbf{s}_2 - \mathbf{s}_1) = R_{uv}(t, t_2 - t_1) = R_{uv}(\tau)$

which will have an error variance:

$$\text{var}(m_{r,s}) = \frac{1}{N} \left(\mu_{2r,2s} - \mu_{r,s}^2 + r^2 \mu_{r-1,s}^2 \mu_{2,0} - 2r \mu_{r+1,s} \mu_{r-1,s} \right. \\ \left. s^2 \mu_{r,s-1}^2 \mu_{0,2} - 2r \mu_{r,s+1} \mu_{r,s-1} + 2rs \mu_{1,1} \mu_{r-1,s} \mu_{r,s-1} \right) \quad (\text{A.14})$$

A.2.2 Statistics derived from a continuous series

If one would know the value of u and v at every instant in time (or space) within a limited amount of time (say T), N would be infinite. However, the extent to which the error variance reduces to zero will depend on the time scale at which u and v vary. This is expressed in the integral time scale:

$$T_{r,s} = \int_0^\infty \rho_{r,s}(\tau) d\tau, \quad (\text{A.15})$$

with

$$\rho_{r,s}(\tau) = \frac{(u^r v^s(t) - \mu_{r,s})(u^r v^s(t + \tau) - \mu_{r,s})}{\mu_{r,s}^2} \quad (\text{A.16})$$

In order to apply expressions (A.12) and (A.14) in this situation, the number of samples N needs to be replaced by the number of independent samples. For the error variance of first and second order moments the number of independent samples, N_{ind} is:

$$N_{ind} = \frac{T}{2T_\alpha} \quad (\text{A.17})$$

for $T \gg T_\alpha$ and where a normal distribution for u has been assumed, as well as an exponential correlation function (Lenschow *et al.*, 1994). The meaning of the integral time scale T_α depends on the statistic under consideration: for the estimation of the error the mean, T_α is the integral time scale of u (i.e. $T_{1,0}$), whereas for the estimate of the error in the (co-)variance μ_{uu} (or μ_{uv}), T is the integral scale of series uu or uv (i.e. $T_{2,0}$ or $T_{1,1}$ respectively).

A.2.3 Statistics derived from discretely sampled series

In practice one will not have a continuous series of observations of u and v , but observations at discrete instances in time. When the spacing in time is much larger than the integral time scale, the expression of section A.2.1 are recovered. Lenschow *et al.* (1994) derived expressions for the situation in which the spacing Δ is not much larger than the integral scale. For the first and second order moments, the following expressions for the number of independent samples can be derived from Lenschow *et al.* (1994):

$$N_{ind} = N \left(\coth \left(\frac{\Delta}{2T_\alpha} \right) \right)^{-1}. \quad (\text{A.18})$$

For $\Delta \gg T_\alpha$ all samples will be independent and $N_{ind} = N$. The situation that Δ is not much greater than T_α seems exotic, since one would design a sampling strategy such that this waste of

samples would be prevented. However, in the case of the spatial averaging of turbulence fields resulting from LES the situation $\Delta \not\gg T_\alpha$ (or more appropriately, $\Delta \not\gg L_\alpha$) may occur. This will depend on the spatial structure of the field under consideration and the details of the discretisation (see the next section).

A.2.4 Extension of error estimates to averaging in more dimensions

Moene and Michels (2002) have extended the analysis of Lenschow *et al.* (1994) to the situation where averaging takes place in more dimensions (i.e. time and one or two space dimensions). Based on here analysis, error estimates for more-dimensional averaging will be given.

The number of independent samples $N_{ind,t}$ in a time series of α is $1 + \frac{1}{2} \frac{T}{T_\alpha}$, which states that even if the time series is infinitely short, there will be at least one observation. Then, if averaging takes place in more than one dimension the total number of independent samples, N_{ind} , will be:

$$N_{ind} = \prod_r \left(1 + \frac{1}{2} \frac{L_r}{L_{\alpha,r}} \right) \quad (\text{A.19})$$

where $L_{\alpha,r}$ is the integral scale of α in direction r , L_r is the length over which averaging takes place in dimension r , and r ranges over all dimensions (space and time). The equivalent of (A.19) for discretely sampled data is:

$$N_{ind} = \prod_r \left(1 + (N - 1) \left(\coth \left(\frac{\Delta_r}{2L_{\alpha,r}} \right) \right)^{-1} \right), \quad (\text{A.20})$$

where Δ_r is the spacing in direction r . This expression for N_{ind} can then be used in the expressions for the error variances, given in section A.2.1.

A.3 Estimation of statistical errors in LDA data and LES results

A.3.1 LDA data

For the estimation of errors in statistics derived from LDA data the one-dimensional formulations of section A.2.3 will be used. Since 4th order moments have not been stored, a normal distribution of the velocities will be assumed (this allows calculation of the errors based on variances and covariances only). Although the sampling rate for the LDA measurements was originally estimated to be such that successive samples would be independent, Δ is probably not much larger than the relevant time scale. Therefore the full expressions for the discrete sampling case will be used (see section A.2.3).

The integral scales needed in those expressions can be derived from the auto-correlation and cross-correlation functions. These in turn can be determined from the high resolution LDA data (see section 3.3.3). The integral scale of α is defined as the integral of ρ_α for lags from 0 to ∞ . However, by definition the autocorrelation function in one-point measurements integrates to zero

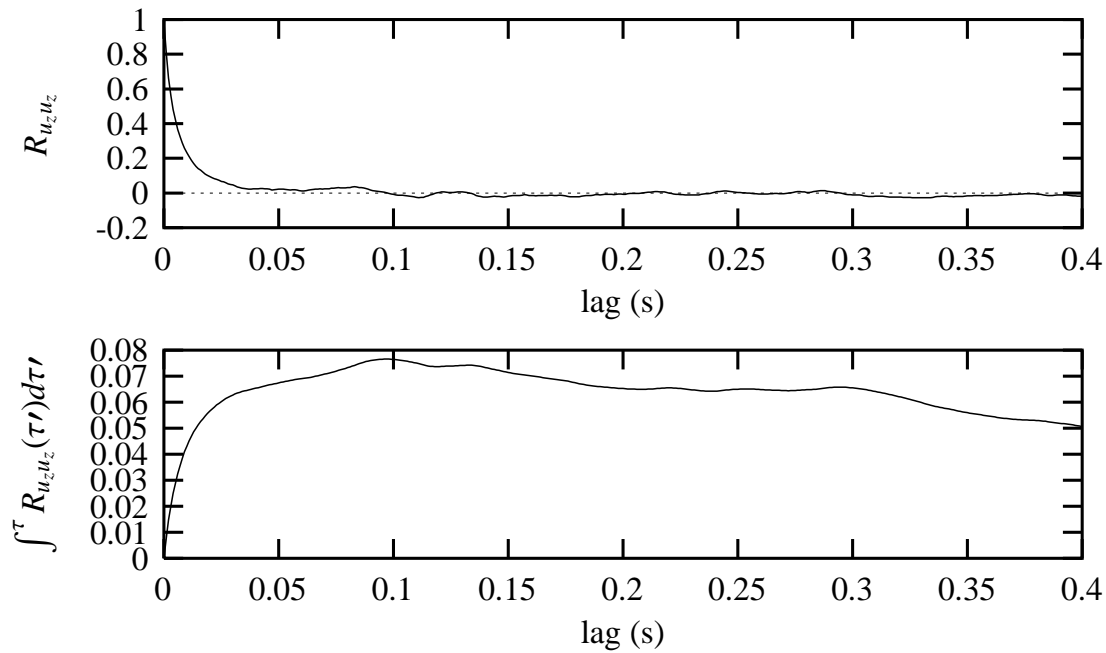


Figure A.1: Example of the problem of integrating autocorrelation functions to obtain the integral time scale. Autocorrelation function for u_z at $z/D = -5.8$, $r/R = 0$, and $Re_D = 10^5$ (top) and integral of $R_{u_z u_z}$ between 0 and the lag under consideration. Only a part of the correlation function is shown.

(see figure A.1 for an illustration of this problem: beyond a certain lag, the integrated correlation function starts to decrease).

In order to obtain an integral scale that indeed gives information about the time or length scale over which correlation exists, the integral scales will be obtained by integrating ρ_α for lags between 0 and the first lag for which ρ_α becomes 0. This is just a practical workaround for a fundamental problem.

A.3.2 LES fields

In the case of LES fields, ensemble means are approximated by a combination of time and space averages. In the case of the straight pipe model, averaging takes place in three dimensions: time, z -direction and θ -direction. In the contraction model the z -direction is no longer a homogeneous direction, so only two averaging dimensions remain. Whether individual samples are independent depends both on the dimension under consideration and on the location in the domain. The time between individual fields, stored for analysis, has been chosen to be roughly equal to, but *not* much larger than, the integral time scale. In the axial direction the integral length scale may change significantly between the pipe axis and the near wall region. But in general, $\Delta_z < L_{z,\alpha}$. In the tangential direction the length scale may differ between the regions near the pipe centre and the pipe wall. But more importantly, the grid spacing Δ_θ changes significantly from very small near the pipe axis to a value of the same order as Δ_z near the wall. The very small number of

independent samples near the pipe axis is especially problematic in the case of the contraction model, since in that case the axial direction is not available as an averaging dimension.

To summarise, the estimates of statistical errors in LES results will be determined with the expressions given in section A.2 with N replaced by N_{ind} from (A.20). For the straight pipe model r includes time, the z -dimension and the θ -dimension. For the contraction model r only includes time, and the θ -dimension.

B

Auxiliary equations

B.1 Equations in cylindrical coordinates

B.1.1 Navier-Stokes equations

The Navier-Stokes equations (2.2) in cylindrical coordinates are:

$$\frac{\partial u_r}{\partial t} + (\mathbf{u} \cdot \nabla) u_r - \frac{u_\theta^2}{r} = -\frac{1}{\rho} \frac{\partial p}{\partial r} + \frac{1}{r} \frac{\partial r \sigma_{rr}}{\partial r} + \frac{1}{r} \frac{\partial \sigma_{r\theta}}{\partial \theta} + \frac{\partial \sigma_{rz}}{\partial z} - \frac{\sigma_{\theta\theta}}{r}, \quad (\text{B.1a})$$

$$\frac{\partial u_\theta}{\partial t} + (\mathbf{u} \cdot \nabla) u_\theta + \frac{u_r u_\theta}{r} = -\frac{1}{\rho r} \frac{\partial p}{\partial \theta} + \frac{1}{r} \frac{\partial r \sigma_{r\theta}}{\partial r} + \frac{1}{r} \frac{\partial \sigma_{\theta\theta}}{\partial \theta} + \frac{\partial \sigma_{z\theta}}{\partial z} + \frac{\sigma_{r\theta}}{r}, \quad (\text{B.1b})$$

$$\frac{\partial u_z}{\partial t} + (\mathbf{u} \cdot \nabla) u_z = -\frac{1}{\rho} \frac{\partial p}{\partial z} + \frac{1}{r} \frac{\partial r \sigma_{rz}}{\partial r} + \frac{1}{r} \frac{\partial \sigma_{\theta z}}{\partial \theta} + \frac{\partial \sigma_{zz}}{\partial z}, \quad (\text{B.1c})$$

with

$$\mathbf{u} \cdot \nabla = u_r \frac{\partial}{\partial r} + \frac{u_\theta}{r} \frac{\partial}{\partial \theta} + u_z \frac{\partial}{\partial z}, \quad (\text{B.1d})$$

$$\boldsymbol{\sigma} = \nu (\nabla \mathbf{u} + (\nabla \mathbf{u})^T) = \nu \mathbf{S}, \quad (\text{B.1e})$$

$$\nabla \mathbf{u} = \begin{pmatrix} \frac{\partial u_r}{\partial r} & \frac{\partial u_\theta}{\partial r} & \frac{\partial u_z}{\partial r} \\ \frac{1}{r} \frac{\partial u_r}{\partial \theta} - \frac{u_\theta}{r} & \frac{1}{r} \frac{\partial u_\theta}{\partial \theta} + \frac{u_r}{r} & \frac{1}{r} \frac{\partial u_z}{\partial \theta} \\ \frac{\partial u_r}{\partial z} & \frac{\partial u_\theta}{\partial z} & \frac{\partial u_z}{\partial z} \end{pmatrix}. \quad (\text{B.1f})$$

B.1.2 Reynolds stress budget equations

The budget equations for the Reynolds stresses in cylindrical coordinates are derived from (2.10). In the derivation axisymmetry is assumed.

Some terms in these budget equations result from the curvature of the coordinate system, rather than from physical processes. The separation between curvature induced terms and the rest can be made by taking the limit $r \rightarrow \infty$. Those terms that tend to zero are the curvature induced terms. Terms of the form

$$\frac{1}{r} \frac{\partial}{\partial r} r X \quad (\text{B.2})$$

contain curvature effects as well, since they can be written as:

$$\frac{X}{r} + \frac{\partial}{\partial r} rX. \quad (\text{B.3})$$

Another matter is the effect of the curvature of the mean streamlines. In an axisymmetric flow in cylindrical coordinates a non-zero \bar{u}_θ signifies mean streamline curvature. All terms in the budget equations below that contain factors of the form \bar{u}_θ/r are affected by streamline curvature.

The budget equation for $\overline{u'_r u'_r}$ reads:

$$\begin{aligned} \underbrace{\frac{\partial \overline{u'_r u'_r}}{\partial t}}_{\text{RC}} &= \underbrace{2\overline{u'_r u'_\theta} \frac{\bar{u}_\theta}{r} - 2\bar{u}_r \frac{\partial \overline{u'_r u'_r}}{\partial r} - 2\bar{u}_z \frac{\partial \overline{u'_r u'_r}}{\partial z}}_{\text{CT}} + \underbrace{2\overline{u'_r u'_\theta} \frac{\bar{u}_\theta}{r} - 2\overline{u'_r u'_r} \frac{\partial \bar{u}_r}{\partial r} - 2\overline{u'_r u'_z} \frac{\partial \bar{u}_r}{\partial z}}_{\text{PR}} \\ &- \underbrace{\frac{1}{r} \frac{\partial r \overline{u'_r u'_r u'_r}}{\partial r} + 2 \frac{\overline{u'_r u'_\theta u'_\theta}}{r} - \frac{\partial \overline{u'_r u'_r u'_z}}{\partial z}}_{\text{TD}} \\ &- \underbrace{\frac{2}{\rho} \overline{u'_r} \frac{\partial p'}{\partial r} + \frac{1}{r} \frac{\partial}{\partial r} \left(r v \frac{\partial \overline{u'_r u'_r}}{\partial r} \right) - 2\nu \left(\frac{\overline{u'_r u'_r}}{r^2} - \frac{\overline{u'_\theta u'_\theta}}{r^2} \right) + \frac{\partial}{\partial z} v \frac{\partial \overline{u'_r u'_r}}{\partial z}}_{\text{VD}} \\ &\quad - \underbrace{2\nu \left(\left(\frac{\partial \overline{u'_r}}{\partial r} \right)^2 + \left(\frac{1}{r} \frac{\partial \overline{u'_r}}{\partial \theta} - \frac{\overline{u'_\theta}}{r} \right)^2 + \left(\frac{\partial \overline{u'_r}}{\partial z} \right)^2 \right)}_{\text{DS}}. \quad (\text{B.4}) \end{aligned}$$

The budget equation for $\overline{u'_\theta u'_\theta}$ reads:

$$\begin{aligned} \underbrace{\frac{\partial \overline{u'_\theta u'_\theta}}{\partial t}}_{\text{RC}} &= - \underbrace{2\overline{u'_r u'_\theta} \frac{\bar{u}_\theta}{r} - 2\bar{u}_r \frac{\partial \overline{u'_\theta u'_\theta}}{\partial r} - 2\bar{u}_z \frac{\partial \overline{u'_\theta u'_\theta}}{\partial z}}_{\text{CT}} - \underbrace{2\overline{u'_r u'_\theta} \frac{\partial \bar{u}_\theta}{\partial r} - 2\overline{u'_\theta u'_\theta} \frac{\bar{u}_r}{r} - 2\overline{u'_z u'_\theta} \frac{\partial \bar{u}_\theta}{\partial z}}_{\text{PR}} \\ &- \underbrace{\frac{1}{r} \frac{\partial r \overline{u'_r u'_\theta u'_\theta}}{\partial r} - 2 \frac{\overline{u'_r u'_\theta u'_\theta}}{r} - \frac{\partial \overline{u'_r u'_\theta u'_\theta}}{\partial z}}_{\text{TD}} \\ &- \underbrace{\frac{2}{\rho} \overline{u'_\theta} \frac{1}{r} \frac{\partial p'}{\partial \theta} + \frac{1}{r} \frac{\partial}{\partial r} \left(r v \frac{\partial \overline{u'_\theta u'_\theta}}{\partial r} \right) + 2\nu \left(\frac{\overline{u'_r u'_r}}{r^2} - \frac{\overline{u'_\theta u'_\theta}}{r^2} \right) + \frac{\partial}{\partial z} v \frac{\partial \overline{u'_\theta u'_\theta}}{\partial z}}_{\text{VD}} \\ &\quad - \underbrace{2\nu \left(\left(\frac{\partial \overline{u'_\theta}}{\partial r} \right)^2 + \left(\frac{1}{r} \frac{\partial \overline{u'_\theta}}{\partial \theta} + \frac{\overline{u'_r}}{r} \right)^2 + \left(\frac{\partial \overline{u'_\theta}}{\partial z} \right)^2 \right)}_{\text{DS}}. \quad (\text{B.5}) \end{aligned}$$

The budget equation for $\overline{u'_z u'_z}$ reads:

$$\begin{aligned}
\underbrace{\frac{\partial \overline{u'_z u'_z}}{\partial t}}_{\text{RC}} &= - \underbrace{\overline{u}_r \frac{\partial \overline{u'_z u'_z}}{\partial r}}_{\text{CT}} - \underbrace{\overline{u}_z \frac{\partial \overline{u'_z u'_z}}{\partial z}}_{\text{CT}} - \underbrace{2 \overline{u'_r u'_z} \frac{\partial \overline{u}_z}{\partial r}}_{\text{PR}} - \underbrace{2 \overline{u'_z u'_z} \frac{\partial \overline{u}_z}{\partial z}}_{\text{PR}} - \underbrace{\frac{1}{r} \frac{\partial r \overline{u'_r u'_z u'_z}}{\partial r}}_{\text{TD}} - \underbrace{\frac{\partial \overline{u'_r u'_z u'_z}}{\partial z}}_{\text{TD}} \\
&- \underbrace{\frac{2}{\rho} \overline{u'_z} \frac{\partial p'}{\partial z}}_{\text{VP}} + \underbrace{\frac{1}{r} \frac{\partial}{\partial r} \left(r v \frac{\partial \overline{u'_z u'_z}}{\partial r} \right)}_{\text{VD}} + \underbrace{\frac{\partial}{\partial z} v \frac{\partial \overline{u'_z u'_z}}{\partial z}}_{\text{VD}} \\
&- 2v \underbrace{\left(\left(\frac{\partial \overline{u'_z}}{\partial r} \right)^2 + \left(\frac{1}{r} \frac{\partial \overline{u'_z}}{\partial \theta} \right)^2 + \left(\frac{\partial \overline{u'_z}}{\partial z} \right)^2 \right)}_{\text{DS}}. \quad (\text{B.6})
\end{aligned}$$

The budget equation for $\overline{u'_r u'_z}$ reads:

$$\begin{aligned}
\underbrace{\frac{\partial \overline{u'_r u'_z}}{\partial t}}_{\text{RC}} &= + \underbrace{\overline{u'_z u'_\theta} \frac{\overline{u}_\theta}{r}}_{\text{CT}} - \underbrace{\overline{u}_r \frac{\partial \overline{u'_r u'_z}}{\partial r}}_{\text{CT}} - \underbrace{\overline{u}_z \frac{\partial \overline{u'_r u'_z}}{\partial z}}_{\text{CT}} \\
&- \underbrace{\overline{u'_r u'_r} \frac{\partial \overline{u}_z}{\partial r}}_{\text{PR}} + \underbrace{\overline{u'_z u'_\theta} \frac{\overline{u}_\theta}{r}}_{\text{PR}} - \underbrace{\overline{u'_r u'_z} \frac{\partial \overline{u}_z}{\partial z}}_{\text{PR}} - \underbrace{\overline{u'_r u'_z} \frac{\partial \overline{u}_r}{\partial z}}_{\text{PR}} - \underbrace{\overline{u'_z u'_z} \frac{\partial \overline{u}_r}{\partial z}}_{\text{PR}} - \underbrace{\frac{1}{r} \frac{\partial r \overline{u'_r u'_r u'_z}}{\partial r}}_{\text{TD}} + \underbrace{\frac{\overline{u'_r u'_\theta u'_\theta}}{r}}_{\text{TD}} - \underbrace{\frac{\partial \overline{u'_r u'_z u'_z}}{\partial z}}_{\text{TD}} \\
&- \underbrace{\frac{1}{\rho} \overline{u'_z} \frac{\partial p'}{\partial r}}_{\text{VP}} - \underbrace{\frac{1}{\rho} \overline{u'_r} \frac{\partial p'}{\partial z}}_{\text{VP}} + \underbrace{\frac{1}{r} \frac{\partial}{\partial r} \left(r v \frac{\partial \overline{u'_r u'_z}}{\partial r} \right)}_{\text{VD}} - \underbrace{v \frac{\overline{u'_r u'_z}}{r^2}}_{\text{VD}} + \underbrace{\frac{\partial}{\partial z} v \frac{\partial \overline{u'_r u'_z}}{\partial z}}_{\text{VD}} \\
&- 2v \underbrace{\left(\frac{\partial \overline{u'_r}}{\partial r} \frac{\partial \overline{u'_z}}{\partial r} + \left(\frac{1}{r} \frac{\partial \overline{u'_r}}{\partial \theta} - \frac{u'_\theta}{r} \right) \frac{1}{r} \frac{\partial \overline{u'_z}}{\partial \theta} + \frac{\partial \overline{u'_r}}{\partial z} \frac{\partial \overline{u'_z}}{\partial z} \right)}_{\text{DS}}. \quad (\text{B.7})
\end{aligned}$$

The budget equation for $\overline{u'_r u'_\theta}$ reads:

$$\begin{aligned}
\underbrace{\frac{\partial \overline{u'_r u'_\theta}}{\partial t}}_{\text{RC}} &= - \underbrace{\overline{u'_r u'_r} \frac{\overline{u_\theta}}{r} + \overline{u'_\theta u'_\theta} \frac{\overline{u_\theta}}{r}}_{\text{CT}} - \overline{u_r} \frac{\partial \overline{u'_r u'_\theta}}{\partial r} - \overline{u_z} \frac{\partial \overline{u'_r u'_\theta}}{\partial z} \\
&- \underbrace{\overline{u'_r u'_r} \frac{\partial \overline{u_\theta}}{\partial r} + \overline{u'_\theta u'_\theta} \frac{\overline{u_\theta}}{r} - \overline{u'_r u'_\theta} \frac{\overline{u_r}}{r} - \overline{u'_r u'_z} \frac{\partial \overline{u_\theta}}{\partial z} - \overline{u'_r u'_\theta} \frac{\partial \overline{u_r}}{\partial r} - \overline{u'_z u'_\theta} \frac{\partial \overline{u_z}}{\partial z}}_{\text{PR}} \\
&- \underbrace{\frac{1}{r} \frac{\partial r \overline{u'_r u'_r u'_\theta}}{\partial r} + \frac{\overline{u'_\theta u'_\theta u'_\theta}}{r} - \frac{\overline{u'_r u'_r u'_\theta}}{r} - \frac{\partial \overline{u'_r u'_\theta u'_z}}{\partial z}}_{\text{TD}} \\
&- \underbrace{\frac{1}{\rho} \overline{u'_\theta} \frac{\partial p'}{\partial r} - \frac{1}{\rho} \overline{u'_r} \frac{1}{r} \frac{\partial p'}{\partial \theta} + \frac{1}{r} \frac{\partial}{\partial r} \left(r v \frac{\partial \overline{u'_r u'_\theta}}{\partial r} \right) - 4\nu \frac{\overline{u'_r u'_\theta}}{r^2} + \frac{\partial}{\partial z} v \frac{\partial \overline{u'_r u'_\theta}}{\partial z}}_{\text{VD}} \\
&- 2\nu \underbrace{\left(\frac{\partial \overline{u'_r} \partial \overline{u'_\theta}}{\partial r \partial r} + \left(\frac{1}{r} \frac{\partial \overline{u'_r}}{\partial \theta} - \frac{\overline{u'_\theta}}{r} \right) \left(\frac{1}{r} \frac{\partial \overline{u'_\theta}}{\partial \theta} + \frac{\overline{u'_r}}{r} \right) + \frac{\partial \overline{u'_r}}{\partial z} \frac{\partial \overline{u'_\theta}}{\partial z} \right)}_{\text{DS}}. \quad (\text{B.8})
\end{aligned}$$

The budget equation for $\overline{u'_z u'_\theta}$ reads:

$$\begin{aligned}
\underbrace{\frac{\partial \overline{u'_z u'_\theta}}{\partial t}}_{\text{RC}} &= - \underbrace{\overline{u'_r u'_z} \frac{\overline{u_\theta}}{r} - \overline{u_r} \frac{\partial \overline{u'_z u'_\theta}}{\partial r} - \overline{u_z} \frac{\partial \overline{u'_z u'_\theta}}{\partial z}}_{\text{CT}} \\
&- \underbrace{\overline{u'_r u'_z} \frac{\partial \overline{u_\theta}}{\partial r} - \overline{u'_r u'_\theta} \frac{\partial \overline{u_z}}{\partial r} - \overline{u'_z u'_\theta} \frac{\partial \overline{u_z}}{\partial z} - \overline{u'_z u'_\theta} \frac{\overline{u_r}}{r} - \overline{u'_z u'_z} \frac{\partial \overline{u_\theta}}{\partial z}}_{\text{PR}} \\
&- \underbrace{\frac{1}{r} \frac{\partial r \overline{u'_r u'_\theta u'_z}}{\partial r} - \frac{\overline{u'_r u'_\theta u'_z}}{r} - \frac{\partial \overline{u'_z u'_\theta u'_\theta}}{\partial z}}_{\text{TD}} \\
&- \underbrace{\frac{1}{\rho} \overline{u'_\theta} \frac{\partial p'}{\partial z} - \frac{1}{\rho} \overline{u'_z} \frac{1}{r} \frac{\partial p'}{\partial \theta} + \frac{1}{r} \frac{\partial}{\partial r} \left(r v \frac{\partial \overline{u'_z u'_\theta}}{\partial r} \right) - \nu \frac{\overline{u'_z u'_\theta}}{r^2} + \frac{\partial}{\partial z} v \frac{\partial \overline{u'_z u'_\theta}}{\partial z}}_{\text{VD}} \\
&- 2\nu \underbrace{\left(\frac{\partial \overline{u'_\theta} \partial \overline{u'_z}}{\partial r \partial r} + \left(\frac{1}{r} \frac{\partial \overline{u'_\theta}}{\partial \theta} + \frac{\overline{u'_r}}{r} \right) \frac{1}{r} \frac{\partial \overline{u'_z}}{\partial \theta} + \frac{\partial \overline{u'_\theta}}{\partial z} \frac{\partial \overline{u'_z}}{\partial z} \right)}_{\text{DS}}. \quad (\text{B.9})
\end{aligned}$$

B.2 Equations in spectral space

The equations of motion in spectral space can be derived from those in physical space through Fourier transformation of the dependent variables. The Fourier transform of a variable a is

denoted by \widehat{a} . Fourier transformed variables are a function of the wave vector \mathbf{k} rather than the spatial coordinate x .

B.2.1 Navier-Stokes equations in spectral space

The Navier-Stokes equations in spectral space read (Lesieur, 1993):

$$\left(\frac{\partial}{\partial t} + \nu \mathbf{k} \cdot \mathbf{k}\right) \widehat{\mathbf{u}} = -i \left(\boldsymbol{\delta} - \frac{\mathbf{k}\mathbf{k}}{\mathbf{k} \cdot \mathbf{k}}\right) \left[\int_{p+q=\mathbf{k}} \widehat{\mathbf{u}}(p) \widehat{\mathbf{u}}(q) d\mathbf{p} \right] \cdot \mathbf{k}, \quad (\text{B.10})$$

where $i^2 = -1$. The term $\boldsymbol{\delta} - \frac{\mathbf{k}\mathbf{k}}{\mathbf{k} \cdot \mathbf{k}}$ is a projector operator that projects onto a plane perpendicular to \mathbf{k} .

B.2.2 Reynolds stress budget equations

For a turbulent flow with a mean shear tensor $\boldsymbol{\lambda}$, the budget equation for the spectral stress tensor $\boldsymbol{\Phi} (= \overline{\mathbf{u}'\mathbf{u}'})$ is (see Bertoglio, 1982):

$$\frac{\partial}{\partial t} \boldsymbol{\Phi} - \mathbf{k} \cdot \boldsymbol{\lambda} \cdot \nabla \boldsymbol{\Phi} = - \left(2 \left(I - \frac{\mathbf{k}\mathbf{k}}{\mathbf{k} \cdot \mathbf{k}} \right) \cdot \boldsymbol{\lambda} \cdot \boldsymbol{\Phi} + 2 \boldsymbol{\Phi} \cdot \boldsymbol{\lambda}^T \cdot \left(I - \frac{\mathbf{k}\mathbf{k}}{\mathbf{k} \cdot \mathbf{k}} \right) \right) - 2\nu \mathbf{k} \cdot \mathbf{k} \boldsymbol{\Phi} + \mathbf{T}, \quad (\text{B.11})$$

where \mathbf{T} is a collection of all non-linear terms (including the so-called slow pressure-strain term). The first term at the right hand side includes the spectral representation of the rapid pressure-strain term. It can be shown that —since the flow is incompressible— this term does not change the turbulent kinetic energy, though it does change the individual components. For isotropic turbulence we can show that pure rotation (i.e. an antisymmetric $\boldsymbol{\lambda}$) does not influence $\boldsymbol{\Phi}$ through the linear terms.

C

On the relationship between streamline curvature and rotation in swirling fbws

In discussions on turbulent swirling flows the effects of streamline curvature and rotation on the turbulence is a recurring topic. In these discussions streamline curvature and rotation seem to be different issues. This distinction, however, partly stems from the origin of the interest in streamline curvature versus rotation: aerodynamics versus geophysical flows. In the first type of flows a natural radius of curvature can be identified (curvature of the wing under consideration), whereas in the second category a natural rotation rate is present (viz. that of the earth). Another reason for the analysis of flows in terms of a rotating reference frame is the fact that the characteristics of the reference frame (the rotation rate in particular) are constant in space and –if appropriate– in time. This makes the mathematical description of phenomena in such a flow simpler.

In this appendix the link between the streamline curvature and rotation will be shown for the special case of swirling flows¹.

C.1 Two reference frames

The discussion will be restricted to incompressible flow of a Newtonian fluid, which can be described with the Navier-Stokes equation:

$$\frac{\partial \mathbf{u}}{\partial t} + \nabla \cdot \mathbf{uu} = -\frac{1}{\rho} \nabla p + \nu \nabla \cdot \mathbf{S} \quad (\text{C.1})$$

This description is valid in an inertial reference frame. In order to clarify the relationship between streamline curvature and rotation, two new reference frames will be introduced:

- a. A reference frame that translates with the local velocity \mathbf{u}_c . The path traced through space by this reference frame follows a streakline and has a local radius of curvature of R_c . Note that although in this frame the velocity \mathbf{u} is zero, the spatial derivatives need not be zero.
- b. A reference frame that rotates at an angular velocity $\mathbf{\Omega}$. The position vector of the point of interest, relative to the axis of rotation is R_r .

¹Here rotation and streamline curvature will be considered as two sides of the same phenomena. However, situations are conceivable in which the streamline curvature and rotation are *not* related, e.g. the fbw through a rotating, curved channel (Matsson and Alfredsson, 1990)

In terms of the first reference frame the Navier-Stokes equation becomes:

$$\frac{\partial \mathbf{u}}{\partial t} + \nabla \cdot \mathbf{u}\mathbf{u} = -\frac{1}{\rho} \nabla p + \nu \nabla \cdot \mathbf{S} - 2 \left(\frac{\mathbf{R}_c}{|\mathbf{R}_c|} \times \frac{\mathbf{u}_c}{|\mathbf{R}_c|} \right) \times \mathbf{u} + \left(\left| \frac{\mathbf{R}_c}{|\mathbf{R}_c|} \times \frac{\mathbf{u}_c}{|\mathbf{R}_c|} \right| \right)^2 \mathbf{R}_c - 2 \left(\frac{\mathbf{R}_c}{|\mathbf{R}_c|} \times \frac{\mathbf{u}_c}{|\mathbf{R}_c|} \right) \times \mathbf{u}_c, \quad (\text{C.2})$$

where the factor $\left(\frac{\mathbf{R}_c}{|\mathbf{R}_c|} \times \frac{\mathbf{u}_c}{|\mathbf{R}_c|} \right)$ can be interpreted as a local rotation rate of the coordinate system. It appears that streamline curvature yields three additional terms:

- a Coriolis-like term
- a centrifugal acceleration
- a term that looks like a Coriolis term, but has one important difference: it relates to the translation velocity vector \mathbf{u}_c rather than the velocity in the moving reference frame.

The first term will be zero, since in the moving reference frame the velocity is zero. Upon closer inspection it appears that the last term is twice the last but one term, (in magnitude and direction). Taking these considerations into account, the following version of the Navier-Stokes equations results:

$$\frac{\partial \mathbf{u}}{\partial t} + \nabla \cdot \mathbf{u}\mathbf{u} = -\frac{1}{\rho} \nabla p + \nu \nabla \cdot \mathbf{S} + 3 \left(\left| \frac{\mathbf{R}_c}{|\mathbf{R}_c|} \times \frac{\mathbf{u}_c}{|\mathbf{R}_c|} \right| \right)^2 \mathbf{R}_c. \quad (\text{C.3})$$

Thus the effect of the curved path is expressed purely as a centrifugal acceleration. For a flow without curvature, i.e. $R_c \rightarrow \infty$, the centrifugal acceleration disappears.

The second reference frame simply yields the Navier Stokes equations with added centrifugal and Coriolis accelerations:

$$\frac{\partial \mathbf{u}}{\partial t} + \nabla \cdot \mathbf{u}\mathbf{u} = -\frac{1}{\rho} \nabla p + \nu \nabla \cdot \mathbf{S} + \Omega^2 \mathbf{R}_r - 2\Omega \times \mathbf{u}. \quad (\text{C.4})$$

For the flow in a system without rotation, i.e. $\Omega = 0$, the extra terms disappear.

C.2 Application to swirling fbws

C.2.1 Solid-body rotation without an axial velocity component

Only for a very simple flow a clear connection can be made between the Navier-Stokes equations in both reference frames. This simple swirling flow² is a two-dimensional rotating flow at constant angular speed. In this flow both a natural radius of curvature and a natural rotation rate can be identified. In terms of the first reference frame the magnitude of \mathbf{u}_c and \mathbf{R}_c are constant as well as the magnitude and direction of $\mathbf{R}_c \times \mathbf{u}_c$ in terms of the first reference frame –for a given point in the flow. In the second reference frame, just Ω is constant.

²According to the definition of a swirling fbw in section 2.2 this is not a swirling fbw

The link between (C.2) and (C.4) for the simple flow under consideration is clear: the latter can be derived from the first by replacing \mathbf{u} by $\mathbf{u} - \mathbf{u}_c$ and $\frac{R_c}{|R_c|} \times \frac{u_c}{|R_c|}$ by $\boldsymbol{\Omega}$. Thus (C.4) is just a special form of (C.2). Note that for this special case the Coriolis term in (C.4) translates into a centrifugal term.

C.2.2 Solid-body rotation including an axial velocity component

In a real swirling flow the radius of curvature is not only determined by the tangential velocity, but by the combined effect of tangential and axial velocity. Indeed, at infinite axial velocity the radius of curvature would also be infinite (no curvature) despite any non-zero tangential velocity component. For the second reference frame again there is a natural rotation rate, viz. the angular velocity corresponding to the solid-body rotation. But now no longer the Coriolis term acts as a centrifugal acceleration due to the fact that $\boldsymbol{\Omega}$ is no longer perpendicular to the velocity vector \mathbf{u} .

C.2.3 General rotation including an axial velocity component

In the case of a general swirling flow the description of the flow in terms of streamline curvature is still useful. On the other hand, only in very special cases a natural rotation rate can be identified to use with the second reference frame. An example where it *is* possible is the flow through a rotating pipe (Imao *et al.*, 1996; Murakami and Kikuyama, 1980; Orlandi and Fatica, 1997; Reich and Beer, 1989). Also parts of a flow in which the tangential velocity profile is that of a solid-body rotation could be analysed in terms of the second reference frame.

As in the previous section, for these more realistic swirling flows, the effect of the rotating reference frame appears as both a centrifugal term and a Coriolis term.

D

Errors in LDA measurements due to geometrical uncertainties

Section 3.2.2 described the way in which various positions and angles in the LDA system have been set to their appropriate values (mutual orientation of the laser beams and orientation of the LDA optics relative to the pipe). These alignments all have a finite accuracy. Steenbergen (1995) has analysed the effect of these inaccuracies on the measured mean velocities and turbulent stresses. For easier reference his results (not the derivations) are reproduced here (from section 4.4 in his thesis).

D.1 Error due to imperfection of theodolite calibration

The mutual angles of the three laser beams (two reference beams and the scattering beam) has been determined with a theodolite. For the front lens with $f = 160\text{mm}$, for which the angle between beam and optical axis is 8° , a typical error in the direction of the beams is 0.02° . The errors in the mean velocities due to inaccuracies in this theodolite calibration are (for a definition of the axes, see below (3.6) on page 47):

$$\begin{aligned}\delta\bar{u}_1 &= \pm 0.003\bar{u}_1 \pm 0.002\bar{u}_2 \pm 0.0005\bar{u}_3 \\ \delta\bar{u}_2 &= \pm 0.003\bar{u}_1 \pm 0.005\bar{u}_2 \pm 0.0005\bar{u}_3\end{aligned}\tag{D.1}$$

Errors in turbulent stresses are:

$$\begin{aligned}\delta\overline{u'_1u'_1} &= \pm 0.006\overline{u'_1u'_1} \pm 0.004\overline{u'_1u'_2} \pm 0.001\overline{u'_1u'_3} \\ \delta\overline{u'_2u'_2} &= \pm 0.006\overline{u'_2u'_2} \pm 0.01\overline{u'_1u'_2} \pm 0.001\overline{u'_2u'_3} \\ \delta\overline{u'_1u'_2} &= \pm 0.008\overline{u'_1u'_2} \pm 0.003\overline{u'_1u'_1} \pm 0.002\overline{u'_2u'_2} \pm 0.0005\overline{u'_1u'_3} \pm 0.0005\overline{u'_2u'_3}\end{aligned}\tag{D.2}$$

D.2 Errors due to imperfections of the positioning of the LDA

If the LDA has been aligned with the pipe perfectly, the velocity components u_1 and u_2 coincide with the axial velocity and the velocity perpendicular to the plane through the pipe axis and the optical axis of the LDA. Imperfections in this alignment can be expressed in rotations around the axes x_1 , x_2 and x_3 ($\psi_i, i = 1, 2, 3$).

D.2.1 Rotation around the x_1 -axis

If the positioning error consists of a rotation around the x_1 axis, cross-talk will appear between velocity components u_2 and u_3 . If the rotation is assumed to be $\pm 0.07^\circ$ the errors in the mean flow will only comprise an error in \bar{u}_2 :

$$\delta\bar{u}_2 = \pm 0.001\bar{u}_3 \quad (\text{D.3})$$

The errors in the Reynolds stresses are:

$$\begin{aligned} \delta\overline{u'_2u'_2} &= \pm 0.002\overline{u'_2u'_3} \\ \delta\overline{u'_1u'_2} &= \pm 0.001\overline{u'_1u'_3} \end{aligned} \quad (\text{D.4})$$

D.2.2 Rotation around the x_2 -axis

If the optical axis of the LDA is not exactly perpendicular to the pipe axis, cross-talk between velocity components u_1 and u_3 will result. Assuming an erroneous rotation of $\pm 15^\circ$, this implies for the mean flow this:

$$\delta\bar{u}_1 = 0.003\bar{u}_3 \quad (\text{D.5})$$

Errors in the Reynolds stresses will be:

$$\begin{aligned} \delta\overline{u'_1u'_1} &= \pm 0.006\overline{u'_1u'_3} \\ \delta\overline{u'_1u'_2} &= \pm 0.003\overline{u'_2u'_3} \end{aligned} \quad (\text{D.6})$$

D.2.3 Rotation around the x_3 -axis

An erroneous rotation around the x_3 -axis (optical axis) will result in cross-talk between the velocity components u_1 and u_2 . For this error a rotation angle of $\pm 0.2^\circ$ is assumed. This gives the following errors in the mean velocity components:

$$\begin{aligned} \delta\bar{u}_1 &= \pm 0.0035\bar{u}_2 \\ \delta\bar{u}_2 &= \mp 0.0035\bar{u}_1 \end{aligned} \quad (\text{D.7})$$

The effect on the Reynolds stresses will be:

$$\begin{aligned} \delta\overline{u'_1u'_1} &= \pm 0.007\overline{u'_1u'_2} \\ \delta\overline{u'_2u'_2} &= \pm 0.007\overline{u'_1u'_2} \\ \delta\overline{u'_1u'_2} &= \pm 0.0035(\overline{u'_1u'_1} - \overline{u'_2u'_2}) \end{aligned} \quad (\text{D.8})$$

D.3 Errors in 3D measurements

In order to derive information about all three velocity components (three mean velocities and six independent Reynolds stresses), measurements need to be performed at three angles ψ (rotations

around the pipe axis, see section 3.2.2 and equation (3.7b). Errors in the angles ψ will result in crosstalk between u_θ and u_r . An error in the angle ψ of 0.05° will be assumed. The errors in the mean velocities depends the choice of the combination of angles ψ . For ψ equal to 0° and 45° :

$$\begin{aligned}\delta\bar{u}_\theta &= \pm 0.001\bar{u}_r, \\ \delta\bar{u}_r &= \pm 0.001\bar{u}_\theta \pm 0.002\bar{u}_r,\end{aligned}\tag{D.9}$$

and for -45° and 45°):

$$\begin{aligned}\delta\bar{u}_\theta &= \pm 0.001\bar{u}_\theta \pm 0.001\bar{u}_r, \\ \delta\bar{u}_r &= \pm 0.001\bar{u}_\theta \pm 0.001\bar{u}_r.\end{aligned}\tag{D.10}$$

The errors in the various Reynolds stresses will be:

$$\begin{aligned}\delta\overline{u'_r u'_r} &= \pm 0.002\overline{u'_r u'_\theta} \pm 0.002\overline{u'_\theta u'_\theta} \\ \delta\overline{u'_\theta u'_\theta} &= \pm 0.007\overline{u'_r u'_\theta} \\ \delta\overline{u'_z u'_\theta} &= \pm 0.001\overline{u'_r u'_z} \\ \delta\overline{u'_r u'_z} &= \pm 0.001\overline{u'_z u'_\theta} \pm 0.002\overline{u'_r u'_z} \\ \delta\overline{u'_r u'_\theta} &= \pm 0.001(\overline{u'_r u'_r} - \overline{u'_\theta u'_\theta})\end{aligned}\tag{D.11}$$

D.4 Application of error estimates

In order to make an estimate of the total error in mean velocities and stresses due to alignment errors, the individual error estimates as given in sections D.1 to D.3 need to be combined. This is done as follows:

- The errors mentioned in D.1 and D.2 are applied to the measured values of means and (co-)variances of u_1 and u_2 for each of the three angles (0° , -45° and $+45^\circ$).
- These errors are summed and translated to errors in the means and (co-)variances of u_z , u_θ and u_r through the same transformation as with which the means and (co-)variances are computed themselves (the inverse of (3.7b) and (3.8c)).
- The resulting error is added to the errors according to the equations presented in section D.3.

E

Details on the LES model

In this appendix some detailed features of the LES model discussed in section 4.2 are shown.

E.1 Example of equations in transformed coordinates

To illustrate the consequences of the coordinate transformation defined in (4.29) and (4.30), the continuity equation and z component of the momentum equations will be given in the transformed coordinate system. The continuity equation in the new coordinate becomes (compare to 2.11):

$$\frac{1}{f(\zeta)\rho} \frac{\partial \rho u_r}{\partial \rho} + \frac{1}{f(\zeta)\rho} \frac{\partial u_\theta}{\partial \phi} + \frac{\partial w}{\partial \zeta} - \frac{\rho}{f(\zeta)} \frac{\partial f(\zeta)}{\partial \zeta} \frac{\partial u_z}{\partial \rho} = 0 \quad (\text{E.1})$$

The z -component of the momentum equations becomes (compare to B.1)

$$\begin{aligned} & \frac{\partial u_z}{\partial t} + \\ & \frac{1}{f(\zeta)\rho} \frac{\partial \rho u_r u_z}{\partial \rho} + \frac{1}{f(\zeta)\rho} \frac{\partial u_\theta u_z}{\partial \phi} + \frac{\partial u_z u_z}{\partial \zeta} - \frac{\rho}{f(\zeta)} \frac{\partial f(\zeta)}{\partial \zeta} \frac{\partial u_z u_z}{\partial \rho} = \\ & - \frac{\partial p}{\partial \zeta} + \frac{\rho}{f(\zeta)} \frac{\partial f(\zeta)}{\partial \zeta} \frac{\partial p}{\partial \rho} + \\ & \frac{1}{f(\zeta)\rho} \frac{\partial \rho \sigma_{rz}}{\partial \rho} + \frac{1}{f(\zeta)\rho} \frac{\partial \sigma_{\theta z}}{\partial \phi} + \frac{\partial \sigma_{zz}}{\partial \zeta} - \frac{\rho}{f(\zeta)} \frac{\partial f(\zeta)}{\partial \zeta} \frac{\partial \sigma_{zz}}{\partial \rho} \end{aligned} \quad (\text{E.2})$$

where the first line is the time rate of change, the second line gives the advection terms, the third line the pressure gradient term and the last line represents the diffusive term. The representation of the different stresses (σ_{rz} , $\sigma_{\theta z}$ and σ_{zz}) is left undefined. In the present implementation these stresses will comprise both the viscous part and the subgrid-scale stress.

E.2 Example of spatial discretisation: divergence

Here one example is given to illustrate the procedure: the divergence.

The divergence is integrated over the grid volume surrounding a pressure point.

$$\int_{\zeta_{k-1}}^{\zeta_k} \int_{\phi_{j-1}}^{\phi_j} \int_{\rho_{i-1}^u}^{\rho_i^u} \left[\frac{1}{f(\zeta)\rho} \frac{\partial \rho u}{\partial \rho} + \frac{1}{f(\zeta)\rho} \frac{\partial v}{\partial \phi} + \frac{\partial w}{\partial \zeta} - \frac{R}{f(\zeta)} \frac{\partial f(\zeta)}{\partial \zeta} \frac{\partial w}{\partial \rho} \right] f^2(\zeta) \rho d\rho d\phi d\zeta \quad (\text{E.3})$$

Integration of the first term gives:

$$\begin{aligned}
& \int_{\zeta_{k-1}}^{\zeta_k} \int_{\phi_{j-1}}^{\phi_j} \int_{\rho_{i-1}^u}^{\rho_i^u} \left[\frac{1}{f(\zeta)\rho} \frac{\partial \rho u_r}{\partial \rho} \right] f^2(\zeta) \rho d\rho d\phi d\zeta \\
&= \int_{\zeta_{k-1}}^{\zeta_k} f(\zeta) \int_{\phi_{j-1}}^{\phi_j} \left[\rho u_r \right]_{\rho_{i-1}^u}^{\rho_i^u} d\phi d\zeta \\
&\approx f_k^p d\phi d\zeta (\rho_i^u \widehat{u}_r^{i,j,k} - \rho_{i-1}^u \widehat{u}_r^{i-1,j,k})
\end{aligned} \tag{E.4}$$

The second term:

$$\begin{aligned}
& \int_{\zeta_{k-1}}^{\zeta_k} \int_{\phi_{j-1}}^{\phi_j} \int_{\rho_{i-1}^u}^{\rho_i^u} \left[\frac{1}{f(\zeta)\rho} \frac{\partial u_\theta}{\partial \phi} \right] f^2(\zeta) \rho d\rho d\phi d\zeta \\
&= \int_{\zeta_{k-1}}^{\zeta_k} f(\zeta) \int_{\rho_{i-1}^u}^{\rho_i^u} \left[u_\theta \right]_{\phi_{j-1}}^{\phi_j} d\rho d\zeta \\
&\approx f_k^p d\rho_i d\zeta (\widehat{u}_\theta^{i,j,k} - \widehat{u}_\theta^{i,j-1,k})
\end{aligned} \tag{E.5}$$

The third term:

$$\begin{aligned}
& \int_{\zeta_{k-1}}^{\zeta_k} \int_{\phi_{j-1}}^{\phi_j} \int_{\rho_{i-1}^u}^{\rho_i^u} \left[\frac{\partial u_z}{\partial \zeta} \right] f^2(\zeta) \rho d\rho d\phi d\zeta \\
&\approx \int_{\phi_{j-1}}^{\phi_j} \int_{\rho_{i-1}^u}^{\rho_i^u} \left[f^2(\zeta) u_z \right]_{\zeta_{k-1}}^{\zeta_k} \rho d\rho d\phi \\
&\approx \left\{ f_k^w \widehat{u}_z^{i,j,k} - f_{k-1}^w \widehat{u}_z^{i,j,k-1} \right\} \rho_i^p d\rho_i d\phi
\end{aligned} \tag{E.6}$$

And finally the fourth term:

$$\begin{aligned}
& \int_{\zeta_{k-1}}^{\zeta_k} \int_{\phi_{j-1}}^{\phi_j} \int_{\rho_{i-1}^u}^{\rho_i^u} \left[-\frac{\rho^2}{f(\zeta)} \frac{\partial f(\zeta)}{\partial \zeta} \frac{\partial u_z}{\partial \rho} \right] f^2(\zeta) d\rho d\phi d\zeta \\
&= - \int_{\phi_{j-1}}^{\phi_j} \int_{\zeta_{k-1}}^{\zeta_k} f(\zeta) \frac{\partial f(\zeta)}{\partial \zeta} \int_{\rho_{i-1}^u}^{\rho_i^u} \left[\rho^2 \frac{\partial u_z}{\partial \rho} \right] d\rho d\zeta d\phi \\
&\approx - \int_{\phi_{j-1}}^{\phi_j} \int_{\zeta_{k-1}}^{\zeta_k} f(\zeta) \frac{\partial f(\zeta)}{\partial \zeta} \left[\rho^2 w \right]_{\rho_{i-1}^u}^{\rho_i^u} d\zeta d\phi \\
&\approx - f_k^p d f_k^p \left[\rho_i^u \frac{1}{4} (\widehat{u}_z^{i+1,j,k-1} + \widehat{u}_z^{i,j,k-1} + \widehat{u}_z^{i+1,j,k} + \widehat{u}_z^{i,j,k}) - \right. \\
&\quad \left. \rho_{i-1}^u \frac{1}{4} (\widehat{u}_z^{i,j,k-1} + \widehat{u}_z^{i-1,j,k-1} + \widehat{u}_z^{i,j,k} + \widehat{u}_z^{i-1,j,k}) \right] d\zeta d\phi
\end{aligned} \tag{E.7}$$

We have made a number of approximations in the derivation of the discrete divergence, in order to obtain a divergence that –when integrated over the entire domain– will reduce to the mass balance at the edges of the domain.

Then we have to divide the terms by the volume of the grid cell ($f_k^{p2} \rho_i^p d\rho_i d\phi d\zeta$), so that the discrete divergence becomes:

$$\begin{aligned} & \frac{(\rho_i^u \widehat{u}_r^{i,j,k} - \rho_{i-1}^u \widehat{u}_r^{i-1,j,k})}{f_k^p \rho_i^p d\rho_i} + \frac{(\widehat{u}_\theta^{i,j,k} - \widehat{u}_\theta^{i,j-1,k})}{f_k^p d\phi \rho_i^p} + \frac{f_k^{w2} \widehat{u}_z^{i,j,k} - f_{k-1}^{w2} \widehat{u}_z^{i,j,k-1}}{f_k^{p2} d\zeta} \\ & - \frac{df_k^p}{f_k^p} \left\{ \rho_i^{u2} \frac{1}{4} (\widehat{u}_z^{i+1,j,k-1} + \widehat{u}_z^{i,j,k-1} + \widehat{u}_z^{i+1,j,k} + \widehat{u}_z^{i,j,k}) - \right. \\ & \left. \rho_{i-1}^{u2} \frac{1}{4} (\widehat{u}_z^{i,j,k-1} + \widehat{u}_z^{i-1,j,k-1} + \widehat{u}_z^{i,j,k} + \widehat{u}_z^{i-1,j,k}) \right\} / (d\rho_i \rho_i^p) \end{aligned} \quad (E.8)$$

E.3 Details on boundary conditions

E.3.1 Implementation of wall boundary condition for u_r

With the use of the discretized divergence equation it can be derived that:

$$\begin{aligned} \widehat{u}_r^{imax+1,j,k} &= \frac{\rho_{imax}^p}{\rho_{imax+1}^p} \widehat{u}_r^{imax-1,j,k} + \\ & df_k^p \left\{ \frac{\rho_{imax+1}^p}{\rho_{imax+1}^p} (\widehat{u}_z^{imax+1,j,k} + \widehat{u}_z^{imax+1,j,k-1}) - \frac{\rho_{imax}^p}{\rho_{imax+1}^p} (\widehat{u}_z^{imax,j,k} + \widehat{u}_z^{imax,j,k-1}) \right\} \end{aligned} \quad (E.9)$$

E.3.2 Implementation of wall boundary condition for \widehat{p}'

The pressure gradient normal to the wall is determined from interpolated pressure values at radial positions $i = imax + 1$ and $i = imax$ and an axial position that lies on the wall normal that passes through the position of $\widehat{u}_r^{imax,j,k}$ at the wall (see figure E.1). The pressure values are obtained from the values at axial positions $k - 1, k$ and $k + 1$) by quadratic interpolation¹:

$$\begin{aligned} \widehat{p}_{interp}^{imax,j,k} &= A_{k-1,k}^{imax} \widehat{p}^{imax,j,k-1} + A_{k,k}^{imax} \widehat{p}^{imax,j,k} + A_{k+1,k}^{imax} \widehat{p}^{imax,j,k} \\ \widehat{p}_{interp}^{imax+1,j,k} &= A_{k-1,k}^{imax+1} \widehat{p}^{imax+1,j,k-1} + A_{k,k}^{imax+1} \widehat{p}^{imax+1,j,k} + A_{k+1,k}^{imax+1} \widehat{p}^{imax+1,j,k} \end{aligned} \quad (E.10)$$

where A^{imax} and A^{imax+1} are matrices². Then, the requirement that $\partial \widehat{p}' / \partial n = 0$ is equivalent to requiring that $\widehat{p}_{interp}^{imax+1,j,k} = \widehat{p}_{interp}^{imax,j,k}$:

$$\sum_{n=1}^{kmax} A_{k,n}^{imax+1} \widehat{p}^{imax+1,j,n} = \sum_{n=1}^{kmax} A_{k,n}^{imax} \widehat{p}^{imax,j,n} \quad (E.11)$$

¹ It is assumed that $\frac{\partial}{\partial z} f(\zeta) = 0$ (or $\alpha = 0$ in figure E.1) for $k = 1$ and $k = kmax$, so that the coefficients for $\widehat{p}^{j,0}$ and $\widehat{p}^{i,j,kmax+1}$ are equal to zero. $\alpha = 0$ at $k = 1$ and $k = kmax$ implies that the pipe walls are parallel at the infbw and outfbw planes. For the present type of calculations, this is not a very serious obstacle

² With reference to figure E.1, the elements of A_{ij}^{imax} are:
 $A_{k-1,k}^{imax} = (x_{imax+1} - 0)(x_{imax+1} - l_{tot}) / (-l_{tot} - 0)(-l_{tot} - l_{tot})$,
 $A_{k,k}^{imax} = (x_{imax+1} + l_{tot})(x_{imax+1} - l_{tot}) / (0 + l_{tot})(0 - l_{tot})$ and
 $A_{k+1,k}^{imax} = (x_{imax+1} + l_{tot})(x_{imax+1} - 0) / (l_{tot} + l_{tot})(l_{tot} - 0)$.
 For A_{ij}^{imax+1} similar expressions hold.

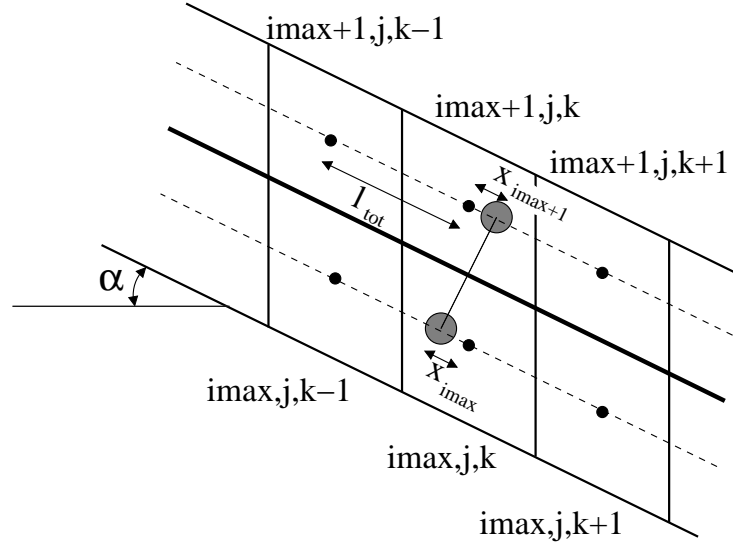


Figure E.1: Determination of the pressure gradient normal to an inclined wall. The location of the interpolated pressure are denoted by large shaded dots, whereas the computational pressure nodes are shown as small black dots.

or:

$$\widehat{p}^{imax+1,j,k} = \sum_{n=1}^{kmax} \left(A^{imax} A^{imax+1-n} \right)_{n,k} \widehat{p}^{imax,j,n} = \sum_{n=1}^{kmax} B_{n,k} \widehat{p}^{imax,j,n}. \quad (\text{E.12})$$

The approximations given above are valid as long as the slope of the wall does not change. In the present case study, however, the pipe walls are parallel at the inflow and outflow plane, and do change slope in between. Therefore, some problems with respect to mass conservation may be expected at the locations where the pipe wall has its maximum curvature (in axial direction).

E.4 Details on the radial grid spacing

The uniformity of the distribution of radial location of the grid points is controlled by a coefficient C . The radial location of the $[r]$ -points (ρ_i^u) is determined with the following recipe:

$$\begin{aligned} x_i &= \frac{i}{imax}, \\ y_i &= \text{atanh}(C)x_i, \\ z_i &= 0.5 \tanh(y_i), \\ \rho_i^u &= z_i + (0.5 - z_{imax}) \frac{i}{imax}. \end{aligned} \quad (\text{E.13})$$

The last step ensures that the $[r]$ -point for $i = imax$ is located at the pipe wall. The factor $i/imax$ is introduced to prevent the points near the pipe axis to be moved away too far from the pipe axis.

The radial positions of the pressure points are taken halfway between the $[r]$ -points:

$$\rho_i^p = \frac{1}{2}(\rho_i^u + \rho_{i-1}^u) . \quad (\text{E.14})$$

E.5 Test of methods to generate swirl

For the LES model of the pipe contraction, the inflow boundary conditions for the velocities are generated with a separate LES model with periodic boundary conditions and parallel walls. For the simulations *with* swirl, the non-zero tangential velocity has to be introduced somehow. Two options have been presented in section 4.2.5: forcing through the tangential shear stress profile (equation (4.42), here method A) or through the mean tangential velocity (equation (4.40), here method B).

To test the quality of both methods low resolution simulations have been made with the LES model (see table E.1). It should be noted that the simulations for method A showed wiggles, even when the damping of those wiggles (see G.3) was increased. The results will be compared with the LDA data obtained at $z/D = -1.8$ in figures E.2 to E.9.

Figure E.2 shows the results for \bar{u}_z . The overall values of \bar{u}_z are correct due the normalisation used. The difference between the two forcing methods occurs near the pipe centre, where method A gives a too pronounced jet. But even the \bar{u}_z -profile for method B gives too high values near the centre. Figure E.3 shows the resulting profiles for \bar{u}_θ . Here and important and anticipated difference between the two methods appears: method A does not give the correct \bar{u}_θ -profile, whereas method B does. The results for the normal stresses are shown in figures E.4 to E.6. In general, the profiles of $\overline{u'_r u'_r}$, $\overline{u'_\theta u'_\theta}$ and $\overline{u'_z u'_z}$ are reproduced reasonably well, except near the centre. There the values are underpredicted by method A and overpredicted by method B. The axial shear stress $\overline{u'_r u'_z}$ is shown in figure E.7. Neither of the forcing methods is able to reproduce the negative value of $\overline{u'_r u'_z}$ near the pipe centre. The profile of $\overline{u'_r u'_z}$ hardly differs from that of a fully developed pipe flow without swirl: this reflects the fact that in the axial direction the flow is forced by a pressure gradient that is independent of the radial position. The $\overline{u'_r u'_\theta}$ -profiles shown in figure E.8 give the anticipated result that method A gives a correct $\overline{u'_r u'_\theta}$ -profile, since that profile was used to determine the forcing. For forcing method B the $\overline{u'_r u'_\theta}$ -profile is reproduced reasonably well in the region $r/R > 0.5$, but near the pipe centre $\overline{u'_r u'_\theta}$ is overestimated strongly. Finally, the profiles of $\overline{u'_z u'_\theta}$ are shown in figure E.9. For forcing method A the results are reasonably correct in the region $r/R < 0.5$, whereas for method B the profile is correct for $r/R > 0.5$.

Based on these results method B will be used in the simulations presented in chapter 6.

quantity	value
N_r	21
N_θ	96
N_z	96
C_s	0.1
$Re = \frac{u_* D}{\nu}$	1150
constant for non-uniform grid (see E.4 page 194)	0.99

Table E.1: Overview of the most important parameters for simulations used for the test of the tangential forcing methods.

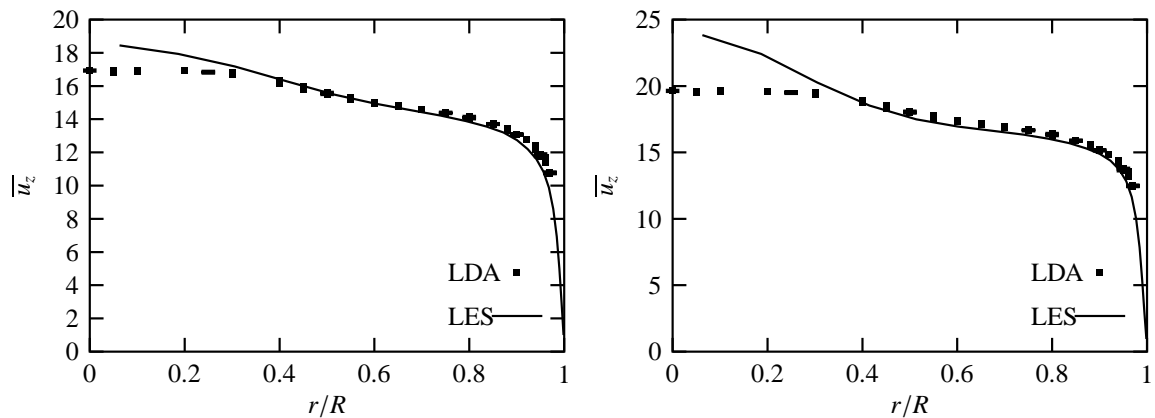


Figure E.2: Mean axial velocity. Comparison of two methods to generate a swirling flow in an LES with periodic boundary conditions: forcing through the tangential shear stress profile (left, equation (4.42)) or through the mean tangential velocity (right, equation (4.40)). The velocity data of the LDA-experiment have been scaled with the bulk velocity from the simulation (giving apparently different LDA data for the two simulations). The LDA data at $r < 0$ have been collapsed to radial positions with $r > 0$. The LDA data also include error bars for a number of radial positions. All radial positions have been normalised with the pipe radius.

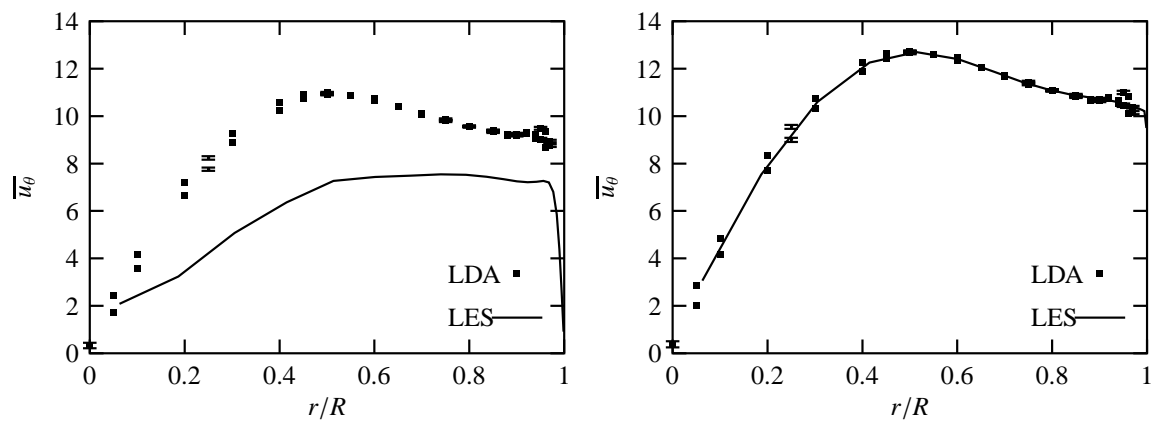


Figure E.3: Mean tangential velocity. Comparison of two methods to generate a swirling flow in an LES with periodic boundary conditions: forcing through the tangential shear stress profile (left, equation (4.42)) or through the mean tangential velocity (right, equation (4.40)). For notes on normalisation, see E.2.

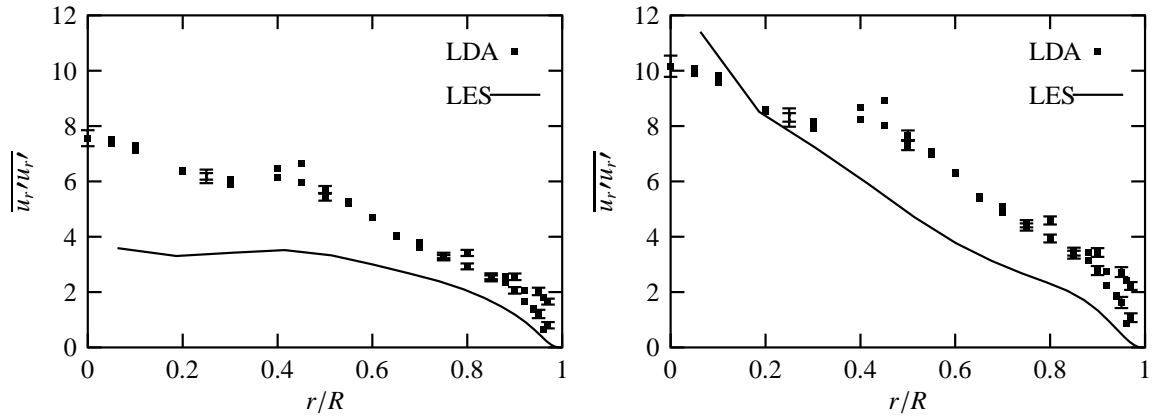


Figure E.4: Normal stress $\overline{u'_r u'_r}$. Comparison of two methods to generate a swirling flow in an LES with periodic boundary conditions: forcing through the tangential shear stress profile (left, equation (4.42)) or through the mean tangential velocity (right, equation (4.40)). For notes on normalisation, see E.2.

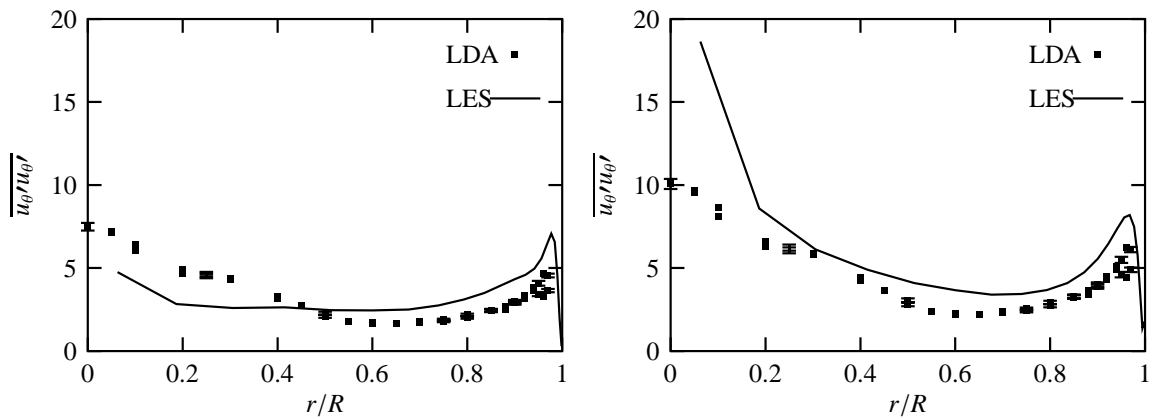


Figure E.5: Normal stress $\overline{u'_\theta u'_\theta}$. Comparison of two methods to generate a swirling flow in an LES with periodic boundary conditions: forcing through the tangential shear stress profile (left, equation (4.42)) or through the mean tangential velocity (right, equation (4.40)). For notes on normalisation, see E.2.

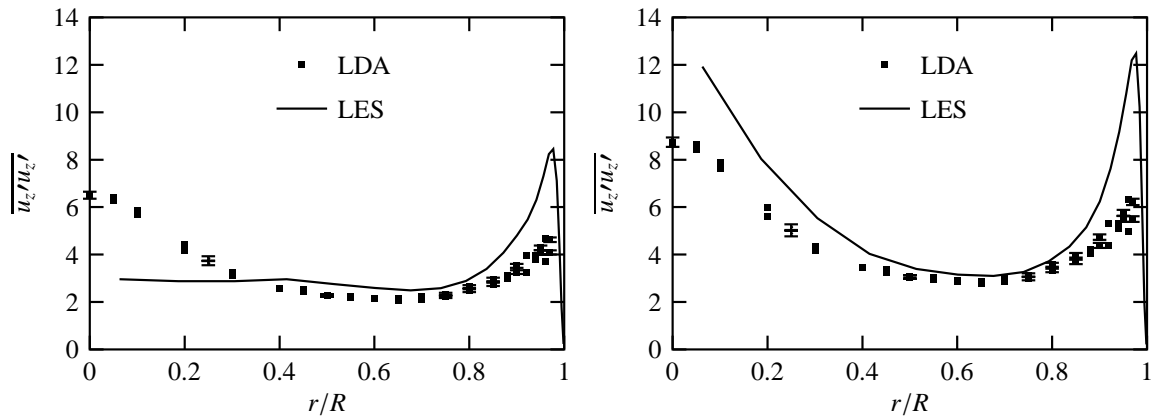


Figure E.6: Normal stress $\overline{u'_z u'_z}$. Comparison of two methods to generate a swirling flow in an LES with periodic boundary conditions: forcing through the tangential shear stress profile (left, equation (4.42)) or through the mean tangential velocity (right, equation (4.40)). For notes on normalisation, see E.2.

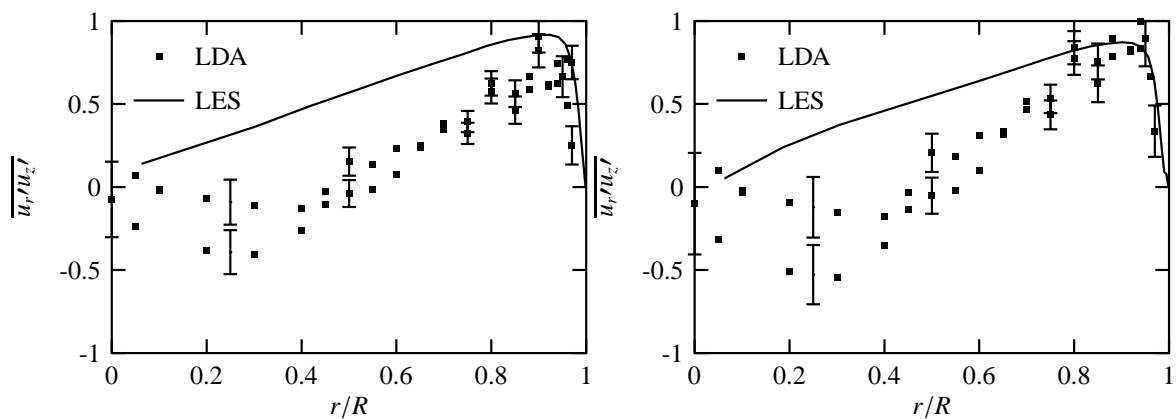


Figure E.7: Shear stress $\overline{u'_r u'_z}$. Comparison of two methods to generate a swirling flow in an LES with periodic boundary conditions: forcing through the tangential shear stress profile (left, equation (4.42)) or through the mean tangential velocity (right, equation (4.40)). For notes on normalisation, see E.2.

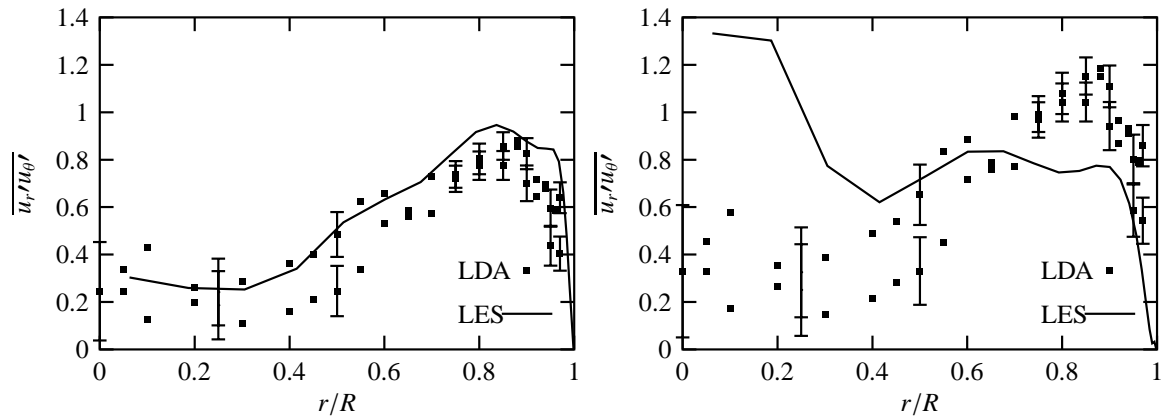


Figure E.8: Shear stress $\overline{u'_r u'_\theta}$. Comparison of two methods to generate a swirling fbw in an LES with periodic boundary conditions: forcing through the tangential shear stress profile (left, equation (4.42)) or through the mean tangential velocity (right, equation (4.40)). For notes on normalisation, see E.2.

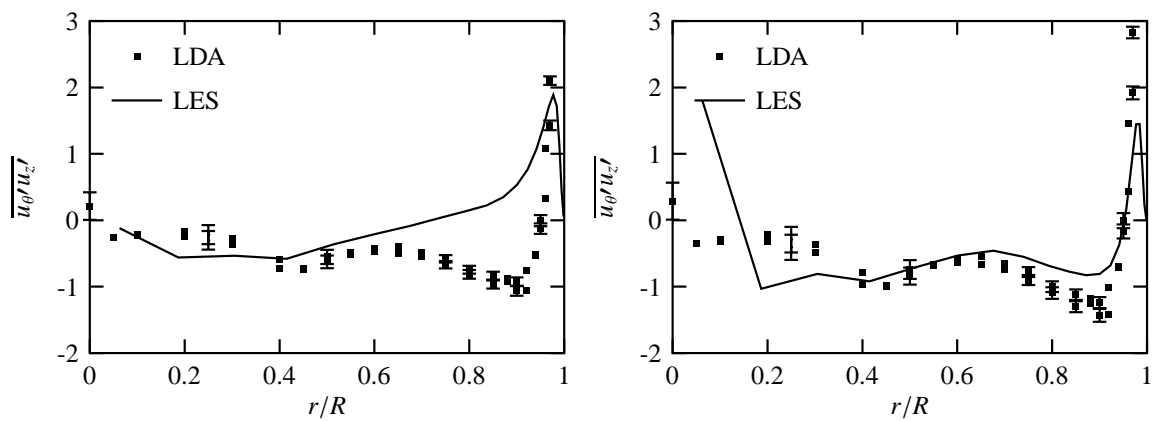


Figure E.9: Shear stress $\overline{u'_\theta u'_z}$. Comparison of two methods to generate a swirling fbw in an LES with periodic boundary conditions: forcing through the tangential shear stress profile (left, equation (4.42)) or through the mean tangential velocity (right, equation (4.40)). For notes on normalisation, see E.2.

F

Dependence of simulations of developed pipe flow on size and shape of the grid

In chapter 4 (sections 4.1.6 and 4.1.4) two issues have been raised with respect to the grid-dependence of simulation results: grid *size* dependence (section 4.1.6) and grid *shape* dependence (section 4.1.4).

F.1 Grid size dependence

The dependence of simulation results on the grid resolution has been tested with three grids. These are summarised in table F.1. The grid dependence of the bulk velocity is shown in figure F.1. For the two largest grids the simulated bulk velocity is well within 1% of the theoretical value of 17.33 for the Reynolds number under consideration. The mean axial velocity, shown in figure F.2, also gives no clear difference between the two highest resolutions. The turbulent normal stresses (figures F.2 and F.3), on the other hand do show differences between all resolutions, where the results of the highest resolution come closest to the experimental data. For the $\overline{u'_r u'_r}$ and $\overline{u'_z u'_z}$ stress the simulation results nearly coincide with the laboratory data, whereas the $\overline{u'_\theta u'_\theta}$ stress is still too low in the near-wall region. Finally the shear stress is shown in figure F.4. Given the fact that this stress should balance the pressure gradient forcing (which is identical for all simulations) the results do hardly differ between the different resolutions.

name	Configuration				Result
	N_r	N_θ	N_z	\tilde{N}_L	U_{bulk}
A	16	96	96	27.8	19.49
B	33	156	156	51.0	17.42
C	48	234	234	75.2	17.18

Table F.1: Characteristics of the three simulations. N_r , N_θ and N_z are the number of grid points in the radial, tangential and axial direction respectively.

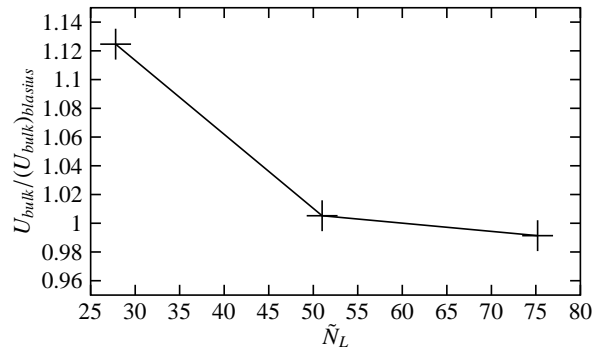


Figure F.1: Bulk velocity as a function of the size of the grid used. This size of the grid is expressed with N_L , i.e. the equivalent number of grid points.

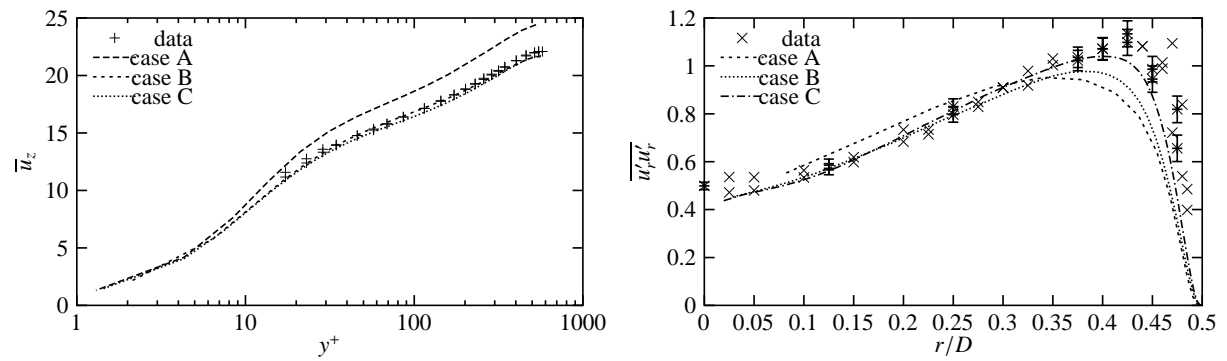


Figure F.2: Mean axial velocity and $\overline{u_r'u_r'}$ stress for different grid sizes. For the experimental data the distance to the wall in wall units has been determined using the theoretical value for u_* / U_{bulk} .

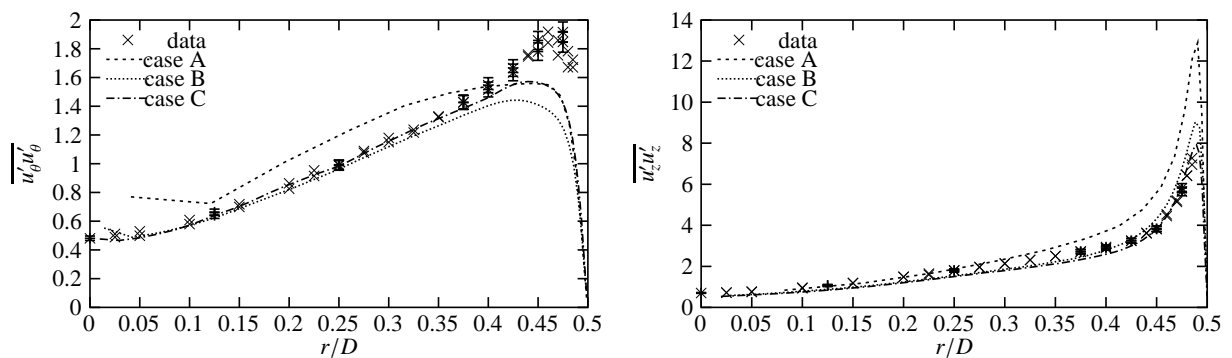


Figure F.3: $\overline{u_\theta'u_\theta'}$ and $\overline{u_z'u_z'}$ stresses for different grid sizes.

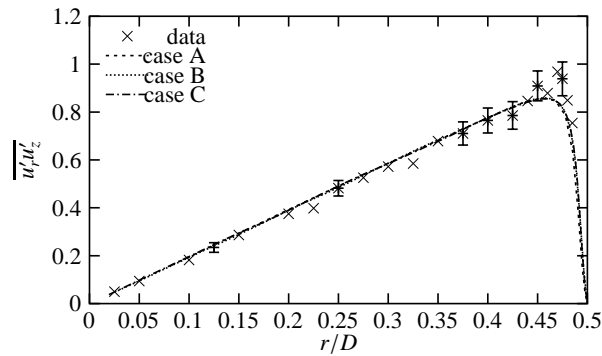


Figure F.4: $\overline{u'_r u'_z}$ shear stress for different grid sizes.

Configuration				Result
name	N_r	N_θ	N_z	U_{bulk}
A	21	128	128	18.35
B	21	96	172	19.94
C	21	172	96	18.02
D	21	224	74	18.12

Table F.2: Characteristics of the four simulations. N_r , N_θ and N_z are the number of grid points in the radial, tangential and axial direction respectively.

F.2 Grid shape dependence

In order to study the dependence of LES results on the aspect ratio of the grid cells, four simulations have been performed. All four simulations have the same number of grid points, but they differ in the allocation of those grid points to the different coordinate directions. The flow used to study the dependence of LES results on the aspect ratio of the grid cells is a simple developed pipe flow through a straight pipe. The domain length is five pipe diameters and the turbulent Reynolds number Re equals 1150. The characteristics of the four simulations are summarised in table F.2. The theoretical value for the bulk velocity (from Blasius' law) is 17.32. It is clear that none of the simulations reaches this value. However, the simulations with a high resolution in the tangential direction come closest to the theoretical value. This might support the claim that in cylindrical coordinates a high tangential resolution is needed to faithfully represent the turbulence in the near-wall region (see section 4.1.4 and figure F.7)

In figures F.6 through F.8 the mean velocities and Reynolds stresses are compared between the four simulations and with experimental data (see chapter 5). In figure F.5 the difference in bulk velocity between the different simulations is clearly visible. Although the differences in the Reynolds stresses are not large, there is a clear tendency that the simulations with the highest tangential resolution (simulations C and D) are closest to the experimental data, especially in the near-wall region.

The bump in the $\overline{u'_\theta u'_\theta}$ stress near the pipe axis seems to be worse for simulations with high

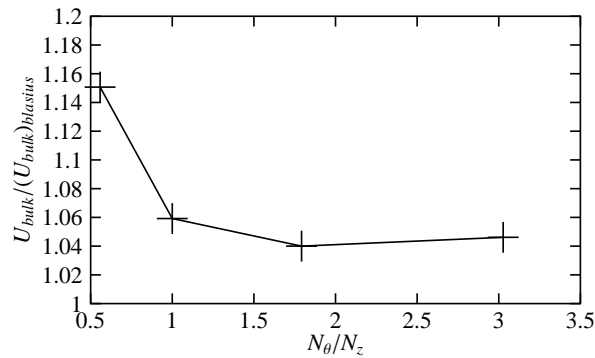


Figure F.5: Bulk velocity as a function of the aspect ratio of the grid used. This aspect ratio is expressed as N_θ/N_z .

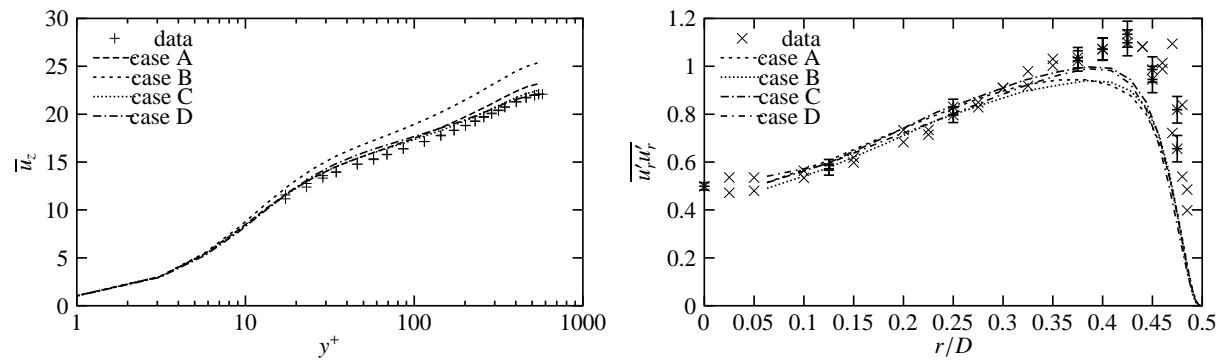


Figure F.6: Mean axial velocity and $\overline{u'_r u'_r}$ stress for different aspect ratios between axial and tangential resolution. For the experimental data the distance to the wall in wall units has been determined using the theoretical value for u_*/U_{bulk} .

tangential resolution. This strengthens the idea that the bump is due to the overresolution of eddies near the pipe axis, where eddies are large, whereas the tangential grid spacing is very small.

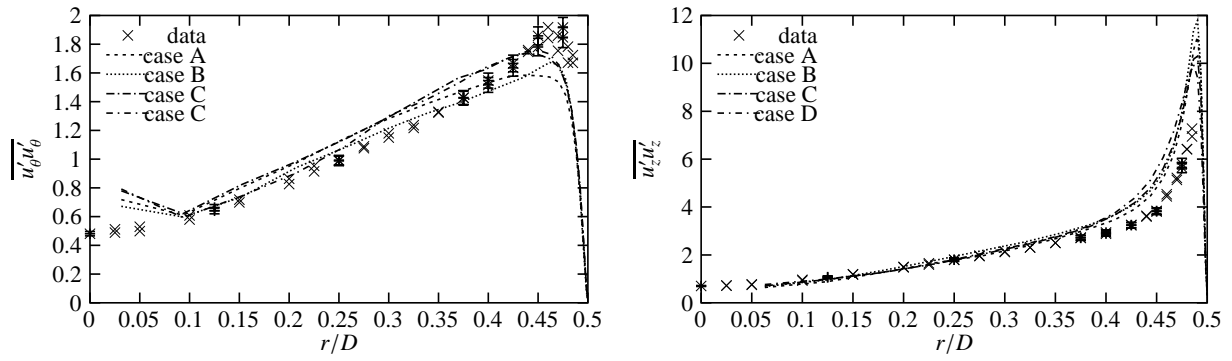


Figure F.7: $\overline{u'_\theta u'_\theta}$ and $\overline{u'_z u'_z}$ stresses for different aspect ratios between axial and tangential resolution.

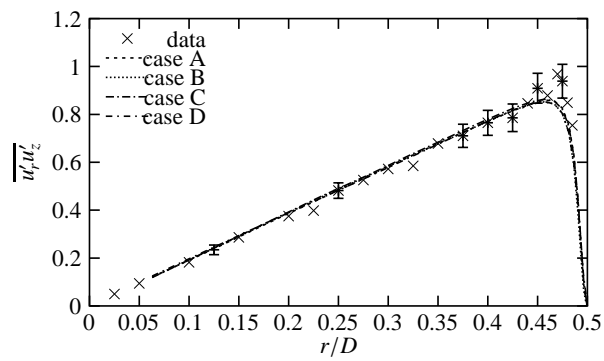


Figure F.8: $\overline{u'_r u'_z}$ shear stress for different aspect ratios between axial and tangential resolution.

G

Wiggles or oscillations in Large Eddy Simulation of swirling pipe flow

G.1 Introduction

In the course of this research as well as in the work of van Haarlem (1995) it was observed that wiggles occur in the near-wall region when making a Large Eddy Simulation of swirling pipe flow. The wiggles only occur in the axial direction. This phenomenon will be described in more detail in section G.2. Possibilities to get rid of these wiggles are discussed in section G.3.

G.2 Wiggles

Wiggles occur in a simulation as waves or oscillations with a wavelength of twice the grid spacing (in the direction of the wiggles). This can be explained either in terms of the mesh-Reynolds number or aliasing.

G.2.1 Role of mesh-Reynolds number

The mesh-Reynolds number (or more general, the mesh-Peclet number) is a Reynolds number based on a convection velocity a and the mesh size Δx : $Re_{mesh} = \frac{a\Delta x}{\alpha}$, where α is the viscosity.

Hirsch (1990a) analyses the role of Re_{mesh} in the occurrence of wiggles using a normal mode representation of the solution of a differential equation. Consider a stationary one-dimensional convection-diffusion equation on a domain $0 \leq x \leq L$ with boundary conditions u_0 at $x = 0$ and u_L at $x = L$. The differential equation is discretized with a centred second-order discretisation:

$$a \frac{u_{i+1} - u_{i-1}}{2\Delta x} = \alpha \frac{u_{i-1} - 2u_i + u_{i+1}}{\Delta x^2}, \quad (\text{G.1})$$

with $i = 1, \dots, N - 1$. This can be written in terms of Re_{mesh} as:

$$(2 - Re_{mesh}) u_{i-1} - 4u_i + (2 + Re_{mesh}) u_{i+1} = 0. \quad (\text{G.2})$$

If the solution is of the form $u = \kappa^i$ G.2 can be written as:

$$(2 - Re_{mesh}) \kappa^2 - 4\kappa + (2 + Re_{mesh}) = 0, \quad (\text{G.3})$$

which has the solution

$$u_i = u_0 + (u_L - u_0) \frac{\kappa_2^i - 1}{\kappa_2^N - 1} \quad (\text{G.4})$$

with

$$\kappa_2 = \frac{2 + Re_{mesh}}{2 - Re_{mesh}} \quad (G.5)$$

From the definition of κ_2 one can see that when Re_{mesh} exceeds 2 an oscillatory solution will occur. The amplitude of the oscillations is proportional to $(u_L - u_0)$, i.e. depending on the boundary conditions.

When Re_{mesh} becomes large, the diffusion term in the original differential equation becomes negligible. What remains is a singular perturbation of the original equation: the order of the differential equation is lowered and the new differential equation can not satisfy both boundary conditions (Roache, 1976).

Given the analysis above, one could question why wiggles do not appear in LES of developed pipe flow (without swirl), whereas in those simulations Re_{mesh} will generally be much larger than 2 (if $Re_D = 20000$, $\Delta x = D/40$, and the SGS viscosity is of the order of the molecular viscosity, $Re_{mesh} = 250$). The answer is most probably that wiggles *do* occur, but that their amplitude, relative to the turbulent fluctuations is too small to observe them. As observed above, the amplitude of wiggles is proportional to $u_L - u_0$. When the boundary conditions are taken at the inflow and outflow plane of the pipe section, $u_L - u_0$ will be nearly zero if the flow is homogeneous in the axial direction (or exactly zero in case of periodic boundary conditions). The largest difference $u_L - u_0$ can be found when focussing on one turbulent structure and will be of the order of u_* .

The analysis in terms of Re_{mesh} does not provide a reason why wiggles are prominent in swirling flow simulations and not discernible in simulations of non-swirling flow.

G.2.2 Aliasing

If the flow under consideration is nearly inviscid, the non-linear advection term $u \frac{\partial u}{\partial x}$ can generate fluctuations with wave numbers as high as twice the wavenumber that can be represented on the grid. This high-wavenumber energy will be aliased to wavenumbers that *can* be represented on the mesh (Hirsch, 1990b) and may occur as fluctuations with wavelength $2\Delta x$ or more.

Hirsch (1990a) gives an example of a centrally discretized gradient of u :

$$\left(u \frac{\partial u}{\partial x} \right)_i \approx u_i \left(\frac{u_{i+1} - u_{i-1}}{2\Delta x} \right). \quad (G.6)$$

u can be represented in terms of a Fourier expansion

$$u_i = \sum_k v(k) e^{jki\Delta x}, \quad (G.7)$$

with $j = \sqrt{-1}$ and k is the wave number. Then the advection term becomes:

$$\left(u \frac{\partial u}{\partial x} \right)_i \approx \sum_{k_1} \left(\sum_{k_2} v(k_2) e^{jk_2 i \Delta x} \right) v(k_1) e^{jk_1 i \Delta x} \frac{1}{2\Delta x} (e^{jk_1 \Delta x} - e^{-jk_1 \Delta x}) \quad (G.8)$$

$$\approx \frac{j}{\Delta x} \sum_{k_1} \sum_{k_2} v(k_1) v(k_2) e^{j(k_1+k_2)\Delta x} \sin k_1 \Delta x \quad (G.9)$$

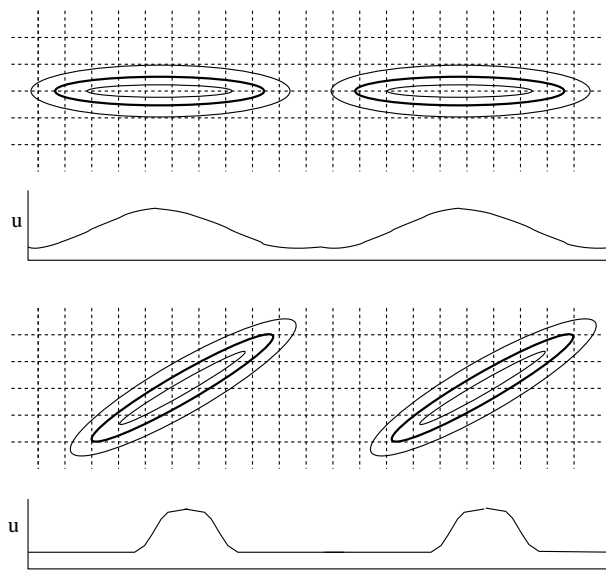


Figure G.1: Illustration of effect of angle between flow structures and axial direction on high wave number fluctuations. The upper figure shows the iso-velocity lines of two flow structures (streaks) aligned with the axial direction. Below the grid a sketch of the axial profile of the velocity is given. The lower figure is representative of a swirling flow in which the streaks make an angle with the axial direction. This angle introduces energy at higher wave numbers in the velocity signal (i.e. steeper velocity profiles and more abrupt changes in velocity).

Thus for combinations of k_1 and k_2 where $(k_1 + k_2)\Delta x > \pi$ the energy with such high wave numbers will occur at wavenumber $\frac{2\pi}{\Delta x} - (k_1 + k_2)$. Whether this aliased energy is a significant amount depends on the energy at wavenumbers k_1 and k_2 .

It is at this point that a swirling flow differs from a developed pipe flow. In the wall region turbulent structures (i.e. organised velocity fluctuations) are present that are aligned with the mean flow. The streamwise extent of these structures or streaks is much larger than the cross-flow extent. In a flow without swirl these structures are aligned with axial direction and the amount of energy at high wave numbers is limited (velocity fluctuations occur at a scale in the axial direction much larger than Δx). In the case of a swirling flow, however, the elongated structures make an angle with the axial direction. As a consequence, large fluctuations occur at wave numbers close to Δx . When the advection term is computed with such field, considerable energy will become available at wavenumbers $\frac{\pi}{\Delta x}$, and this energy will be aliased to wave numbers less than $\frac{\pi}{\Delta x}$ (see figure G.1).

Thus aliasing may be the reason why wiggles do occur in simulations of swirling flow but not in simulations of non-swirling flow.

G.3 Solutions

Given that aliasing has been identified as the source of wiggles in the simulation of swirling flow, here possible solutions will be discussed.

The most fundamental way to remove aliasing is to find a way to resolve the energy that occurs at wave numbers above $\frac{\pi}{\Delta x}$ due to the advection term. Once that energy has been represented correctly it could be removed (filtered) from the simulation and the original resolution should be sufficient to represent the resulting velocity field. In spectral space this should be rather straightforward, but in physical space the solution is less obvious.

In the case of LES a similar approach is possible. If in an LES the size of the filter with which the equations have been filtered is sufficiently larger than the grid size the fluctuations with wave numbers above the wave number of the filter can still be represented. What should be done then is to remove those high wave number fluctuations in order to prevent them from destroying the simulation. In the case that the Smagorinsky model is used the filter size can be increased by increasing C_s .

One could be tempted to increase the resolution since in that case waves with higher wave numbers can be represented. But if the filterlength in an LES model is tied to the grid size a decrease in Δz at the same time implies a decrease of the filter length $2\Delta^*$ (see 4.15b), although it depends on the formulation of the effective grid spacing Δ^* what the effect of a decrease in Δz on Δ^* is ¹.

The most commonly used method to eliminate wiggles that are due to aliasing is to make the simulation less inviscid, i.e. to increase the viscosity:

- One could choose a discretisation that has a leading discretisation error of odd order. This error will introduce an artificial viscosity. The first-order upwind discretisation is an example of this. Tests with this discretisation have shown that indeed the wiggles disappear but at the cost of a very large artificial viscosity.
- One could decrease the Reynolds number of the flow to be simulated. This will result in a simulation of a flow that differs from the original problem.
- In the case of LES with the Smagorinsky model for SGS stresses, an increase of the filter length through an increase of C_s indeed decreases the effective Reynolds number as well (where the effective Reynolds number is a Reynolds number based on the sum of molecular and SGS viscosity).
- One could filter the velocity fields at each time step to *suppress* the wiggles.

In the present simulations extra diffusion is applied based on an indicator for the occurrence of wiggles. This will be discussed below.

In simulations of swirling flows with the present model it was observed that the wiggles only occur in the axial direction. Furthermore, they were most obvious in u_r . In order to remove or suppress wiggles one needs an indicator for the presence of wiggles. Here the second order transverse structure function of u_r will be used, for two separations, viz. $r = \Delta z$ and $r = 2\Delta z$:

$$F_{u_r,z}(r) = \overline{[u_r(z+r) - u_r(z)]^2} \quad (\text{G.10})$$

¹The formulation used in the present model, equation 4.37 has the special property that when Δz becomes very small, Δ^* no longer decrease. Consequently the filterlength does not decrease monotonously with Δz . For this particular choice of Δ^* , an increase in the axial resolution may actually help to reduce aliasing.

When r is within the inertial subrange, the dependence of F_{u_r} on r should follow a $\frac{2}{3}$ power law. However, when wiggles are present on the smallest scale, $F_{u_r,z}$ for $r = \Delta z$ will give relatively elevated values when compared to the $F_{u_r,z}$ for $r = 2\Delta z$. Therefore, the following expression can be used as an indicator of wiggles:

$$w_1 = \frac{F_{u_r,z}(\Delta z)}{F_{u_r,z}(2\Delta z)} \left(\frac{\Delta z}{2\Delta z} \right)^{-2/3} \quad (\text{G.11})$$

$w = 1$ when the turbulent field exhibits a normal inertial subrange, but in case of wiggles (occurring mainly at $r = \Delta z$) $w > 1$. The link between this indicator in terms of the structure function and the increased viscosity needed to increase diffusion is the structure function SGS model (see (4.24) in section 4.1.3). The ratio given in (G.11) is translated into a ratio of SGS viscosities (see (4.24)):

$$w_2 = \frac{\sqrt{F_{u_r,z}(\Delta z)}}{\sqrt{F_{u_r,z}(2\Delta z)}} \left(\frac{\Delta z}{2\Delta z} \right)^{-4/3} . \quad (\text{G.12})$$

The SGS viscosity is then modified as follows:

$$\nu_{t,new} = \nu_t (1 + \gamma(w_2 - 1)) , \quad (\text{G.13})$$

where ν_t is the standard SGS viscosity (described in section 4.2.4). w_2 is as defined in (G.12) where the structure functions have been determined by averaging in the homogeneous z and θ directions. γ is a factor with a value of at least one. If $\gamma = 1$ does not give sufficient damping, the value of γ could be increased. One reason why $\gamma = 1$ would not give sufficient damping is that the wiggles usually do occur only in a part of the pipe, whereas the structure functions have been averaged over a complete cylinder with a given r .

G.4 Conclusion

In the context of LES of swirling pipe flow, the occurrence of wiggles (or oscillations with a wavelength of twice the grid spacing) are not the result of a too high mesh-Reynolds number. Rather, they are the result of aliasing, which is most pronounced in nearly inviscid flows but occurs in any simulation where non-linear advection terms are present. In order to suppress the wiggles an empirical method has been developed which introduces extra diffusion at radial positions where it is needed.

It has not been tested, but the use of a numerical scheme with artificial diffusion (i.e. 3rd order upwind) would have helped as well.

H

Pressure strain terms in turbulent flow through an axially rotating pipe: test of models with DNS results

H.1 Intro

One of the terms in the budget equations for the Reynolds stresses is a covariance term that is the covariance of a velocity component and the a pressure gradient (see appendix B). In the case of an incompressible flow this term can be rewritten as the sum of a pressure-strain term and a pressure diffusion term. In the practice of second order the latter is then combined with the modelling of the turbulence diffusion term. The pressure-strain tensor is (here written in index notation for Cartesian coordinates, for convenience)

$$\Pi_{ij} = \frac{1}{\rho} \overline{p' S'_{ij}} \quad (\text{H.1})$$

On one hand this term can not be measured in any physical experiment. On the other hand, it is the dominant term in the budgets of those Reynolds stresses that have no direct production.

During the research for the current thesis, a side step has been made to analyse the data from a Direct Numerical Simulation (DNS) by Eggels *et al.* (1995) (a DNS of the turbulent flow through an axially rotating pipe). Since this flow bears some resemblance to the swirling flow studied in the current research, the results will be presented here. The DNS results will be used here to determine the the pressure strain term as well as its *rapid* and *slow* part (section H.4.1). Furthermore, various models for the pressure strain tensor (section H.2) will be tested (section H.4.2). It should be kept in mind that this is an *off-line* test. It does not give direct information on the skill of complete second-order closure models to model the flow under consideration.

H.2 Models for the pressure strain tensor

The modelling of Π_{ij} generally involves the decomposition of the pressure fluctuations in a *rapid* and a *slow* part. This decomposition is based on the Poisson equation for p' :

$$\frac{1}{\rho} \nabla^2 p' = -2 \frac{\partial \bar{u}_i}{\partial x_j} \frac{\partial u'_j}{\partial x_i} - \frac{\partial^2}{\partial x_i \partial x_j} (u'_i u'_j - \overline{u'_i u'_j}), \quad (\text{H.2})$$

where the first term on the RHS is the RHS for the Poisson equation of p'_{slow} and the second is the RHS of the Poisson equation of p'_{rapid} . The problem in devising closures for Π_{ij} is that p' is

not a locally determined quantity, as the Poisson equation shows. Therefore, local closures are incorrect in principle, though they may be useful in practice.

If the turbulent quantities are *locally* homogeneous and all derivatives higher than first order are zero for the mean flow, the Poisson equation can be solved to yield the following expression for Π_{ij} :

$$\begin{aligned}\Pi_{ij} &= A_{ij} + M_{ijkl} \frac{\partial \bar{u}_k}{\partial x_l}, \\ &= \psi_{ij,1} + \psi_{ij,2}\end{aligned}\quad (\text{H.3})$$

where the first term is the *slow* term and the second term is the *rapid* term. The tensors A_{ij} and M_{ijkl} involve integrals of velocity fluctuations gradients over the entire domain. When a solid boundary is present in the domain, an extra term occurs in (H.3): a wall-reflection term. Below, a more or less random choice of models for the pressure-strain term will be summarised.

Rotta (1951) devised the following model for A_{ij} :

$$\psi_{ij,1} = -C_1 \frac{\epsilon}{k} \left(\overline{u'_i u'_j} - \frac{2}{3} k \delta_{ij} \right), \quad (\text{H.4})$$

where ϵ is the dissipation ($= \frac{1}{2} \epsilon k k$), k is the turbulent kinetic energy ($= \frac{1}{2} \overline{u'_i u'_i}$) and δ_{ij} is the Kronecker delta. For C_1 a value of 1.8 will be used. For the normal stresses, A_{ij} is proportional to the deviation of a normal stress to its isotropic value. This mechanism has led to the name *return-to-isotropy* term. For the shear stresses, the Rotta hypothesis leads to a return to a zero shear stress, as A_{ij} is proportional to the deviation of the shear stress from zero. Two types of extensions have been made to this model: the constant C_1 has been made a function of the flow (more specifically: the stress invariants; see Launder (1989)) and an additional term has been added (see the model of Speziale *et al.* (1991), discussed below).

For the rapid term a number of closures have been devised (for an overview, see Wilcox (1993)). The "Quasi-isotropic" model (QI-model, due to Launder *et al.* (1975)) is formulated as:

$$\psi_{ij,2} = -\alpha \left(P_{ij} - \frac{1}{3} P_{kk} \delta_{ij} \right) - \beta \left(D_{ij} - \frac{1}{3} D_{kk} \delta_{ij} \right) - \gamma k S_{ij}, \quad (\text{H.5})$$

with

$$\begin{aligned}P_{ij} &= \overline{u'_i u'_m} \frac{\partial \bar{u}_j}{\partial x_m} + \overline{u'_j u'_m} \frac{\partial \bar{u}_i}{\partial x_m} \\ D_{ij} &= \overline{u'_i u'_m} \frac{\partial \bar{u}_m}{\partial x_j} + \overline{u'_j u'_m} \frac{\partial \bar{u}_m}{\partial x_i} \\ \alpha &= \frac{8 + C_2}{11}, \beta = \frac{8C_2 - 2}{11}, \gamma = \frac{60C_2 - 4}{55}, 0.4 < C_2 < 0.6\end{aligned}\quad (\text{H.6})$$

A modified version of the the "Isotropisation of Production" model (IP-model) of Naot *et al.* (1970) due to Fu *et al.* (1987) is:

$$\psi_{ij,2} = -C_2 \left(P_{ij} - \frac{1}{3} P_{kk} \delta_{ij} \right) - C_2 \left(C_{ij} - \frac{1}{3} C_{kk} \delta_{ij} \right), \quad (\text{H.7})$$

with P_{ij} as above and

$$C_{ij} = \bar{u}_l \frac{\partial \overline{u'_i u'_j}}{\partial x_l}. \quad (\text{H.8})$$

For the wall-reflection term, various models have been proposed. Here, the wall correction of Gibson and Launder (1978) is used as a correction relative to the QI-model (contrary to what is done in the original paper where the formulation of the rapid part only includes the first term of the QI-model). The wall corrections for the slow and rapid part are:

$$\psi_{ij,1w} = C'_1 \frac{\epsilon}{k} \left(\overline{u'_k u'_m n_k n_m} \delta_{ij} - \frac{3}{2} \overline{u'_k u'_i n_k n_j} - \frac{3}{2} \overline{u'_k u'_j n_k n_i} \right) \frac{k^{3/2}}{2.5\epsilon y} \quad (\text{H.9})$$

$$\psi_{ij,2w} = C'_2 \left(G_{km} n_k n_m \delta_{ij} - \frac{3}{2} G_{ik} n_k n_j - \frac{3}{2} G_{jk} n_k n_i \right) \frac{k^{3/2}}{2.5\epsilon y} \quad (\text{H.10})$$

with: n_i is the i -component of the normal to the wall, $C'_1 = 0.5$, $C'_2 = 0.3$, $G_{ij} = -C_2 (P_{ij} - \delta_{ij} P_{kk})$. Note that in the original paper of Gibson and Launder (1978) the length scale correction is $\frac{k^{3/2}}{\kappa \epsilon y}$ with κ the Von Karman constant, rather than $\frac{k^{3/2}}{2.5\epsilon y}$. The second wall correction tested is the one due to Craft and Launder (1992). The correction for the slow term is identical to the one use above. The correction for the rapid term is:

$$\begin{aligned} \psi_{ij,2w} = & -C_{2a} \frac{\partial \bar{u}_l}{\partial x_m} \overline{u'_l u'_m} (\delta_{ij} - 3n_i n_j) \frac{k^{\frac{3}{2}}}{2.5\epsilon y} \\ & - C_{2b} k a_{lm} \left(\frac{\partial \bar{u}_k}{\partial x_m} n_l n_k \delta_{ij} - \frac{3}{2} \frac{\partial \bar{u}_i}{\partial x_m} n_l n_j - \frac{3}{2} \frac{\partial \bar{u}_j}{\partial x_m} n_l n_i \right) \frac{k^{3/2}}{2.5\epsilon y} \\ & + C_{2c} k \frac{\partial \bar{u}_l}{\partial x_m} n_l n_m \left(n_i n_j - \frac{1}{3} \delta_{ij} \right) \frac{k^{3/2}}{2.5\epsilon y} \end{aligned} \quad (\text{H.11})$$

with $a_{ij} = (\overline{u'_i u'_j} - \frac{2}{3} \delta_{ij} k) / k$, $C'_{2a} = 0.08$, $C'_{2b} = 0.1$ and $C'_{2c} = 0.4$.

Finally the model of Speziale *et al.* (1991) will be tested. This model (SSG-model) gives an expression for the total pressure strain term (for a flow without system rotation):

$$\begin{aligned} \Pi_{ij} = & -(C''_1 \epsilon + C''_{1*} P_{kk}) a_{ij} + C''_2 \epsilon \left(a_{ij} a_{kj} - \frac{1}{3} a_{mn} a_{nm} \delta_{ij} \right) \\ & + (C''_3 - C''_{3*} \sqrt{\Pi}) k S_{ij} + C''_4 k \left(a_{ik} S_{jk} + a_{jk} S_{ik} - \frac{2}{3} a_{mn} S_{mn} \delta_{ij} \right) + C''_5 k (a_{ik} W_{jk} + b_{jk} W_{ik}), \end{aligned} \quad (\text{H.12})$$

with S_{ij} is the strain tensor, W_{ij} is the vorticity tensor $\frac{1}{2} \left(\frac{\partial \bar{u}_i}{\partial x_j} - \frac{\partial \bar{u}_j}{\partial x_i} \right)$, $C''_1 = 3.4$, $C''_{1*} = 1.8$, $C''_2 = 4.2$, $C''_3 = 0.8$, $C''_{3*} = 1.3$, $C''_4 = 1.25$, $C''_5 = 0.4$. Pourahmadi and Humphrey (1985) show that the QI-model and the IP-model are just special cases of the SSG model (albeit with different values for the coefficients).

H.3 The fbw and the simulation

In order to test the relative importance of the rapid and slow part of the pressure strain correlation, as well as the quality of the different parameterisations, use will be made of velocity and pressure fields of the DNS 'C' experiment of Eggels *et al.* (1995). This DNS experiment concerns a rotating pipe with a domain length of 5 diameters D . The bulk Reynolds number Re_b is 5860, the turbulent Reynolds number Re equals 360. The tangential velocity of the wall, $\bar{u}_{\theta,w}$ is $0.61U_{bulk}$. The number of grid points in radial, tangential and axial direction is 96, 128, 256, respectively. Forty fields of u_i and p are used in the analysis, all taken from the quasi-steady period after $10t^*$ ($t^* = D/u_*$), spanning a period of about $5t^*$.

H.4 Results

H.4.1 Simulation results

Before discussing the results presented here, two remarks based on the work of Eggels *et al.* (1995) need to be made:

- In most budgets the pressure strain term is the largest term;
- All stresses are positive in this flow. Thus a positive sign of a budget term always signifies a gain term and vice versa.

Figures H.1 to H.3 show the pressure strain terms for the normal stresses $\overline{u'_r u'_r}$, $\overline{u'_\theta u'_\theta}$ and $\overline{u'_z u'_z}$, respectively. Π_{rr} is a gain term in the budget, except near the wall. The slow part and the rapid part counteract, the slow term being the major gain term. For $\Pi_{\theta\theta}$ the situation is quite different: except near the wall, the slow term is neglectable and the rapid part is the major gain term. For Π_{zz} the following can be noted: as could be expected –since the pressure-strain terms allow a for a return to isotropy– the pressure-strain term is a loss term for $\overline{u'_z u'_z}$. The rapid and slow part play a role of about equal magnitude.

Figures H.4 to H.6 show the results for the shear stresses $\overline{u'_r u'_\theta}$, $\overline{u'_r u'_z}$ and $\overline{u'_z u'_\theta}$, respectively. In figure H.4 it can be seen that for $\overline{u'_r u'_\theta}$ the pressure strain correlation is a loss term, except near the wall. The slow part is practically zero throughout most of the crosssection, but acts as a gain term near the wall (contrary to the assumption of a return-to-isotropy). Π_{rz} is neglectable or slightly positive in the central part of the pipe (up to $r/D = 0.2$). Except near the wall, the slow part is a loss term, whereas the rapid part is negative throughout. The $\overline{u'_r u'_z}$ stress is the only shear stress that is being fed through the pressure-strain interactions also *outside* the wall region. The rapid part gives by far the largest contribution. The slow part is neglectable, except near the wall, where it is positive and this conflicting the idea of a return to isotropy.

H.4.2 Results on the parameterisations

The results for the parameterisations of Π_{rr} are shown in figures H.1. The models for the rapid part differ in their ability to predict the negative rapid part near the wall. Only the models that include a wall-correction do show that negative value. The models for the slow part of Π_{rr} do show the correct tendency, but give too high values and do not show the negative value near the

wall. The wall-correction does not help much in this case. The results for the total pressure-strain term are that all models overestimate Π_{rr} , except for the SSG model that predicts a Π_{rr} that is too negative. In figure H.2 it can be seen that the results for $\Pi_{\theta\theta}$ are less diverse. Both for the rapid and the slow part all models give the correct tendency, although again the values are too high. Contrary to what occurred in the results of Π_{rr} , the models including wall-correction give *higher* values. The SSG model severely *underestimates* $\Pi_{\theta\theta}$. The results for Π_{zz} (figure H.3) are very comparable to those of $\Pi_{\theta\theta}$, except for the fact that $|\Pi_{rr}|$ is mostly positive and $\Pi_{\theta\theta}$ is positive. This trend is correctly predicted by the models, but again with too large values. The large deviation of the results of the SSG model from those of the other models appears to be mainly due to the term involving C''_{1*} . The peaks in the pressure strain term coincide with the location of the peak in the production of the turbulent kinetic energy (P_{kk}). When C''_{1*} is set to zero more reasonable values result.

The results for $\Pi_{r\theta}$ are given in figure H.4. For the slow part the various models give values that are neglectable relative to the slow part derived from the DNS results. For the rapid part the models diverge. The models show the correct tendency for $r/D < 0.4$ but for the region near the wall the results are incorrect. the local maximum at $r/D \approx 0.48$ is only present in the results of the model of Craft and Launder (1992). For the total $\Pi_{r\theta}$ all models show the correct tendency, with most models giving too high (negative) values. Figure H.5 shows the results for Π_{rz} . Both for the rapid part, slow part and the total pressure-strain term the models with wall-correction show the correct tendency. The SSG is completely off again. The first thing that is apparent in figure H.6 for $\Pi_{\theta z}$ is that there is no difference between the models with and without wall-correction. The models for the rapid part show the correct r -dependence, but the values are too low. The model results for the slow part are completely wrong. The results for the total $\Pi_{\theta z}$ are incorrect, with the SSG model being closest to the DNS results.

H.5 Conclusion

From the analysis presented above it can be concluded that in the case of turbulent flow through a rotating pipe the rapid part of the pressure-strain terms is at least as important as the slow part. For some stresses, $\overline{u'_\theta u'_\theta}$, $\overline{u'_r u'_\theta}$ and $\overline{u'_z u'_\theta}$, the rapid part is the only important contributor to the pressure-strain term. All models for the pressure-strain terms tested in this appendix are unable to represent the pressure-strain term correctly, except for a region close to the pipe centre. For some stresses the models do show the correct tendency. For the normal stresses the values are generally too large, for the shear stresses the values are of the correct order of magnitude.

It can be concluded that the present flow is still an interesting benchmark flow for Reynolds-stress models.

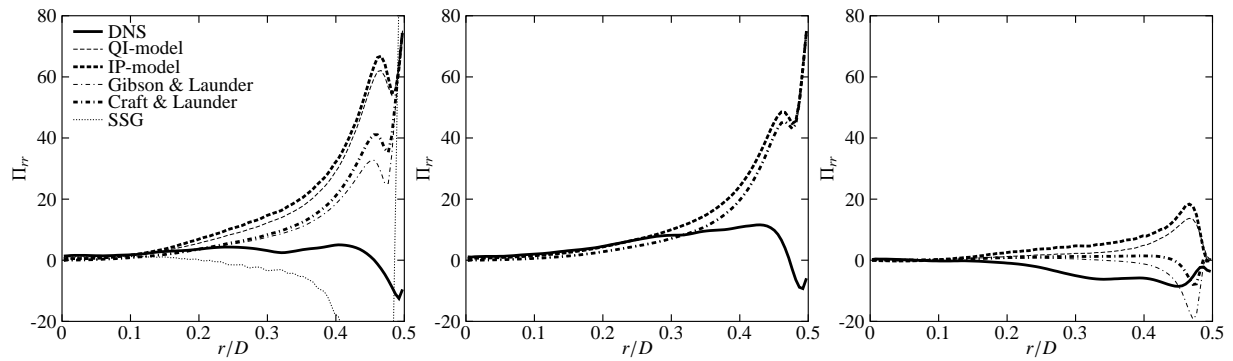


Figure H.1: Pressure strain term for $\overline{u_r'u_r'}$ stress: total term (left), slow part (centre) and rapid part (right). Comparison between DNS results and four models for the respective terms

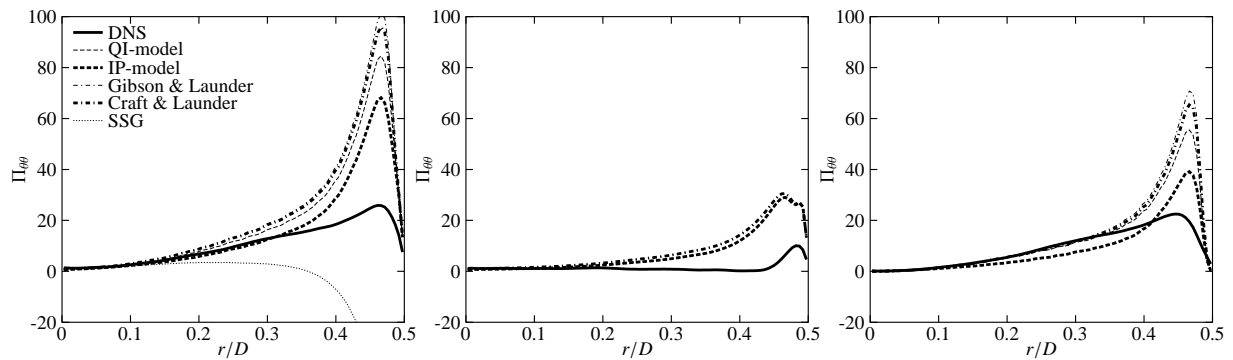


Figure H.2: Pressure strain term for $\overline{u_\theta'u_\theta'}$ stress: total term (left), slow part (centre) and rapid part (right). Comparison between DNS results and four models for the respective terms

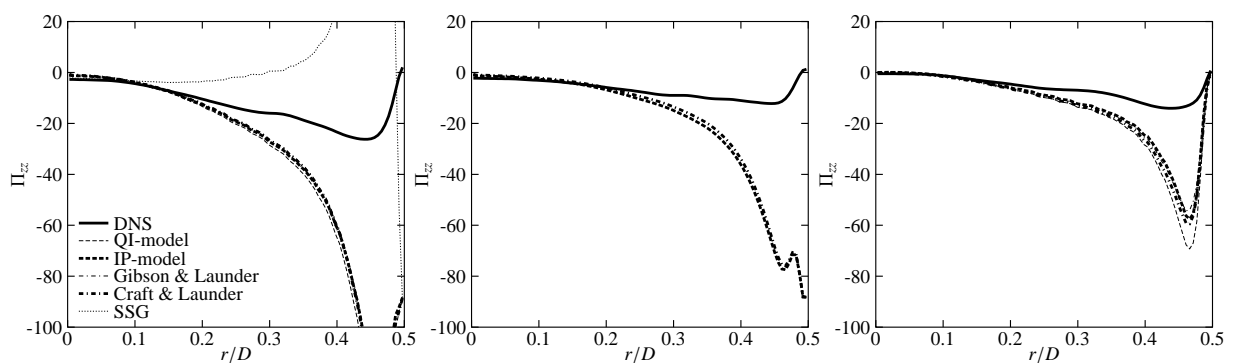


Figure H.3: Pressure strain term for $\overline{u_z'u_z'}$ stress: total term (left), slow part (centre) and rapid part (right). Comparison between DNS results and four models for the respective terms

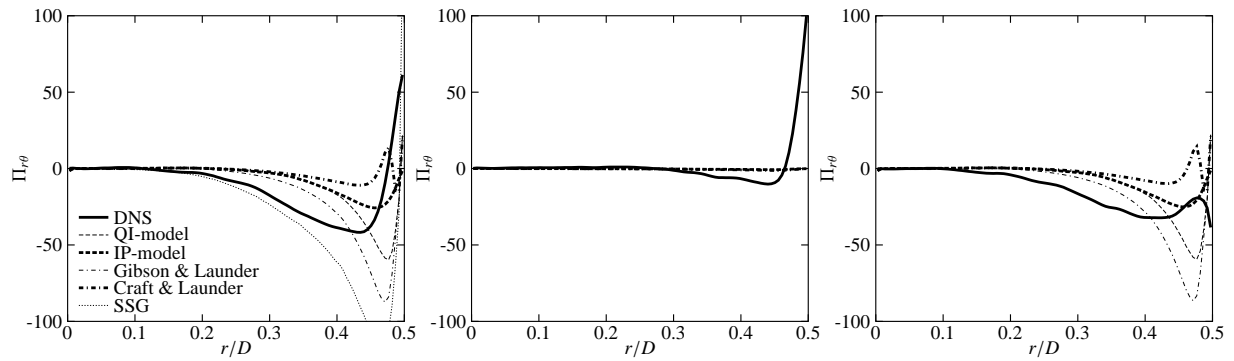


Figure H.4: Pressure strain term for $\overline{u_r'u_\theta'}$ stress: total term (left), slow part (centre) and rapid part (right). Comparison between DNS results and four models for the respective terms

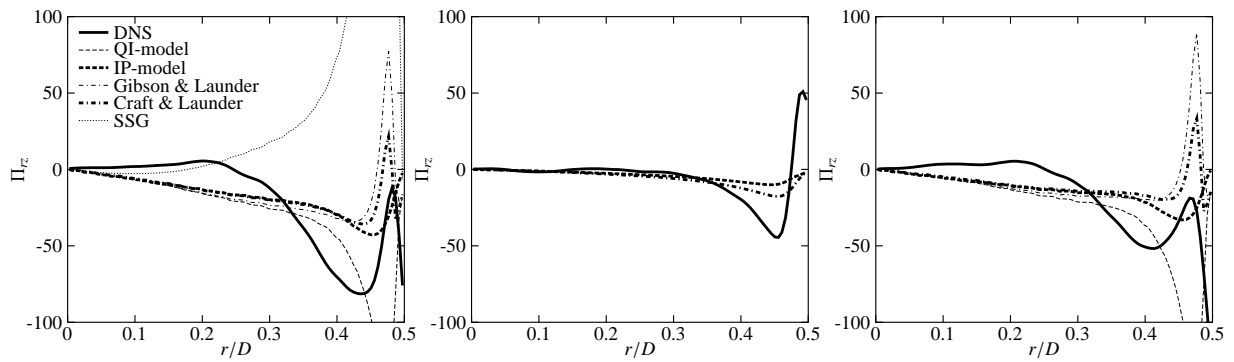


Figure H.5: Pressure strain term for $\overline{u_r'u_z'}$ stress: total term (left), slow part (centre) and rapid part (right). Comparison between DNS results and four models for the respective terms

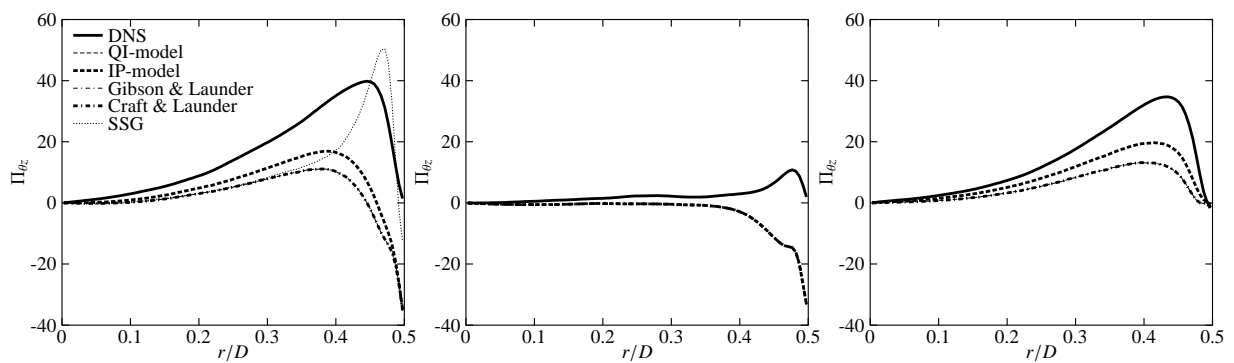


Figure H.6: Pressure strain term for $\overline{u_z'u_\theta'}$ stress: total term (left), slow part (centre) and rapid part (right). Comparison between DNS results and four models for the respective terms

Bibliography

- Adrian R. (1996). Laser velocimetry. In: *Fluid Mechanics Measurements* (editor R. Goldstein), pp. 175–299. Taylor & Francis, Washington etc.
- Aldama A.A. (1990). *Filtering Techniques for Turbulent Flow Simulation*, volume 56 of *Lecture Notes in Engineering*. Springer Verlag, Berlin etc.
- Aris R. (1989). *Vectors, Tensors, and the Basic Equations of Fluid Mechanics*. Dover, Mineola NY. (first published in 1962).
- Arnal M. and Friedrich R. (1993). Large-eddy simulation of a turbulent flow with separation. In: Durst *et al.* (1993), pp. 169–187.
- Barbin A.R. and Jones J.B. (1963). Turbulent flow in the inlet region of a smooth pipe. *J. Basic Engg.*, **85**, 29–34.
- Bardina J., Ferziger J.H. and Reynolds W.C. (1981). Improved subgrid models for large eddy simulation. AIAA Paper 80-1357.
- Bardina J., Ferziger J.H. and Rogallo R.S. (1985). Effect of rotation on isotropic turbulence: computation and modelling. *J. Fluid Mech.*, **154**, 321–336.
- Batchelor G.K. (1967). *An Introduction to Fluid Dynamics*. Cambridge University Press.
- Batchelor G.K. and Proudman I. (1954). The effect of rapid distortion of a fluid in turbulent motion. *Quart. J. Mech. Appl. Math.*, **7**, 83–103.
- Bendat J.S. and Piersol A.G. (1986). *Random Data: Analysis and Measurement Procedures*. John Wiley & Sons, 2nd edition.
- Benedict L.H. and Gould R.D. (1996). Uncertainty estimates for any turbulence statistic. In: *Proceedings of the 8th International Symposium on Applications of Laser Techniques to Fluid Mechanics, July 8-11*. Paper 36.1.
- van den Berg B. (1988). A European collaborative investigation of the three-dimensional turbulent shear layers of a swept wing. In: *Fluid Dynamics of Three-dimensional Turbulent Shear Flows and Transition*. AGARD. AGARD-CP-438.
- van den Berg B., Elsenaar A., Lindhout J.P.F. and Wesseling P. (1975). Measurements in an incompressible three-dimensional turbulent boundary layer, under infinite swept-wing conditions, and comparison with theory. *J. Fluid Mech.*, **70**, 127–148.
- Bertoglio J.P. (1982). Homogeneous turbulent field within a rotating frame. *AIAA Journal*, **20** (9), 1175–1181.
- Bissonette L.R. and Mellor G.L. (1974). Experiments on the behaviour of an axisymmetric turbulent boundary layer with a sudden circumferential strain. *J. Fluid Mech.*, **63**, 369–.
- Blasius H. (1908). Grenzschichten in Flüssigkeiten mit kleiner Reibung. *Z. Math. u Phys.*, **56**, 1–37.
- Boris G. and Orszag S.A. (editors) (1993). *Large Eddy Simulation of Complex Engineering and Geophysical Flows*. Cambridge University Press, New York.
- Boris J.P., Grinstein F.F., Oran E.S. and Kolbe R.L. (1992). New insights into large eddy simu-

- lation. *Fluid Dyn. Res.*, **10**, 199–228.
- Bradshaw P. (1969). The analogy between streamline curvature and buoyancy in turbulent shear flow. *J. Fluid Mech.*, **36**, 177–191.
- Bradshaw P. (1973). Effects of streamline curvature on turbulent flows. *AGARDograph*, **169**.
- Bradshaw P. (1975). REVIEW: Complex turbulent flows. *J. Fluids Engrng.*, **97**, 146–154.
- Bradshaw P. (1990). Effects of extra rates of strain – Review. In: *Near-wall Turbulence* (editors S.J. Kline and N.H. Afgan), pp. 106–122. Hemisphere Publishing Corporation.
- Bradshaw P. and Pontikos N.S. (1985). Measurements in the turbulent boundary layer on an "infinite" swept wing. *J. Fluid Mech.*, **159**, 105–130.
- Brouwers J.J.H. (2002). On diffusion theory in turbulence. *J. of Engineering Mathematics*, **44**, 277–295.
- Bruns J.M., Fernholz H.H. and Monkewitz P.A. (1999). An experimental investigation of a three-dimensional turbulent boundary layer in an 's'-shaped duct. *J. Fluid Mech.*, **393**, 175–213.
- Bullen P.R., Cheeseman D.J. and Hussain L.A. (1996). A study of turbulent flow in pipe contractions. *Proc. Instn. Mech. Engrs.*, **210**, 171–180.
- Cambon C., Benoit J.P., Shao L. and Jacquin L. (1994). Stability analysis and large-eddy simulation of rotating turbulence with organized eddies. *J. Fluid Mech.*, **278**, 175–200.
- Cambon C. and Jacquin L. (1989). Spectral approach to non-isotropic turbulence subjected to rotation. *J. Fluid Mech.*, **202**, 295–317.
- Canuto V.M. and Cheng Y. (1997). Determination of the Smagorinsky-Lilly constant c_s . *Phys. Fluids*, **9**, 1368–1378.
- Compton D.A. and Eaton J.K. (1997). Near-wall measurements in a three-dimensional turbulent boundary layer. *J. Fluid Mech.*, **350**, 189–209.
- Craft T.J. and Launder B.E. (1992). New wall-reflection model applied to the turbulent impinging jet. *AIAA Journal*, **30** (12), 2970–2972.
- Deardorff J.W. (1972). Numerical investigation of neutral and unstable planetary boundary layers. *J. Atmos. Sci.*, **29**, 91–115.
- Deardorff J.W. (1974). Three-dimensional numerical study of the height and mean structure of a heated planetary boundary layer. *Bound. Layer Meteor.*, **7**, 81–106.
- Deardorff J.W. (1980). Stratocumulus-capped mixed layers derived from a three-dimensional model. *Bound. Layer Meteor.*, **18**, 495–527.
- Dellenback P., Metzger D.E. and Neitzel G.P. (1988). Measurements in turbulent swirling flow through an abrupt axisymmetric expansion. *AIAA Journal*, **26** (6), 669–681.
- Desphande M.D. and Giddens D.P. (1980). Turbulence measurements in a constricted tube. *J. Fluid Mech.*, **97**, 65–89.
- van Dijk A. (1999). *Aliasing in one-point turbulence measurements - Theory, DNS and hotwire experiments*. Ph.D. thesis, Delft University of Technology.
- Draad A.A. (1996). *Laminar-Turbulent Transition in Pipe Flow for Newtonian and Non-Newtonian Fluids*. Ph.D. thesis, Delft University of Technology.
- van Driest E.R. (1956). On turbulent flow near a wall. *J. Aero. Sci.*, **23**, 1007–1011.
- Dupeuble A. and Cambon C. (1994). Linear analysis of the coupled action of rotation and axisymmetric contraction on a homogeneous turbulence, initially isotropic. *C. R. Acad. Sci. Paris*, **318**, 871–876.

- Durst F., Friedrich R., Launder B., Schmidt F., Shumann U. and Whitelaw J. (editors) (1993). *Turbulent Shear Flows. Selected Papers from the Eighth International Symposium on Turbulent Shear Flows, Munich, September 9-11, 1991*. Springer-Verlag, Berlin Heidelberg.
- Durst F., Jovanović J. and Sender J. (1995a). Detailed measurements of the near-wall region of a turbulent pipe flow. In: Durst *et al.* (1995b), pp. 225–240.
- Durst F., Kasagi N., Launder B.E., Schmidt F.W., Suzuki K. and Whitelaw J.H. (editors) (1995b). *Turbulent Shear Flows. Selected Papers from the Ninth International Symposium on Turbulent Shear Flows, Kyoto, Japan, August 16-18, 1993*. Springer-Verlag, Berlin Heidelberg.
- Eggels J.G.M. (1994). *Direct and Large Eddy Simulation of Turbulent Flow in a Cylindrical Pipe Geometry*. Ph.D. thesis, Delft University of Technology.
- Eggels J.G.M., Boersma B.J. and Nieuwstadt F.T.M. (1995). Direct and large-eddy simulations of turbulent flow in an axially rotating pipe. *submitted to J. Fluid Mech.; never published*.
- Eggels J.G.M., Unger F., Weiss M.H., Westerweel J., Adrian R.J., Friedrich R. and Nieuwstadt F.T.M. (1994). Fully developed turbulent pipe flow: a comparison between direct numerical simulation and experiment. *J. Fluid Mech.*, **268**, 175–209.
- Escudier M. (1987). Confined vortices in flow machinery. *Ann. Rev. Fluid Mech.*, **19**, 27–52.
- Ferziger J.H. (1993). Subgrid-scale modeling. In: Boris and Orszag (1993), pp. 37–54.
- Ferziger J.H. and Perić M. (1996). *Computational Methods for Fluid Dynamics*. Springer Verlag, Berlin etc.
- Ferziger J.H. and Shaanan S. (1976). Effect of anisotropy and rotation on turbulence production. *Phys. Fluids*, **19** (4), 596–597.
- Fu S., Launder B.E. and Leschziner M.A. (1987). Modelling strongly swirling recirculating jet flow with Reynolds-stress transport closures. In: *Proc. 6th Symp. on Turbulent Shear Flows*.
- Gao S., Yang Z. and Voke P.R. (1994). *Balance Equations in Finite-Volume Large-Eddy Simulations*. Departmental Working Paper ME-FD/94.27, Department of Mechanical Engineering, Surrey University.
- Garg A.K. and Leibovich S. (1979). Spectral characteristics of vortex breakdown flowfields. *Phys. Fluids*, **22**, 2053–2064.
- Garrat J.R. (1992). *The Atmospheric Boundary Layer*. Cambridge University Press, Cambridge.
- Germano M. (1992). Turbulence: the filtering approach. *J. Fluid Mech.*, **238**, 325–336.
- Ghosal S. and Moin P. (1995). The basic equations for the large eddy simulation of turbulent flows in complex geometry. *J. Comput. Phys.*, **118**, 24–37.
- Gibson M.M. and Launder B.E. (1978). Ground effects on pressure fluctuations in the atmospheric boundary layer. *J. Fluid Mech.*, **86**, 491–511.
- Goldstein M.E. and Durbin P.A. (1980). The effect of finite turbulence spatial scale on the amplification of turbulence by a contracting stream. *J. Fluid Mech.*, **98**, 473–508.
- van Haarlem B.A. (1995). *Large Eddy Simulation of Swirling Pipe Flow*. Master's thesis, Delft University of Technology, Department of Applied Physics. MEAH-126.
- Harlow F.H. and Welch J.E. (1965). Numerical calculation of time-dependent viscous incompressible flow of fluid with free surface. *Phys. Fluids*, **8** (12), 2182–2189.
- Hinze J.O. (1975). *Turbulence*. McGraw-Hill, 2nd edition.
- Hirsch C. (1990a). *Numerical Computation of Internal and External Flows 1: Fundamentals of Numerical Discretization*. John Wiley & Sons, Chichester etc.

- Hirsch C. (1990b). *Numerical Computation of Internal and External Flows 2: Computational Methods for Inviscid and Viscous Flows*. John Wiley & Sons, Chichester etc.
- Holloway A.G.L. and Tavoularis S. (1992). The effects of curvature on sheared turbulence. *J. Fluid Mech.*, **237**, 569–603.
- Holloway A.G.L. and Tavoularis S. (1998). A geometric explanation of the effects of mild streamline curvature on the turbulence anisotropy. *Phys. Fluids*, **10**, 1733–1741.
- Horiuti K. (1993). A proper velocity scale for modeling subgrid-scale eddy viscosities in large eddy simulation. *Phys. Fluids A*, **5**, 146–157.
- Hornung H.G. and Joubert P.N. (1962). The mean velocity profile in three-dimensional turbulent boundary layers. *J. Fluid Mech.*, **15**, 368–384.
- Hultgren L.S. and Cheng S.C. (1983). Rapid distortion of small-scale turbulence by an axisymmetric contraction. *Phys. Fluids*, **26** (2), 409–415.
- Hunt J.C.R. (1973). A theory of turbulent flow round two-dimensional bluff bodies. *J. Fluid Mech.*, **61**, 625–706.
- Imao S., Itoh M. and Harada T. (1996). Turbulent characteristics of the flow in an axially rotating pipe. *Int. J. Heat and Fluid Flow*, **17**, 444–451.
- Jacquín L., Leuchter O., Cambon C. and Mathieu J. (1990). Homogeneous turbulence in the presence of rotation. *J. Fluid Mech.*, **220**, 1–52.
- Jakirlić S., Hanjalić K. and Tropea C. (2000). Second-moment closure analysis of rotating and swirling confined flows. In: *Proc. European Congress on Computational Methods in Applied Sciences and Engineering, ECCOMAS 2000. Barcelona, 11-14 September 2000* (editors E. Onate, G. Bugenda and B. Suárez), pp. Proceedings on CD, 24 p.
- Johnston J.P., Halleen R.M. and Lezius D.K. (1972). Effects of spanwise rotation on the structure of two-dimensional fully developed turbulent channel flow. *J. Fluid Mech.*, **56**, 533–557.
- Kendall M.G. and Stuart A. (1958). *The advanced theory of statistics: Vol. 1, Distribution Theory*. Charles Griffin & Co Ltd, London.
- Kim J. and Moin P. (1985). Application of a fractional step method to incompressible Navier-Stokes equations. *J. Comput. Phys.*, **59**, 308–323.
- Kito O. (1984). Axi-symmetric character of turbulent swirling flow in a pipe. *Bull. of JSME.*, **28** (226), 683–690.
- Kitoh O. (1991). Experimental study of turbulent swirling flow in a straight pipe. *J. Fluid Mech.*, **225**, 445–479.
- Klein A. (1981). REVIEW: Turbulent developing pipe flow. *J. Fluids Engrng.*, **103**, 243–249.
- Kraichnan R. (1976). Eddy viscosity in two and three dimensions. *J. Atmos. Sci.*, **33**, 1521–1536.
- Kravchenko A.G. and Moin P. (1997). On the effect of numerical errors in large eddy simulations of turbulent flows. *J. Comput. Phys.*, **131**, 310–322.
- Kundu P.K. (1990). *Fluid Mechanics*. Academic Press, Inc., San Diego etc.
- Kuroda C. and Ogawa K. (1986). Turbulent swirling pipe flow. In: *Encyclopedia of Fluid Mech.*, Vol.1 (editor N.P. Cheremisinoff), pp. 611–637. Gulf, London.
- Launder B.E. (1989). Phenomenological modelling: Present, . . . and future? In: Lumley (1989), pp. 439–485.
- Launder B.E. (1990). Turbulence modelling for the Nineties: second moment closure . . . and beyond? In: *Lecture Notes in Physics No. 371* (editor K.W. Morton), pp. 1–18. Springer-

- Verlag.
- Launder B.E., Reece G.J. and Rodi W. (1975). Progress in the development of a Reynolds -stress turbulence closure. *J. Fluid Mech.*, **68**, 537–577.
- Laws E.M., Lim E.H. and Livesey J.L. (1987). Momentum balance in highly distorted turbulent pipe flows. *Exp. Fluids*, **5**, 36–42.
- Leibovich S. (1984). Vortex stability and breakdown: survey and extension. *AIAA Journal*, **22** (9), 1192–1206.
- Leibovich S. and Stewartson K. (1983). A sufficient condition for the stability of columnar vortices. *J. Fluid Mech.*, **126**, 335–356.
- Lenschow D.H., Mann J. and Kristensen L. (1994). How long is long enough when measuring fluxes and other turbulent statistics? *J. Atmos. Oceanic Technol.*, **11**, 661–673.
- Leonard A. (1974). Energy cascade in large-eddy simulation of turbulent fluid flows. *Adv. Geophys.*, **18A**, 237–248.
- Lesieur M. (1993). *Turbulence in Fluids*. Kluwer, Dordrecht, 2nd edition.
- Lesieur M. and Méttais O. (1996). New trends in large-eddy simulation of turbulence. *Ann. Rev. Fluid Mech.*, **28**, 45–82.
- Leslie D.C. and Quarini G.L. (1979). The application of turbulence theory to the formulation of subgrid modelling procedures. *J. Fluid Mech.*, **91**, 65–91.
- Leuchter O. (1997). Rotation effects on strained homogeneous turbulence. *ERCOfTAC Bulletin*, **32**, 52–57.
- Leuchter O. and Bertoglio J. (1995). Non-linear spectral approach to rotating turbulence in the presence of strain. Presented at the Tenth Symposium on Turbulent Shear Flows, Pennsylvania State University, August 14-16, 1995.
- Leuchter O. and Dupeuble A. (1993). Rotating homogeneous turbulence subjected to axisymmetric contraction. Presented at the 9th Symposium on Turbulent Shear Flow, Kyoto (Japan), August 16-18, 1993.
- Lilly D.K. (1992). A proposed modification of the Germano subgrid-scale closure method. *Phys. Fluids A*, **4**, 633–635.
- Lissenburg R.C.D., Hinze J.O. and Leijdens H. (1974). *An experimental investigation of the effect of a constriction on turbulent pipe flow*. Technical Report WTHD 76, Department of Mechanical Engineering, Delft University of Technology, Delft.
- Lumley J.L. (1978). Computational modelling of turbulent flows. In: *Advances in Applied Mechanics, Vol. 18* (editor C.S. Yih). Academic press.
- Lumley J.L. (editor) (1989). *Whither Turbulence? Turbulence at the Crossroads*. Springer-Verlag.
- Lumley J.L., Hestad D.E. and Morel P. (1985). Modelling the effect of buoyancy and rotation on turbulence. In: *Turbulence Measurements and Flow Modeling. Proceedings of the International Symposium on Refined Flow Modeling and Turbulence Measurements*. Hemisphere Publishing Corporation, New York, etc.
- Lumley J.L. and Panofsky H.A. (1964). *The Structure of Atmospheric Turbulence*. John Wiley & Sons.
- Mackrodt P.A.M. (1976). Stability of Hagen-Poiseuille flow with superimposed rigid rotation. *J. Fluid Mech.*, **73**, 153–164.

- Mansour N.N., Cambon C. and Speciale C.G. (1992). Theoretical and computational study of rotating isotropic turbulence. In: *Studies in Turbulence* (editor T.B.e.a. Gatski), pp. 59–75. Springer Verlag.
- Mason P. (1994). Large-eddy simulation: a critical review of the technique. *Q. J. R. Meteorol. Soc.*, **120**, 1–26.
- Mason P.J. and Callen N.S. (1986). On the magnitude of the subgrid-scale eddy coefficient in large-eddy simulations of turbulent channel flow. *J. Fluid Mech.*, **162**, 439–462.
- Mason P.J. and Thomson D.J. (1992). Stochastic backscatter in large-eddy simulations of boundary layers. *J. Fluid Mech.*, **242**, 51–78.
- Matsson O.J.E. and Alfredsson P.H. (1990). Curvature- and rotation-induced instabilities in channel flow. *J. Fluid Mech.*, **210**, 537–563.
- Mizushima T., Ito R., Ueda H., Tsubata S. and Hayashi H. (1970). Flow in the entrance region of a circular tube. *J. Chem. Eng. Japan*, **3**, 34–38.
- Moene A.F. and Michels B.I. (2002). Estimation of the statistical error in large eddy simulation results. In: *15th Symposium on Boundary Layers and Turbulence, 15-19 July 2002, Wageningen, The Netherlands*, pp. 287–288.
- Moin P. and Kim J. (1982). Numerical investigation of turbulent channel flow. *J. Fluid Mech.*, **118**, 341–377.
- Moin P. and Mahesh K. (1998). Direct numerical simulation: a tool in turbulence research. *Ann. Rev. Fluid Mech.*, **30**, 539–578.
- Monin A.S. and Yaglom A.M. (1971). *Statistical Fluid Mechanics: Mechanics of Turbulence*, volume Volume 1. The MIT Press, Cambridge etc.
- Murakami M. and Kikuyama K. (1980). Turbulent flow in axially rotating pipes. *J. Fluids Engrmg.*, **102**, 97–103.
- Naot D., Shavit A. and Wolfstein M. (1970). Interactions between components of the turbulent velocity correlation tensor. *Israel J. Tech.*, **8**, 259–269.
- Nieuwstadt F.T.M., Mason P.J., Moeng C.H. and Schumann U. (1993). Large-eddy simulation of the convective boundary layer: a comparison of four computer codes. In: Durst *et al.* (1993), pp. 343–367.
- Orlandi P. and Fatica M. (1997). Direct simulations of turbulent flow in a pipe rotating about its axis. *J. Fluid Mech.*, **343**, 43–72.
- Parchen R.R. and Steenbergen W. (1998). An experimental and numerical study of turbulent swirling pipe flows. *J. Fluids Engrmg.*, **120**, 54–61.
- Pedley T.J. (1969). On the stability of viscous flow in a rapidly rotating pipe. *J. Fluid Mech.*, **35**, 97–115.
- Phillips H.B. (1948). *Vector Analysis*. John Wiley & Sons, New York, tenth printing edition.
- Piomelli U. P.M. and Ferziger J.H. (1988). Model consistency in large eddy simulation of turbulent channel flows. *Phys. Fluids*, **31**, 1884–1891.
- Piomelli U. (1993). Applications of large eddy simulations in engineering: an overview. In: Boris and Orszag (1993), pp. 119–137.
- Pourahmadi F. and Humphrey J.A.C. (1985). Prediction of curved channel flow with an extended $k - \epsilon$ model of turbulence. *AIAA J.*, **21**, 1365.
- Pourquié M.J.B.M. (1994). *Large-eddy Simulation of a Turbulent Jet*. Ph.D. thesis, Delft Uni-

- versity of Technology.
- Prandtl L. (1961). Einfluss stabilisierender Kräfte auf die Turbulenz. In: *Gesammelte Abhandlungen zur angewandte Mechanik, Hydro- und Aerodynamik* (editors W. Tollmien, H. Schlichting and H. Goertler), pp. 778–785. Springer, Berlin.
- Rayleigh J.W.S. (1916). On the dynamics of revolving fluids. *Proc. Roy. Soc. A*, **43**, 148–154.
- Reich G. and Beer H. (1989). Fluid flow and heat transfer in an axially rotating pipe - i. effect of rotation on turbulent pipe flow. *Int. J. Heat Mass Transfer*, **32** (3), 551–561.
- Reichert J.K. and Azad R.S. (1976). Nonasymptotic behavior of developing turbulent pipe flow. *Can. J. Phys.*, **54**, 268–278.
- Reynolds A.J. and Tucker H.J. (1975). The distortion of turbulence by general uniform irrotational strain. *J. Fluid Mech.*, **68**, 674–693.
- Reynolds O. (1895). On the dynamical theory of incompressible viscous fluids and the determination of the criterion. *Phil. Trans. Roy. Soc. London*, **186**, 123–161.
- Reynolds W.C. (1989). The potential and limitations of direct and large eddy simulation. In: Lumley (1989).
- Richman J.W. and Azad R.S. (1973). Developing turbulent flow in smooth pipes. *Appl. Sci. Res.*, **28**, 419–441.
- Roache P.J. (1976). *Computational Fluid Dynamics*. Hermosa Publishers, Albuquerque, N. M., revised printing edition. Direct poisson solvers on page 132.
- Rodi W. (1976). A new algebraic relation for calculation of the Reynolds stresses. *ZAMM*, **56**, 219–221.
- Rotta J.C. (1951). Statistische Theorie nichthomogener Turbulenz. *Zeitschrift für Physik*, **129**, 547–572.
- Savill A.M. (1987). Recent developments in rapid-distortion theory. *Ann. Rev. Fluid Mech.*, **19**, 531–575.
- Schlichting H. (1979). *Boundary-Layer Theory*. McGraw-Hill, New York etc., 7th edition.
- Schmidt H. and Schumann U. (1989). Coherent structure of the convective boundary layer derived from large-eddy simulations. *J. Fluid Mech.*, **200**, 511–562.
- Schumann U. (1975a). Linear stability of finite difference equation for three-dimensional flow problems. *J. Comput. Phys.*, **18**, 465–470.
- Schumann U. (1975b). Subgrid scale model for finite difference simulations of turbulent flows in plane channels and annuli. *J. Comput. Phys.*, **18**, 376–404.
- Scotti A., Meneveau C. and Fatica M. (1997). Dynamic Smagorinsky model on anisotropic grids. *Phys. Fluids*, **9**, 1856–1858.
- Scotti A., Meneveau M. and Lilly D.K. (1993). Generalized Smagorinsky model for anisotropic grids. *Phys. Fluids A*, **5**, 2306–2308.
- Silveira Neto A., Grand D., Métais O. and Lesieur M. (1993). A numerical investigation of the coherent vortices in turbulence behind a backward-facing step. *J. Fluid Mech.*, **256**, 1–25.
- Smagorinsky J. (1993). *Some historical remarks on the use of nonlinear viscosities*, chapter 1, pp. 3–36. In: Boris and Orszag (1993).
- Smeets R. and van Nijmweegen F. (1993). *User manual PhyBUS PARSAM-25/250 Parallel Sampling ADC*. Physical and Technical Laboratory Automation Group; Department of Physics; University of Technology Eindhoven, Eindhoven, 1.0 edition. BL 92-02.

- Spencer A.J.M. (1988). *Continuum Mechanics*. Longman Mathematical Texts. Longman Scientific & Technical.
- Spencer E.A., Heitor M.V. and Castro I.P. (1995). Intercomparison of measurements and computations of flow through a contraction and a diffuser. *Flow Meas. Instrum.*, **6** (1), 3–14.
- Speziale C.G. (1985). Galilean invariance of subgrid scale stress models in the large eddy simulation of turbulence. *J. Fluid Mech.*, **156**, 55–62.
- Speziale C.G. (1987). On nonlinear $k-l$ and $k-\epsilon$ models of turbulence. *J. Fluid Mech.*, **178**, 459–475.
- Speziale C.G. (1989). Turbulence modelling: Present and future, comment 2. In: Lumley (1989), pp. 490–512.
- Speziale C.G., Abid R. and Anderson E.C. (1992). A critical evaluation of two-equation turbulence models for near wall flows. *AIAA J.*, **30**, 324–331.
- Speziale C.G., Sarkar S. and Gatski T.B. (1991). Modeling the Pressure-Strain correlation of turbulence. *J. Fluid Mech.*, **227**, 245–272.
- Sreenivasan K.R. (1985). The effect of contraction on a homogeneous turbulent shear flow. *J. Fluid Mech.*, **154**, 187–213.
- Steenbergen W. (1995). *Turbulent Pipe Flow with Swirl*. Ph.D. thesis, Eindhoven University of Technology.
- Steenbergen W. (1996). Reduction of beam refraction in optical pipe flow experiments: use of sheet-fabricated pipe walls. *Exp. Fluids*, **22**, 165–173.
- Steenbergen W. and Voskamp J. (1998). The rate of decay of swirl in turbulent pipe flow. *Flow Meas. Instrum.*, **9**, 67–78.
- Stull R.B. (1988). *An Introduction to Boundary Layer Meteorology*. Kluwer Academic Publishers, Dordrecht, Boston and London.
- Taylor G.I. (1923). Stability of a viscous liquid contained between two rotating cylinders. *Phil. Trans. Roy. Soc. A*, **223**, 289–343.
- Tennekes H. and Lumley J.L. (1972). *A First Course in Turbulence*. MIT Press.
- Traugott S.J. (1958). *Influence of solid-body rotation on screen-produced turbulence*. Technical Note 4135, NACA.
- Tritton D.J. (1992). Stabilization and destabilization of turbulent shear flow in a rotating fluid. *J. Fluid Mech.*, **241**, 503–523.
- Tsugé S. (1984). Effects of flow contraction on evolution of turbulence. *Phys. Fluids*, **27**, 1948–1956.
- Čantrák S. (1981). *Experimentelle Untersuchungen statistischer Eigenschaften turbulenter drall-behafteter Rho- und Diffusorströmungen*. Ph.D. thesis, Fakultät für Maschinenbau der Universität Karlsruhe (TH).
- van der Ven H. (1995). A family of large eddy simulation (LES) filters with nonuniform filter widths. *Phys. Fluids*, **7**, 1171–1172.
- Veronis G. (1970). The analogy between rotating and stratified fluids. *Ann. Rev. Fluid Mech.*, **2**, 37–66.
- Voskamp J.H., Nijmwegen van F.C. and Wal van der A.J. (1989). PHYDAS, een integraal systeem voor data-acquisitie en besturing van fysische experimenten (*in dutch*). *Ned. Tijdschr. v. Natuurk.*, **A55** (1/2), 50–55.

- Vreman B., Geurts B. and Kuerten H. (1997). Large-eddy simulation of the turbulent mixing layer. *J. Fluid Mech.*, **339**, 357–390.
- Wesseling P. (1996). Von Neumann stability conditions for the convection-diffusion equation. *IMA Journal of Numerical Analysis*, **16**, 583–598.
- Wigeland R.A. (1978). *Grid Generated Turbulence with and without Rotation about the Stream-wise Direction*. Ph.D. thesis, Illinois Institute of Technology.
- Wilcox D.C. (1993). *Turbulence Modeling for CFD*. DCW Industries, Inc.
- Wilcox W.C. (1988). Reassessment of the scale-determining equation for advanced turbulence models. *AIAA J.*, **26**, 1299–1310.
- Wyngaard J.C. and Peltier L.J. (1996). Experimental micrometeorology in an era of turbulence simulation. *Bound. Layer Meteor.*, **78**, 71–86.
- Yakhot A., Orszag S.A., Yakot V. and Israeli M. (1990). Renormalization group formulation of large-eddy simulation. *J. Sci. Comput.*, **4**, 139–158.
- Yeh T.T. and Mattingly G.E. (1994). Pipe flow downstream of a reducer and its effects on flowmeters. *Flow Meas. Instrum.*, **5**, 181–187.
- Zhang Z. and Wu J. (1987). On principle noise of the laser doppler velocimeter. *Exp. Fluids*, **5**, 193–196.
- Zhou Y. (1995). A phenomenological treatment of rotating turbulence. *Phys. Fluids*, **7** (8), 2092–2094.

Samenvatting

Het onderwerp van dit proefschrift is de stroming van een vloeistof door een pijp met ronde doorsnede. Maar dan wel een stroming met drie extra complicaties: de stroming is turbulent, de vloeistof roteert om de lengte-as van de pijp (een kurkentrekker-beweging, *swirl*) en de stroming ondervindt een vervorming in de lengte-richting (stroming door een vernauwing, *axial strain*). De onderzochte stroming is een prototype voor een scala van stromingen dat in de praktijk voorkomt. In cycloon scheiders wordt de *swirl* gebruikt om stoffen met verschillende dichtheden (bijvoorbeeld olie en water) te scheiden. De *axial strain* kan zowel als functie hebben dat de *swirl* versterkt wordt, als dat de terugstroming noodzakelijk voor het scheidingsproces, vergroot wordt. Een ander voorbeeld van de combinatie van *swirl* en *axial strain* is de verbrandingskamer. Daarin worden beide stromingseigenschappen gebruikt om de vlam te stabiliseren.

Het algemene doel van het onderzoek is het vergroten van het inzicht in het stromingstype 'turbulente stroming met *swirl* en *axial strain*'. De middelen om dat doel te bereiken zijn laboratorium experimenten en numerieke simulaties. Op grond van het algemene doel zijn de volgende doelen en vragen geformuleerd:

- Wat is de huidige kennis in de literatuur over turbulente stromingen met *swirl*, *axial strain* en de combinatie van die twee?
- Wat zijn de karakteristieken van, en mechanismen in, turbulente pijpstroming met *swirl* en *axial strain* zoals die blijken uit laboratorium metingen?
- Welke aanpassingen moeten worden gedaan aan een bestaand *Large Eddy Simulation* (LES) model voor pijpstroming om het geschikt te maken voor de simulatie van een stroming met *swirl* door een contractie? Hoe goed presteert dat aangepaste model in vergelijking met de verzamelde laboratoriummetingen?
- Welke extra inzichten kunnen worden ontleend aan de LES resultaten m.b.t. de turbulente stroming met *axial strain* (en *swirl*)?

Een analyse van de bestaande literatuur met betrekking tot turbulente stromingen met *swirl*, *axial strain* of een combinatie van die twee, leidt tot het volgende beeld. Het stromingsdomein kan worden verdeeld in drie gebieden. Stroomopwaarts van de contractie, de contractie zelf, en stroomafwaarts van de contractie.

Stroomopwaarts van de contractie is de stroming een langzaam uitdovende *swirl*-stroming, die gedomineerd wordt door niet-lineaire processen. Enerzijds zijn er de effecten van stroomlijnkromming: stabiliserend nabij de pijp-as, en destabiliserend nabij de wand. Verder wordt de turbulente dissipatie onderdrukt door de rotatie in de stroming. Tenslotte is de stroming drie-dimensionaal het wandgebied.

Vervolgens beweegt de vloeistof door de contractie: een combinatie van *swirl* en *axial strain*. Het effect van de vervorming wordt goed beschreven door lineaire theory, maar het wordt sterk beïnvloed door niet lineaire processen als gevolg van stroomlijnkromming.

Tenslotte, is er stroomafwaarts van de contractie weer een gebied met een uitdovende *swirl*-stroming. Het snelheidsveld is echter ernstig vervormd door de *axial strain*. Daardoor heeft de stroming ook de karakteristieken van een ontwikkelende pijpstroming. Maar er zijn complicaties: de terugkeer naar een volledig ontwikkelde stroming kan beïnvloed worden door de effecten van stroomlijnkromming. Bovendien is de stroming pas weer volledig in evenwicht wanneer ook de *swirl* uitgedoofd is.

In het laboratorium is een uitgebreide dataset verzameld met betrekking tot een prototype van de bestudeerde stroming: turbulente pijpstroming (water) door een contractie (die zorgt voor de *axial strain*), zowel met als zonder *swirl*, en bij twee Reynoldsgetallen. Metingen aan het snelheids veld zijn gedaan door middel van Laser Doppler Anemometry (LDA) op twee locaties stroomopwaarts van de contractie, en vier locaties stroomafwaarts. Behalve voor het beantwoorden van die vraag is de gegevensset ook van belang voor turbulentie-modellereurs. Zij kunnen de gegevens gebruiken als toetssteen voor hun modellen.

De experimentele resultaten voor de stroming zonder *swirl* laten zien dat stroomafwaarts van de contractie de axiale snelheid uniform geworden is over de pijpdwarsdoorsnede, evenals de turbulente normaalspanningen. De anisotropie van de turbulente stressen verandert geheel in overeenstemming met resultaten van lineaire theorie (de axiale normaalspanning neemt af ten gunste van de normaalspanningen loodrecht op de stromingsrichting). 40 pijpdiameters stroomafwaarts van de contractie heeft de gemiddelde snelheid zich weer ontwikkeld tot een profiel karakteristiek voor een ontwikkelde pijpstroming. Dit geldt echter niet volledig voor de turbulente schuifspanning.

In het geval van de stroming met *swirl* is eerst gekeken naar het effect van de contractie op de profielen van de gemiddelde axiale en tangentiële snelheid. Dat effect is op zijn minst kwalitatief in overeenstemming met de wrijvingsloze benadering van Batchelor (1967): de axial snelheid ontwikkelt neemt toe nabij de pijp-as, en het profiel van de tangentiële snelheid wordt gekromd. De contractie beïnvloedt de uitdoving van de *swirl*-sterkte nauwelijks. In de laag nabij de pijpwand zijn de gemiddelde stroming, de schering en de schuifspanning min of meer parallel: er is geen sprake van een sterk drie-dimensionale grenslaag. Het gedrag van de turbulente normaal- en schuifspanningen is uitgebreid bestudeerd. De belangrijkste conclusies zijn als volgt. Het effect van de contractie op de anisotropie van de spanningstensor (op de pijp-as) is zwakker voor de stroming met *swirl* dan voor die met *swirl* (kwalitatief in overeenstemming met lineaire theorie). Verder stroomafwaarts is er een duidelijk verschil tussen de stromingen met verschillende Reynolds getallen: dit is waarschijnlijk het gevolg van het feit dat bij het lagere Reynolds getal de rotatie sneller uitdooft, en de reistijd van de vloeistof tot het gegeven punt langer is zodat de turbulentie meer tijd heeft gehad om zich te herstellen van de vervorming in de contractie. Tenslotte blijkt dat het karakter van de turbulente spanningstensor sterk verschilt tussen de stromingen met en zonder *swirl*: in de stroming zonder *swirl* is de tensor bijna overal (axiale en radiale locaties) axisymmetrisch met één hoofdas. In de stroming met *swirl* de tensor is minder axisymmetrisch, en heeft nabij de pijp-as één hoofdas, en nabij de wal twee hoofdassen. Het is belangrijk om te bedenken dat een aantal van de hier gevonden resultaten specifiek zijn voor deze stroming: wanneer de *swirl* op een andere wijze was gegenereerd zouden in ieder geval details van de stroming anders zijn.

Het in dit onderzoek gebruikte Large Eddy Simulation (LES) model, is gebaseerd op een

model voor pijpstroming dat ontwikkeld is aan de Technische Universiteit Delft. Om het model geschikt te maken voor de simulatie van een stroming met *swirl*, door een contractie moesten een groot aantal aanpassingen worden gemaakt. Het coördinaatstelsel moest worden aangepast om een domein met een variabele pijpdiameter te kunnen genereren. Naast consequenties voor de gediscrètiseerde vergelijkingen, had dit ook een grote verandering in de tot gevolg in de methode voor het uitrekenen van het drukveld. Verder waren veranderingen in de tijdsdiscrètisatie noodzakelijk: op een aantal plaatsen in het domein, en voor een aantal termen moest een impliciete tijdsdiscrètisatie worden gebruikt om te voorkomen dat de numerieke tijdstap te zeer gelimiteerd zou worden. In het sub-grid stress model moest de demping door de nabijheid van de wand worden aangepast, omdat de afstand tot de wand in termen van de visceuze lengteschaal y^+ (zoals gebruikt in de Van Driest demping) in het huidige domein slecht gedefinieerd is. Omdat de onderzochte stroming zich ontwikkelt in de axiale richting kan geen gebruik meer worden gemaakt van periodieke randvoorwaarden. Aan de uitstroomzijde van het domein wordt een convectieve randvoorwaarde gebruikt. Aan de instroomzijde wordt een snelheidsveld opgelegd dat is verkregen uit een aparte simulatie in een rechte pijp met periodieke randvoorwaarden. Voor de stroming met *swirl* wordt de *swirl* ook opgewekt in die aparte simulatie. Hiertoe wordt een forcering aan de u_θ -vergelijking toegevoegd die afhankelijk is van het \bar{u}_θ -profiel in de simulatie en het in de metingen waargenomen \bar{u}_θ -profiel. Tenslotte heeft het feit dat het model niet langer homogeen is in de axiale richting ook een belangrijk effect op het berekenen van statistische grootheden uit de LES resultaten: er is één homogene richting, waarover gemiddeld kan worden, minder. Dit heeft vergaande consequenties voor de statistische fout in de resultaten.

De resultaten van de LES van de stroming zonder *swirl*, bij een bulk Reynolds getal van 20000, laten zien dat het model goed in staat is deze stroming te simuleren. De belangrijkste tekortkoming is dat stroomafwaarts van de contractie de radiale snelheidsfluctuaties nabij de wand door het model worden overschat. Bij de stroming met *swirl* zijn de discrepanties groter. De snelheidsvelden die gebruikt worden als randvoorwaarde aan de instroomzijde van het domein komen al niet geheel overeen met de metingen. Het \bar{u}_θ -profiel klopt wel, omdat dat door de methode voor het forceren van de *swirl* wordt opgelegd. Maar de forceringsmethod levert niet de juiste profielen voor \bar{u}_z (niet de juiste vorm) en turbulente grootheden (niet de juiste intensiteit) op. Dit is het gevolg van het feit dat de stroming stroomopwaarts van de contractie sterk bepaald wordt door niet-lokale effecten die niet in een lokale focering kunnen worden gevat. Als gevolg van de discrepantie in de stroomopwaartse profielen, kunnen de profielen stroomafwaarts van de contractie slechts kwalitatief worden vergeleken met de metingen. Binnen die beperking blijkt het model de metingen op een aantal punten goed te reproduceren. Wel wordt de axiale afname van \bar{u}_θ in het model onderschat. De ontwikkeling van de anisotropie van de turbulente spanningstensor in het model is echter zowel in overeenstemming met de metingen, als met de lineaire theorie.

De LES resultaten zijn ook gebruikt om te kijken naar de ontwikkeling van gemiddelde snelheden en de turbulente spanningstensor op plaatsen waar geen metingen beschikbaar zijn, door het maken van een dwarsdoorsnede van de pijp. Het blijkt dat de aanwezigheid van de contractie de stroming slechts over een axiale afstand van een halve pijp diameter zichtbaar is in het snelheidsveld. De in het model gebruikte afstand tussen het instroomvlak en de contractie (1.8 pijp diameters) was dus ruim voldoende. Verder konden uit de velden van de elementen van

de spanningstensor variaties in profielen stroomafwaarts van contractie verklaard worden. Deze hadden hun oorsprong binnen de contractie.

Tenslotte zijn ook de budget-termen voor de turbulente stresstensor berekend. Hieruit blijkt dat de profielen voor die budgettermen stroomopwaarts en stroomafwaarts van de contractie niet veel verschillen in vorm, maar wel in grootte. In het geval van de stroming zonder *swirl* zijn de termen met name groot nabij de wand, terwijl in de stroming met *swirl* het gebied rond de pijpas minstens even hoge waarden laat zien. Naast de profielen van de budget-termen, zijn ook de budgettermen in de gehele doorsnede van het domein bekeken. Daaruit blijkt dat in de contractie de budgettermen zich geheel anders gedragen. Voor een aantal elementen van de spanningstensor veranderen termen zelfs van teken.

De in dit proefschrift gepresenteerde laboratoriummetingen van een turbulente stroming met *swirl* en *axial strain* kunnen uitstekend gebruikt worden als toetssteen voor turbulentie modellen. Verder is aangetoond dat het in principe mogelijk is om een LES van deze stroming te doen. De methode voor het forceren van de *swirl* in de instroom randvoorwaarde heeft echter nog verbetering. Verder moet er aandacht geschonken worden aan het probleem van de grote statistische fout in turbulente grootheden wanneer slechts twee homogene richtingen (tijd en de tangentiële richting) beschikbaar zijn voor middeling.

Dankwoord

Het produceren van een proefschrift is nooit het werk van een eenling. Ook al was het vaak een eenzame bezigheid, toch hebben velen op uiteenlopende wijzen bijgedragen aan het feit dat dit proefschrift er nu ligt.

Aan de wieg van het onderzoeksvoorstel stonden mijn promotoren Gert-Jan van Heijst (TU Eindhoven) en Frans Nieuwstadt (TU Delft). Zij hebben mij op pad gestuurd met een –naar achteraf blijkt– nogal omvangrijke opdracht. Maar ze hebben mij ook –ondanks hun mogelijke wanhoop– zonder ophouden gestimuleerd om door te gaan en af te ronden (“Wat je nu hebt is meer dan voldoende, begin snel met opschrijven!”). Jan Voskamp wil ik graag hartelijk danken voor zijn dagelijkse begeleiding. Volgens mij is het voor een begeleider niet eenvoudig om vat te krijgen op iemand die zo zelfstandig werkt als ik. Achteraf gezien denk ik dat ik jouw capaciteiten onvoldoende benut heb. Verder wil ik de overige leden van de kerncommissie (Bert Brouwers en Bert Holtslag) danken voor inzet om zich door dit proefschrift heen te werken.

De twee onderzoekstechnieken die ik in dit onderzoek heb gebruikt (LDA en LES) waren voor mij zo goed als onbekend terrein toen ik aan het onderzoek begon. Om te beginnen wil ik Wiendelt Steenbergen (mijn ‘voorganger’) hartelijk danken voor het feit dat hij mij heeft willen inwerken in de meettechniek en de opstelling, op het moment dat hij zelf druk doende was zijn proefschrift af te ronden. Bendiks-Jan Boersma ben ik veel dank verschuldigd voor zijn inzet om mij wegwijs te maken in het LES-model van Jack Eggels. Ook het werk van Bas van Haarlem, die als student gewerkt heeft aan LES van uitdovende swirl stroming is voor mij van belang geweest (Bas heeft, net als vele anderen, mij ingehaald wat promoveren betreft).

Toen ik begon was er een opstelling voor het meten van uitdoving van swirl. Om die geschikt te maken voor het meten aan een stroming met swirl en axial strain moest er nogal wat gebeuren. Allereerst heeft Johan Stouthart mij zonder ophouden geholpen bij het uitdenken, ontwerpen en laten maken van de aanpassingen die nodig waren. Hij introduceerde me in de faculteitswerkplaats en hield zelf ook in de gaten of alles liep zoals het moest. Na zijn vertrek is zijn werk overgenomen door Pim Sluijter en Gerald Oerlemans (die toen hij nog in de werkplaats werkte ook al tekende voor het construeren van een aantal onderdelen). Voor hun hulp bij alle stappen die te maken hebben met het registreren, opslaan en verwerken van de meetgegevens wil ik graag bedanken: Jan Niessen, Gerard Trines en Roger van Galen. Van buiten de vakgroep wil ik graag de heer Sonnemans bedanken die mij een theodoliet beschikbaar stelde voor het opnieuw uitlijnen van de LDA-optica (nadat een glazenwasser zo verstandig was geweest met zijn ladder achter de opstelling langs te lopen!).

Verder wil ik alle collega’s van de vakgroep Transportfysica TU/e en het Lab voor Aero- en Hydrodynamica TUD bedanken voor hun discussies, praatjes, en hun gezelschap tijdens koffie-, thee- en lunchpauzes en andere gemeenschappelijke activiteiten (en met name mijn kamergenoten op verschillende momenten en plekken: Wiendelt Steenbergen, Fred Stoffels, Herbert Zondag en Bendiks-Jan Boersma).

Mijn huidige collega's van de Leerstoelgroep Meteorologie en Luchtkwaliteit van Wageningen Universiteit wil ik hartelijk danken voor hun niet aflatende vragen naar 'het boekje' en 'de datum': altijd belangstellend, nooit venijnig. Ik was blij om na $4\frac{1}{2}$ jaar laboratorium onderzoek terug te mogen keren naar het grootste lab met de hoogste Reynolds getallen: de atmosfeer.

As an aside I would like to express my gratitude to all people that have contributed to the open source software that I have used extensively: GNU/Linux, the GNU Compiler Collection (among others: Toon Moene, my brother, who contributed to, and maintains, the g77 FORTRAN-compiler), gnuplot, pplot-library, xfig, L^AT_EX, Python (with all numerical extensions), the NSPCG library (University of Texas, Austin), OpenOffice.org, and probably others whom I forgot. I have tried, and will try, to give back some effort to the open source community.

Buiten de werkomgeving ben ik veel dank verschuldigd aan vrienden, familie en kennissen die ook altijd maar weer durfden te vragen naar de inhoud en de voortgang van mijn proefschrift. Met name mijn ouders wil ik bedanken omdat ze me hebben grootgebracht met het adagium dat je moet afmaken waaraan je begint. Zonder die opvoeding had dit proefschrift hier nu niet gelegen. Maar ook hun eindeloze vertrouwen in de goede afloop en hun toegewijde taakopvatting als opa en oma (oppas) hebben dit proefschrift mogelijk gemaakt.

Ten slotte wil hen die het van heel dichtbij hebben moeten doorstaan danken voor hun liefde, incasseringsvermogen en vertrouwen: Berenice, Christine en Elianne. De vraag of het het allemaal waard was is nu niet meer relevant. Het is af! Ik hoef niet meer aan "papa's boekje" te werken.

Curriculum Vitae

2 mei 1967	geboren te Amsterdam
1979-1985	VWO, Christelijk Scholengemeenschap Pascal te Amsterdam
1985-1986	HTS werktuigbouw, Amstel HTS te Amsterdam
1986-1992	Tropische Cultuurtechniek en Bodem, Water en Atmosfeer (beide vrije oriëntatie, beide <i>cum laude</i>), Landbouw Universiteit Wageningen
1992	onderzoeksassistent Vakgroep Meteorologie, Landbouw Universiteit Wageningen (april-juli: data-analyse EFEDA-experiment)
1992	onderzoeksassistent Winand Staring Centrum (augustus-oktober: meteorologisch-hydrologisch veldwerk in Niger, West-Afrika)
1992-1993	vervangend dienstplicht, Vakgroep Meteorologie, Landbouw Universiteit Wageningen en Koninklijk Meteorologisch Instituut ('Validation of the surface parametrization of HIRLAM using surface-based measurements and remote sensing data')
1994-1998	assistent in opleiding, Vakgroep Transportfysica, Technische Universiteit Eindhoven ('Swirling flows with axial strain')
1998-nu	toegevoegd onderzoeker, Leerstoelgroep Meteorologie en Luchtkwaliteit, Wageningen Universiteit